Université de Liège

Wallonia-Europe University Academy

Faculty of Applied Sciences

GIGA-Cardiovascular Sciences
Thermodynamics of Irreversible Processes

Numerical modeling of the cardiac mechano-electric feedback within a thermo-electro-mechanical framework

Study of its consequences on arrhythmogenesis

by **Arnaud Collet**
Master in Engineering Physics

supervised by Professor P. C. Dauby
and co-supervised by Professor J. P. Ponthot

A thesis submitted in partial fulfillment of the requirements
for the degree of Doctor of Philosophy in Engineering Sciences

May 2015

The present dissertation has been examined by the jury members

- Ph.D. R. Boman, University of Liège, Belgium
- Pr. J. Bragard, University of Navarra, Spain
- Pr. P. C. Dauby, supervisor, University of Liège, Belgium
- Ph.D. T. Desaive, University of Liège, Belgium
- Pr. L. Geris, University of Liège, Belgium
- Pr. P. Kolh, University of Liège, Belgium
- Pr. J. P. Ponthot, co-supervisor, University of Liège, Belgium

The research described in the present dissertation was financially supported by the Research Training Fund for Industry and Agriculture (FRIA) and the Wallonia-Brussels Federation (Joint Research Actions).

Remerciements

Je tiens à remercier le Fonds pour la formation à la Recherche dans l'Industrie et dans l'Agriculture (FRIA) et l'Université de Liège pour le support financier qu'ils m'ont apporté au cours de ces années de doctorat. Grâce à leur soutien, j'ai pu m'investir totalement dans mon projet de recherche. Je remercie également la Fédération Wallonie-Bruxelles qui m'a permis, dans le cadre du Concours des bourses de voyage 2012, de séjourner trois mois au sein du Cardiac Mechanics Research Group (CMRG) de l'Université de Californie à San Diego.

En premier lieu, je tiens à remercier mon promoteur de thèse, le Professeur Pierre C. Dauby. Pierre, j'ai particulièrement apprécié ton sens critique, ta rigueur scientifique ainsi que ta disponibilité tout au long de mes années de recherche au sein de ton labo. Tu as toujours répondu présent avec enthousiasme lorsque j'en éprouvais le besoin et les échanges que nous avons eus étaient toujours très enrichissants.

Je remercie également le Dr. Thomas Desaive. Thomas, merci pour tes nombreuses relectures et pour tes commentaires souvent pertinents. Je te remercie également car tu as très souvent eu les mots justes pour dédramatiser certaines situations. Les PhD comics que tu affiches dans le couloir du deuxième étage du B5a m'ont fait très souvent sourire et ils reflètent bien, je trouve, le recul que tu sais prendre sur la recherche et les ‘problèmes’ quotidiens des chercheurs lorsque c’est nécessaire.

Je me dois également de remercier très sincèrement le Professeur Jean Bragard. Jean, merci pour ton accueil chaleureux lors de mon séjour en Espagne. J’ai vraiment apprécié travailler avec toi. Nos discussions m’ont très souvent permis de débloquer des situations qui me semblaient parfois insurmontables. Tu as souvent eu des idées très pertinentes qui m’ont permis d’aborder les choses avec un autre angle de vue. J’ai également apprécié les échanges que nous avons eus en dehors du cadre académique.

Je tiens à remercier le Professeur Jean-Philippe Ponthot et le Dr. Romain Boman pour les différents échanges que nous avons eus, notamment au sujet de problématiques liées à la mécanique des grandes déformations.

Évidemment, je remercie également tous mes collègues de labo, Hatim, Sabine, Sophie, Antoine, Sarah et Chris. Tous, à leur façon, ils m’ont permis de passer d’agréables moments au cours de ces années de doctorat. Je me souviens notamment de discussions philosophiques mémorables avec certains d’entre eux. J’ai également apprécié leur écoute à de nombreuses reprises.

Inno, François, Dodji, Berni, j’ai passé des temps de midi hors du temps grâce à vous. Le petit groupe que nous avons formé au fil de ces années avec nos petits rituels et nos discussions où on refaisait le monde autour d’un café me manque déjà. Vous m’avez toujours soutenu et compris dans les moments difficiles. Tous ces moments de vie, de rire, de tristesse, de joie, de stress, bref, tous ces moments de partage resteront gravés dans mon esprit.

Les sorties running légendaires du mardi avec Marc, *alias* le métronome ou le sage, avec Bernard, *alias* Berni ou la machine, avec Charles *alias* Sharlo ou l’homme des îles, m’ont permis de m’évader et de découvrir les nombreux sentiers du domaine du Sart Tilman. Et puis, quelle décharge d’endorphines pour le reste de l’après-midi du mardi. Merci XXL à la running team du B5a.

Je remercie également toutes mes amies et tous mes amis pour leur présence et leur patience. J’ai souvent dû répondre par la négative à leurs invitations. J’espère qu’ils en comprennent la raison. À vrai dire, je n’en doute pas. Merci à vous.

Sans ma famille, je ne serais pas celui que je suis. En particulier, Papa, Maman, Doudou, merci à vous d'avoir toujours soutenu mes choix et d'avoir été aussi présents tout au long de cette tranche de vie que représente cette thèse de doctorat. Il est difficile de résumer en quelques lignes tout ce que vous m'avez apporté, chacun à votre manière. Merci à vous de m'avoir transmis le goût de l'effort et du dépassement de soi. Merci à vous de m'avoir montré à de nombreuses reprises votre amour et votre fierté vis-à-vis de ce que je réalisais. Tout cela m'a donné beaucoup de courage et de motivation pour avancer malgré les obstacles qui se sont présentés sur cette longue route.

Caro, Amour, tu nous qualifiais d'électrons non appariés qui se sont finalement rencontrés et ont fait des étincelles. Je te répondrai que tu es pour moi une particule fondamentale d'une très grande valeur humaine et très complémentaire à celle que je suis. Il m'est impossible de résumer toutes les marques d'amour que tu m'as montrées au cours de ces deux dernières années au travers de gestes simples, au travers de gestes au quotidien. Tu es sans doute la personne qui comprend le mieux la complexité que je renferme. Tu comprends ma folie, mes angoisses, mes obsessions et surtout, ma façon d'aimer. Merci à toi d'être toi, Amour.

Abstract

This doctoral study characterizes, for simple geometries, the cardiac autonomous electrical activity induced by the mechanical deformations of the myocardium *via* the mechano-electric feedback within a thermo-electro-mechanical framework. The underlying fundamental mechanisms are highlighted and discussed in detail.

In a healthy heart, the mechano-electric feedback acts as a regulator able to damp mechanical perturbations undergone by the heart, by appropriately modulating electrical activity shortly after these perturbations. In this way, a new healthy electromechanical situation is recovered. However, under certain conditions, this feedback can be a generator of dramatic cardiac arrhythmias by inducing local electrical depolarizations resulting from abnormal cardiac muscle tissue deformations. These local perturbations can then propagate in the whole heart and, thus, lead to global cardiac dysfunctions.

The one- and two-dimensional models developed in this work to study the arrhythmogenic consequences of the mechano-electric feedback within a thermo-electro-mechanical framework account for three couplings: the excitation-contraction coupling, the mechano-electric feedback, and the thermo-electric coupling. The excitation-contraction coupling allows the mechanical contraction of cardiac muscle cells resulting from the electrical excitation of these cells, triggered by a propagating action potential initially generated by the sino-atrial node in a healthy heart. The mechano-electric feedback takes into account the influence of mechanical deformations on the electrical activity, both at the cell and the macroscopic level. The thermo-electric coupling then modulates certain electrical properties due to a temperature change.

The excitation-contraction coupling is modeled in a phenomenological way by combining the Aliev–Panfilov model and the Rogers–McCulloch model. The propagation of the electrical excitation through cardiac muscle tissue is modeled by using the monodomain approach. The mechano-electric feedback is taken into account by considering two different contributions, namely the physiological contribution (physiological feedback) and the geometric contribution (geometric feedback). The physiological feedback consists in the onset of stretch-activated currents due to the deformations of the cardiac muscle tissue *via* specific mechanosensitive channels. Regarding the geometric feedback, it simply reflects that the propagation of the depolarization waves is altered by the deformations of the geometry. The thermo-electric coupling is modeled *via* a dependence with respect to the temperature which is exponential for the gating kinetics of ion channels, exponential for the kinetics of the active tension development in cardiomyocytes, and linear for the ionic conductances.

This study shows that the mechano-electric feedback can be arrhythmogenic under specific conditions. In particular, this work clearly reveals that the size of the domain and the importance of stretch-activated currents are key factors in the behavior of the autonomous electrical activity induced by the mechano-electric feedback. This doctoral study also shows that temperature variations such as those undergone by the heart during therapeutic hypothermia or hyperthermia play a central role in the cardiac electromechanical behavior. Moreover, this work emphasizes the influence of the initial conditions on the electromechanical behavior of cardiac tissue. In the one-dimensional framework, an important result of this work is that the disappearance of the autonomous electrical activity induced by the deformations of the cardiac muscle can be associated with different types of bifurcation phenomena, depending on the values of the parameters. These bifurcations, which correspond in fact to different ways for the AEA to vanish, are emphasized and discussed in detail.

Résumé

Cette étude doctorale caractérise, dans le cadre de géométries simples, l'activité électrique autonome cardiaque induite par les déformations mécaniques du myocarde au travers du feedback mécano-électrique dans un contexte thermo-électro-mécanique. Les mécanismes fondamentaux sous-jacents sont mis en évidence et discutés en détails.

Dans un cœur sain, le feedback mécano-électrique agit comme un régulateur capable d'amortir des perturbations mécaniques ressenties par le cœur, en modulant de manière appropriée l'activité électrique subséquente à ces perturbations. De cette façon, une nouvelle situation électromécanique saine est retrouvée. En revanche, dans certaines conditions particulières, ce feedback peut être à l'origine d'arythmies cardiaques importantes en induisant localement des dépolarisations électriques générées par des déformations anormales du tissu musculaire cardiaque. Ces perturbations locales peuvent alors se propager à l'ensemble du tissu et de ce fait, induire des dysfonctionnements cardiaques globaux.

Les modèles unidimensionnels et bidimensionnel développés dans ce travail afin d'étudier les conséquences arythmogènes du feedback mécano-électrique dans un cadre thermo-électro-mécanique prennent en compte trois couplages : le couplage excitation-con-

traction, le feedback mécano-électrique et le couplage thermo-électrique. Le couplage excitation-contraction permet la contraction mécanique des cellules musculaires cardiaques qui résulte de l'excitation électrique de ces dernières provoquée par le passage d'un potentiel d'action, initialement généré au sein du nœud sinusal dans un cœur sain. Le feedback mécano-électrique rend compte de l'influence des déformations mécaniques sur l'activité électrique tant au niveau cellulaire qu'au niveau macroscopique. Enfin, le couplage thermo-électrique module certaines propriétés électriques suite à un changement de température.

Le couplage excitation-contraction est modélisé de manière phénoménologique en combinant les modèles de Aliev–Panfilov et de Rogers–McCulloch. La propagation de l'excitation électrique au sein du tissu musculaire cardiaque est modélisée en utilisant l'approche monodomaine. Le feedback mécano-électrique est pris en compte en considérant deux contributions distinctes, à savoir la contribution physiologique (feedback physiologique) et la contribution géométrique (feedback géométrique). Le feedback physiologique consiste en l'apparition de courants induits par les déformations du tissu musculaire cardiaque au travers de canaux mécano-sensibles particuliers. Quant au feedback géométrique, il traduit simplement que la propagation des ondes de dépolarisation est altérée par les déformations de la géométrie qui les supporte. Le couplage thermo-électrique est modélisé *via* une dépendance vis-à-vis de la température qui est exponentielle pour la cinétique d'ouverture et de fermeture des canaux ioniques, exponentielle pour la cinétique relative au développement de la tension active au sein des cardiomyocytes et linéaire pour les conductances ioniques.

Cette étude montre que le feedback mécano-électrique peut dans certaines conditions particulières être arythmogène. En particulier, cette étude montre clairement que la taille du domaine ainsi que la présence plus ou moins importante des courants induits par les déformations sont des facteurs déterminants dans le comportement de l'activité électrique autonome induite par le feedback mécano-électrique. Ce travail montre aussi que des variations de température telles que celles subies par le cœur lors d'une hypothermie thérapeutique ou lors d'une hyperthermie jouent un rôle central sur le comportement électromécanique cardiaque. Par ailleurs, cette étude met également en évidence l'importance des conditions initiales d'excitation sur le comportement électromécanique du tissu musculaire cardiaque. Dans le contexte unidimensionnel, un résultat important de ce travail est que la disparition de l'activité électrique autonome

induite par les déformations du muscle cardiaque peut être associée à différents types de phénomènes de bifurcation qui dépendent des valeurs des paramètres. Ces bifurcations, correspondant en fait à différents chemins que l'activité électrique autonome emprunte pour disparaître, sont mises en évidence et discutées en profondeur.

Contents

Glossary of acronyms

ADP	Adenosine Diphosphate
AEA	Autonomous Electrical Activity
AF	Atrial Fibrillation
AlP	Aliev–Panfilov
AP	Action Potential
APD	Action Potential Duration
ARP	Absolute Refractory Period
ARS	Absolute Refractory State
AV	Atrio-Ventricular
BC	Boundary Condition
CEC	Contraction-Excitation Coupling
CICR	Ca^{2+}-Induced Ca^{2+} Release
CKRKM	Cash–Karp Runge–Kutta Method
CV	Conduction Velocity
CVD	Cardiovascular Disease
DRS	Dark Red Spot
ECC	Excitation-Contraction Coupling

ERP	Effective Refractory Period
ERS	Effective Refractory State
FEM	Finite Element Method
FDM	Finite Difference Method
FH	FitzHugh
FK	Fenton–Karma
HH	Hodgkin–Huxley
HMT	Hunter–McCulloch–ter Keurs
IBVP	Initial Boundary-Value Problem
IC	Initial Condition
IVP	Initial Value Problem
LHS	Left-Hand Side
MEF	Mechano-Electric Feedback
ODE	Ordinary Differential Equation
PDE	Partial Differential Equation
PK2	Second Piola–Kirchhoff
PVW	Principle of Virtual Work
RHS	Right-Hand Side
RKMs	Runge–Kutta Methods
RM	Rogers–McCulloch
RRP	Relative Refractory Period
RRS	Relative Refractory State
SA	Sino-Atrial
SACs	Stretch-Activated Currents/Channels
SP	Supernormal Period
SR	Sarcoplasmic Reticulum
SS	Supernormal State
TEC	Thermo-Electric Coupling
TEM	Thermo-Electro-Mechanical
TH	Therapeutic Hypothermia
VF	Ventricular Fibrillation

Introduction

Motivations and framework

Cardiovascular diseases (CVDs) are the most common cause of death in the industrialized world. In 2008, an estimated 17.3 million people died from CVDs, representing 30 % of all global deaths [1]. The number of people who die from CVDs (mainly from heart disease and stroke) is forecast to reach 23.3 million by 2030 [1, 2] and CVDs will most probably remain the leading cause of death [2]. Within CVDs, a major cause of death is sudden cardiac arrest attributed to *ventricular fibrillation (VF)*[1], which is a specific kind of *cardiac arrhythmia*[2]. Another kind of rhythm disturbance called *atrial fibrillation (AF)* is also very common. Although not as immediately life-threatening as VF, AF causes a significant proportion of all strokes due to clot formation from stagnation of blood in the atria. As a result, AF is a very important pathology to deal with.

Some arrhythmias in ventricles [3] and atria [4] have been shown to be caused by me-

---

[1] Ventricular fibrillation consists in a fast-developing electrical disturbance in the heart's rhythm that renders the pumping function inefficient or completely null.

[2] Cardiac arrhythmia is a generic term used to refer to any rhythm disorder in the heart.

chanical changes inducing several electrophysiological alterations *via mechano-electric feedback (MEF)*. MEF is also called *contraction-excitation coupling (CEC)* [5] in reference and in contrast with the *excitation-contraction coupling (ECC)* [6], which describes the contraction of cardiomyocytes as a result of electrical excitation previously triggered inside these cells. The terms *cardiac MEF* refer to the various phenomena related to modulation of electrophysiology by mechanical deformation of cells and tissues of the heart [7]. Under specific conditions, a very interesting phenomenon induced by the MEF can be observed in the cardiac tissue that is referred to in this work as *autonomous electrical activity (AEA)*. This phenomenon consists in the onset of spontaneous electrical activity in the cardiac tissue due to mechanical deformation of the latter. Depending on several parameters, this AEA can be more or less organized in space and time.

Although advances in the field of cardiac resuscitation have led to the return of spontaneous circulation in many victims of cardiac arrest, only a small proportion of these survive to hospital discharge. The main causes of this fact are brain and cardiovascular damages due to global ischemia/reperfusion injuries. So far, *therapeutic hypothermia (TH)* is known as the most efficient treatment for reducing post-resuscitation brain damage from a cardiac arrest. The mechanisms underlying the neuroprotection of TH are multifaceted. For instance, one of them is the fact that TH reduces glucose and oxygen consumption in the cerebral metabolism, so that existing stores last longer before damage occurs [8, 9, 10]. In addition, some preclinical studies have shown that TH also has a protective effect on the myocardium. Although the mechanisms by which TH enhances cardioprotection have not been as thoroughly elucidated as in the brain, several potential explanations have been proposed such as preservation of cellular energy and viability [11, 12, 13, 14, 15].

In this context, this work aims at gaining insight into the mechanisms leading to the modulation of the electrical activity of cardiac muscle due to its deformations (*e.g.* atrial stretching) *via* the MEF within a *thermo-electro-mechanical (TEM)* framework. In particular, the spatio-temporal behavior of the AEA generated and sustained by the MEF will be studied with respect to the different model parameters. The influence of temperature variations, such as those observed during TH or hyperthermia, on the electromechanical behavior of cardiac muscle will be characterized, taking into account three temperature-dependent electrophysiological properties. For this purpose, computational models in one-dimensional and two-dimensional geometries will be developed and will take into account different coupled submodels:

i. a cell model describing cardiac electrical excitation
ii. a model accounting for the propagation of electrical excitation through cardiac tissue
iii. a model providing passive and active mechanical properties of cardiac muscle
iv. a model taking into account the influence of a temperature variation on cardiac electrical activity

Outline

Chapter 1 introduces the general framework within which the heart works. The structure and anatomy of the latter are described from a macroscopic and a microscopic point of view as well. Some main concepts relative to the physiology of the heart are also introduced.

Chapter 2 aims at introducing general concepts about cardiac electrophysiology modeling. First, this chapter emphasizes the underlying theoretical key points for modeling cardiac electrophysiology. Second, it describes some important phenomenological (or qualitative) and quantitative models mimicking the membrane potential dynamics at the cellular level, resulting from the dynamics of all ionic currents through the cell membranes. The famous formulation established by *Hodgkin* and *Huxley* in 1952 [16] is presented for the three main ionic currents in the giant axon of squid: the sodium current, the potassium current, and a so-called leakage current. This formulation is still used nowadays in a lot of state-of-the-art ionic models. Then, three phenomenological models for describing electrical cardiac excitation, based on the formulation developed by Hodgkin and Huxley, are described. The equations and the main features of the *FitzHugh model* [17], the *Rogers–McCulloch model* [18], and the *Aliev–Panfilov model* [19] are presented. These kinds of models are very interesting because their properties can be analytically studied using phase space diagrams. To emphasize the complexity of biophysical models in comparison with phenomenological ones, the *Fenton–Karma model* [20] is also described briefly. Finally, this chapter presents two different approaches to model the propagation of a local depolarization:

i. the monodomain formulation
ii. the bidomain formulation

Chapter 3 deals with cardiac mechanics. This part of the work has been written with the intention to provide an overview of general assumptions and to define key notions relative to continuum mechanics. The kinematics of a continuous body is described and the balance principles controlling all continuous bodies independently of their intrinsic properties are presented. Moreover, this chapter presents some general implications on the macroscopic models resulting from the microstructural architecture of the cardiac muscle. Finally, the procedure to account for the active tension is explained as well as the assumptions associated with this active tension.

Chapter 4 describes the strong (bidirectional) cardiac electromechanical coupling, including both ECC and MEF, which are essential for normal functioning of a healthy heart. More specifically, the active tension development, resulting from the ECC and the *stretch-activated currents (SACs)*, one of the main physiological contributions to the MEF, are briefly introduced. Two different ways for modeling the active tension development in cardiomyocytes are depicted:

i. the *Hunter–McCulloch–ter Keurs model* [21], specially designed for electromechanical simulations at the cardiac tissue-level
ii. the *single ordinary differential equation*, the approach adopted in this work

Modeling of the SACs, which are the physiological contribution to the MEF taken into account in this work, is then explained. In addition, the modeling of the influence of mechanical deformations on depolarization wave propagation is introduced by rewriting the monodomain equation in an appropriate way. Finally, the weak (unidirectional) *thermo-electric coupling (TEC)*, mimicking the modulation of cardiac electrophysiology due to a temperature variation, is taken into account by three temperature dependent properties:

i. the gating kinetics of ion channels, which shows an exponential dependence with respect to the temperature
ii. the kinetics relative to the active tension development in cardiomyocytes, which shows an exponential dependence with respect to the temperature
iii. the ionic conductances, which show linear dependencies with respect to the tem-

perature

All these key theoretical and modeling elements relative to the different couplings have been taken into account to develop one single mathematical method. This time-dependent thermo-electro-mechanical (TEM) model of the cardiac muscle tissue is presented at the end of this chapter.

Chapter 5 introduces the methods used and developed in this doctoral study and extensively discusses the original results obtained in this work. This chapter is made up of two parts. The first part is dedicated to a one-dimensional framework whereas the second one considers a two-dimensional framework. Chapter 5 presents and discusses results from numerical simulations performed with the time-dependent TEM model developed in chapter 4 for specific conditions. Due to the intrinsic complexity of this model, additional difficulties arising from realistic geometries or three-dimensional spatial configurations are avoided by using simplified geometries.

The first part of chapter 5 introduces a one-dimensional time-dependent TEM model and a simplified version of this model. A comparison between these two models is then performed which enables to show that the simplified model is suitable to describe the thermo-electro-mechanical behavior of cardiac tissue in a one-dimensional configuration. Besides, a parametric study of the simplified model is conducted to determine the role played by the different model parameters. The arrhythmogenic effects of the MEF are then characterized in terms of the key parameters regarding the MEF phenomenon and the underlying mechanisms are highlighted and discussed. The influence of temperature changes on these arrhythmogenic effects is also examined in detail. In addition, the role played by the initial conditions on the electromechanical behavior in a TEM framework is underlined and discussed. Finally, a Floquet stability analysis is conducted to characterize the way the autonomous electrical activity induced by the MEF disappears.

The second part of chapter 5 is devoted to an extension of the one-dimensional study to a two-dimensional framework. This two-dimensional study is mainly qualitative and is conducted in the spirit of paving the way for further more extensive and quantitative studies. Similar questions to those addressed in the one-dimensional framework are examined from a qualitative point of view. For this purpose, a finite element model has been developed using the software COMSOL Multiphysics®.

Finally, the original key results from this doctoral study are summarized and some perspectives are suggested to go further into the different issues tackled in this work.

Some mathematical notations

In the literature, different conventions are used to write vector and second-order tensor operations. Therefore, to avoid any confusion, the notations used in this work are presented here.

Both lowercase and uppercase Latin or Greek letters are used for *scalars*. Lowercase and uppercase bold-face Latin letters are used for *vectors* and *second-order tensors*.

The *dot product* (*scalar product* or *inner product*) of two vectors **a** and **b** is a scalar and denoted by

$$\mathbf{a} \cdot \mathbf{b} \,.$$

The *cross product* (or *vector product*) of two vectors **a** and **b** is a vector perpendicular to both **a** and **b** and denoted by

$$\mathbf{a} \times \mathbf{b} \,.$$

The *dot product* of two second-order tensors **C** and **D** is a second-order tensor and denoted by

$$\mathbf{C} \cdot \mathbf{D} \,.$$

The *scalar product* of two second-order tensors **C** and **D** is a scalar and denoted by

$$\mathbf{C} : \mathbf{D} \,.$$

The *dot product* of a second-order tensor **C** with a vector **a** is a vector and denoted by

$$\mathbf{C} \cdot \mathbf{a} \,.$$

The Einstein summation convention is used in this work. Repeated index implies summation over this index. For instance, the dot product of two vectors **a** and **b** may be written as

$$\mathbf{a} \cdot \mathbf{b} = \sum_{i=1}^{3} a_i \, b_i = a_i \, b_i \,.$$

CHAPTER 1

Background: cardiac physiology and anatomy

This doctoral study is mainly focused on the modeling of the electromechanical behavior of cardiac tissue from a macroscopic point of view. This approach often requires simplifications or assumptions regarding the stream of complex molecular mechanisms leading to the final cardiac contraction for reasons of computational cost. However, to present a complete picture of cardiac contraction, it is important to provide some background to the key elements of the basic microscopic mechanisms leading to the synchronized contraction of the entire cardiac muscle. This chapter establishes a global view of the structure of cardiac tissue at a microscopic level to provide context for the modeling of the macroscopic level. It also briefly introduces the context in which the heart works.

Contents

1.1 Global anatomy of the heart

The heart can be viewed as two separate pumps in series. The first one is called the *left heart*, and the second one the *right heart*. The left heart pumps blood through the peripheral organs (*systemic circulation*) and the right one pumps blood through the lungs (*pulmonary circulation*) (Fig. 1.1). Each heart is composed of two chambers: an *atrium* and a *ventricle* (Fig. 1.2). The atria are weak pumps that help blood to move into the ventricles while the left and right ventricles act as the main pumps and propel the blood through the systemic and pulmonary circulations, respectively.

As shown in Fig. 1.2, there are also four *valves* in the heart. These valves enable unidirectional blood flow through the heart by restricting retrograde flow. The *atrio-ventricular (AV)* valves are found between atria and ventricles. The left one is called the *mitral* valve while the right one is referred to as the *tricuspid* valve. The *aortic* valve is located between the left ventricle and the *aorta*. As a result, it controls the blood flow between the left ventricle and the aorta. The *pulmonary* valve is found between the right ventricle and the *pulmonary artery* and, therefore, controls the blood flow between the right ventricle and the pulmonary pathway.

1.2 Structure of cardiac tissue

The pumping function of the heart is the result of a rhythmic cycle of contraction and relaxation of about 10 billion muscle cells called *cardiomyocytes*. These cells are cable-like structures, approximately cylindrical in shape, and typically 100 μm long and

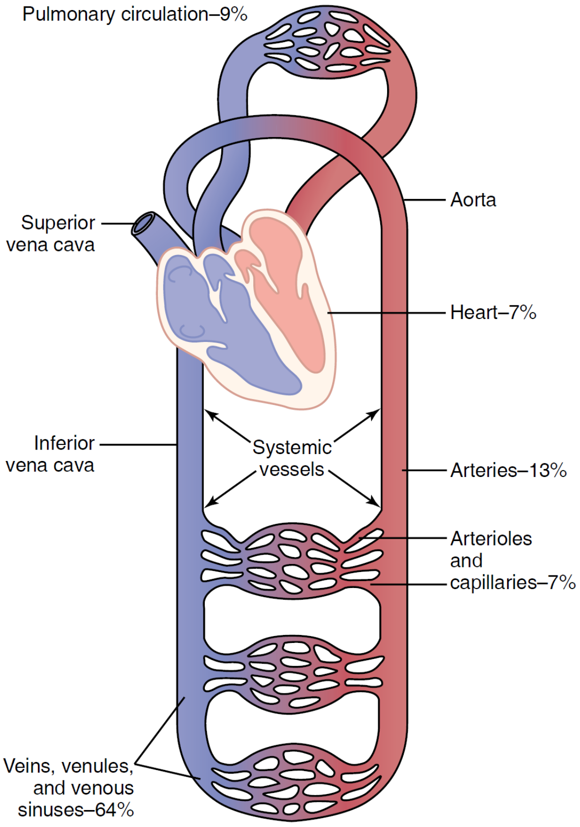

Fig. 1.1 – **Schematic representation of the cardiovascular system (CVS). The distribution of the amount of blood in each part of the CVS is indicated in terms of percentages of the total amount of blood contained in the CVS [22].**

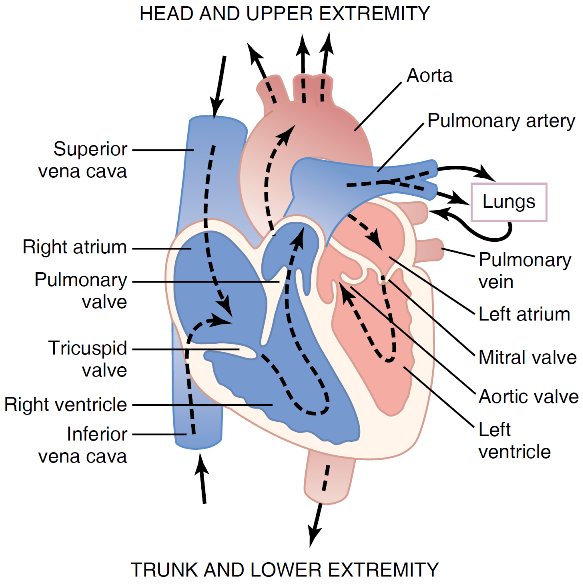

Fig. 1.2 – **Global structure of the heart. The black dashed arrows indicate the pathway of the blood flow through the different parts of the heart [22].**

15 μm in diameter. The spatial organization of the cardiomyocytes looks like a three-dimensional irregular brick-like packing, surrounded by extracellular medium (Fig. 1.3) [23].

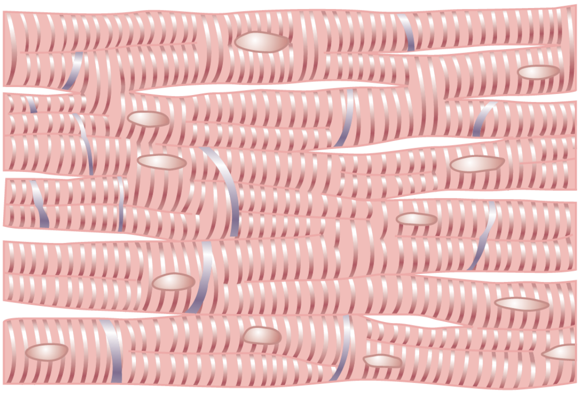

Fig. 1.3 – Cardiomyocytes are mechanically and electrically interconnected due to intercalated discs [22].

Cardiac muscle works as a *syncytium* due to the interconnection between cardiomyocytes. Each cardiomyocyte is connected with its neighboring cells, mainly in an end-to-end fashion, due to specialized contacts called *intercalated discs* (Fig. 1.3). These structures enable mechanical and electrical coupling of the cardiomyocytes.

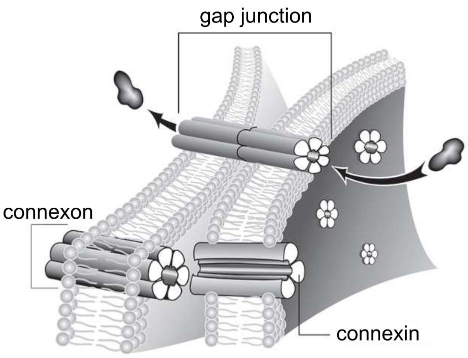

Fig. 1.4 – Structure of gap junctions [24].

Intercalated discs consist of three components: *gap junctions* (electrical coupling), *desmosomes*, and *fasciae adherents* (mechanical coupling). Gap junctions consist of intercellular channels, which form direct contact between the intracellular spaces of two neighboring cells. As shown in Fig. 1.4, each gap junction is built of two *hemichannels* (or *connexons*). Each connexon is made up of six protein subunits called *connexins*[1],

---

[1] There are several kinds of connexins, named for their atomic weight, ranging from 25 to 50 kD. In addition, there are four kinds of connexins in the heart, namely, connexin37 (Cx37), connexion40 (Cx40), connexin43 (Cx43) (the most abundant in the heart) and connexin45 (Cx45).

which are barrel-like structures with a length of about 75 Å [25]. These gap junctions constitute a low-resistance electrical pathway between two neighboring cells because the effective resistance is significantly less than which would result from two cell membranes butted together. Nevertheless, compared to the internal cytoplasm of cardiac cells, gap junctions are characterized by a very high-resistance. This relatively high resistance results from the greatly reduced cross-sectional area for electrical conduction through gap junctions compared with cardiac cells [23].

In cardiac tissue, there are several different kinds of cardiomyocyte depending on their function, which is closely related to their anatomy. The volume, surface area, and distribution of cellular components are different due to functional reasons. There are three major kinds of cardiac muscle fibers:

i. *atrial muscle fibers*
ii. *ventricular muscle fibers*
iii. *specialized excitatory* and *conductive muscle fibers*

Atrial and ventricular cardiomyocytes contract in a similar way as skeletal myocytes. However, the duration of contraction is much longer for cardiomyocytes in comparison with skeletal myocytes. The specialized excitatory and conductive muscle fibers are characterized by very few contractile fibrils (or *myofibrils*). As a result, they contract only feebly. This type of fiber either generates rhythmical electrical discharge in the form of action potentials in a spontaneous way or conducts the action potentials through the heart in an efficient manner. Thus, this kind of fiber provides an excitatory and conductive system that controls the rhythmical beating of the heart [22].

In normal conditions, cardiac impulse arises in the *sino-atrial (SA) node* (Fig. 1.5). But, the SA node is not the only part of the excitatory and conductive system that exhibits intrinsic rhythmical excitation. The *atrio-ventricular (AV) node* and the *Purkinje fibers* are also characterized by a similar activity (Fig. 1.6). However, the frequency at which the intrinsic rhythmical excitation is provided in the AV node and Purkinje fibers is lower than in the SA node, namely $40-60$ times per minute ($2/3-1\,\mathrm{Hz}$) and $15-40$ times per minute ($1/4-2/3\,\mathrm{Hz}$), respectively. For comparison, the SA node provides excitation at a frequency of $70-80$ times per minute ($7/6-4/3\,\mathrm{Hz}$). Due to this difference related to the natural self-excitatory discharge frequency, the heart's rhythm is controlled by the SA node. Thus, the SA node is referred to as the *pacemaker* of the normal heart.

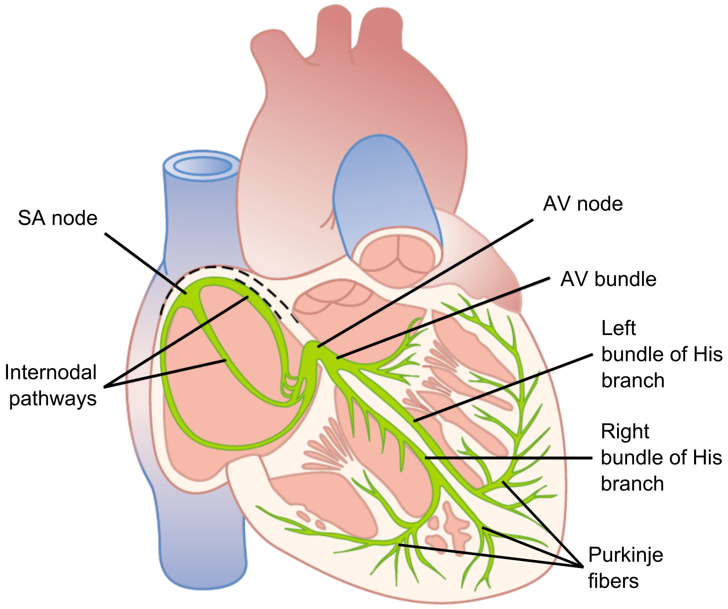

Fig. 1.5 – Specialized excitatory and conductive system of the heart [22].

It can be readily understood why it is the SA node that controls the rhythmical activity of the heart. Each time that a discharge is generated in the SA node, it is conducted towards both the AV node and the Purkinje fibers, which are in turn excited by this impulse. The next natural self-excitatory discharge in the SA node is triggered a very few moments after the previous one and has already reached the AV node and the Purkinje fibers before these can reach their own threshold for self-excitation. As a result, the new impulse from the SA node discharges both the AV node and the Purkinje fibers before self-excitation can occur in either of these [22].

1.2.1 Pathway of the heart's conduction system

As previously mentioned, in a healthy heart, the electrical excitation is initiated at the SA node, located in the upper part of the right atrium. The excitation propagates through both atria *via* atrial cells and reaches the AV node, located at the floor of the right atrium (Fig. 1.5). This AV node acts like an *electrical bridge* between atria and ventricles, which are separated by a septum composed of non excitable cells. This septum prevents the direct propagation of excitation from atrial to ventricular cells.

As shown in Fig. 1.6, the conduction of the excitation signal is quite slow through the AV node. As a result, there is a latency between atrial and ventricular excitation that is useful for the pumping action of the heart. When the excitation exits the AV node, it propagates through the *bundle of His*, which is composed of *Purkinje fibers* (Fig. 1.5). The network of Purkinje fibers then spreads to both the left and right *bundle branches* where the excitation rapidly propagates throughout the interior of the ventricles, ending at the *endocardial surface* of the ventricles. The electrical excitation then propagates through the ventricular wall outward *via* ventricular cells from the endocardial surface to the *epicardial surface*.

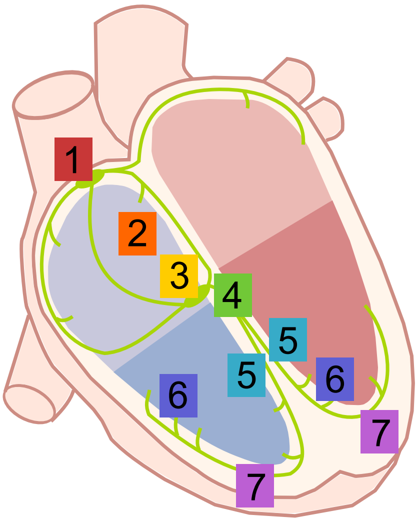

Normal Activation Sequence	Structure	Conduction velocity (m/sec)	Pacemaker rate (beats/min)
1	SA node	< 0.01	60 - 90
2	Atrial myocardium	1.0 - 1.2	None
3	AV node	0.02 - 0.05	40 - 60
4	Bundle of His	1.2 - 2.0	25 - 40
5	Bundle branches	2.0 - 4.0	25 - 40
6	Purkinje network	2.0 - 4.0	15 - 40
7	Ventricular myocardium	0.3 - 1.0	None

Fig. 1.6 – Pathway of the conduction system of the heart: sequence of electrical activation [26]. Tabulation of the activation sequence adapted from [27].

1.2.2 Working myocardium

Cardiomyocytes in the myocardium (atrial and ventricular cardiomyocytes) produce a mechanical tension resulting from specialized contractile elements, called *sarcomeres*. These sarcomeres are approximately $2\,\mu\mathrm{m}$ long and are the elementary sections of *myofibrils* (Fig. 1.7D). The myofibrils are tube-shaped contractile elements making up $41-53\,\%$ and $45-54\,\%$ of the volume of atrial and ventricular myocytes, respectively [28]. Each cardiac fiber contains several hundred to several thousand myofibrils. In addition, each myofibril consists of approximately 1500 sarcomeres butted together, which contain the *myofilaments* (Fig. 1.7E). The myofilaments are composed of so-called *actin* filaments (referred to as *thin* filaments) and *myosin* filaments (referred to as *thick* filaments). As shown in Fig. 1.7E, actin and myosin filaments overlap in a partial way leading to alternating light and dark bands in myofibrils (Fig. 1.7D). The light bands consist of only of actin filaments and are referred to as *I bands* due to isotropy with respect to polarized light. The dark bands contain both myosin filaments and the ends of the actin filaments and are referred to as *A bands* because they are anisotropic to polarized light [22].

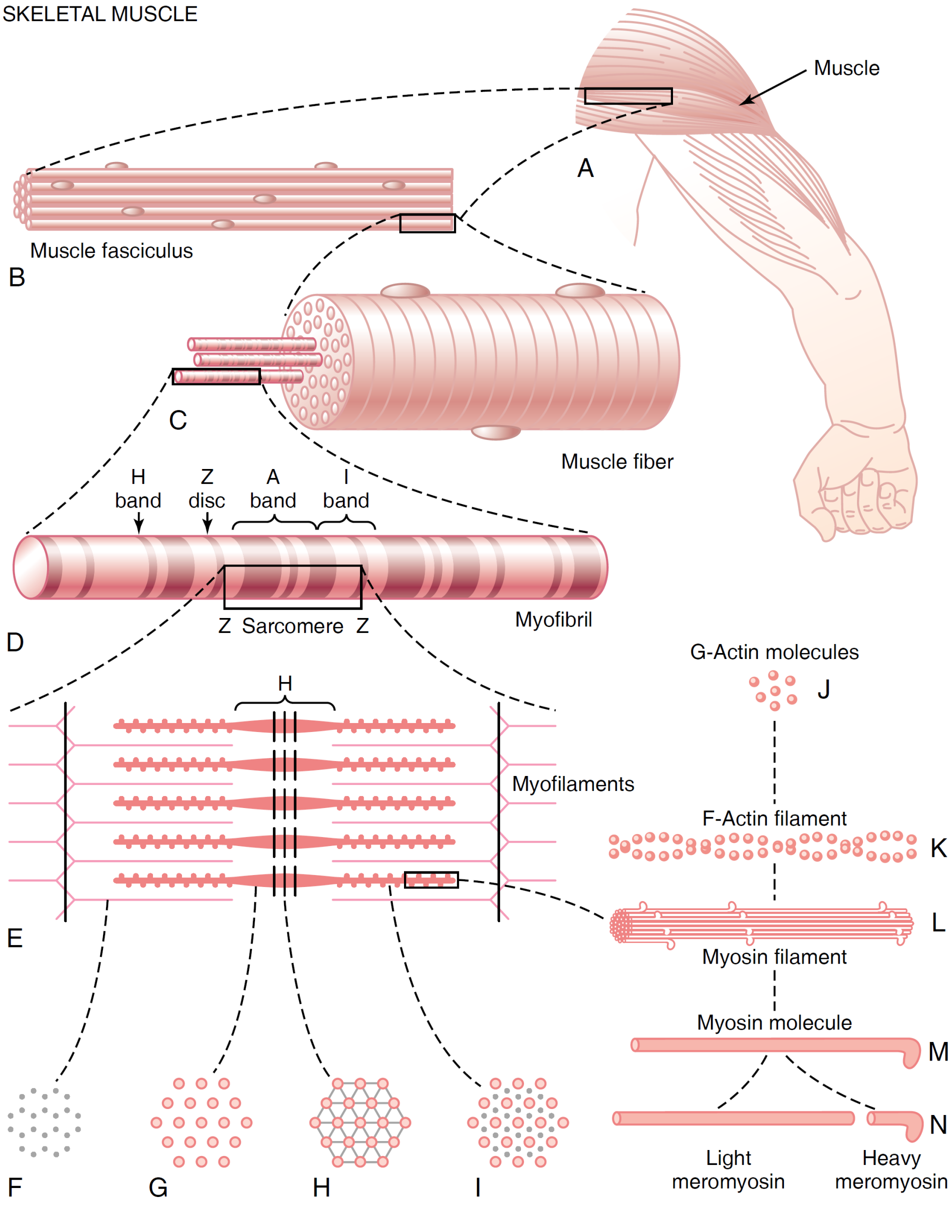

Fig. 1.7 – **Muscle structure, from the macroscopic to the molecular level [22]. Note that this illustration presents the skeletal striated muscle but this is also suitable for the cardiac striated muscle regarding the particular structural points that are introduced in this section.**

1.2.2.1 Actin filaments

The actin filaments are approximately 1 μm long and are composed of three protein components, namely *actin*, *tropomyosin*, and *troponin* (Fig. 1.8).

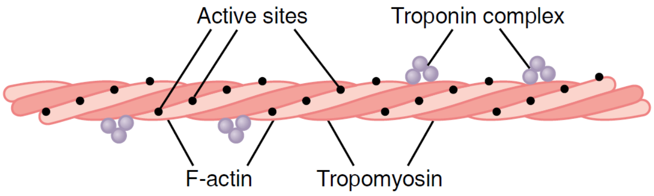

Fig. 1.8 – Composition of actin filaments [22].

The backbone of the actin filament is built up of a *double F-actin helix* (Fig. 1.7K). Each strand of the double F-actin helix is composed of polymerized *G-actin molecules* (Fig. 1.7J). These molecules are plate-shaped proteins, with a molecular weight of 42 kD. In addition, each of these G-actin molecules is connected to a *adenosine diphosphate (ADP)* molecule. As reported in [22], ADP molecules are believed to be the active sites on the actin filaments interacting with the cross-bridges of the myosin filaments. Each active site is found approximately every 2.7 nm on the actin filaments (Fig. 1.9).

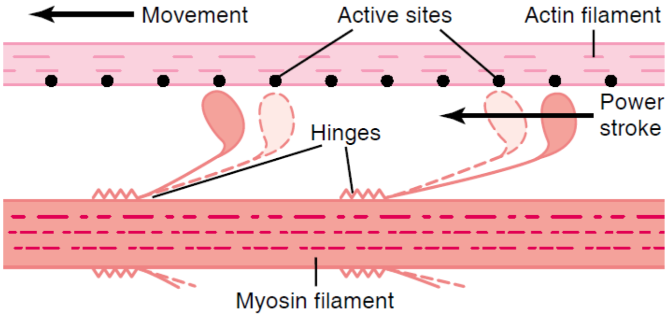

Fig. 1.9 – Interaction between actin and myosin filaments [22].

Actin filaments also contain two strands of tropomyosin molecules that fit in the grooves between the actin strands (Fig. 1.8). Moreover, tropomyosin is characterized by seven actin binding sites and one binding site for *troponin*. Troponin is a complex, built up by three loosely bound protein subunits, namely *troponin I*, *troponin T*, and *troponin C*. Each subunit has a specific function in controlling cardiac muscle contraction. Troponin I has a strong affinity for actin, troponin T for tropomyosin and troponin C for calcium ions.

1.2.2.2 Myosin filaments

Myosin filaments are made up of 200 or more individual myosin molecules. The structure of each myosin molecule can be split into two different parts: a *tail* and two *heads* (Fig. 1.10A). The tail of the myosin molecule is composed of two heavy chains wrapped around each other in a spiral, forming a double helix. One end of each heavy chain displays a globular polypeptide structure, forming a myosin head.

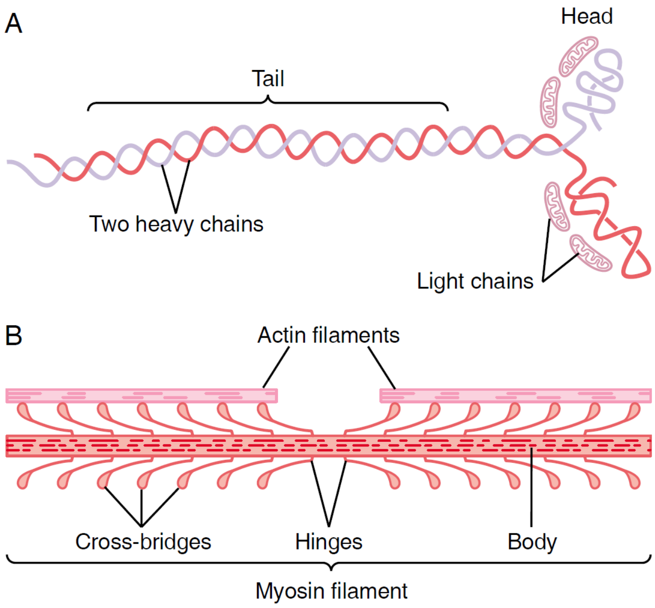

Fig. 1.10 – Structure of a myosin molecule (A) and spatial configuration of actin and myosin filaments (B) [22].

The myosin filament can be viewed as a *body*, constituted of many myosin molecules butted together, with many heads of the molecules hanging out of the sides of the body (Fig. 1.10B). Note that another part of the body of each molecule also hangs outward to the side along with the myosin head, usually called the *arm*. The arm allows the head to extend outward from the body. These structures are referred to as *cross-bridges* (Fig. 1.10B). Each cross-bridge is flexible due to *hinges* located at two specific points, where the arm leaves the body, and where the head is connected to the arm.

Each myosin filament is approximately 1.6 μm long. As shown in Fig. 1.10B, there are no cross-bridges in the center of the myosin filament for a distance of about 0.2 μm due to the configuration of the hinged arms, as they extend away from the center.

Moreover, sarcomeres also contain elongated proteins called *titin* and *nebulin*. Titin is the third most abundant protein after myosin and actin in cardiomyocytes. Each titin molecule has a molecular weight of about 3 MD. In addition, titin molecules are filamentous and as a result, are very *springy*. These elastic titin molecules act as a framework that holds the myosin and actin filaments in place [22]. Besides, from a spatial configuration point of view, titin molecules span from Z discs towards the center of the sarcomeres parallel to the myofilaments.

CHAPTER 2

Cardiac electrical activity

Cardiac electrical activity in the heart has already been described in the previous chapter from a macroscopic point of view. Here, key cellular mechanisms leading to the onset of electrical excitation in cardiomyocytes, implying their contraction, are introduced in detail. An overview of cardiac electrophysiology is presented before explaining how the cellular electrical phenomena are modeled from both qualitative and quantitative points of view. Modeling of these phenomena at a larger spatial scale, namely at a tissue level, is then performed by taking into account the propagation of the local electrical excitation.

Contents

2.1 Electrical activity at the cellular level

2.1.1 Description

Like all biological cells, cardiac cells are surrounded by a membrane. The cell membrane is composed of a double layer of phospholipid molecules[1] about 7.5 nm thick, containing many kinds of proteins. As a result, the cell is separated from its external environment. The membrane acts as a barrier separating the *intracellular* and *extracellular media* (note that properties of the intracellular and extracellular media are labeled by the subscripts ‘i’ and ‘e’, respectively) and preventing the free passage of molecules, such as ions, from one side to the other.

Specialized proteins embedded in the cell membrane, called *ion channels*, possess the remarkable property of *selective permeability.* These channels allow particular species of ions to cross the cell membrane. There are many types of ion channels, each being

---

[1] *Phospho-* because each molecule has a globular head containing a phosphate group, which is hydrophilic, and *-lipid* due to two fatty acid tails, which are hydrophobic [29].

specific to a certain ion, *e.g.* Na^+ and Ca^+. In addition, these channels can be open or closed, controlling the passage of the specific ion species.

The gating process (opening or closing) is regulated by several physico-chemical properties of the intracellular and extracellular environments, the most important being the value of the electrical potential difference across the membrane. This *membrane potential* (or *transmembrane potential*) is labeled V_m. By convention, V_m is defined as the difference between the internal and external electrical potentials [23, 29]:

$$V_m \quad = \quad \phi_\mathrm{i} - \phi_\mathrm{e}\,. \tag{2.1}$$

The value of V_m is used by the cardiomyocyte as a signal which indicates to the cell whether the contraction must be triggered. In a resting state, a cardiomyocyte is typically characterized by a membrane potential ranging from approximately $-90\,\mathrm{mV}$ to $-80\,\mathrm{mV}$. These values are close to the *Nernst potential* (discussed later in this chapter), E_K, of the potassium ion. This potential reflects the high permeability of the membrane (in a resting state) to potassium ions.

Many biological cells maintain a stable equilibrium membrane potential. If sufficiently strong currents are applied to such cells for a short period of time, the membrane potential can either [23]:

i. directly return to the equilibrium value after the applied current is removed;
ii. experiences a large excursion, called an *action potential (AP)*, before eventually returning to rest.

The behaviors described in (i) and (ii) define *nonexcitable* and *excitable* cells, respectively.

Excitability is a very powerful natural selective tool to distinguish background noise from a healthy stimulus. If a stimulus of sufficient amplitude, enabling to exceed the *threshold potential*, is applied to an excitable cell, the latter responds in full to this stimulus. If the amplitude of a stimulus is too low, the excitable cell does not respond at all. The five main phases of a given AP are shown in Fig. 2.1:

- phase 0: rapid depolarization of the cell, from the resting state ($-90\,\mathrm{mV}$ for this specific AP) to the overshoot ($30\,\mathrm{mV}$ for this specific AP)

- phase 1: rapid partial repolarization of the cell, just after the overshoot
- phase 2: plateau of the AP
- phase 3: recovery of the cell back to the resting state (repolarization)
- phase 4: resting state, around 300 ms after the initial depolarization for this specific cardiomyocyte

Note that each kind of cardiomyocyte is characterized by a particular AP[2] but each type of AP displays these five main phases.

Phase 0, consisting in a sharp upstroke (rapid depolarization), is due to a *supra-threshold stimulus* leading to a rapid influx of sodium ions generating the sodium current, I_{Na}. The membrane potential then rapidly decreases due to an outward potassium current, I_{K} (phase 1). Just after phase 1, there is a plateau due to inward calcium currents, I_{Ca}, compensating the potassium current (phase 2). During the entire AP, potassium currents exist and tend to bring the membrane potential back to the resting state. Just after the plateau-phase, the calcium currents can no longer hold the membrane potential in a depolarized state (phase 3) and finally, potassium currents return the cell to its resting state (phase 4).

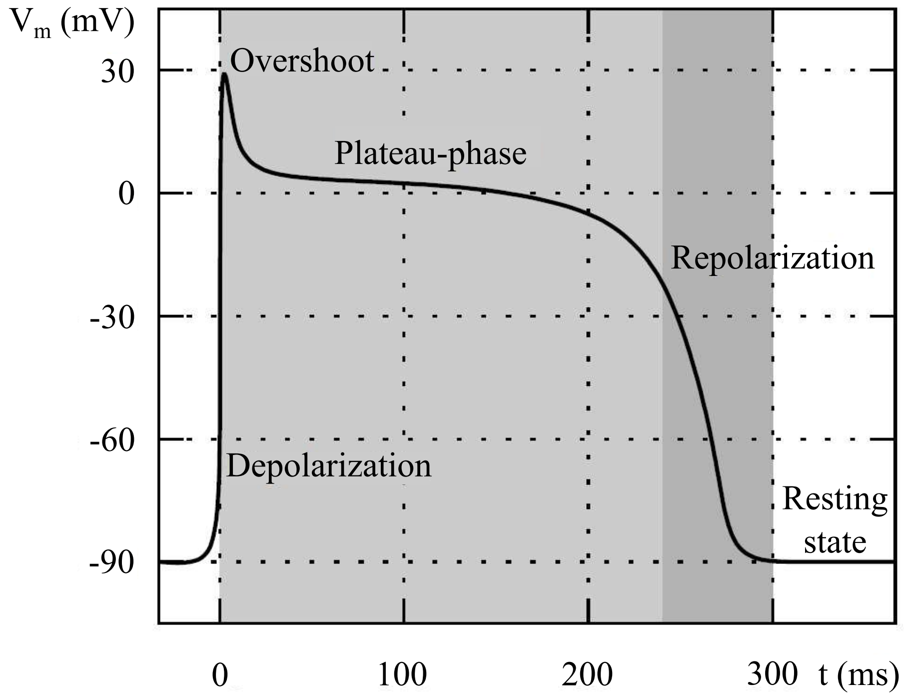

Fig. 2.1 – Typical phases of an action potential from a particular cardiac muscle cell, adapted from [28].

---

[2] APs differ depending on the stimulus frequency, tissue type, and location in the heart.

Three important time periods must be highlighted to understand some mechanisms further in this work:

- The *effective* or *absolute refractory period (ERP/ARP)* is defined as the time period during which no AP can be initiated, regardless of the strength of the stimulus. This period includes phases 0, 1, 2, and the first part of phase 3.
- The *relative refractory period (RRP)*, directly follows the ERP. The RRP is the time period in which an AP can be elicited, but requires a stimulus much stronger than that needed for the resting cell. This period ends slightly before the end of phase 3.
- The *supernormal period (SP)*, directly follows the RRP. During this period, the cardiomyocyte can undergo an AP with a stimulus slightly smaller than the normal phase 4 supra-threshold stimulus.

These three periods make up the full recovery time after the onset of an AP.

2.1.2 Modeling

Almost all cardiac cell models are based on the model developed by *Hodgkin and Huxley* in 1952 [16]. For this reason, the key concepts of this model are introduced here. In 1952, Hodgkin and Huxley wrote a series of five papers [16, 30, 31, 32, 33] whose the general aim was to determine the laws which govern movements of ions through the cell membrane during electrical activity in the giant axon of *Loligo*[3]. They performed numerous measurements of individual ion currents at the cellular level. From these experimental results, Hodgkin and Huxley derived the first mathematical model that quantitatively accounts for the time evolution of ion currents. In particular, the evolution of the three major components of the total ionic current were modeled: the sodium current I_{Na}, the potassium current I_{K}, and a small 'leakage' current I_{l} made up by chloride and other ions.

From a modeling point of view, Hodgkin and Huxley suggested to describe the electrical activity at a cellular level by considering the membrane as an electrical circuit. This circuit was composed of a capacitor, with a capacitance C_m, in parallel with branches containing three different ion currents: I_{Na}, I_{K}, and I_{l} (Fig. 2.2).

---

[3] *Loligo* is a genus of squids.

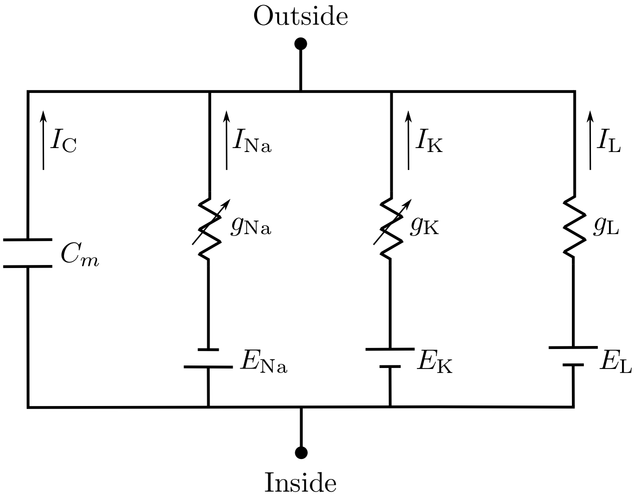

Fig. 2.2 – **Equivalent circuit of an axon membrane assuming no current applied to the cell.**

The total transmembrane current is referred to as I_m and is written as follows:

$$I_m = I_C + I_{\text{ion}} \tag{2.2}$$

$$= C_m \frac{\mathrm{d}V_m}{\mathrm{d}t} + \sum_{S=1}^{3} I_S\,, \tag{2.3}$$

where I_C is a capacitive current, I_{ion} is the total ion current, and S is the label relative to the S-ion, e.g. Na^+. The Kirchhoff's first law[4] applied to the electrical circuit shown in Fig. 2.2 gives $I_m = 0$ and, therefore, due to Eq. (2.3),

$$\frac{\mathrm{d}V_m}{\mathrm{d}t} = -\frac{1}{C_m} \sum_{S=1}^{3} I_S\,. \tag{2.4}$$

Most state-of-the-art cell models describe the total transmembrane current, I_m, as in Eq. (2.2). The difference between cell models boils down to the description of the total ion current through the cell membrane: the term I_{ion} in Eq. (2.2). Some models, like the *Hodgkin–Huxley (HH) model*, only take into account a few different ion currents whereas others introduce many ion currents. According to Hodgkin and Huxley, each individual ion current can be satisfactorily described by the following *current-voltage law* [16]:

$$I_S(V_m, t) = g_S(V_m, t)\,(V_m - E_S)\,, \tag{2.5}$$

---

[4] Kirchhoff's first law says that the algebraic sum of currents in a network of conductors meeting at a node is zero.

where $g_{\mathrm{S}}\left(V_m, t\right)$ is the *conductance* of the membrane for the S-ion and represents a measure of the membrane S-ion permeability. Note that g_{S} is voltage- and time-dependent and is measured in Siemens per unit area. It is also the reciprocal of resistance per unit area. E_{S} represents the so-called Nernst potential for the S-ion, already mentioned earlier in this chapter. Its value is given by the *Nernst equation*:

$$E_{\mathrm{S}} = \frac{RT}{z_{\mathrm{S}}\, F} \ln \frac{[S]_e}{[\mathrm{S}]_i}, \tag{2.6}$$

where $[\mathrm{S}]_{\mathrm{e}}$ and $[\mathrm{S}]_{\mathrm{i}}$ are the extracellular and intracellular concentrations of the ion S, R is the universal gas constant, T is the absolute temperature, z_{S} is the valence of ion S and F is Faraday's constant. The meaning of the Nernst potential, E_{S}, can be stated in two ways [25]:

i. If the pores in a membrane are permeable only to ions of type S, a few ions would move and the membrane potential will change to E_{S}.
ii. If the membrane potential is held somehow at E_{S}, there will be no net flux of S-ions through S-selective pores.

The Nernst potential, E_{S}, represents an equilibrium potential between diffusion and electrostatic forces. First, assume that, due to several kinds of cellular mechanisms, the cell membrane is permeable only to the S-ions and that there is a concentration difference across the cell membrane regarding this S-ion. As a result, S-ions will diffuse from the high concentration side to the lower concentration side. The diffusion of S-ions causes a buildup of charges across the membrane and consequently, sets up an electric field that opposes the further diffusion. An equilibrium state is reached when the electric field and the corresponding potential difference exactly balance the diffusion process. This potential difference is the Nernst potential. As a result of these considerations, the net force acting on the S-ion depends on the electrical potential and concentration gradients and is known as the *electrochemical gradient*, or *driving force*, and is defined as $(V_m - E_{\mathrm{S}})$ [25].

Eq. (2.5) is effectively a modification of Ohm's law and is empirical like Ohm's law itself. To a first approximation, this law is often suitable, but many pores are known to be characterized by other nonlinear current-voltage relations when open. Assuming the current-voltage relation given by Eq. (2.5), the direction of I_{S} across the cell membrane depends on the sign of the driving force. The magnitude of I_{S} is determined by both the driving force and the conductance of the membrane to the S-ion. Substituting Eq. (2.5) into Eq. (2.3) and assuming an applied current I_{app}, I_m becomes

$$I_m\left(V_m,t\right) \;=\; C_m\,\frac{\mathrm{d}V_m}{\mathrm{d}t}+V_m\sum_{\mathrm{S}=1}^{3}g_{\mathrm{S}}\left(V_m,t\right)-\sum_{\mathrm{S}=1}^{3}g_{\mathrm{S}}\left(V_m,t\right)\,E_{\mathrm{S}}+I_{\mathrm{app}}\,. \tag{2.7}$$

From the experimental data obtained by Hodgkin and Huxley, showing that sodium and potassium conductances behave in a nonlinear way with respect to time and voltage, it is reasonable to expect that g_{S} obeys a nonlinear *ordinary differential equation (ODE)* such as

$$\frac{\mathrm{d}g_{\mathrm{S}}}{\mathrm{d}t} \;=\; f\left(V_m,t\right)\,, \tag{2.8}$$

where f is a nonlinear function of V_m and t. However, rather than writing a nonlinear ODE directly for each ion conductance, Hodgkin and Huxley realized that it would be easier to express $g_{\mathrm{S}}\left(V_m,t\right)$ as a maximum conductance $\bar{g}_{\mathrm{S}}$ multiplied by some power of different variables (n, m, and h), which are controlled by linear ODEs. Thereby, they wrote g_{K}, g_{Na}, and g_{l} as follows:

$$g_{\mathrm{K}}\left(V_m,t\right) \;=\; \bar{g}_{\mathrm{K}}\,\left[n\left(V_m,t\right)\right]^4\,, \tag{2.9}$$

$$g_{\mathrm{Na}}\left(V_m,t\right) \;=\; \bar{g}_{\mathrm{Na}}\,\left[m\left(V_m,t\right)\right]^3\,h\left(V_m,t\right)\,, \tag{2.10}$$

$$g_{\mathrm{l}} \;=\; \bar{g}_{\mathrm{l}}\,. \tag{2.11}$$

Note that n, m, and h are often called *gating variables* and their values are ranged from 0 to 1. As shown in Eqs (2.9)-(2.11), there is an upper limit to each possible conductance. Originally, Hodgkin and Huxley described the *gating process* of each ion channel in terms of *independent membrane-bound 'particles'*. To trigger the opening of a particular ion channel, all the particles involved in the gating process of the channel have to be in the 'correct position'. Following this approach, each gating variable (n, m, and h) represents the probability that a particle is in the correct position to allow the opening of the channel. Moreover, given that the opening depends on the membrane potential, the hypothetical particles are assumed to bear an electric charge that makes their distribution in the membrane voltage-dependent. In this context, it is interesting to stress that all the kinetic properties of the model are contained in the time dependence of the three gating variables n, m, and h [25].

The mathematical expressions given by Eqs (2.9)-(2.11) were proposed by Hodgkin and Huxley further to their experimental observations of the time dependence of each ionic conductance considered in the model. They observed that the increase of g_{K} on depolarization results in an S-shaped time course, whereas the decrease on repolarization behaves exponentially. They also noticed that such kinetics would be obtained if the opening of a K-channel was controlled by four identical particles able to move between two positions: a *permissive position* and a *nonpermissive position.* The probabilities that one particle is in the permissive position and the nonpermissive position are given by n and $1 - n$, respectively. As a result, the probability that all four particles are in a permissive position, resulting in the opening of the channel, is equal to n^4.

The kinetics of transitions between permissive and nonpermissive positions are first-order. When the membrane potential is changed, the probability, n, relaxes exponentially towards a new value. In this way, the delayed increase on an S-shaped curve on depolarization and the decrease of g_{K} is well modeled by n^4. If n rises exponentially from zero, n^4 rises along an S-shaped curve and if n falls exponentially, n^4 falls exponentially as well.

Hodgkin and Huxley used a similar approach for the Na conductance. They described the behavior of g_{Na} using four gating particles that make transitions between permissive and nonpermissive positions in an independent way with first-order kinetics. However, they used two different kinds of gating particles because there are two opposing gating mechanisms: activation and inactivation. Hodgkin and Huxley assumed three particles to control the activation process and one particle to describe the inactivation process. The two kinds of particle are in a permissive position with a probability m (activation) and h (inactivation). Therefore, the probability that the Na channel is open, namely all particles are in the permissive position, is $m^3\,h$ [25].

For practical application, Hodgkin and Huxley rewrite Eqs (2.9)-(2.11) by introducing a shifted potential, $v = V_m - V_{\mathrm{eq}}$, where V_{eq} is the equilibrium membrane potential[5] or resting potential. As V_{eq} is a constant, $\mathrm{d}v/\mathrm{d}t = \mathrm{d}V_m/\mathrm{d}t$. From Eq. (2.7), V_{eq} can be

---

[5] The equilibrium membrane potential is model-dependent.

written as

$$V_{\mathrm{eq}} = \frac{E_{\mathrm{Na}}\, g_{\mathrm{Na}} + E_{\mathrm{K}}\, g_{\mathrm{K}} + E_{\mathrm{l}}\, g_{\mathrm{l}}}{g_{\mathrm{Na}} + g_{\mathrm{K}} + g_{\mathrm{l}}}\,. \tag{2.12}$$

V_{eq} actually represents the balance between the *reversal potentials*[6] for the three ionic currents. Substituting v for V_m, the gating variables $n\,(v,t)$, $m\,(v,t)$, and $h\,(v,t)$ satisfy the following set of linear ODEs:

$$\frac{dn}{dt} = \alpha_n\,(v)\;(1-n) - \beta_n\,(v)\;n\,, \tag{2.13}$$

$$\frac{dm}{dt} = \alpha_m\,(v)\;(1-n) - \beta_m\,(v)\;m\,, \tag{2.14}$$

$$\frac{dh}{dt} = \alpha_h\,(v)\;(1-n) - \beta_h\,(v)\;h\,, \tag{2.15}$$

accounting for the voltage- and time-dependent changes of n, m, and h. Eqs (2.13)-(2.15) describe in fact the first-order kinetics of transitions between nonpermissive and permissive states. This kind of kinetics can be written in the form

$$1 - y \underset{\beta_y(v)}{\overset{\alpha_y(v)}{\rightleftharpoons}} y\,, \tag{2.16}$$

where $y = n$, m, or h; $\alpha_y\,(v)$ and $\beta_y\,(v)$ are the voltage-dependent rate constants (s^{-1}) regarding y and are given by [23]

$$\alpha_n = 0.01\,\frac{10-v}{\exp\left(\dfrac{10-v}{10}\right)-1}\,, \tag{2.17}$$

$$\beta_n = 0.125\,\exp\left(\frac{-v}{80}\right), \tag{2.18}$$

$$\alpha_m = 0.1\,\frac{25-v}{\exp\left(\dfrac{25-v}{10}\right)-1}\,, \tag{2.19}$$

$$\beta_m = 4\,\exp\left(\frac{-v}{18}\right), \tag{2.20}$$

$$\alpha_h = 0.07\,\exp\left(\frac{-v}{20}\right), \tag{2.21}$$

$$\beta_h = \frac{1}{\exp\left(\dfrac{30-v}{10}\right)+1}\,. \tag{2.22}$$

---

[6] The reversal potential is actually the same quantity as the Nernst potential and represents the potential at which the chemical and electrical forces acting on a single ion species are in equilibrium [29]. Depending on circumstances, either the term 'reversal potential' or the expression 'Nernst potential' is used.

Eqs (2.13)-(2.15) are also reported in the literature in terms of voltage-dependent time constants, $\tau_y(v)$ (s), and steady-state values, y_∞, as follows:

$$\frac{\mathrm{d}y(v,t)}{\mathrm{d}t} = \frac{y_\infty(v) - y(v,t)}{\tau_y(v)}, \tag{2.23}$$

where $y = n$, m, or h. The solution of this equation is given by

$$y(v,t) = y_\infty(v) - [y_\infty(v) - y(0)] \exp\left(-\frac{t}{\tau_y(v)}\right), \tag{2.24}$$

with the following relations:

$$\tau_y(v) = \frac{1}{\alpha_y(v) + \beta_y(v)}, \tag{2.25}$$

$$y_\infty(v) = \frac{\alpha_y(v)}{\alpha_y(v) + \beta_y(v)}, \tag{2.26}$$

which describe τ_y and y_∞ in terms of α_y and β_y. Fig. 2.3 shows the quantities given by Eqs (2.25) and (2.26).

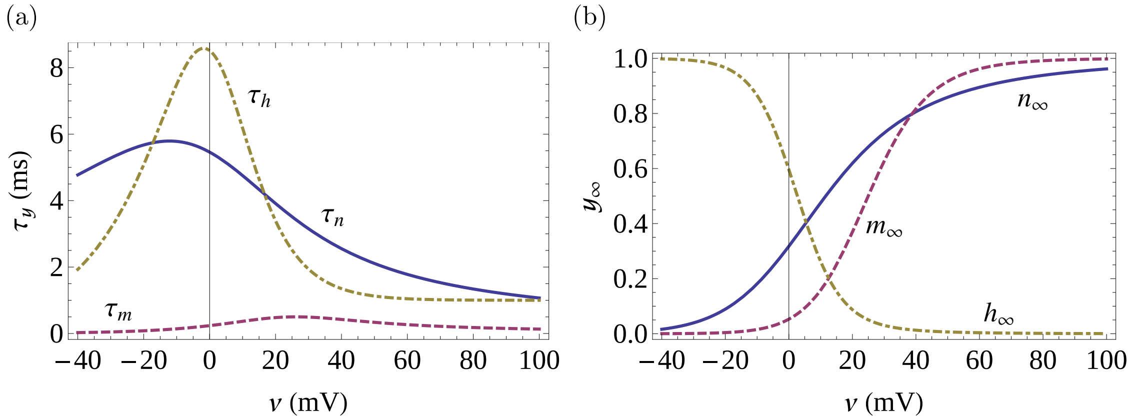

Fig. 2.3 – (a) Time constants and (b) steady-state values of gating variables as functions of the shifted potential, $v = V_m - V_{\mathrm{eq}}$. Depolarizations increase m_∞ and n_∞ and decrease h_∞. The time constants of relaxation are maximal near the resting potential and become shorter on either side.

In summary, the HH model is given by

$$\begin{aligned} -I_{\mathrm{app}} &= C_m \frac{\mathrm{d}v}{\mathrm{d}t} + \bar{g}_{\mathrm{Na}}\, m^3\, h\, (v - v_{\mathrm{Na}}) + \bar{g}_{\mathrm{K}}\, n^4\, (v - v_{\mathrm{K}}) + \bar{g}_{\mathrm{l}}\, (v - v_l)\;, && (2.27) \\ \frac{\mathrm{d}m}{\mathrm{d}t} &= \alpha_m\, (1 - m) - \beta_m\, m\,, && (2.28) \\ \frac{\mathrm{d}h}{\mathrm{d}t} &= \alpha_h\, (1 - h) - \beta_m\, h\,, && (2.29) \\ \frac{\mathrm{d}n}{\mathrm{d}t} &= \alpha_n\, (1 - n) - \beta_m\, n\,. && (2.30) \end{aligned}$$

As an example, Fig. 2.4a shows the time course of the shifted potential, v, following a supra-threshold stimulus using the parameter values given in Tab. 2.1. Fig. 2.4b is a plot of the time course of the gating variables $n\,(v,t)$, $m\,(v,t)$, and $h\,(v,t)$ during the action potential shown in Fig. 2.4a.

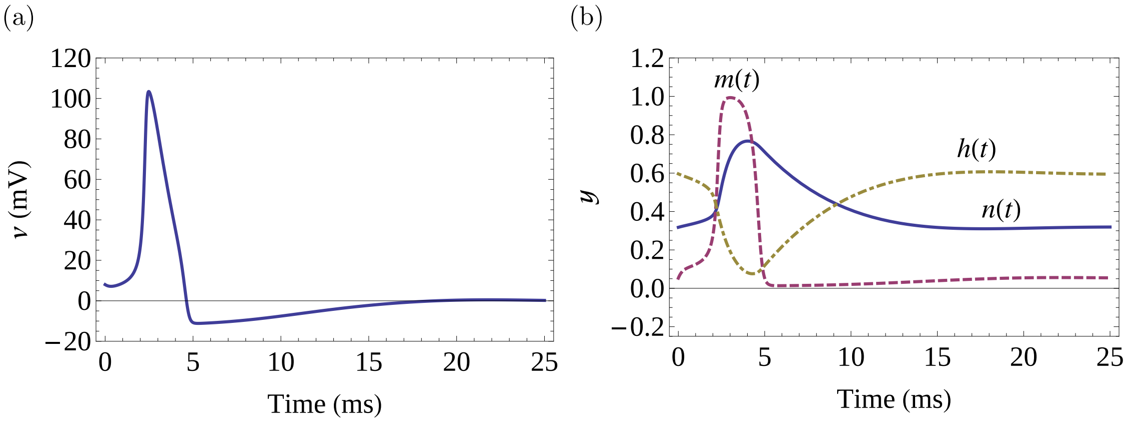

Fig. 2.4 – (a) Action potential generated by a supra-threshold stimulus mimicked with the HH model and (b) time courses of the gating variables during the same action potential.

Parameter	Value	Units
C_m	1	$\mu\mathrm{F\,cm}^{-2}$
v_{Na}	115	mV
v_{K}	−12	mV
v_{l}	10.6	mV
$\bar{g}_{\mathrm{Na}}$	120	$\mathrm{mS\,cm}^{-2}$
$\bar{g}_{\mathrm{K}}$	36	$\mathrm{mS\,cm}^{-2}$
$\bar{g}_{\mathrm{l}}$	0.3	$\mathrm{mS\,cm}^{-2}$

Tab. 2.1 – Parameter values of the HH model [16].

2.1.3 Models of cardiac muscle cells

Cardiac muscle cells are modeled using two different approaches: a *biophysical* approach and a *phenomenological* approach (non-biophysical). Biophysical models attempt to describe the AP of a single cell by mimicking the biophysics related to the underlying subcellular processes. The complexity inherent to this kind of model has increased over the time in a significant way. The first biophysically-based model, established by Hodgkin and Huxley, only included 3 ionic currents and 3 gating variables [16] whereas the more recent model developed by *Noble*, *Varghese*, *Kohl* and *Noble* (*NVKN*) [34] contains 27 ionic currents, 5 fluxes, 3 subcellular spaces, and tracks 9 ion concentrations.

Biophysical models aim at describing a specific type of cardiomyocyte for a particular species (*e.g.* human, rabbit, or pig). For a given species, they can be split into 5 categories: *SA node models* (*e.g.* [35]), *atrial models* (*e.g.* [36]), *AV node models*, *Purkinje fiber models* (*e.g.* [37]), and *ventricular models* (*e.g.* [38]). Sometimes, it is not necessary to describe each ionic current and each subcellular process in an accurate way: it depends strongly on the purpose of the conducted study.

This work presents the phenomenological approach, mainly for reasons of computational cost. Indeed, this kind of model aims at reproducing the global properties of an AP without concern for the complex individual ionic mechanisms leading to the AP. These types of model are particularly interesting for investigating physical phenomena on large spatial and temporal scales because they consist of only a small number of ODEs, resulting in a reduced computational cost. The differences between all simplified models are due to the different descriptions used for I_{ion} in Eq. (2.3). In this section, three simplified phenomenological models (FH model, RM model, and AlP model) are presented. Besides, one biophysical minimal model (FK model) of cardiomyocytes is also described to emphasize the difference between the two approaches.

Adding an applied current, I_{app}, to Eq. (2.3), the vanishing of the total membrane current (Kirchhoff's first law), I_m, gives

$$\frac{\mathrm{d}V_m}{\mathrm{d}t} = -\frac{1}{C_m}\left(I_{\mathrm{ion}} + I_{\mathrm{app}}\right) , \tag{2.31}$$

which is a relation valid for all models studied below. Note also that the three simplified models presented in this section were originally formulated to describe *dimensionless* excitation and recovery variables. However, in this section, they are also formulated in terms of the dimensional AP controlled by the time course of the dimensional membrane potential, V_m [Eq. (2.31)]. For a particular simplified model, the relation between the membrane potential, V_m, and the dimensionless excitation variable, labeled u, is [29]

$$u = \frac{V_m - V_\mathrm{r}}{V_\mathrm{p} - V_\mathrm{r}}, \tag{2.32}$$

where V_r and V_p represent the resting potential and the plateau potential, respectively. Therefore, from Eqs (2.31) and (2.32), $\mathrm{d}V_m/\mathrm{d}t$ and $\mathrm{d}u/\mathrm{d}t$ are related by

$$\frac{\mathrm{d}V_m}{\mathrm{d}t} = V_\mathrm{a}\frac{\mathrm{d}u}{\mathrm{d}t}, \tag{2.33}$$

where V_a is given by

$$V_\mathrm{a} = V_\mathrm{p} - V_\mathrm{r}. \tag{2.34}$$

2.1.3.1 FitzHugh model (1961)

The well-known *FitzHugh model (FH model)*, originally called the *Bonhoeffer–van der Pol model (BVP model)* in [17], presents the same qualitative dynamical properties as the HH model. However, the FH model has only two state variables instead of the four in the HH model. Thus, its properties can be examined and discussed in a *phase plane* (as illustrated later in this section). The FH model can qualitatively describe a wide class of *nonlinear systems* showing *excitable* and *oscillatory* behavior, including the HH model [17].

FitzHugh showed, using *phase space methods* [39], that the essence of the HH model is contained in a two-dimensional reduction of itself [40]. Further, FitzHugh showed that the four variables can be split into two subsystems of variables, characterized by two different dynamics, like the fast and slow variables of the FH model. In the HH model, V_m (or similarly v) and m change relatively rapidly while h and n change relatively slowly (Fig. 2.4). The FH model is given by the following two ODEs [17]:

$$\frac{\mathrm{d}u}{\mathrm{d}t} = f\,(u,v) - i_{\mathrm{app}} = c_1\,u\,(u-a)\,(1-u) - c_2\,v - i_{\mathrm{app}}, \tag{2.35}$$

$$\frac{\mathrm{d}v}{\mathrm{d}t} = \varepsilon\,g\,(u,v) = \varepsilon\,(u - \gamma\,v)\,. \tag{2.36}$$

Eq. (2.35) describes the time course of excitation in terms of a cubic polynomial of the normalized membrane potential, u. Parameter c_1 is an excitation rate constant, c_2 is an excitation decay constant, a represents the normalized threshold potential, which can be related to the dimensional threshold potential, V_{th}, by [29]

$$a = \frac{1}{V_{\mathrm{a}}}\,(V_{\mathrm{th}} - V_{\mathrm{r}})\,, \tag{2.37}$$

and i_{app} is the normalized applied current which can be related to I_{app} by

$$i_{\mathrm{app}} = \frac{1}{V_{\mathrm{a}}\,C_m}\,I_{\mathrm{app}}\,. \tag{2.38}$$

Eq. (2.36) mimics the time course of the recovery variable, v. Parameter ε is a recovery rate constant and γ is a recovery decay constant. Using Eqs (2.32)-(2.34) and Eqs (2.37)-(2.38), the FH model [Eqs (2.35)-(2.36)] can be written in terms of the dimensional membrane potential, V_m, as follows:

$$\frac{\mathrm{d}V_m}{\mathrm{d}t} = \frac{c_1}{V_{\mathrm{a}}^2}\,(V_m - V_{\mathrm{r}})\,(V_m - V_{\mathrm{th}})\,(V_{\mathrm{p}} - V_m) - c_2\,V_{\mathrm{a}}\,v - \frac{I_{\mathrm{app}}}{C_m}\,, \tag{2.39}$$

$$\frac{\mathrm{d}v}{\mathrm{d}t} = \varepsilon\left(\frac{V_m - V_{\mathrm{r}}}{V_{\mathrm{a}}} - \gamma\,v\right)\,. \tag{2.40}$$

Note that in the literature, there are different forms used to describe the FH model. The form used here is taken from [18, 29].

The time courses of the membrane potential, V_m, and the gate variable, v, are shown in Figs 2.5a and 2.5b, respectively. To study the dynamics of the original FH model (in terms of u and v), its phase plane is established (Fig. 2.6).

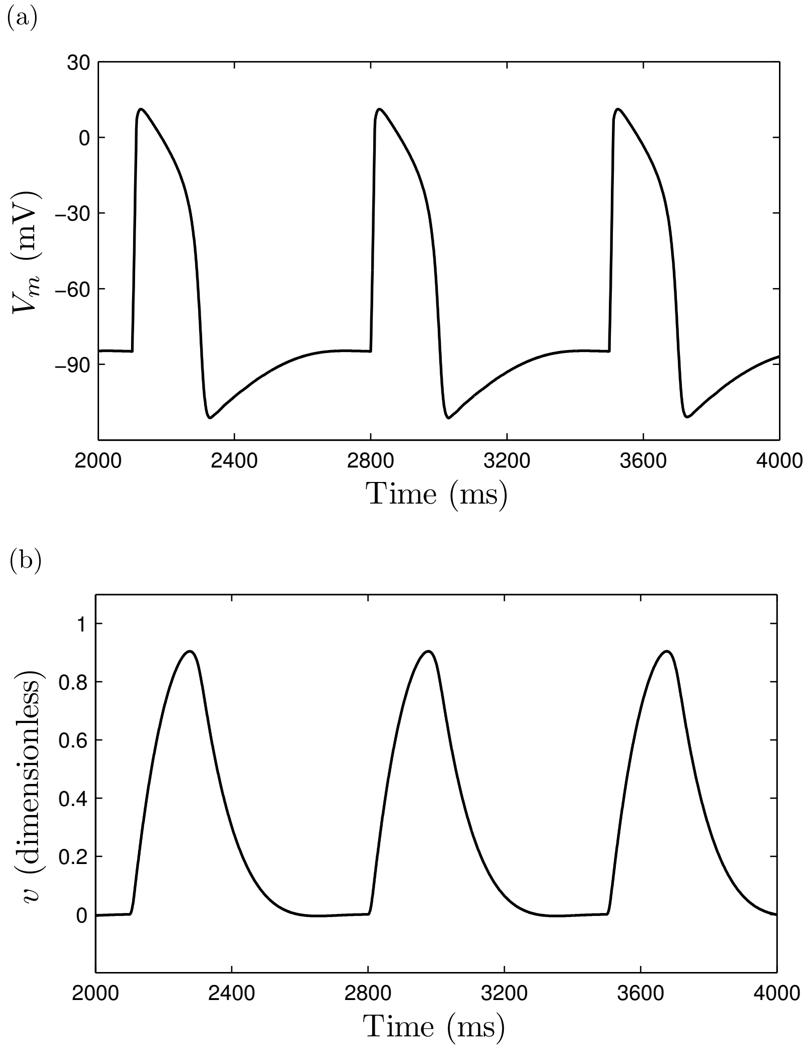

Fig. 2.5 – FitzHugh model: time courses of the membrane potential, V_m (a), and the gate variable, v (b), for an applied stimulus of $6.25\,\mu\mathrm{A\,cm^{-2}}$ at a frequency of $10/7\,\mathrm{Hz}$ and with a duration of $12.5\,\mathrm{ms}$. FH model parameter values are given in Tab. 2.2.

Parameter	Value	Units
C_m	1	$\mu\mathrm{F\,cm^{-2}}$
V_r	−85	mV
V_th	−75	mV
V_p	15	mV
c_1	0.175	$\mathrm{ms^{-1}}$
c_2	0.03	$\mathrm{ms^{-1}}$
ε	0.011	$\mathrm{ms^{-1}}$
γ	0.55	dimensionless

Tab. 2.2 – Parameter values of the FH model [18, 29, 41].

The nullclines are obtained by imposing conditions: $f(u,v) - i_\mathrm{app} = 0$ and $g(u,v) = 0$. As a result, when $i_\mathrm{app} = 0\,\mathrm{ms^{-1}}$, the u-nullcline and v-nullcline are given by the following equations, respectively:

$$v = \frac{c_1}{c_2} u \left(u - a\right) \left(1 - u\right) , \tag{2.41}$$

$$v = \frac{1}{\gamma} u \, . \tag{2.42}$$

Fig. 2.6 shows that the two nullclines have a single intersection point. This point represents the steady state of the FH system defined by $\mathrm{d}u/\mathrm{d}t = \mathrm{d}v/\mathrm{d}t = 0$. When $\varepsilon \longrightarrow 0$, it can be shown that this point is a linearly stable point if it is on the left branch (namely on the left side of the minimum of the u-nullcline) or the right branch (namely on the right side of the maximum of the u-nullcline) of the u-nullcline.

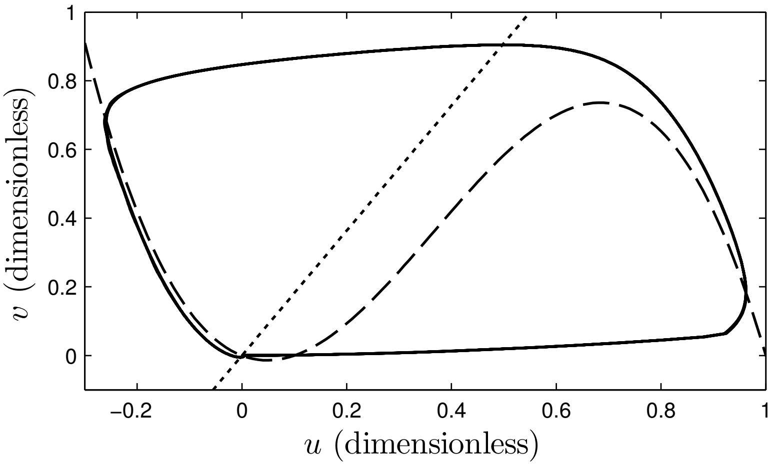

Fig. 2.6 – Phase plane of the original FH model in terms of u and v. Long dashed line represents the u-nullcline (Eq. 2.41) when $i_{\mathrm{app}} = 0\,\mathrm{ms}^{-1}$, short dashed line corresponds to the v-nullcline (Eq. 2.42) when $i_{\mathrm{app}} = 0\,\mathrm{ms}^{-1}$, and solid curve is the path of the phase point describing the state of the FH system from $2\,\mathrm{s}$ to $4\,\mathrm{s}$.

When the point corresponding to the steady state is on the left branch but not so far from the minimum of the u-nullcline (as it is the case in Fig. 2.6), the FH system is excitable [23]. This is due to the fact that even if the steady state is linearly stable, a sufficiently large perturbation from this point allows the excitation variable u to run far away from the steady state before eventually returning to the steady state (Fig. 2.6). The phase point (describing the state of the FH system) goes rapidly to the right branch and then it goes slowly upward following the right branch. When it reaches the maximum of the u-nullcline (top of the right branch), it goes rapidly to the left branch and eventually returns to the steady state staying close to this branch.

2.1.3.2 Rogers–McCulloch model (1994)

The *Rogers–McCulloch (RM) model* [18] consists in a modification of the original FH model. This modification was proposed mainly to prevent the hyperpolarization from the refractory part of the AP corresponding to the excursion of V_m below its resting value in Fig. 2.5a and the negative excursion of u in Fig. 2.6.

This hyperpolarization is not observed in actual cardiac APs and in addition, can affect the recovery properties of the model. The method used by *Rogers and McCulloch* [18] to eliminate this effect consists in modifying the last term in Eq. (2.35) as shown in Eq. (2.43). The RM model is mathematically described by the following two ODEs:

$$\frac{\mathrm{d}u}{\mathrm{d}t} = c_1\, u\, (u-a)\, (1-u) - c_2\, u\, v - i_{\mathrm{app}}, \tag{2.43}$$

$$\frac{\mathrm{d}v}{\mathrm{d}t} = b\, (u - d\, v)\ . \tag{2.44}$$

As with the FH model, the RM model [Eqs (2.43)-(2.44)] can be written in terms of the dimensional membrane potential, V_m:

$$\frac{\mathrm{d}V_m}{\mathrm{d}t} = \frac{c_1}{V_{\mathrm{a}}^2}\, (V_m - V_{\mathrm{r}})\, (V_m - V_{\mathrm{th}})\, (V_{\mathrm{p}} - V_m) - c_2\, (V_m - V_{\mathrm{r}})\, v - \frac{I_{\mathrm{app}}}{C_m}\ , \tag{2.45}$$

$$\frac{\mathrm{d}v}{\mathrm{d}t} = b\left(\frac{V_m - V_{\mathrm{r}}}{V_{\mathrm{a}}} - d\, v\right)\ . \tag{2.46}$$

As shown in Fig. 2.7a, the hyperpolarization does not occur anymore in the time course of the membrane potential. Thus, in comparison with the FH model, this model is closer to the actual behavior of an AP. Fig. 2.7b depicts the time course of the gate variable, v, simulated with the RM model.

Note that the original RM system [Eqs (2.43)-(2.44)] is characterized by two nullclines. When $i_{\mathrm{app}} = 0\,\mathrm{ms}^{-1}$, the u-nullcline is made up of two parts given by

$$v = \frac{c_1}{c_2}\, (u-a)\, (1-u)\ , \tag{2.47}$$

$$u = 0\,. \tag{2.48}$$

Regarding the v-nullcline, it consists of a single part given by a form similar to Eq. (2.42): $v = \dfrac{1}{d}\, u$.

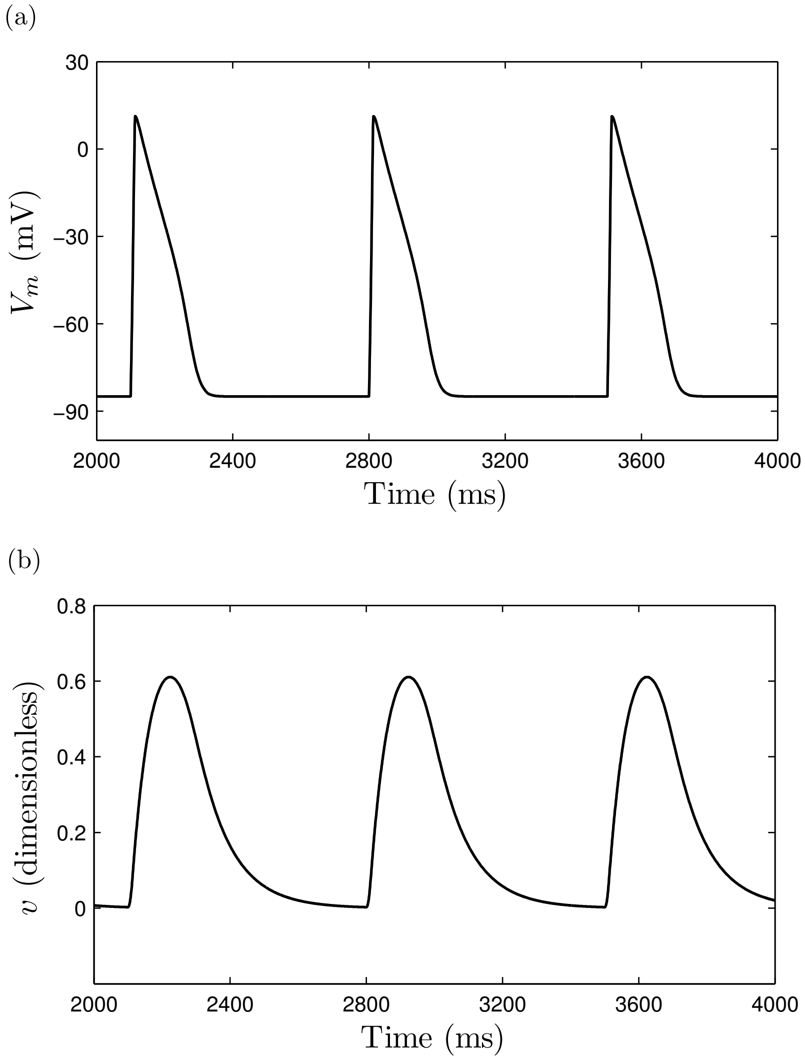

Fig. 2.7 – Rogers–McCulloch model: time courses of the membrane potential, V_m (a), and the gate variable, v (b), for an applied stimulus of $6.25\,\mu\mathrm{A\,cm^{-2}}$ at a frequency of $10/7\,\mathrm{Hz}$ and with a duration of $12.5\,\mathrm{ms}$. RM model parameter values are given in Tab. 2.3.

Parameter	Value	Units
C_m	1	$\mu\mathrm{F\,cm^{-2}}$
V_r	−85	mV
V_th	−75	mV
V_p	15	mV
c_1	0.26	$\mathrm{ms^{-1}}$
c_2	0.1	$\mathrm{ms^{-1}}$
b	0.013	$\mathrm{ms^{-1}}$
d	0.8	dimensionless

Tab. 2.3 – Parameter values of the RM model [18, 29, 41].

2.1.3.3 Aliev–Panfilov model (1996)

The *Aliev–Panfilov model (AlP model)*[7] [19] consists in another modification of the original FH model to mimic the cardiac electrophysiology in a more realistic way. More precisely, this model accounts for one important *restitution property* of cardiac tissue which is the *action potential duration (APD)* as a function of the cycle length of stimulation. Besides, the AlP model adequately represents the shape of an AP.

In a similar way to the FH model, the AlP model accounts for both fast and slow processes with only two variables controlled by the following two ODEs:

$$\begin{aligned} \frac{du}{dt} &= k_1\, u\, (u-a)\, (1-u) - k_2\, u\, v - i_{\text{app}}\,, &(2.49)\\ \frac{dv}{dt} &= \varepsilon\,(u,v)\; g_{\text{AlP}}\,(u,v) \;=\; \varepsilon\,(u,v)\, \left[-v - k_1\, u\, (u-a-1)\right]\,, &(2.50) \end{aligned}$$

where $\varepsilon\,(u,v)$ is given by

$$\varepsilon\,(u,v) \;=\; \varepsilon_0 + \frac{\mu_1\, v}{u+\mu_2}\,. \qquad (2.51)$$

As in the RM model, the second term on the right-hand side (RHS) of Eq. (2.35) is replaced by $-u\,v$ to prevent the hyperpolarization phenomenon. In addition, the original linear function g from Eq. (2.36) is replaced in Eq. (2.50) by the nonlinear function, g_{AlP}, to better fit the reality [19]. The AlP model can be written, in terms of the dimensional membrane potential, V_m:

$$\begin{aligned} \frac{\mathrm{d}V_m}{\mathrm{d}t} &= \frac{k_1}{V_{\text{a}}^2}\,(V_m - V_{\text{r}})\,(V_m - V_{\text{th}})\,(V_{\text{p}} - V_m) - k_2\,(V_m - V_{\text{r}})\,v - \frac{I_{\text{app}}}{C_m}\,, &(2.52)\\ \frac{\mathrm{d}v}{\mathrm{d}t} &= \varepsilon\,(V_m, v)\left[-v - \frac{k_1}{V_a^2}\,(V_m - V_{\text{r}})\,(V_m - V_{\text{th}} - V_{\text{a}})\right]\,, &(2.53) \end{aligned}$$

where

$$\varepsilon\,(V_m, v) \;=\; \varepsilon_0 + \frac{\mu_1\, v\, V_{\text{a}}}{V_m - V_{\text{r}} + \mu_2\, V_{\text{a}}}\,. \qquad (2.54)$$

The time courses of V_m and v are shown in Figs 2.8a and 2.8b, respectively.

---

[7] The abbreviations of ‘action potential’ and ‘Aliev Panfilov’ used in this work are AP and AlP, respectively.

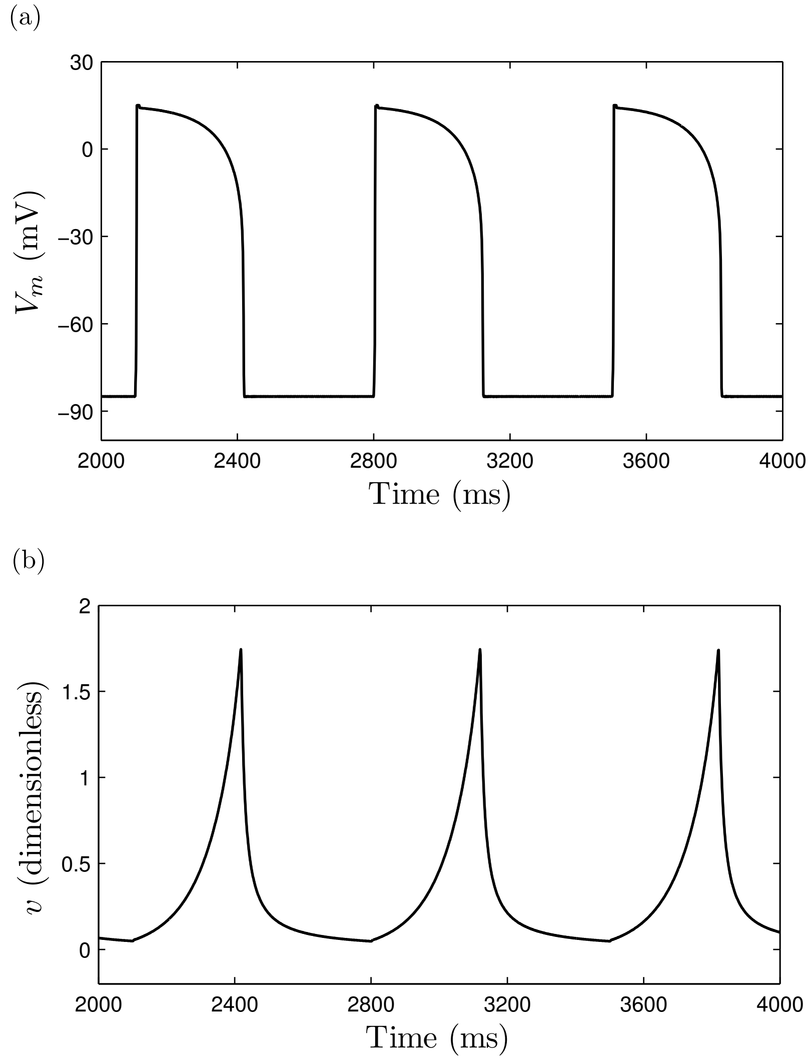

Fig. 2.8 – Aliev–Panfilov model: time courses of the membrane potential, V_m (a), and the gate variable, v (b), for an applied stimulus of $6.25\,\mu\mathrm{A\,cm^{-2}}$ at a frequency of $10/7\,\mathrm{Hz}$ and with a duration of $12.5\,\mathrm{ms}$. AlP model parameter values are given in Tab. 2.4.

Parameter	Value	Units
C_m	1	$\mu\mathrm{F\,cm^{-2}}$
V_r	-85	mV
V_th	-75	mV
V_p	15	mV
k_1	8	$\mathrm{ms^{-1}}$
k_2	1	$\mathrm{ms^{-1}}$
ε_0	0.0002	$\mathrm{ms^{-1}}$
μ_1	0.0155	$\mathrm{ms^{-1}}$
μ_2	0.3	dimensionless

Tab. 2.4 – Parameter values of the AlP model [19].

Note that the original AlP system [Eqs (2.49)-(2.51)] is characterized by two nullclines. When $i_{\mathrm{app}} = 0\,\mathrm{ms}^{-1}$, the u-nullcline is composed of two parts given by

$$\begin{aligned} v &= \frac{k_1}{k_2}\,(u-a)\,(1-u)\;, && (2.55)\\ u &= 0\,. && (2.56) \end{aligned}$$

Regarding the v-nullcline, it is made up of a single part:

$$v = -k_1\,u\,(u-a-1)\;. \qquad (2.57)$$

2.1.3.4 Fenton–Karma model (1998)

The *Fenton–Karma (FK) model* [20], known as the *three-variable model*, aims at *quantitatively* mimicking the ventricular AP and its restitution properties by retaining the minimal ionic complexity. This model describes the total ionic current as the sum of three ionic currents:

$$I_{\mathrm{ion}} = I_{\mathrm{fi}} + I_{\mathrm{so}} + I_{\mathrm{si}}\,, \qquad (2.58)$$

where I_{fi} is a fast inward current (sodium current) that is responsible for depolarization of the membrane, I_{so} is a slow outward current (potassium current) that is responsible for repolarization of the membrane, and I_{si} is a slow inward current (calcium current) that balances I_{so}. Note that I_{fi} depends on membrane potential V_m and on one *inactivation–reactivation* gate variable v. I_{so} depends only on the membrane potential V_m, and I_{si} depends on V_m and on one inactivation–reactivation gate variable w.

As already noted, reducing the dynamics of the membrane to the sodium, potassium, and calcium currents is an oversimplification of the actual dynamics [42]. However, taking into account only these three currents retains the minimal ionic complexity providing the membrane recovery processes that give rise to generic restitution curves [20]. Fenton and Karma refer to these currents as fast inward, slow inward, and slow outward currents rather than sodium, calcium, and potassium currents to emphasize that they do not represent quantitatively individual measured currents, but rather their activation, inactivation, and reactivation dynamics needed to reproduce restitution properties in a quantitative way.

For convenience, Fenton and Karma introduced a dimensionless membrane potential, u, and scaled currents (ms^{-1}) in the following way:

$$u = \frac{V_m - V_0}{V_{\mathrm{fi}} - V_0}\,, \tag{2.59}$$

$$J_{\mathrm{fi}} = \frac{I_{\mathrm{fi}}}{C_m\,(V_{\mathrm{fi}} - V_0)}\,, \tag{2.60}$$

$$J_{\mathrm{so}} = \frac{I_{\mathrm{so}}}{C_m\,(V_{\mathrm{fi}} - V_0)}\,, \tag{2.61}$$

$$J_{\mathrm{si}} = \frac{I_{\mathrm{si}}}{C_m\,(V_{\mathrm{fi}} - V_0)}\,, \tag{2.62}$$

where V_{fi}, V_{so}, and V_{si} represent the reversal potentials of the fast inward, slow outward, and slow inward currents, respectively, while V_0 is the resting membrane potential. As a result, from Eq. (2.31) and Eqs (2.59)-(2.62), the following ODE is obtained:

$$\frac{\mathrm{d}u}{\mathrm{d}t} = -\left(J_{\mathrm{fi}} + J_{\mathrm{so}} + J_{\mathrm{si}}\right) - J_{\mathrm{app}}\,, \tag{2.63}$$

where $J_{\mathrm{app}} = I_{app}\,C_m^{-1}\,(V_{\mathrm{fi}} - V_0)^{-1}$ is an applied scaled current. In Eq. (2.63), J_{fi} behaves as a function of u and v, J_{so} depends only on u, and J_{si} is a function of u and w. The dynamics of the gate variables, v and w, depicted in Fig. 2.9, are controlled by the following two ODEs:

$$\frac{\mathrm{d}v}{\mathrm{d}t} = \frac{1-v}{\tau_v^-}\,\Theta\left(u_c^{\mathrm{fi}} - u\right) - \frac{v}{\tau_v^+}\,\Theta\left(u - u_c^{\mathrm{fi}}\right)\,, \tag{2.64}$$

$$\frac{\mathrm{d}w}{\mathrm{d}t} = \frac{1-w}{\tau_w^-}\,\Theta\left(u_c^{\mathrm{fi}} - u\right) - \frac{w}{\tau_w^+}\,\Theta\left(u - u_c^{\mathrm{fi}}\right)\,, \tag{2.65}$$

where τ_v^- and τ_v^+ are the time constants that govern the reactivation and the inactivation of the fast inward current, respectively, τ_w^- and τ_w^+ represent the time constants that govern the reactivation and the inactivation of the slow inward current, u_c^{fi} is the threshold membrane potential for activation of J_{fi}, and Θ represents the well-known Heaviside function. In addition, Fenton and Karma found that it was necessary to express τ_v^- separately over two voltage ranges as follows:

$$\tau_v^- = \tau_{v1}^-\,\Theta\left(u_v - u\right) + \tau_{v2}^-\,\Theta\left(u - u_v\right)\,, \tag{2.66}$$

where u_v is a threshold membrane potential. As a result, $\tau_v^- = \tau_{v1}^-$ if u is smaller than u_v and $\tau_v^- = \tau_{v2}^-$ otherwise.

Finally, the three scaled currents which control the dynamics of u (Fig. 2.9) are given by

$$\begin{aligned} J_{\text{fi}}(u,v) &= -\frac{v}{\tau_d}\,(1-u)\,\left(u-u_c^{\text{fi}}\right)\,\Theta\left(u-u_c^{\text{fi}}\right)\,, && (2.67)\\ J_{\text{so}}(u) &= \frac{u}{\tau_o}\,\Theta\left(u_c^{\text{fi}}-u\right)+\frac{1}{\tau_r}\,\Theta\left(u-u_c^{\text{fi}}\right)\,, && (2.68)\\ J_{\text{si}}(u,w) &= -\frac{w}{2\,\tau_{\text{si}}}\,\left(1+\tanh\left[k\,\left(u-u_c^{\text{si}}\right)\right]\right)\,. && (2.69) \end{aligned}$$

In Eq. (2.69), u_c^{si} is the threshold membrane potential for activation of J_{si} and k is a parameter. In addition, τ_d, τ_o, τ_r, and τ_{si} represent the time scales to depolarize the membrane, the time constant to repolarize the membrane when $u < u_c^{\text{fi}}$, the time constant to repolarize the membrane when $u > u_c^{\text{fi}}$, and the time constant of the slow inward current, respectively. They are given by $\tau_d = C_m/\bar{g}_{\text{fi}}$, $\tau_o = C_m/\bar{g}_{\text{so}}$, $\tau_r = C_m/\bar{I}_{\text{so}}$, and $\tau_{si} = C_m/\bar{I}_{\text{si}}$.

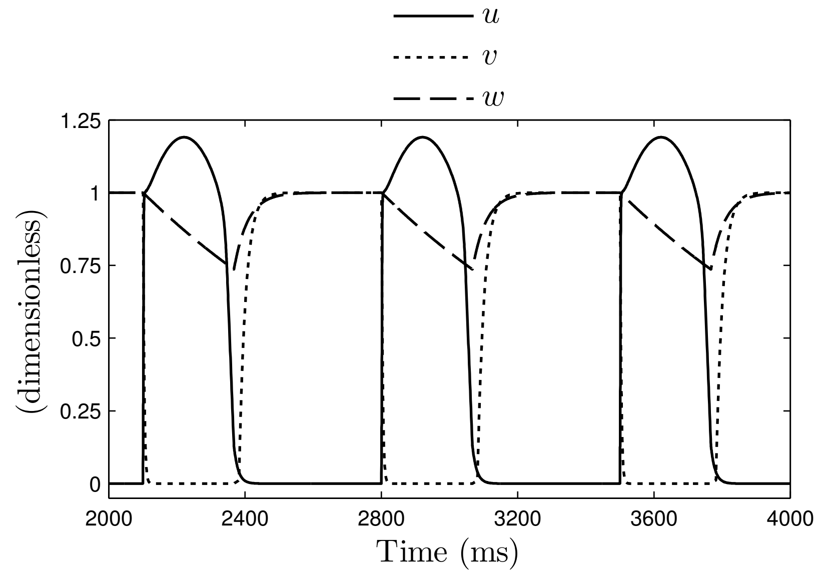

Fig. 2.9 – Fenton–Karma model: time courses of the dimensionless membrane potential, u (solid line), the inactivation-reactivation gate variable, v (long dashed line), and the inactivation-reactivation gate variable, w (short dashed line), for an applied scaled stimulus of $0.2\,\text{ms}^{-1}$ at a frequency of $10/7\,\text{Hz}$ and with a duration of $1\,\text{ms}$. FK model parameter values are given in Tab. 2.5.

Parameter	set 1	set 2	set 3	set 4	Units
$\bar{g}_{\mathrm{fi}}$	4	4	5.8	8.7	dimensionless
C_m	1	1	1	1	$\mu\mathrm{F\,cm}^{-2}$
V_0	-85	-85	-85	-85	mV
τ_r	33.33	50	130	25	ms
τ_{si}	29	44.84	127	22.22	ms
τ_o	12.5	8.3	12.5	12.5	ms
τ_v^+	3.33	3.33	10	10	ms
τ_{v1}^-	1250	1000	18.2	333	ms
τ_{v2}^-	19.6	19.2	18.2	40	ms
τ_w^+	870	667	1020	1000	ms
τ_w^-	41	11	80	65	ms
u_c^{fi}	0.13	0.13	0.13	0.13	dimensionless
u_v	0.04	0.055	–	0.025	dimensionless
u_c^{si}	0.85	0.85	0.85	0.85	dimensionless
k	10	10	10	10	dimensionless

Tab. 2.5 – Parameter values of the FK model [20].

2.2 Electrical activity in the whole heart

As already described in section 1.2, an electrical excitation (depolarization of cell membrane) is spontaneously generated by specialized cells in a specific region (SA node). The coordinated contraction of the whole cardiac tissue is the consequence of the propagation of this electrical excitation throughout the heart in a rapid and highly coordinated fashion. Previous sections have shown the way to model the electrical activity at a cell level. However, the overall goal of this work is to study this activity at a tissue level. Thus, a mathematical model is needed to describe the propagation of the depolarization wave through the cardiac tissue.

2.2.1 Cardiac tissue is modeled as a continuous medium

To avoid difficulties arising from the discrete nature of the cardiac tissue, which is composed of cells, a common convenient way is to consider that any physical quantity at a ‘point’ within the cardiac tissue is defined as the average over a small (in comparison with the scales of the study) but multicellular volume around the considered point. As a result, the cardiac tissue can be modeled as a *volume conductor* [41]. Consequently, from Maxwell’s equations, it is known that for a volume conductor, the *electric field* $\mathbf{E}$

and the *magnetic field* **B** are related by the following equation:

$$\operatorname{curl}\mathbf{E} \;=\; -\frac{\partial \mathbf{B}}{\partial t}\,, \tag{2.70}$$

known as the *Faraday's law of induction.* In cardiac tissue, the *quasi-stationarity condition* can be considered [43] and therefore, Eq. (2.70) reduces to

$$\operatorname{curl}\mathbf{E} \;=\; \mathbf{0}\,. \tag{2.71}$$

From Eq. (2.71), the electric field can be written as the negative gradient of a *scalar electric potential function*, ϕ:

$$\mathbf{E} \;=\; -\operatorname{grad}\phi\,. \tag{2.72}$$

In addition, it is known that any volume conductor is characterized by its intrinsic properties, taken into account by a constitutive equation, which will be chosen as *Ohm's law.* From this law, the *current density vector*, **J**, is known to be proportional to the electric field:

$$\mathbf{J} \;=\; \boldsymbol{\sigma}\cdot\mathbf{E}\,, \tag{2.73}$$

where $\boldsymbol{\sigma}$ is the *conductivity tensor.* Combining Eq. (2.72) and Eq. (2.73), the following relation may be written:

$$\mathbf{J} \;=\; -\boldsymbol{\sigma}\cdot\operatorname{grad}\phi\,. \tag{2.74}$$

Moreover, considering a part of the volume conductor characterized by a volume, $\mathcal{V}$, surrounded by a surface, $\mathcal{S}$, and assuming that there are no current sources or sinks and there is no build-up of charge at any spatial point inside $\mathcal{V}$, the following equality must be satisfied:

$$\int_{\mathcal{S}} \mathbf{n}\cdot\mathbf{J}\,\mathrm{d}\mathcal{S} \;=\; 0\,, \tag{2.75}$$

where $\mathbf{n}$ is the outward unit normal to the surface $\mathcal{S}$. Using the divergence theorem, Eq. (2.75) can also be written as

$$\int_{\mathcal{V}} \operatorname{div} \mathbf{J} \, \mathrm{d}\mathcal{V} \;=\; 0 \tag{2.76}$$

and given that Eq. (2.76) must be satisfied for any volume $\mathcal{V}$, the integrand must vanish:

$$\operatorname{div} \mathbf{J} \;=\; 0\,. \tag{2.77}$$

2.2.2 The bidomain model

The *bidomain model* was introduced for the first time in [44] to describe the spatial distribution of macroscopic electric potentials as they are measured on the heart surface. The bidomain model aims at describing quantities associated with both intracellular and extracellular domains at a macroscopic scale.

Intracellular and extracellular quantities are defined in the bidomain model in an averaged sense. They consist in spatial averages of the corresponding (local) microscopic quantities. As a result, the bidomain model considers the cardiac tissue as a *two-phase medium* where the extracellular and intracellular domains occupy the same macroscopic three-dimensional space and overlap at every point. At the microscopic scale, these two domains are actually physically separated by cell membranes and interconnected by specific structures embedded in cell membranes.

Each domain is considered separately as a distinct and homogeneous structure. Moreover, the electrical properties of each domain mainly depend on:

i. the passive electrical properties of each domain;
ii. the electrical properties of gap junctions between neighboring cells;
iii. the geometric configuration of the cardiac cells.

In addition, the coupling between both domains is provided by the transmembrane current, I_m, through the cell membrane. The cell membrane can be viewed from a macroscopic point of view as a volume-distributed boundary which separates the intracellular and extracellular domains [44, 45, 46].

2.2.2.1 Mathematical description of the bidomain model

Let $\boldsymbol{\sigma}_{\mathrm{i}}$ and $\boldsymbol{\sigma}_{\mathrm{e}}$ be the conductivity tensors of the intracellular and extracellular domains, respectively. At each spatial point in the cardiac tissue, the current density vector $\mathbf{J}$ can be split into two components in the following way:

$$\mathbf{J} \;=\; \mathbf{J}_{\mathrm{i}} + \mathbf{J}_{\mathrm{e}}\,, \tag{2.78}$$

where $\mathbf{J}_{\mathrm{i}}$ and $\mathbf{J}_{\mathrm{e}}$ are the current density vectors relative to the intracellular and extracellular domains, respectively. For each domain, Ohm's law can be applied from Eq. (2.73). Therefore, $\mathbf{J}_{\mathrm{i}}$ and $\mathbf{J}_{\mathrm{e}}$ are given by

$$\mathbf{J}_{\mathrm{i}} \;=\; -\boldsymbol{\sigma}_{\mathrm{i}} \cdot \mathrm{grad}\, \phi_{\mathrm{i}}\,, \tag{2.79}$$

$$\mathbf{J}_{\mathrm{e}} \;=\; -\boldsymbol{\sigma}_{\mathrm{e}} \cdot \mathrm{grad}\, \phi_{\mathrm{e}}\,. \tag{2.80}$$

From Eqs (2.77)-(2.80), at each spatial point, the following relation is satisfied:

$$\mathrm{div}\left(\boldsymbol{\sigma}_{\mathrm{i}} \cdot \mathrm{grad}\, \phi_{\mathrm{i}} + \boldsymbol{\sigma}_{\mathrm{e}} \cdot \mathrm{grad}\, \phi_{\mathrm{e}}\right) \;=\; 0\,. \tag{2.81}$$

As $V_m = \phi_{\mathrm{i}} - \phi_{\mathrm{e}}$, Eq. (2.81) can also be written as

$$\mathrm{div}\left(\boldsymbol{\sigma}_{\mathrm{i}} \cdot \mathrm{grad}\, V_m\right) \;=\; -\mathrm{div}\left[\left(\boldsymbol{\sigma}_{\mathrm{i}} + \boldsymbol{\sigma}_{\mathrm{e}}\right) \cdot \mathrm{grad}\, \phi_{\mathrm{e}}\right]\,. \tag{2.82}$$

The transmembrane current, I_m, at a spatial point, is considered positive when it leaves the intracellular domain to enter the extracellular domain through the volume-distributed cell membrane. Note that any current leaving one domain must enter the other as a transmembrane current [44]:

$$I_m \;=\; -\mathrm{div}\mathbf{J}_{\mathrm{i}} \;=\; \mathrm{div}\left(\boldsymbol{\sigma}_{\mathrm{i}} \cdot \mathrm{grad}\, \phi_{\mathrm{i}}\right)\,, \tag{2.83}$$

$$I_m \;=\; \mathrm{div}\mathbf{J}_{\mathrm{e}} \;=\; -\mathrm{div}\left(\boldsymbol{\sigma}_{\mathrm{e}} \cdot \mathrm{grad}\, \phi_{\mathrm{e}}\right)\,. \tag{2.84}$$

As already mentioned in section 2.1.2, the transmembrane current consists of both ionic and capacitive currents. From Eqs (2.2) and (2.83), the following relation is obtained:

$$\chi \left(C_m \frac{\partial V_m}{\partial t} + I_{\mathrm{ion}}\right) \;=\; \mathrm{div}\left(\boldsymbol{\sigma}_{\mathrm{i}} \cdot \mathrm{grad}\, \phi_{\mathrm{i}}\right)\,, \tag{2.85}$$

where χ is a constant that represents the ratio of the membrane area to volume of the myocytes[8]. Given that $V_m = \phi_{\rm i} - \phi_{\rm e}$, Eq. (2.85) can be written as

$$\chi\left(C_m\,\frac{\partial V_m}{\partial t} + I_{\rm ion}\right) = \operatorname{div}\left(\boldsymbol{\sigma}_{\rm i}\cdot\operatorname{grad}V_m\right) + \operatorname{div}\left(\boldsymbol{\sigma}_{\rm i}\cdot\operatorname{grad}\phi_{\rm e}\right)\;. \qquad (2.86)$$

Eqs (2.82) and (2.86) provide the classical formulation of the bidomain model.

2.2.3 The monodomain model

The *monodomain model* is a simplification of the bidomain model based on the assumption of *equal anisotropy ratios*:

$$\boldsymbol{\sigma}_{\rm e} = \alpha\,\boldsymbol{\sigma}_{\rm i}\,, \qquad (2.87)$$

where α is a constant scalar [23, 41]. Taking into account Eq. (2.87), Eq. (2.82) becomes

$$\operatorname{div}\left(\boldsymbol{\sigma}_{\rm i}\cdot\operatorname{grad}V_m\right) = -\left(1+\alpha\right)\,\operatorname{div}\left(\boldsymbol{\sigma}_{\rm i}\cdot\operatorname{grad}\phi_{\rm e}\right) \qquad (2.88)$$

or, equivalently,

$$\frac{1}{1+\alpha}\operatorname{div}\left(\boldsymbol{\sigma}_{\rm i}\cdot\operatorname{grad}V_m\right) = -\operatorname{div}\left(\boldsymbol{\sigma}_{\rm i}\cdot\operatorname{grad}\phi_{\rm e}\right)\;. \qquad (2.89)$$

Substituting Eq. (2.89) into Eq. (2.86), the following relation is obtained:

$$\chi\left(C_m\,\frac{\partial V_m}{\partial t} + I_{\rm ion}\right) = \operatorname{div}\left(\boldsymbol{\sigma}_{\rm i}\cdot\operatorname{grad}V_m\right) - \frac{1}{1+\alpha}\operatorname{div}\left(\boldsymbol{\sigma}_{\rm i}\cdot\operatorname{grad}V_m\right)\;. \qquad (2.90)$$

The monodomain equation can then be written as

$$\chi\left(C_m\,\frac{\partial V_m}{\partial t} + I_{\rm ion}\right) = \frac{\alpha}{1+\alpha}\operatorname{div}\left(\boldsymbol{\sigma}_{\rm i}\cdot\operatorname{grad}V_m\right)\;, \qquad (2.91)$$

---

[8] Considering a single cell, the transmembrane current is given by Eq. (2.2). Assuming an element of volume $\mathrm{d}\mathcal{V}$ containing n cells, each one characterized by an area, $\mathcal{S}$, the total transmembrane current inside $\mathrm{d}\mathcal{V}$ is given by multiplying Eq. (2.2) by $n\,\mathcal{S}$. If the result of this product is divided by $\mathrm{d}\mathcal{V}$, χ naturally appears and represents the ratio of the area of the surface of a cell over the volume $\mathrm{d}\mathcal{V}/n$ occupied by the considered cell inside $\mathrm{d}\mathcal{V}$.

or,

$$\chi \left(C_m \frac{\partial V_m}{\partial t} + I_{\text{ion}} \right) \quad = \quad \operatorname{div} \left(\boldsymbol{\sigma} \cdot \operatorname{grad} V_m \right) \,, \tag{2.92}$$

where

$$\boldsymbol{\sigma} \quad = \quad \frac{\alpha}{1+\alpha} \, \boldsymbol{\sigma}_{\text{i}} \,. \tag{2.93}$$

CHAPTER 3

Cardiac mechanics

During the heart cycle, cardiomyocytes undergo large deformations. Their length can be stretched by up to 20 % with respect to their unstressed length [47]. Therefore, the linearized theory of elasticity is not suitable to describe the motion of the cardiac tissue. The finite deformation theory (the nonlinear theory of elasticity) is necessary. In this chapter, a general theoretical framework for modeling cardiac tissue mechanics enabling to account for most intrinsic properties of the heart is presented. First, the basic assumptions of the continuum mechanics are reminded and key notions therein as well. Secondly, some basic elements of kinematics (the study of motion and deformation), which are required to describe cardiac mechanics, are discussed. Third, the physical laws (the balance principles) which govern the spatio-temporal behavior of all continuous media, independently of the intrinsic nature of materials, are briefly reviewed. The constitutive laws are also discussed briefly. Finally, the general framework is particularized to the specific cases examined in this work.

Contents

3.1 Preliminaries

3.1.1 Key assumptions and notions

3.1.1.1 Particles and continuous bodies

By nature, matter is discontinuous due to its atomic structure. Nevertheless, when a *macroscopic system* in the sense that the typical spatial scales of phenomena involved are large enough with respect to the intermolecular spacings is studied, the matter can then be successfully described with a continuous approach (macroscopic approach). In the continuum mechanics theory, a fundamental assumption states that a body, labeled $\mathcal{B}$, may be considered as having a continuous distribution of matter with respect to space and time. Moreover, the body $\mathcal{B}$ can be viewed as a continuous set of *particles*, labeled $\mathcal{P}$. Note that a particle can also be referred to as a *material point* in the field of continuum mechanics. A very important notion to emphasize is that the particle does not have to be understood as the point mass of the Newtonian mechanics or as the discrete particle of the atomistic theory. Actually, a continuous particle is a part of a continuous body and typically, involves an accumulation of a large number molecules but small enough to be considered as a particle.

3.1.1.2 Frame of reference and coordinate system

In common life, people and other objects occupy particular positions, which are sets of points in a three-dimensional space. The properties of these points are given once and for all and are not modulated by the presence or absence of people. Besides, the changes that people observe in themselves or in their environment are considered to be at specific instants, which are points in a one-dimensional space altogether independent on the space of positions. Positions and instants are associated with *events*. The totality of events is called the *event world* $\mathcal{W}$. As very nicely depicted in [48], *'the event world is the blank canvas on which pictures of nature may be painted, the quarry for blocks from which statues of nature may be carved. This canvas, this quarry, must be chosen by the artist before he sets to work. It lays limitations upon his art, but it by no means determines the images he will fashion.'*

Each event, referred to as e, occurs at a specific instant. All these instants are elements of a given *Euclidean space* $\mathcal{T}$. Different events that take place at the same instant are said to be *simultaneous*. The totality of the simultaneous events at the instant t is referred to as $\mathcal{W}_t$ and it assumed to be a three-dimensional Euclidean space.

Assuming a three-dimensional Euclidean point space $\mathcal{E}$, an event e is mathematically described in terms of a frame of reference $\mathcal{O}$ defined as a function

$$\mathcal{O} \ : \ \mathcal{W} \mapsto \mathcal{E} \times \mathcal{T} \tag{3.1}$$

such that

$$\mathcal{O}\left(e\right) \ = \ \left(\mathbf{x}, t\right) \ , \tag{3.2}$$

where $\mathcal{O}$ is a bijection such that $\mathcal{O}_t$, namely the restriction of $\mathcal{O}$ to $\mathcal{W}_t$, is a bijection of $\mathcal{W}_t$ onto $\mathcal{E}$ for each instant t. Formally, it can be written as follows:

$$\mathcal{O}_t \ : \ \mathcal{W}_t \mapsto \mathcal{E} \, , \quad \mathcal{O}_t\left(e\right) = \mathbf{x} \, , \tag{3.3}$$

if

$$\mathcal{O}\left(e\right) = \left(\mathbf{x}, t\right) \ . \tag{3.4}$$

The different elements of $\mathcal{E}$ are referred to as $\mathbf{x}$ and are called positions in $\mathcal{E}$. In a more physical way, a frame of reference can be viewed as a moving rigid-body with its own time clock and given the nature of physical phenomena involved in this doctoral study, it is reasonable to consider the continuous medium as governed by *classical mechanics* and therefore, time is independent of the frame of reference used. As a result, time is an *absolute* notion. In addition, a coordinate system can be assigned to $\mathcal{T}$. The coordinate of an instant is the *time* of this instant. Commonly, the unit and origin of time in a particular frame of reference $\mathcal{O}$ are considered as set in advance by the observer and $\mathcal{T}$ is identified with the real line $\mathcal{R}$ regarding this choice of coordinate and metric. As a result, Eq. (3.1) may be rewritten as

$$\mathcal{O} \;:\; \mathcal{W} \mapsto \mathcal{E} \times \mathcal{R}\,. \tag{3.5}$$

Moreover, to quantify the motion of a particle[1] $\mathcal{P}$ embedded in a continuous medium, it is needed to introduce a coordinate system in the chosen frame of reference. In other words, the coordinate system allows to mathematically describe the behavior of a continuous medium in a specific frame of reference. It is important to note that an infinity of coordinate systems can be defined in a particular frame of reference.

3.1.2 Configurations and motion

When a continuous body $\mathcal{B}$ moves in space from one instant of time to another, it occupies a continuous sequence of geometrical regions referred to as the configurations of the body. Mathematically, the motion, labeled $\boldsymbol{\chi}$, of the continuous body $\mathcal{B}$ can be written as

$$\boldsymbol{\chi} \;:\; \mathcal{B} \times \mathcal{R} \mapsto \mathcal{E} \tag{3.6}$$

and explicitly,

$$\mathbf{x} \;=\; \boldsymbol{\chi}\left(\mathcal{P}, t\right)\,, \quad \mathcal{P} \in \mathcal{B}\,, \quad t \in \mathcal{I}\,. \tag{3.7}$$

Eq. (3.7) means that $\mathbf{x}$ is the position in $\mathcal{E}$ that the particle $\mathcal{P}$ occupies at the time t in the motion $\boldsymbol{\chi}$. In addition, the configuration Ω of $\mathcal{B}$ at the time t is the set of positions that the particles occupy. As a result, the following relation can be written:

$$\Omega \;=\; \boldsymbol{\chi}\left(\mathcal{B}, t\right) \tag{3.8}$$

$$\;=\; \left\{\boldsymbol{\chi}\left(\mathcal{P}, t\right) : \mathcal{P} \in \mathcal{B}\right\}\,. \tag{3.9}$$

---

[1] In the sense defined in section 3.1.1.1.

In addition, for each t, the mapping $\boldsymbol{\chi}(\bullet, t)$ is assumed to be a *homeomorphism* of $\mathcal{B}$ onto its configuration $\boldsymbol{\chi}(\mathcal{B}, t)$ and has an inverse $\boldsymbol{\chi}^{-1}(\bullet, t)$, defined over the configuration $\boldsymbol{\chi}(\mathcal{B}, t)$ as follows:

$$\mathcal{P} \;=\; \boldsymbol{\chi}^{-1}(\mathbf{x}, t)\;, \quad \mathbf{x} \in \boldsymbol{\chi}(\mathcal{B}, t)\;, \quad t \in \mathcal{I}\,. \tag{3.10}$$

Note that in mechanics, it is customary to consider that such motions $\boldsymbol{\chi}$ are differentiable with respect to t at least twice and often as many times as desired for each particle $\mathcal{P}$ [48]. In particular, the velocity $\mathbf{v}$ of the particle $\mathcal{P}$ is given by

$$\mathbf{v} \;=\; \frac{\partial \boldsymbol{\chi}(\mathcal{P}, t)}{\partial t}\,. \tag{3.11}$$

3.1.2.1 Material description

The *material description* defines the motion in terms of the particles embedded in the body and the time t. Therefore, the motion can symbolically be written as in Eq. (3.7).

3.1.2.2 Referential description

The *referential description* defines the motion with respect to an arbitrarily chosen reference configuration, in which the particle $\mathcal{P}$ occupies the position $\mathbf{X}$, and the time t. Mathematically, the motion is written as follows:

$$\mathbf{x} \;=\; \boldsymbol{\chi}(\mathbf{X}, t)\;. \tag{3.12}$$

Note that in elasticity, the reference configuration is very often chosen as the initial unstressed state. When the chosen reference configuration corresponds to the initial configuration at time $t = 0$, the referential description is called the *Lagrangian description*. Note also that, in the literature, the distinction between the referential description and the material description is not very straightforward. The main reason is that most of the authors use the position $\mathbf{X}$ of the particle $\mathcal{P}$ in the reference configuration as a label for the particle and therefore refer to Eq. (3.12) as the material description.

3.1.2.3 Spatial description

The spatial description or *Eulerian description* describes the motion in terms of the current position $\mathbf{x}$ occupied by the particle at time t and the present time t. This description is very popular in the field of fluid mechanics.

3.1.2.4 Conventions used in this thesis

The conventions used to describe the motion in this work are now emphasized. First, most of the time, the reference configuration of a body corresponds to the initial configuration of this body at time $t = 0$, namely the Lagragian description. Moreover, the coordinates associated with the position $\mathbf{X}$ of the particle $\mathcal{P}$ in the reference configuration are called *material coordinates* while the ones associated with the position $\mathbf{x}$ in the current configuration are called *spatial coordinates*.

3.1.3 Position vector, base vectors, covariant and contravariant components

A *position vector* of a position $\mathbf{x}$ in $\mathcal{E}$ is a vector that translates some given origin $\mathbf{x}_0$ into $\mathbf{x}$. Therefore, a *position vector field*, $\mathbf{p}$, associated with the motion $\boldsymbol{\chi}$ is defined as follows:

$$\mathbf{p}\,(\mathcal{P}, t) \;=\; \boldsymbol{\chi}\,(\mathcal{P}, t) - \mathbf{x}_0\,. \tag{3.13}$$

To each coordinate system, a set of *base vectors*, forming a *basis*, can be associated. If the basis consists of mutually orthogonal unit vectors, it is an *orthonormal basis*. For instance, such a basis is usually associated with Cartesian coordinates and in this case, $\mathbf{p}$ is given by

$$\mathbf{p} \;=\; z^1\,\mathbf{i}_1 + z^2\,\mathbf{i}_2 + z^3\,\mathbf{i}_3\,, \tag{3.14}$$

where z^1, z^2, and z^3 are the three components of the vector $\mathbf{p}$ and the coordinates of $\mathcal{P}$ in the Cartesian coordinate system, and $\mathbf{i}_1$, $\mathbf{i}_2$, and $\mathbf{i}_3$ are the unit vectors parallel to the coordinate axes. Using the *summation convention* of Einstein[2], Eq. (3.14) can be rewritten in the form

$$\mathbf{p} \;=\; z^r\, \mathbf{i}_r \tag{3.15}$$

and the position vector increment, $\mathrm{d}\mathbf{p}$, is written as follows:

$$\mathrm{d}\mathbf{p} \;=\; \mathrm{d}z^r\, \mathbf{i}_r\,. \tag{3.16}$$

Now, a set of base vectors[3], $\mathbf{g}_m$ ($m = 1,\, 2,\, 3$), associated with a general curvilinear coordinate system, x^m ($m = 1,\, 2,\, 3$), called the *natural basis* of the general curvilinear coordinate system, is introduced. The position vector increment, $\mathrm{d}\mathbf{p}$, can also be written, in terms of the general curvilinear coordinate system, in the following way:

$$\mathrm{d}\mathbf{p} \;=\; \mathrm{d}x^m\, \mathbf{g}_m\,, \tag{3.17}$$

where the base vectors $\mathbf{g}_m$ are defined by

$$\mathbf{g}_m \;=\; \frac{\partial \mathbf{p}}{\partial x^m} \tag{3.18}$$

and are thus tangent to the coordinate lines. Note that the base vectors regarding the Cartesian coordinate system can also be defined by the same relation:

$$\mathbf{i}_r \;=\; \frac{\partial \mathbf{p}}{\partial z^r} \quad \text{with } r = 1,\, 2,\, 3\,. \tag{3.19}$$

In addition, $\mathbf{g}_m$ can be decomposed in terms of the base vectors $\mathbf{i}_r$:

$$\mathbf{g}_m \;=\; \frac{\partial \mathbf{p}}{\partial z^r}\,\frac{\partial z^r}{\partial x^m} \tag{3.20}$$

$$\;=\; \frac{\partial z^r}{\partial x^m}\,\mathbf{i}_r\,. \tag{3.21}$$

Now, consider another set of base vectors, $\bar{\mathbf{g}}_m$ ($m = 1,\, 2,\, 3$), which is the natural basis of another general curvilinear coordinate system, $\bar{x}_m$ ($m = 1,\, 2,\, 3$). The position vector

---

[2] For components associated with an arbitrary curvilinear coordinate system, summation is only implied by repeated indices if one of the repeated indices appears as a superscript and one as a subscript.

[3] The base vectors associated with a general curvilinear coordinate system are not necessarily unit vectors.

increment, d$\mathbf{p}$, is then written as follows:

$$\mathrm{d}\mathbf{p} \;=\; \mathrm{d}\bar{x}^m\,\bar{\mathbf{g}}_m\,, \tag{3.22}$$

where both systems of base vectors are related by the following relations:

$$\bar{\mathbf{g}}_m \;=\; \frac{\partial x^r}{\partial \bar{x}^m}\,\mathbf{g}_r\,, \tag{3.23}$$

$$\mathbf{g}_r \;=\; \frac{\partial \bar{x}^m}{\partial x^r}\,\bar{\mathbf{g}}_m\,. \tag{3.24}$$

Besides, the position vector increment, d$\mathbf{p}$, can also be described in terms of a set of *contravariant* base vectors, $\mathbf{g}^m$ ($m = 1,\,2,\,3$). These vectors constitute the *dual basis* to the natural basis, $\mathbf{g}_m$ ($m = 1,\,2,\,3$), previously introduced. The *dual base vectors* $\mathbf{g}^m$ ($m = 1,\,2,\,3$) are defined as the set of vectors satisfying the conditions

$$\mathbf{g}^m \cdot \mathbf{g}_n \;=\; \delta^m_n\,,\quad m = 1,\,2,\,3,\quad n = 1,\,2,\,3)\,, \tag{3.25}$$

where δ^m_n is the *Kronecker delta*. By definition, $\delta^m_n = 1$ if $m = n$ and $\delta^m_n = 0$ otherwise. Fundamentally, Eq.(3.25) means that each vector of a basis is orthogonal to the two vectors of the other basis whose indices are different. Considering the particular case of an *orthogonal curvilinear coordinate system*[4], magnitudes of the covariant and contravariant base vectors are related in the following way:

$$|\mathbf{g}^m| \;=\; \frac{1}{|\mathbf{g}_m|}\,. \tag{3.26}$$

Eq. (3.26) is readily obtained by developing the scalar product between $\mathbf{g}^m$ and $\mathbf{g}_m$ and taking into account the orthogonality. Using the dual base vectors, $\mathbf{g}^m$, the vector position increment, d$\mathbf{p}$, can be written as follows:

$$\mathrm{d}\mathbf{p} \;=\; \mathrm{d}x_m\,\mathbf{g}^m\,, \tag{3.27}$$

where dx_m are the covariant components of d$\mathbf{p}$ with respect to the dual basis. For the curvilinear coordinate system, x^m, the contravariant base vectors $\mathbf{g}^m$ may be defined

---

[4] For such a system, the following relations are satisfied: $\hat{\mathbf{g}}_m \cdot \hat{\mathbf{g}}_n = \delta_{mn}$ where $\hat{\mathbf{g}}_m = \mathbf{g}_m/h_m$ with the scale factor $h_m = (\mathbf{g}_m \cdot \mathbf{g}_m)^{1/2}$.

by

$$\mathbf{g}^m = \frac{\partial x^m}{\partial z^r}\,\mathbf{i}^r\,, \tag{3.28}$$

where $\mathbf{i}^r = \mathbf{i}_r$ for a Cartesian basis because covariant and contravariant base vectors are the same for any orthonormal basis. Besides, as observed in the different previous expressions, superscript and subscript indices refer to *contravariant* and *covariant* quantities, respectively.

3.1.4 The metric tensor

Another very important notion is the *metric tensor*[5], $\mathbf{g}$. It is naturally introduced by writing the scalar-invariant quadratic form, $(ds)^2$, defined as the square of the length of $\mathrm{d}\mathbf{p}$, called the *metric* of the space [49]:

$$(\mathrm{d}s)^2 = \mathrm{d}\mathbf{p}\cdot\mathrm{d}\mathbf{p} \tag{3.29}$$

$$= g_{mn}\,\mathrm{d}x^m\,\mathrm{d}x^n\,, \tag{3.30}$$

where $\mathrm{d}x^m$ and $\mathrm{d}x^n$ are the general curvilinear coordinate increments of the vector position increment $\mathrm{d}\mathbf{p}$, and g_{mn} are the covariant components of the metric tensor, $\mathbf{g}$, in terms of the base vectors $\mathbf{g}^m$. In addition, the components g_{mn} of the metric tensor are given by the scalar products

$$g_{mn} = \mathbf{g}_m\cdot\mathbf{g}_n\,, \tag{3.31}$$

where the quantities are symmetric with respect to the indices m and n. Moreover, when the curvilinear coordinates are orthogonal (*e.g.* polar, cylindrical, or spherical coordinates), $g_{mn} = 0$ for $m \neq n$. In other words, in that case, only the diagonal elements of the matrix do not vanish. For example, considering a cylindrical coordinate system (r, θ, z), the metric of the space is written in the form

$$(\mathrm{d}s)^2 = (\mathrm{d}r)^2 + (r\,\mathrm{d}\theta)^2 + (\mathrm{d}z)^2\,. \tag{3.32}$$

---

[5] Note that the metric tensor is also called the *unit tensor* or the *fundamental tensor* [49].

Using Eqs (3.30) and (3.32), the covariant components, g_{mm}, of the metric tensor, $\mathbf{g}$, with respect to the base vectors $\mathbf{g}^m$ (dual basis) associated with the cylindrical coordinates, can be easily written as follows:

$$g_{11} \;=\; 1\,, \quad g_{22} \;=\; r^2\,, \quad g_{33} \;=\; 1\,. \tag{3.33}$$

Note that when a curvilinear coordinate system is orthogonal, the contravariant components, g^{mm}, of the metric tensor, $\mathbf{g}$, with respect to the base vectors $\mathbf{g}_m$ are equal to $1/g_{mm}$. Regarding a general (non-orthogonal) curvilinear coordinate system, the matrices of the components, $[g^{mn}]$ and $[g_{mn}]$, with respect to a particular natural basis and the corresponding dual basis of the metric tensor, $\mathbf{g}$, satisfy the relation $[g^{mn}] = [g_{mn}]^{-1}$. Due to Eq. (3.31), it is obvious that the matrix $[g_{mn}]$ is symmetric. Similarly to Eq. (3.31), $g^{mn} = \mathbf{g}^m \cdot \mathbf{g}^n$ and thus, the matrix $[g^{mn}]$ is also symmetric.

3.1.5 Christoffel symbols

A very useful tool in tensor calculus is the Christoffel symbols of the first and the second kind. The *Christoffel symbols of the second kind* Γ^l_{mn} and Γ^m_{nl} naturally arise when the spatial partial derivative of the covariant and contravariant base vectors $\mathbf{g}_m$ and $\mathbf{g}^m$, respectively, is taken:

$$\frac{\partial \mathbf{g}_m}{\partial x^n} \;=\; \Gamma^l_{mn}\,\mathbf{g}_l\,, \tag{3.34}$$

$$\frac{\partial \mathbf{g}^m}{\partial x^n} \;=\; -\Gamma^m_{nl}\,\mathbf{g}^l\,, \tag{3.35}$$

where Γ^l_{mn} can be written, in terms of the components of the metric tensor, in the form

$$\Gamma^l_{mn} \;=\; \frac{g^{lk}}{2}\left(\frac{\partial g_{nk}}{\partial x^m} + \frac{\partial g_{km}}{\partial x^n} - \frac{\partial g_{mn}}{\partial x^k}\right) \tag{3.36}$$

$$\;=\; g^{lk}\,[mn,k]\,, \tag{3.37}$$

where $[mn,k]$ represent by definition the *Christoffel symbols of the first kind.*

In addition, as shown in Eq. (3.36), the Christoffel symbols are symmetric with respect to the indices m and n:

$$\Gamma^l_{mn} = \Gamma^l_{nm} \, , \tag{3.38}$$

$$[mn, k] = [nm, k] \; . \tag{3.39}$$

Note that in Cartesian coordinates, $\Gamma^l_{mn} = 0$ and $[mn, k] = 0$.

3.1.6 Covariant derivatives

Consider an arbitrary vector $\mathbf{v}$ which is decomposed in terms of its contravariant components v^m relative to the natural basis $\mathbf{g}_m$ associated with a general curvilinear coordinate system x^m in the following way:

$$\mathbf{v} = v^m \, \mathbf{g}_m \, . \tag{3.40}$$

The partial derivative of $\mathbf{v}$ with respect to coordinate x^n is given by

$$\begin{aligned} \frac{\partial \mathbf{v}}{\partial x^n} &= \frac{\partial v^m}{\partial x^n} \, \mathbf{g}_m + v^m \, \frac{\partial \mathbf{g}_m}{\partial x^n} && (3.41) \\ &= \frac{\partial v^m}{\partial x^n} \, \mathbf{g}_m + v^m \, \Gamma^l_{mn} \, \mathbf{g}_l && (3.42) \\ &= \left(\frac{\partial v^m}{\partial x^n} + \Gamma^m_{ln} \, v^l \right) \mathbf{g}_m \, . && (3.43) \end{aligned}$$

In Eq. (3.43), the expression in parentheses is the so-called covariant derivative of v^m with respect to x^n and is noted $v^m|_n$. In the special case of a Cartesian coordinate system, this covariant derivative is written as

$$v^m|_n = \frac{\partial v^m}{\partial x^n} \, , \tag{3.44}$$

because all the Christoffel symbols are equal to zero for such a coordinate system.

3.2 Kinematics

Consider a continuous body $\mathcal{B}$ (closed system) whose reference configuration is Ω_0 (at time $t = 0$), with a volume $\mathcal{V}_0$ and bounded by a surface $\partial\Omega_0$, characterized by an area

$\mathcal{A}_0$. The continuous body $\mathcal{B}$ is submitted to a motion $\boldsymbol{\chi}$ resulting in a deformation and so, in a new configuration, namely the current configuration Ω (at time t). In this configuration, the body $\mathcal{B}$ occupies a volume $\mathcal{V}$, bounded by a surface $\partial\Omega$, characterized by an area $\mathcal{A}$. In addition, the motion of each particle, embedded in the body $\mathcal{B}$, is characterized by a velocity and an acceleration (which can be described either using the material description or the spatial description). Besides, as already discussed previously, the motion $\boldsymbol{\chi}$, given by Eq. (3.12), is assumed to be uniquely invertible (homeomorphism). As a result, the inverse motion $\boldsymbol{\chi}^{-1}$ can be written as

$$\mathbf{X} = \boldsymbol{\chi}^{-1}(\mathbf{x}, t) \; . \tag{3.45}$$

For a given time t, Eq. (3.45) gives the material position $\mathbf{X}$ (located in Ω_0) of the particle occupying the spatial position $\mathbf{x}$ (located in Ω).

3.2.1 Material time derivative

Consider two smooth functions $g(\mathbf{x}, t)$ and $G(\mathbf{X}, t)$ having the same value f for properly corresponding arguments [Eq. (3.12)]: $g = f$ and $G = f$. It is rather common in physics to denote both functions by using the unique symbol f, which is the value of the functions. In this context, functional operations can be ambiguous since the independent variables are not explicitly written. To avoid any confusion, different symbols can be introduced for the differential operators [48, 49]. $\mathrm{D}f/\mathrm{D}t$ and $\mathrm{Grad}\, f$ will be used to represent the partial time derivative and the gradient of the function $G(\mathbf{X}, t)$, respectively:

$$\frac{\mathrm{D}f}{\mathrm{D}t} = \frac{\partial G(\mathbf{X}, t)}{\partial t} \, , \tag{3.46}$$

$$\mathrm{Grad}\, f = \frac{\partial G(\mathbf{X}, t)}{\partial \mathbf{X}} \; . \tag{3.47}$$

Note that $\mathrm{Grad}(\bullet)$ is sometimes called the *material gradient* operator [50]. On the other hand, the partial time derivative and the gradient of the function $g(\mathbf{x}, t)$ are denoted by $\partial f/\partial t$ and $\operatorname{grad} f$ (also called the *spatial gradient* [50]), respectively:

$$\begin{aligned} \frac{\partial f}{\partial t} &= \frac{\partial g\left(\mathbf{x},t\right)}{\partial t}\,, && (3.48)\\ \operatorname{grad} f &= \frac{\partial g\left(\mathbf{x},t\right)}{\partial \mathbf{x}}\,. && (3.49) \end{aligned}$$

Since g and G are related by the relations

$$\begin{aligned} g\left(\mathbf{x},t\right) &= G\left(\boldsymbol{\chi}^{-1}\left(\mathbf{x},t\right),t\right)\,, && (3.50)\\ G\left(\mathbf{X},t\right) &= g\left(\boldsymbol{\chi}\left(\mathbf{X},t\right),t\right)\,, && (3.51) \end{aligned}$$

and applying the chain rule of differentiation to Eq. (3.51), the following relation can be written:

$$\frac{\partial G}{\partial t} = \frac{\partial g}{\partial t} + \frac{\partial g}{\partial \mathbf{x}} \cdot \frac{\partial \boldsymbol{\chi}}{\partial t}\,. \qquad (3.52)$$

In terms of f, Eq. (3.52) can be written as

$$\frac{\mathrm{D}f}{\mathrm{D}t} = \frac{\partial f}{\partial t} + \mathbf{v}\cdot \operatorname{grad} f\,, \qquad (3.53)$$

where $\mathbf{v} = \partial\boldsymbol{\chi}/\partial t = \partial\mathbf{x}/\partial t$ is the velocity. The operator $\mathrm{D}\left(\bullet\right)/\mathrm{D}t$ is the material time derivative and can thus be expressed in terms of $\partial(\bullet)/\partial t$ and $\operatorname{grad}\left(\bullet\right)$:

$$\frac{\mathrm{D}\left(\bullet\right)}{\mathrm{D}t} = \left(\frac{\partial}{\partial t} + \mathbf{v}\cdot\operatorname{grad}\right)\left(\bullet\right)\,. \qquad (3.54)$$

3.2.2 Deformation gradient

Consider the motion $\boldsymbol{\chi}$ of $\mathcal{B}$ from configuration Ω_0 to configuration Ω. The *deformation gradient tensor* $\mathbf{F}$ at a given t is defined as the tensor that operates on an arbitrary infinitesimal material vector $\mathrm{d}\mathbf{X}$ at $\mathbf{X}$ (in Ω_0) and gives its corresponding vector $\mathrm{d}\mathbf{x}$ at $\mathbf{x}$ (in Ω):

$$\mathrm{d}\mathbf{x} = \mathbf{F}\cdot\mathrm{d}\mathbf{X}\,, \qquad (3.55)$$

with

$$\mathbf{F} \;=\; \frac{\partial \boldsymbol{\chi}\left(\mathbf{X},t\right)}{\partial \mathbf{X}} \;=\; \frac{\partial \mathbf{x}}{\partial \mathbf{X}}\,. \tag{3.56}$$

Consider then two independent coordinate systems X^M and x^m in the reference configuration, Ω_0, and the current configuration, Ω, respectively. The motion can then be written as

$$x^m \;=\; \boldsymbol{\chi}^m\left(X^M,t\right)\,, \quad m=1,\,2,\,3\,, \quad M=1,\,2,\,3\,, \tag{3.57}$$

and the components of the deformation gradient tensor are given by

$$F^m_{\;\;M} \;=\; \frac{\partial \boldsymbol{\chi}^m\left(X^M,t\right)}{\partial X^M} \;=\; \frac{\partial x^m}{\partial X^M}\,, \quad m=1,\,2,\,3\,, \quad M=1,\,2,\,3\,. \tag{3.58}$$

Note that $\mathbf{F}$ is a *two-point tensor* because it involves points in two distinct configurations. The inverse of the deformation gradient tensor, $\mathbf{F}^{-1}$, which operates on $\mathrm{d}\mathbf{x}$ at $\mathbf{x}$ (in Ω) to relate it with $\mathrm{d}\mathbf{X}$ at $\mathbf{X}$ (in Ω_0), can then be written as

$$\mathrm{d}\mathbf{X} \;=\; \mathbf{F}^{-1}\cdot \mathrm{d}\mathbf{x}\,, \tag{3.59}$$

with

$$\mathbf{F}^{-1} \;=\; \frac{\partial \boldsymbol{\chi}^{-1}\left(\mathbf{x},t\right)}{\partial \mathbf{x}} \;=\; \frac{\partial \mathbf{X}}{\partial \mathbf{x}}\,. \tag{3.60}$$

3.2.3 Displacement, velocity, and acceleration fields

The *displacement field* of a typical particle can be expressed either in terms of the reference configuration or in terms of the current one:

$$\mathbf{U}\left(\mathbf{X},t\right) \;=\; \boldsymbol{\chi}\left(\mathbf{X},t\right) - \mathbf{X}\,, \tag{3.61}$$

$$\mathbf{u}\left(\mathbf{x},t\right) \;=\; \mathbf{x} - \boldsymbol{\chi}^{-1}\left(\mathbf{x},t\right)\,. \tag{3.62}$$

Obviously, these two functions $\mathbf{U}$ and $\mathbf{u}$ have the same value for corresponding $\mathbf{x}$ and $\mathbf{X}$, and represent the same physical quantity. They are related by means of the motion:

$$\mathbf{U}(\mathbf{X},t) = \mathbf{u}(\boldsymbol{\chi}(\mathbf{X},t),t) \,. \tag{3.63}$$

In addition, any particle is characterized by a *velocity field* (already mentioned) and an *acceleration field.* Using the material description, these are described, respectively, by the following functions:

$$\mathbf{V}(\mathbf{X},t) = \frac{\partial\boldsymbol{\chi}(\mathbf{X},t)}{\partial t}\,, \tag{3.64}$$

$$\mathbf{A}(\mathbf{X},t) = \frac{\partial^2\boldsymbol{\chi}(\mathbf{X},t)}{\partial t^2}\,. \tag{3.65}$$

In terms of the spatial description, these fields are described by the two functions $\mathbf{v}(\mathbf{x},t)$ and $\mathbf{a}(\mathbf{x},t)$. As previously performed for the displacement field, the two descriptions are transformed into each other by using the motion $\boldsymbol{\chi}$:

$$\mathbf{V}(\mathbf{X},t) = \mathbf{v}(\boldsymbol{\chi}(\mathbf{X},t),t) \,, \tag{3.66}$$

$$\mathbf{A}(\mathbf{X},t) = \mathbf{a}(\boldsymbol{\chi}(\mathbf{X},t),t) \,. \tag{3.67}$$

3.2.4 Volume ratio and Nanson's formula

This section examines how an infinitesimal material volume element $\mathrm{d}\mathcal{V}_0$ and an infinitesimal material surface element $\mathrm{d}\mathcal{A}_0$ map onto the associated infinitesimal spatial volume element $\mathrm{d}\mathcal{V}$ and the infinitesimal spatial surface element $\mathrm{d}\mathcal{A}$ following the motion $\boldsymbol{\chi}$.

3.2.4.1 Volume ratio

Assume three infinitesimal vector elements in the reference configuration $\mathrm{d}\mathbf{X}$, $\mathrm{d}\mathbf{Y}$, and $\mathrm{d}\mathbf{Z}$. The infinitesimal material volume element $\mathrm{d}\mathcal{V}_0$, encompassed by these three vectors, is given by the following mixed product:

$$\mathrm{d}\mathcal{V}_0 = (\mathrm{d}\mathbf{X}\times\mathrm{d}\mathbf{Y})\cdot\mathrm{d}\mathbf{Z}\,. \tag{3.68}$$

Following the motion $\boldsymbol{\chi}$, $\mathrm{d}\mathbf{X}$, $\mathrm{d}\mathbf{Y}$, and $\mathrm{d}\mathbf{Z}$ map onto $\mathrm{d}\mathbf{x}$, $\mathrm{d}\mathbf{y}$, and $\mathrm{d}\mathbf{z}$, respectively. As a result, the infinitesimal material volume element maps onto the infinitesimal spatial volume element, which is written as

$$\mathrm{d}\mathcal{V} = (\mathrm{d}\mathbf{x} \times \mathrm{d}\mathbf{y}) \cdot \mathrm{d}\mathbf{z} \,. \tag{3.69}$$

Taking into account Eqs (3.55) and (3.68), it can be shown that [49, 50]

$$\mathrm{d}\mathcal{V} = J\left(\mathbf{X}, t\right) \, \mathrm{d}\mathcal{V}_0 \,, \tag{3.70}$$

where

$$J = \det \mathbf{F}\left(\mathbf{X}, t\right) \,. \tag{3.71}$$

J represents the determinant of the deformation gradient tensor and is known as the *volume ratio* or the *Jacobian determinant.* Since $\boldsymbol{\chi}$ is invertible, $J \neq 0$. In addition, given that $\boldsymbol{\chi}$ and $\boldsymbol{\chi}^{-1}$ are continuous and $J = 1$ in the reference configuration, $J > 0$ for all $\mathbf{X}$ and for all times t.

3.2.4.2 Nanson's formula

Consider an infinitesimal surface element, $\mathrm{d}\mathcal{A}_0$, in the reference configuration, given by $|\mathrm{d}\mathbf{X} \times \mathrm{d}\mathbf{Y}|$, where $\mathrm{d}\mathbf{X}$ and $\mathrm{d}\mathbf{Y}$ are infinitesimal material vector elements. This surface element is characterized by the *outward unit normal* $\widehat{\mathbf{N}}$ (normal to $\mathrm{d}\mathcal{A}_0$) and a *vector area* $\mathrm{d}\mathbf{A}_0 = \widehat{\mathbf{N}}\,\mathrm{d}\mathcal{A}_0$. Due to the motion $\boldsymbol{\chi}$, $\mathrm{d}\mathcal{A}_0$ maps onto the infinitesimal surface element $\mathrm{d}\mathcal{A}$ in the current configuration, characterized by the outward unit normal $\widehat{\mathbf{n}}$ (normal to $\mathrm{d}\mathcal{A}$) and the vector area $\mathrm{d}\mathbf{A} = \widehat{\mathbf{n}}\,\mathrm{d}\mathcal{A}$.

The way $\mathrm{d}\mathbf{A}_0$ maps onto $\mathrm{d}\mathbf{A}$ is now examined. For this purpose, consider the infinitesimal volume element, encompassed by $\mathrm{d}\mathbf{A}_0$ and $\mathrm{d}\mathbf{Z}$, can also be written as a dot product:

$$\mathrm{d}\mathcal{V}_0 = \mathrm{d}\mathbf{A}_0 \cdot \mathrm{d}\mathbf{Z} \,. \tag{3.72}$$

Using Eq. (3.70), Eq. (3.72) can be rewritten as

$$\mathrm{d}\mathcal{V} \;=\; J\,\mathrm{d}\mathbf{A}_0\cdot\mathrm{d}\mathbf{Z}\,. \tag{3.73}$$

Taking into account Eq. (3.55) and subtracting Eq. (3.73) from Eq. (3.72), the following relation is found:

$$\Big(\mathbf{F}^{\mathrm{T}}\cdot\mathrm{d}\mathbf{A} - J\,\mathrm{d}\mathbf{A}_0\Big)\cdot\mathrm{d}\mathbf{Z} \;=\; 0\,. \tag{3.74}$$

Given that Eq. (3.74) must be satisfied for any $\mathrm{d}\mathbf{Z}$, the so-called *Nanson's formula* giving the mapping between the vector areas $\mathrm{d}\mathbf{A}_0$ and $\mathrm{d}\mathbf{A}$ is obtained:

$$\mathrm{d}\mathbf{A} \;=\; J\,\mathbf{F}^{-\mathrm{T}}\cdot\mathrm{d}\mathbf{A}_0\,. \tag{3.75}$$

3.2.5 Right and left Cauchy–Green deformation tensors

The *right Cauchy–Green deformation tensor*, $\mathbf{C}$, gives the new squared length, $(\mathrm{d}s)^2$, of a spatial line element, $\mathrm{d}\mathbf{x}$, in terms of the corresponding material line element, $\mathrm{d}\mathbf{X}$, in the following way:

$$\begin{aligned}(\mathrm{d}s)^2 &= \mathrm{d}\mathbf{x}\cdot\mathrm{d}\mathbf{x} && (3.76)\\ &= \Big(\mathrm{d}\mathbf{X}\cdot\mathbf{F}^{\mathrm{T}}\Big)\cdot(\mathbf{F}\cdot\mathrm{d}\mathbf{X}) && (3.77)\\ &= \mathrm{d}\mathbf{X}\cdot\mathbf{C}\cdot\mathrm{d}\mathbf{X}\,, && (3.78)\end{aligned}$$

where

$$\mathbf{C} \;=\; \mathbf{F}^{\mathrm{T}}\cdot\mathbf{F}\,. \tag{3.79}$$

In terms of components, Eqs (3.76) and (3.79) can be written as

$$\begin{aligned}(\mathrm{d}s)^2 &= g_{mn}\,\mathrm{d}x^m\,\mathrm{d}x^n && (3.80)\\ &= g_{mn}\,F^m{}_M\,F^n{}_N\,\mathrm{d}X^M\,\mathrm{d}X^N && (3.81)\\ &= C_{MN}\,\mathrm{d}X^M\,\mathrm{d}X^N\,, && (3.82)\end{aligned}$$

where g_{mn} are the covariant components of the metric tensor, $\mathbf{g}$, of the current configuration, Ω. The quantities

$$C_{MN} \;=\; g_{mn}\, F^m_{\ M}\, F^n_{\ N} \tag{3.83}$$

are the components of $\mathbf{C}$. Note that $\mathbf{C}$ is a *symmetric* and *positive definite* tensor, defined on the reference configuration.

Moreover, the *left Cauchy–Green deformation tensor*, $\mathbf{b}$, can also be introduced. It gives the squared length, $(\mathrm{d}S)^2$, of a material line element, $\mathrm{d}\mathbf{X}$, in terms of the corresponding spatial line element, $\mathrm{d}\mathbf{x}$, as follows:

$$\begin{aligned}(\mathrm{d}S)^2 &= \mathrm{d}\mathbf{X}\cdot\mathrm{d}\mathbf{X} && (3.84)\\ &= \left(\mathrm{d}\mathbf{x}\cdot\mathbf{F}^{-\mathrm{T}}\right)\cdot\left(\mathbf{F}^{-1}\cdot\mathrm{d}\mathbf{x}\right) && (3.85)\\ &= \mathrm{d}\mathbf{x}\cdot\mathbf{b}^{-1}\cdot\mathrm{d}\mathbf{x}\,, && (3.86)\end{aligned}$$

where

$$\mathbf{b}^{-1} \;=\; \mathbf{F}^{-\mathrm{T}}\cdot\mathbf{F}^{-1}\,. \tag{3.87}$$

As a result, $\mathbf{b}=\mathbf{F}\cdot\mathbf{F}^{\mathrm{T}}$. In terms of components, Eqs (3.84) and (3.87) can be written as

$$\begin{aligned}(\mathrm{d}S)^2 &= G_{MN}\,\mathrm{d}X^M\,\mathrm{d}X^N && (3.88)\\ &= G_{MN}\,F^M_{\ m}\,F^N_{\ n}\,\mathrm{d}x^m\,\mathrm{d}x^n\,, && (3.89)\end{aligned}$$

where G_{MN} are the covariant components of the metric tensor, $\mathbf{G}$, of the reference configuration, Ω_0. Comparing Eqs (3.86) and (3.89), the following relation can be written:

$$b^{-1}_{mn} \;=\; G_{MN}\,F^M_{\ m}\,F^N_{\ n}\,. \tag{3.90}$$

Note that $\mathbf{b}$ is a *symmetric* and *positive definite* tensor, defined on the current configuration. In addition, taking into account Eq. (3.71) allows to write

$$\det\mathbf{C} \;=\; \det\mathbf{b} \;=\; J^2 > 0\,. \tag{3.91}$$

3.2.6 Green–Lagrange and Euler–Almansi strain tensors

The *Green–Lagrange strain tensor*, $\mathbf{E}$, is defined so that it gives the change in squared length of a material vector, $\mathrm{d}\mathbf{X}$, as follows:

$$(\mathrm{d}s)^2 - (\mathrm{d}S)^2 \;=\; 2\,\mathrm{d}\mathbf{X}\cdot\mathbf{E}\cdot\mathrm{d}\mathbf{X}\,. \tag{3.92}$$

The *Euler–Almansi strain tensor*, $\mathbf{e}$, is defined so that it gives the change in squared length of a spatial vector, $\mathrm{d}\mathbf{x}$, as follows:

$$(\mathrm{d}s)^2 - (\mathrm{d}S)^2 \;=\; 2\,\mathrm{d}\mathbf{x}\cdot\mathbf{e}\cdot\mathrm{d}\mathbf{x}\,. \tag{3.93}$$

Substituting Eqs (3.78) and (3.84) into Eq. (3.92), the relation between $\mathbf{E}$ and $\mathbf{C}$ is obtained:

$$2\,\mathbf{E} \;=\; \mathbf{C} - \mathbf{G}\,. \tag{3.94}$$

The components of the Green–Lagrange strain tensor are thus given by

$$2\,E_{MN} \;=\; C_{MN} - G_{MN}\,. \tag{3.95}$$

In a similar way, substituting Eqs (3.76) and (3.86) into Eq. (3.93), the relation between $\mathbf{e}$ and $\mathbf{b}^{-1}$ is found:

$$2\,\mathbf{e} \;=\; \mathbf{g} - \mathbf{b}^{-1}\,. \tag{3.96}$$

In terms of components, Eq. (3.96) may be written as

$$2\,e_{mn} \;=\; g_{mn} - b^{-1}_{mn}\,. \tag{3.97}$$

3.2.7 Polar decomposition

The *polar decomposition* is a fundamental theorem in continuum mechanics consisting in the decomposition of the gradient deformation tensor $\mathbf{F}$ relative to a local motion into a *pure stretch* and a *pure rotation*. This decomposition is *unique* and, at each point $\mathbf{X} \in \Omega_0$ and each time t, is written in the form

$$\mathbf{F} \;=\; \mathbf{R} \cdot \mathbf{U}\,, \tag{3.98}$$

where the *rotation tensor* $\mathbf{R}$ is a *proper orthogonal* tensor and the *right stretch tensor* $\mathbf{U}$ is a *symmetric positive definite* tensor. Therefore, these tensors have to satisfy the following relations:

$$\mathbf{R}^{\mathrm{T}} \cdot \mathbf{R} \;=\; \mathbf{G}\,, \tag{3.99}$$

$$\det \mathbf{R} \;=\; 1\,, \tag{3.100}$$

$$\mathbf{U}^{\mathrm{T}} \;=\; \mathbf{U}\,. \tag{3.101}$$

Moreover, substituting Eq. (3.98) into Eq. (3.79) and taking into account Eqs (3.99) and (3.101), the following relation can be written:

$$\mathbf{C} \;=\; \left(\mathbf{U}^{\mathrm{T}} \cdot \mathbf{R}^{\mathrm{T}}\right) \cdot \left(\mathbf{R} \cdot \mathbf{U}\right) \;=\; \mathbf{U}^2\,. \tag{3.102}$$

Eventually, Eqs (3.91) and (3.102) give

$$\det \mathbf{U} \;=\; J > 0\,. \tag{3.103}$$

3.3 Balance principles

3.3.1 Conservation of mass

When the body, $\mathcal{B}$, moves from configuration Ω_0 to configuration Ω, its mass m is conserved:

$$m\left(\Omega_0\right) \;=\; m\left(\Omega\right)\,. \tag{3.104}$$

The fundamental law described by Eq. (3.104) is satisfied for any time t and is known as the *conservation of mass.* Let introduce the positive continuous scalar fields $\rho_0\left(\mathbf{X}\right)$ and $\rho\left(\mathbf{x}, t\right)$ characterizing the same particle, $\mathcal{P}$, in the reference and current configurations, respectively. ρ_0 is called the *reference mass density* and depends only on the position

$\mathbf{X} \in \Omega_0$ whereas ρ is called the *spatial mass density* and depends on the position $\mathbf{x} \in \Omega$ and time t as well. The aforesaid particle, $\mathcal{P}$, is characterized by an infinitesimal mass element $\mathrm{d}m > 0$ and occupies the infinitesimal volume elements $\mathrm{d}\mathcal{V}_0$ and $\mathrm{d}\mathcal{V}$ in the reference and current configurations, respectively. Therefore, by definition of ρ_0 and ρ, the following relations can be written:

$$\mathrm{d}m\left(\mathbf{X}\right) = \rho_0\left(\mathbf{X}\right)\, \mathrm{d}\mathcal{V}_0\,, \tag{3.105}$$

$$\mathrm{d}m\left(\mathbf{x},t\right) = \rho\left(\mathbf{x},t\right)\, \mathrm{d}\mathcal{V}\,. \tag{3.106}$$

The conservation of the infinitesimal mass element of the particle, $\mathcal{P}$, enables to write

$$\rho_0\, \mathrm{d}\mathcal{V}_0 = \rho\, \mathrm{d}\mathcal{V}\,. \tag{3.107}$$

Eq. (3.107) shows that the volume of the particle increases when the mass density decreases. Actually, Eq. (3.107) is the equivalent local form of Eq. (3.104). It is readily observed by integrating the left-hand side (LHS) and the right-hand side (RHS) of Eq. (3.107) over Ω_0 and Ω, respectively:

$$m\left(\Omega_0\right) = \int_{\Omega_0} \rho_0\, \mathrm{d}\mathcal{V}_0 = \int_{\Omega} \rho\, \mathrm{d}\mathcal{V} = m\left(\Omega\right) = \text{const}\,. \tag{3.108}$$

Therefore, for all times t, the following relation can be written:

$$\frac{\mathrm{d}}{\mathrm{d}t}\int_{\Omega} \rho\left(\mathbf{x},t\right)\, \mathrm{d}\mathcal{V} = 0\,. \tag{3.109}$$

3.3.1.1 Continuity equation

The continuity equation is a consequence of the conservation of mass. Indeed, taking into account Eq. (3.70) and $J > 0$, Eq. (3.108) can be rewritten as

$$\int_{\Omega_0} \left[\rho_0\left(\mathbf{X}\right) - \rho\left(\boldsymbol{\chi}\left(\mathbf{X},t\right),t\right)\, J\left(\mathbf{X},t\right)\right] \mathrm{d}\mathcal{V}_0 = 0\,. \tag{3.110}$$

Since the integral of Eq. (3.110) vanishes for an arbitrary choice of Ω_0, the integrand must therefore vanish at each point $\mathbf{X} \in \Omega_0$. Hence, the continuity equation finally writes in the material description in the form

$$\rho_0 \left(\mathbf{X}\right) \;=\; \rho \left(\boldsymbol{\chi} \left(\mathbf{X}, t\right), t\right) \; J \left(\mathbf{X}, t\right) \, . \tag{3.111}$$

Taking the time derivative of the two members of Eq. (3.111), the following relation can be written:

$$\begin{aligned} 0 \;&=\; \frac{\mathrm{D} \left(\rho \, J\right)}{\mathrm{D}t} && (3.112) \\ &=\; J \, \frac{\mathrm{D}\rho}{\mathrm{D}t} + \rho \, \frac{\mathrm{D}J}{\mathrm{D}t} \, . && (3.113) \end{aligned}$$

In addition, it can then be shown that [49]

$$\frac{\mathrm{D}J}{\mathrm{D}t} \;=\; J \operatorname{div} \mathbf{v} \, . \tag{3.114}$$

Substituting Eq. (3.114) into Eq. (3.113) gives

$$J \left(\frac{\mathrm{D}\rho}{\mathrm{D}t} + \rho \operatorname{div} \mathbf{v} \right) \;=\; 0 \, . \tag{3.115}$$

Due to Eq. (3.54) and taking into account the constraint $J > 0$, Eq. (3.115) can eventually be written as

$$\frac{\partial \rho \left(\mathbf{x}, t\right)}{\partial t} + \operatorname{div} \left[\rho \left(\mathbf{x}, t\right) \; \mathbf{v} \left(\mathbf{x}, t\right) \right] \;=\; 0 \, , \tag{3.116}$$

which is the continuity equation in the spatial description.

3.3.2 Linear momentum balance principle

3.3.2.1 Spatial description

As already introduced, the motion, $\boldsymbol{\chi}$, of the body, $\mathcal{B}$, is characterized by a spatial velocity, $\mathbf{v} \left(\mathbf{x}, t\right)$, and a spatial mass density, $\rho \left(\mathbf{x}, t\right)$. The total linear momentum, referred to as $\mathbf{L}$, is defined, in the spatial description, by

$$\mathbf{L} \left(t\right) \;=\; \int_\Omega \rho \left(\mathbf{x}, t\right) \; \mathbf{v} \left(\mathbf{x}, t\right) \, \mathrm{d}\mathcal{V} \tag{3.117}$$

and is time-dependent. The linear momentum principle states that the time rate of change of the total momentum of a given set of particles which fill an arbitrary region, Ω, equals the vector sum of external forces acting on the particles of the set. Hence, the balance of linear momentum is given by

$$\frac{\mathrm{d}\mathbf{L}\,(t)}{\mathrm{d}t} \;=\; \frac{\mathrm{d}}{\mathrm{d}t}\int_{\Omega}\rho\,\mathbf{v}\,\mathrm{d}\mathcal{V} \;=\; \mathbf{F}\,(t)\;. \tag{3.118}$$

In a general way, the resultant external force, $\mathbf{F}$, can be split into two contributions as follows:

$$\mathbf{F}\,(t) \;=\; \int_{\partial\Omega}\mathbf{t}\,(\mathbf{x},t,\hat{\mathbf{n}})\;\mathrm{d}\mathcal{A}+\int_{\Omega}\rho\,\mathbf{b}\,(\mathbf{x},t)\;\mathrm{d}\mathcal{V}\,. \tag{3.119}$$

In Eq. (3.119), $\mathbf{t}$ (force measured per unit surface area in the current configuration) and $\mathbf{b}$ (force measured per unit mass) represent the *Cauchy traction vector*[6] and the *body force*, respectively. Note that $\mathbf{t}$, which acts across the infinitesimal surface element $\mathrm{d}\mathcal{A}\in\partial\Omega$, is described exclusively in terms of $\mathbf{x}$, t, and the unit outward normal vector, $\hat{\mathbf{n}}$ (*Cauchy's postulate*). Substituting Eq. (3.119) into Eq. (3.118), the linear momentum balance can be written as

$$\frac{\mathrm{d}}{\mathrm{d}t}\int_{\Omega}\rho\,\mathbf{v}\,\mathrm{d}\mathcal{V} \;=\; \int_{\partial\Omega}\mathbf{t}\,\mathrm{d}\mathcal{A}+\int_{\Omega}\rho\,\mathbf{b}\,\mathrm{d}\mathcal{V}\,. \tag{3.120}$$

The LHS of Eq. (3.120) can be rewritten as[7]

$$\frac{\mathrm{d}}{\mathrm{d}t}\int_{\Omega}\rho\,\mathbf{v}\,\mathrm{d}\mathcal{V} \;=\; \int_{\Omega}\rho\,\frac{\mathrm{D}\mathbf{v}}{\mathrm{D}t}\,\mathrm{d}\mathcal{V}\,. \tag{3.121}$$

The *Cauchy's stress theorem* states that the dependence of $\mathbf{t}$ with respect to $\hat{\mathbf{n}}$ is linear. Therefore, there exists a unique second-order tensor field, $\boldsymbol{\sigma}$, called the *Cauchy stress*

---

[6] $\mathbf{t}$ is also referred to as *surface traction*, *contact force*, *stress vector* or *load.*

[7] Consider a smooth field f (note that f may be a scalar, a vector, or a tensor) described in terms of the current configuration by $f\,(\mathbf{x},t)$. The *Reynolds transport theorem* allows to write $\frac{\mathrm{d}}{\mathrm{d}t}\int_{\Omega}f\,\mathrm{d}\mathcal{V} = \int_{\Omega}\left(\frac{\mathrm{D}f}{\mathrm{D}t}+f\,\mathrm{div}\,\mathbf{v}\right)\mathrm{d}\mathcal{V}$. Assuming $f\,(\mathbf{x},t) = \rho\,(\mathbf{x},t)\;f^{\star}\,(\mathbf{x},t)$ where $f^{\star}$ is defined per unit mass, $\frac{\mathrm{d}}{\mathrm{d}t}\int_{\Omega}\rho\,f^{\star}\,\mathrm{d}\mathcal{V} = \int_{\Omega}\left(\frac{\mathrm{D}(\rho\,f^{\star})}{\mathrm{D}t}+\rho\,f^{\star}\,\mathrm{div}\,\mathbf{v}\right)\mathrm{d}\mathcal{V}$ can be written. Using Eqs (3.54) and (3.115), $\frac{\mathrm{d}}{\mathrm{d}t}\int_{\Omega}\rho\,f^{\star}\,\mathrm{d}\mathcal{V} = \int_{\Omega}\rho\,\frac{\mathrm{D}f^{\star}}{\mathrm{D}t}\,\mathrm{d}\mathcal{V}$ is obtained.

tensor or *true stress tensor*, relating t and $\widehat{\mathbf{n}}$:

$$\begin{aligned} \mathbf{t}\left(\mathbf{x}, t, \widehat{\mathbf{n}}\right) &= \boldsymbol{\sigma}\left(\mathbf{x}, t\right) \cdot \widehat{\mathbf{n}} && (3.122) \\ &= \widehat{\mathbf{n}} \cdot \boldsymbol{\sigma}^{\mathrm{T}}\left(\mathbf{x}, t\right) \, . && (3.123) \end{aligned}$$

Note that, for non polar media, $\boldsymbol{\sigma}$ is a *symmetric*[8] tensor field ($\boldsymbol{\sigma}^{\mathrm{T}} = \boldsymbol{\sigma}$), defined in terms of the current configuration. Taking into account Eq. (3.122) and using the *divergence theorem* [49] allows to write the RHS of Eq. (3.120) in the following way:

$$\int_{\partial\Omega} \mathbf{t} \, \mathrm{d}\mathcal{A} + \int_{\Omega} \rho \, \mathbf{b} \, \mathrm{d}\mathcal{V} = \int_{\Omega} \left(\mathrm{div}\boldsymbol{\sigma} + \rho \, \mathbf{b}\right) \, \mathrm{d}\mathcal{V} \, . \tag{3.124}$$

Finally, the *global form of the Cauchy's first equation of motion* is given by

$$\int_{\Omega} \rho \, \frac{\mathrm{D}\mathbf{v}}{\mathrm{D}t} \, \mathrm{d}\mathcal{V} = \int_{\Omega} \left(\mathrm{div}\boldsymbol{\sigma} + \rho \, \mathbf{b}\right) \, \mathrm{d}\mathcal{V} \, . \tag{3.125}$$

Given that Eq. (3.125) must be satisfied for any arbitrary volume $\mathcal{V}$, it follows that

$$\rho \, \frac{\mathrm{D}\mathbf{v}}{\mathrm{D}t} = \mathrm{div}\boldsymbol{\sigma} + \rho \, \mathbf{b} \tag{3.126}$$

must be satisfied for each point $\mathbf{x}$ and for all times t. Eq. (3.126) is referred to as the *local form of the Cauchy's first equation of motion.* In terms of contravariant components, Eq. (3.126) can be written as

$$\rho \, \frac{\mathrm{D}v^m}{\mathrm{D}t} = \sigma^{mn}\big|_n + \rho \, b^m \, , \quad m = 1, \, 2, \, 3. \tag{3.127}$$

3.3.2.2 Material description

The linear momentum balance may also be written in terms of the material description. In other words, Eq. (3.120) may be transported in the reference configuration. Using Eqs (3.70) and (3.111), the following relation can be written:

$$\int_{\Omega} \rho \, \mathbf{b} \, \mathrm{d}\mathcal{V} = \int_{\Omega_0} \rho_0 \, \mathbf{B} \, \mathrm{d}\mathcal{V}_0 \, . \tag{3.128}$$

---

[8] The symmetry of the Cauchy stress tensor is a consequence of the *moment of momentum balance principle* for a non polar continuous medium [49, 50].

with $\mathbf{B}(\mathbf{X},t)=\mathbf{b}(\boldsymbol{\chi}(\mathbf{X},t),t)$. Moreover, the transformation of the Cauchy stress vector $\mathbf{t}$ is obtained by using the *first Piola–Kirchhoff traction vector* (force measured per unit surface area in the reference configuration), $\mathbf{T}\left(\mathbf{X},t,\widehat{\mathbf{N}}\right)$, introduced by claiming that for every surface element, according to Fig. 3.1,

$$\mathrm{d}\mathbf{F} \;=\; \mathbf{t}\,\mathrm{d}\mathcal{A} \;=\; \mathbf{T}\,\mathrm{d}\mathcal{A}_0\,, \tag{3.129}$$

where $\mathrm{d}\mathbf{F}$ is the infinitesimal load acting on the current configuration, Ω. Thus, $\mathbf{T}$ is the force acting on the current configuration per unit surface area in the reference configuration. From Eq. (3.129), the following relation is readily obtained:

$$\int_{\partial\Omega}\mathbf{t}\,\mathrm{d}\mathcal{A} \;=\; \int_{\partial\Omega_0}\mathbf{T}\,\mathrm{d}\mathcal{A}_0\,. \tag{3.130}$$

Substituting Eqs (3.128) and (3.130) into Eq. (3.120), and transforming the LHS of Eq. (3.120) by using Eq. (3.70), the linear momentum balance can eventually be written, with respect to the reference configuration, as follows:

$$\frac{\mathrm{d}}{\mathrm{d}t}\int_{\Omega_0}\rho_0\,\mathbf{V}\,\mathrm{d}\mathcal{V}_0 \;=\; \int_{\partial\Omega_0}\mathbf{T}\,\mathrm{d}\mathcal{A}_0+\int_{\Omega_0}\rho_0\,\mathbf{B}\,\mathrm{d}\mathcal{V}_0\,. \tag{3.131}$$

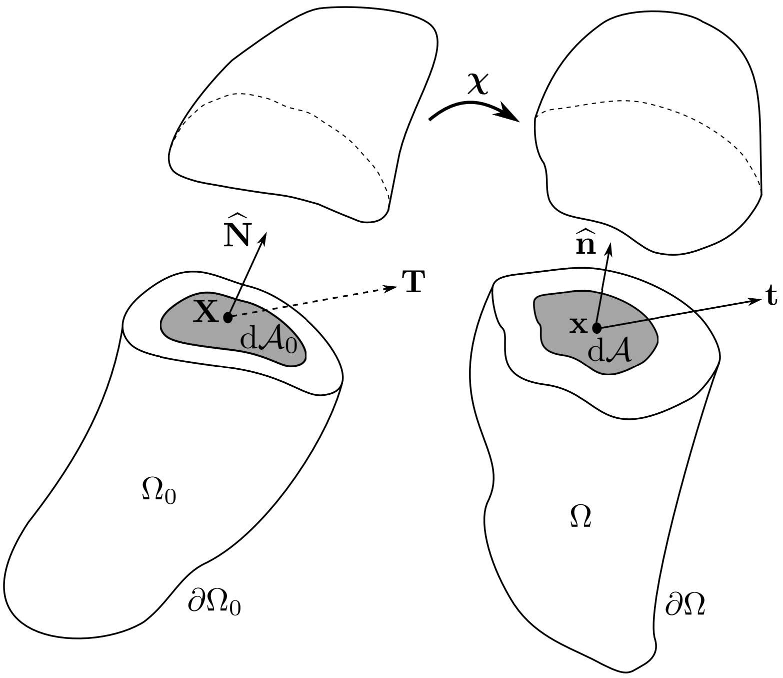

Fig. 3.1 – Traction vectors t and T acting across the surface elements $\mathrm{d}\mathcal{A}$ and $\mathrm{d}\mathcal{A}_0$ with respective outward unit normals $\widehat{\mathbf{n}}$ and $\widehat{\mathbf{N}}$.

In Eq. (3.131), it is important to note that $\mathbf{T}$ acts on the region Ω but it is a function of the referential position $\mathbf{X}$ and the unit outward normal vector $\widehat{\mathbf{N}}$ with respect to the infinitesimal surface element $\mathrm{d}\mathcal{A}_0 \in \partial\Omega_0$. This is why $\mathbf{T}$ is often referred to as the *nominal traction vector* as well.

In addition, as previously, the Cauchy's stress theorem allows to write

$$\mathbf{T}\left(\mathbf{X}, t, \widehat{\mathbf{N}}\right) \;=\; \mathbf{P}\left(\mathbf{X}, t\right) \cdot \widehat{\mathbf{N}}\,, \tag{3.132}$$

where $\mathbf{P}$ is called the *first Piola–Kirchhoff (PK1) stress tensor.* This is a *two-point* tensor field and in general, *not symmetric.* Taking into account Eq. (3.132) and using the divergence theorem, Eq. (3.131) can eventually be written as

$$\int_{\Omega_0} \rho_0 \, \frac{\partial \mathbf{V}}{\partial t} \, \mathrm{d}\mathcal{V}_0 \;=\; \int_{\Omega_0} \left(\mathrm{Div}\, \mathbf{P} + \rho_0 \, \mathbf{B}\right) \, \mathrm{d}\mathcal{V}_0\,, \tag{3.133}$$

which is the global form of the equation of motion in the reference configuration. Note that $\mathrm{Div}\,(\bullet)$ (with an upper-case 'D') is often referred to as the *material divergence operator* whereas $\mathrm{div}\,(\bullet)$ (with a lower-case 'd') is often referred to as the *spatial divergence operator* [50] with a similar meaning as the one for the gradient operator previously introduced. In addition, given that Eq. (3.133) must be satisfied for any arbitrary volume $\mathcal{V}_0$, the associated local form is obtained:

$$\rho_0 \, \frac{\partial \mathbf{V}}{\partial t} \;=\; \mathrm{Div}\, \mathbf{P} + \rho_0 \, \mathbf{B}\,. \tag{3.134}$$

In terms of components, Eq. (3.134) can be written as

$$\rho_0 \, \frac{\partial V^m}{\partial t} \;=\; P^{mN}\Big|_N + \rho_0 \, B^m\,, \quad m = 1,\, 2,\, 3\,. \tag{3.135}$$

The relation between $\boldsymbol{\sigma}$ and $\mathbf{P}$ is found by using Eq. (3.129) and taking into account Eqs (3.122) and (3.132):

$$\boldsymbol{\sigma} \cdot \hat{\mathbf{n}} \, \mathrm{d}\mathcal{A} \;=\; \mathbf{P} \cdot \widehat{\mathbf{N}} \, \mathrm{d}\mathcal{A}_0\,. \tag{3.136}$$

Using Eq. (3.75) (Nanson's formula), the *Piola transformation* is finally obtained:

$$\mathbf{P} \;=\; J \, \boldsymbol{\sigma} \cdot \mathbf{F}^{-\mathrm{T}}\,. \tag{3.137}$$

The first Piola–Kirchhoff stress tensor have two main inconveniences, namely it is a two-point tensor (neither spatial nor material) and non symmetric. That is why the *second Piola–Kirchhoff (PK2) stress tensor*, $\mathbf{S}$, is often introduced. It is a *material* and *symmetric* tensor field. The traction vector $\mathbf{T}^\star$, associated with the PK2 stress tensor, acts on the region Ω_0 (contrary to the traction vector associated with the PK1 stress tensor that acts on the region Ω) and is a function of the referential position $\mathbf{X}$ and the unit outward normal vector $\widehat{\mathbf{N}}$ with respect to the infinitesimal surface element $\mathrm{d}\mathcal{A}_0 \in \partial\Omega_0$:

$$\mathrm{d}\mathbf{F}_0 \;=\; \mathbf{T}^\star\,\mathrm{d}\mathcal{A}_0\,, \tag{3.138}$$

where $\mathrm{d}\mathbf{F}_0$ is a force related to the actual force $\mathrm{d}\mathbf{F}$ in the same way as an arbitrary infinitesimal material vector $\mathrm{d}\mathbf{X}$ at $\mathbf{X}$ is related to the corresponding spatial vector $\mathrm{d}\mathbf{x}$ at $\mathbf{x}$ [Eq. (3.59)]:

$$\mathrm{d}\mathbf{F}_0 \;=\; \mathbf{F}^{-1}\cdot\mathrm{d}\mathbf{F}\,. \tag{3.139}$$

Moreover, the Cauchy's stress theorem allows to write

$$\mathbf{T}^\star\,\mathrm{d}\mathcal{A}_0 \;=\; \mathbf{S}\cdot\widehat{\mathbf{N}}\,\mathrm{d}\mathcal{A}_0\,. \tag{3.140}$$

Taking into account Eqs (3.136)-(3.140), the relations between $\mathbf{S}$, $\mathbf{P}$, and $\boldsymbol{\sigma}$ are found:

$$\begin{aligned}\mathbf{S} &= \mathbf{F}^{-1}\cdot\mathbf{P} && (3.141)\\ &= J\,\mathbf{F}^{-1}\cdot\boldsymbol{\sigma}\cdot\mathbf{F}^{-\mathrm{T}}\,. && (3.142)\end{aligned}$$

Substituting Eq. (3.141) into Eq. (3.134), the local form of the Cauchy's first equation of motion may be written in terms of the PK2 stress tensor as follows:

$$\rho_0\,\frac{\partial\mathbf{V}}{\partial t} \;=\; \mathrm{Div}\,(\mathbf{F}\cdot\mathbf{S}) + \rho_0\,\mathbf{B}\,. \tag{3.143}$$

In terms of components, Eq. (3.143) is written as

$$\rho_0\,\frac{\partial V^m}{\partial t} \;=\; \left(F^m_{\ M}\,S^{MN}\right)\Big|_N + \rho_0\,B^m\,,\quad m = 1,\,2,\,3\,. \tag{3.144}$$

3.4 Cauchy-elastic materials

A *Cauchy-elastic* or *elastic material* is characterized by a stress field that is independent of the deformation path, In other words, for such a material, the stress field at time t depends only on the state of the deformation (and the temperature) at this time t and not on the deformation history (and temperature history). However, in general, the work done by the stress field on an elastic material depends on the deformation path.

3.4.1 Basics about constitutive equations

A *constitutive equation* describes the *intrinsic physical properties* of a continuous body. For the case of deformable bodies, a constitutive equation describes generally the state of stress at any point of that body submitted to any arbitrary motion at time t. Assuming an *isothermal* ($\mathrm{D}T/\mathrm{D}t = 0$ where T is the absolute temperature) elastic body, the constitutive equation relates the Cauchy stress tensor, $\boldsymbol{\sigma}$, at each spatial point, $\mathbf{x} = \boldsymbol{\chi}(\mathbf{X}, t)$, with the deformation gradient tensor, $\mathbf{F}(\mathbf{X}, t)$. Mathematically, the constitutive equation can be written in the general form

$$\boldsymbol{\sigma} = \boldsymbol{\mathfrak{g}}\left(\mathbf{F}(\mathbf{X}, t), \mathbf{X}\right) , \tag{3.145}$$

where $\boldsymbol{\mathfrak{g}}$ is referred to as the *response function* associated with the Cauchy stress tensor $\boldsymbol{\sigma}$. From a mathematical point of view, $\boldsymbol{\mathfrak{g}}$ is a *tensor-valued tensor function*[9]. In Eq. (3.145), $\boldsymbol{\sigma}$ depends on $\mathbf{F}$ and the referential position $\mathbf{X}$ as well. It means that the stress response can vary from one particle to the other due to inhomogeneities. In the particular case where *homogeneous* continuous bodies are considered, Eq. (3.145) becomes

$$\boldsymbol{\sigma} = \boldsymbol{\mathfrak{g}}(\mathbf{F}) , \tag{3.146}$$

which determines the Cauchy stress tensor, $\boldsymbol{\sigma}$, from the given deformation gradient tensor, $\mathbf{F}$. A constitutive equation such as Eq. (3.146) is often referred to as a stress relation.

---

[9] A tensor-valued tensor function is a function whose arguments are one or more tensor variables and whose value is a tensor.

The *principle of material frame-indifference*[10], which states that material properties do not depend on the observer, imposes certain restrictions on the function $\boldsymbol{\mathfrak{g}}$. Consider two motions $\mathbf{x} = \boldsymbol{\chi}\left(\mathbf{X}, t\right)$ and $\mathbf{x}^{+} = \boldsymbol{\chi}^{+}\left(\mathbf{X}, t^{+}\right)$ of the same body, which differ from each other by a superimposed *rigid-body motion* and a *time-shift.* The pairs $(\mathbf{x}, t)$ and $(\mathbf{x}^{+}, t^{+})$, defined on the configurations Ω and Ω^{+}, respectively, are related by the *Euclidean transformation* (appendix A.1). Choosing to use Cartesian coordinates to describe the two motions, χ and χ^{+}, the transformation can be written as

$$\mathbf{x}^{+} = \mathbf{c}\left(t\right) + \mathbf{Q}\left(t\right) \cdot \mathbf{x}\,, \tag{3.147}$$

$$t^{+} = t + \alpha\,, \tag{3.148}$$

where $\mathbf{c}$ represents a rigid-body translation, $\mathbf{Q}$ represents a rigid-body rotation about an axis of rotation, and α is a real number that represents the time-shift. The deformation gradient tensors $\mathbf{F}$ and $\mathbf{F}^{+}$ are related by

$$\mathbf{F}^{+} = \mathbf{Q} \cdot \mathbf{F}\,, \tag{3.149}$$

enabling to state that the deformation gradient tensor is objective. It can be shown that the Cauchy stress tensor transforms as

$$\boldsymbol{\sigma}^{+} = \mathbf{Q} \cdot \boldsymbol{\sigma} \cdot \mathbf{Q}^{\mathrm{T}}\,, \tag{3.150}$$

meaning that the Cauchy stress tensor is also objective.

Since the constitutive law [Eq. (3.146)] is assumed objective, the stress relation in configuration Ω^{+} must be written as

$$\boldsymbol{\sigma}^{+} = \boldsymbol{\mathfrak{g}}\left(\mathbf{F}^{+}\right)\,, \tag{3.151}$$

where $\boldsymbol{\mathfrak{g}}$ is the *same* function as in Eq. (3.146). Due to Eqs (3.149)-(3.151), the response function $\boldsymbol{\mathfrak{g}}$ must satisfy

$$\mathbf{Q} \cdot \boldsymbol{\mathfrak{g}}\left(\mathbf{F}\right) \cdot \mathbf{Q}^{\mathrm{T}} = \boldsymbol{\mathfrak{g}}\left(\mathbf{Q} \cdot \mathbf{F}\right)\,, \tag{3.152}$$

for every nonsingular gradient deformation tensor $\mathbf{F}$ and any orthogonal tensor $\mathbf{Q}$.

---

[10] This principle is also known as the principle of material objectivity or as objectivity.

Inserting the polar decomposition [Eq. (3.98)] into the RHS of Eq. (3.152),

$$\mathbf{Q} \cdot \mathfrak{g}\,(\mathbf{F}) \cdot \mathbf{Q}^{\mathrm{T}} \;=\; \mathbf{R} \cdot \mathfrak{g}\,(\mathbf{U}) \cdot \mathbf{R}^{\mathrm{T}}\,. \tag{3.153}$$

Since Eq. (3.153) holds for all proper orthogonal tensors $\mathbf{Q}$, it is also satisfied for the particular choice $\mathbf{Q} = \mathbf{R}^{\mathrm{T}}$. As a result, Eq. (3.152) eventually boils down to

$$\mathfrak{g}\,(\mathbf{F}) \;=\; \mathbf{R} \cdot \mathfrak{g}\,(\mathbf{U}) \cdot \mathbf{R}^{\mathrm{T}}\,, \tag{3.154}$$

for the function $\mathfrak{g}$ and for every $\mathbf{F}$ and $\mathbf{R}$.

Eq. (3.146) may also be written in terms of the PK1 stress tensor, $\mathbf{P}$. Taking into account Eq. (3.137), Eq. (3.146) becomes

$$\begin{aligned} \mathbf{P} &= \det \mathbf{F}\, \mathfrak{g}\,(\mathbf{F}) \cdot \mathbf{F}^{-\mathrm{T}} && (3.155)\\ &= \mathfrak{G}\,(\mathbf{F})\,, && (3.156) \end{aligned}$$

where $\mathfrak{G}$ is a tensor-valued tensor function associated with the PK1 stress tensor, $\mathbf{P}$, which must verify the restriction

$$\mathbf{Q} \cdot \mathfrak{G}\,(\mathbf{F}) \;=\; \mathfrak{G}\,(\mathbf{Q} \cdot \mathbf{F})\,, \tag{3.157}$$

for every $\mathbf{F}$ and $\mathbf{Q}$ to satisfy the principle of material frame-indifference. Using the same reasoning that enables to establish Eq. (3.154) from Eq. (3.152), Eq. (3.157) boils down to

$$\mathfrak{G}\,(\mathbf{F}) \;=\; \mathbf{R} \cdot \mathfrak{G}\,(\mathbf{U})\,. \tag{3.158}$$

A very useful alternative form of Eq. (3.146) can be written in terms of the PK2 stress tensor, $\mathbf{S}$. Taking into account Eq. (3.142), Eq. (3.146) becomes

$$\begin{aligned} \mathbf{S} &= \det \mathbf{F}\, \mathbf{F}^{-1} \cdot \mathfrak{g}\,(\mathbf{F}) \cdot \mathbf{F}^{-\mathrm{T}} && (3.159)\\ &= \mathfrak{H}\,(\mathbf{F})\,, && (3.160) \end{aligned}$$

where $\mathfrak{H}$ is a tensor-valued tensor function associated with the PK2 stress tensor, $\mathbf{S}$. Using the polar decomposition [Eq. (3.98)] and Eq. (3.154), and taking into account the symmetry of the right stretch tensor, $\mathbf{U}$, Eq. (3.159) may be written as

$$\mathbf{S} \;=\; \det\mathbf{U}\,\mathbf{U}^{-1}\cdot\mathfrak{g}\left(\mathbf{U}\right)\cdot\mathbf{U}^{-1}\,. \tag{3.161}$$

Given that $\mathbf{U} = \mathbf{C}^{1/2}$ [Eq. (3.102)], Eq. (3.161) may eventually be written in the form

$$\mathbf{S} \;=\; \mathfrak{H}_{\mathbf{C}}\left(\mathbf{C}\right)\;, \tag{3.162}$$

where $\mathfrak{H}_{\mathbf{C}}$ is a tensor-valued tensor function associated with the PK2 stress tensor, $\mathbf{S}$.

3.4.1.1 Isotropic Cauchy-elastic materials

Assume that the Cauchy stress tensor, $\boldsymbol{\sigma}$, depends on the left Cauchy–Green deformation tensor, $\mathbf{b}$ (section 3.2.5). In this case, Eq. (3.146) can be written as

$$\boldsymbol{\sigma} \;=\; \mathfrak{h}\left(\mathbf{b}\right)\;, \tag{3.163}$$

where $\mathfrak{h}$ is a tensor-valued tensor function associated with $\mathbf{b}$. A Cauchy-elastic material which can be described by a constitutive equation such as Eq. (3.163) and which satisfies the fundamental invariance relation

$$\mathbf{Q}\cdot\mathfrak{h}\left(\mathbf{b}\right)\cdot\mathbf{Q}^{\mathrm{T}} \;=\; \mathfrak{h}\left(\mathbf{Q}\cdot\mathbf{b}\cdot\mathbf{Q}^{\mathrm{T}}\right)\;, \tag{3.164}$$

for any orthogonal tensor $\mathbf{Q}$, is said to be *isotropic.*

3.4.1.2 Incompressible Cauchy-elastic materials

In the case of an *incompressible Cauchy-elastic material*, the stress relation is determined only up to an arbitrary scalar p which can be identified as a pressure-like quantity. Therefore, Eqs (3.146) and (3.162) are replaced by

$$\boldsymbol{\sigma} \;=\; -p\,\mathbf{g} + \mathfrak{g}\left(\mathbf{F}\right)\;, \tag{3.165}$$

and

$$\mathbf{S} \;=\; -p\,\mathbf{C}^{-1} + \mathfrak{H}_{\mathbf{C}}\left(\mathbf{C}\right)\;, \tag{3.166}$$

respectively. Note that the tensor-valued tensor functions $\mathfrak{g}(\mathbf{F})$ and $\mathfrak{H}_{\mathbf{C}}(\mathbf{C})$ need only to be defined for the kinematic constraints $\det \mathbf{F} = 1$ and $\det \mathbf{C} = 1$, respectively. In addition, the scalar p required to maintain incompressibility is obtained by the equilibrium conditions and the boundary conditions and is not specified by a constitutive equation. Moreover, in any stress relation associated with an incompressible material, the scalar p must always be included.

3.4.2 Hyperelastic materials

In the case of a purely mechanical theory (thermal effects are ignored), the existence of a *Helmholtz free-energy* defined per unit reference volume, Ψ, is postulated for a *hyperelastic* material (or *Green-elastic* material). This Helmholtz free-energy, can be described by a *scalar-valued tensor function* that depends only on one of the strain or deformation tensors for homogeneous materials, *e.g.* $\Psi = \Psi_{\mathbf{F}}(\mathbf{F})$. This Helmholtz free-energy, Ψ, is related to the Helmholtz free-energy defined per unit mass on the current configuration, ψ, by $\Psi = \rho_0 \, \psi$ [49]. For heterogeneous materials, the Helmholtz free-energy is additionally dependent on the position of a point in the considered medium. For the following considerations, only homogeneous materials are discussed without loss of generality. In the case of an isothermal deformation of a hyperelastic material, the Helmholtz free-energy is called the *strain-energy.*

An isothermal hyperelastic material is defined as a *subclass* of an isothermal elastic material for which the response functions introduced in Eqs (3.146), (3.156), and (3.162), depend only on a strain-energy function (provided by the model considered) and are given by

$$\boldsymbol{\sigma} = \mathfrak{g}(\mathbf{F}) = J^{-1} \frac{\partial \Psi_{\mathbf{F}}(\mathbf{F})}{\partial \mathbf{F}} \cdot \mathbf{F}^{\mathrm{T}}, \tag{3.167}$$

$$\mathbf{P} = \mathfrak{G}(\mathbf{F}) = \frac{\partial \Psi_{\mathbf{F}}(\mathbf{F})}{\partial \mathbf{F}}, \tag{3.168}$$

$$\mathbf{S} = \mathfrak{H}_{\mathbf{C}}(\mathbf{C}) = 2 \frac{\partial \Psi_{\mathbf{C}}(\mathbf{C})}{\partial \mathbf{C}}, \tag{3.169}$$

where $\Psi_{\mathbf{F}}(\mathbf{F})$ and $\Psi_{\mathbf{C}}(\mathbf{C})$ are two different strain-energy functions with the same scalar value, Ψ.

It can now be shown that Eqs (3.168)-(3.169) are directly derived from the *Clausius–*

Planck form of the second law of thermodynamics[11]. By definition, an isothermal deformation of a hyperelastic material produces locally no entropy (the internal dissipation is zero or in other words, the isothermal deformation of a hyperelastic material is a reversible process). Assuming such an isothermal reversible process, the Clausius–Planck inequality degenerates to an equality and may be written in the reference configuration, in terms of $\mathbf{P}$ or $\mathbf{S}$, as follows:

$$\mathbf{P} : \frac{\partial \mathbf{F}}{\partial t} - \frac{\partial \Psi_{\mathbf{F}}(\mathbf{F})}{\partial t} = \left(\mathbf{P} - \frac{\partial \Psi_{\mathbf{F}}(\mathbf{F})}{\partial \mathbf{F}}\right) : \frac{\partial \mathbf{F}}{\partial t} = 0\,, \tag{3.170}$$

$$\mathbf{S} : \frac{\partial \mathbf{E}}{\partial t} - \frac{\partial \Psi_{\mathbf{E}}(\mathbf{E})}{\partial t} = \left(\mathbf{S} - \frac{\partial \Psi_{\mathbf{E}}(\mathbf{E})}{\partial \mathbf{E}}\right) : \frac{\partial \mathbf{E}}{\partial t} = 0\,, \tag{3.171}$$

where $\Psi_{\mathbf{E}}$ is another strain-energy function with the same value than $\Psi_{\mathbf{F}}$ and $\Psi_{\mathbf{C}}$. Since $\mathbf{F}$ and thus $\partial\mathbf{F}/\partial t$ can be chosen arbitrarily in Eq. (3.170), the expressions in parentheses must vanish and Eq. (3.168) is thus obtained. For similar reasons, the expressions in parentheses in Eq. (3.171) must vanish. As a result, the following relation must be satisfied:

$$\mathbf{S} = \frac{\partial \Psi_{\mathbf{E}}(\mathbf{E})}{\partial \mathbf{E}}\,. \tag{3.172}$$

Due to Eq. (3.94), the PK2 stress tensor may also be written as

$$\mathbf{S} = 2\,\frac{\partial \Psi_{\mathbf{C}}(\mathbf{C})}{\partial \mathbf{C}}\,, \tag{3.173}$$

which is Eq. (3.169). As well explained in [49, 51], Ψ is only dependent on the stretching part of $\mathbf{F}$, namely the symmetric right stretch tensor, $\mathbf{U}$ (section 3.2.7). This result is obtained from the principle of material frame-indifference. From this principle, the following relation must be satisfied:

$$\Psi_{\mathbf{F}}(\mathbf{F}) = \Psi_{\mathbf{F}}(\mathbf{U})\,. \tag{3.174}$$

In addition, expressing the strain-energy as a function of $\mathbf{E}$ or $\mathbf{C}$, the stress tensors $\boldsymbol{\sigma}$

---

[11] The Clausius–Planck form of the second law of thermodynamics is a stronger form than the Clausius–Duhem form [50].

and $\mathbf{P}$ may also be written as [51]

$$\boldsymbol{\sigma} = J^{-1}\,\mathbf{F}\cdot\frac{\partial\Psi_{\mathbf{E}}(\mathbf{E})}{\partial\mathbf{E}}\cdot\mathbf{F}^{\mathrm{T}} = 2\,J^{-1}\,\mathbf{F}\cdot\frac{\partial\Psi_{\mathbf{C}}(\mathbf{C})}{\partial\mathbf{C}}\cdot\mathbf{F}^{\mathrm{T}}\,, \tag{3.175}$$

$$\mathbf{P} = \mathbf{F}\cdot\frac{\partial\Psi_{\mathbf{E}}(\mathbf{E})}{\partial\mathbf{E}} = 2\,\mathbf{F}\cdot\frac{\partial\Psi_{\mathbf{C}}(\mathbf{C})}{\partial\mathbf{C}}\,. \tag{3.176}$$

3.4.2.1 Isotropic hyperelastic material

Regarding the particular case of an *isotropic hyperelastic material*, it can be shown [49] that the strain-energy can be written in a unique way in terms of the *principal invariants* of $\mathbf{C}$:

$$\Psi = \Psi^*_{\mathbf{C}}\left[I_1(\mathbf{C}),I_2(\mathbf{C}),I_3(\mathbf{C})\right]\,, \tag{3.177}$$

where

$$I_1(\mathbf{C}) = \operatorname{tr}\mathbf{C}\,, \tag{3.178}$$

$$I_2(\mathbf{C}) = \frac{1}{2}\left[(\operatorname{tr}\mathbf{C})^2 - \operatorname{tr}\mathbf{C}^2\right]\,, \tag{3.179}$$

$$I_3(\mathbf{C}) = \det\mathbf{C} = J^2\,. \tag{3.180}$$

Taking into account Eq. (3.173) and Eqs (3.177)-(3.180), and using the chain rule of differentiation, the PK2 stress tensor is given by

$$\mathbf{S} = 2\sum_{\alpha=1}^{3}\frac{\partial\Psi^*_{\mathbf{C}}}{\partial I_\alpha}\frac{\partial I_\alpha}{\partial\mathbf{C}} \tag{3.181}$$

$$= 2\left[\left(\frac{\partial\Psi^*_{\mathbf{C}}}{\partial I_1} + I_1\frac{\partial\Psi^*_{\mathbf{C}}}{\partial I_2}\right)\mathbf{G} - \frac{\partial\Psi^*_{\mathbf{C}}}{\partial I_2}\,\mathbf{C} + I_3\frac{\partial\Psi^*_{\mathbf{C}}}{\partial I_3}\,\mathbf{C}^{-1}\right]\,. \tag{3.182}$$

3.4.2.2 Compressible hyperelastic material

For a compressible hyperelastic material, the only restriction is $J > 0$. Moreover, for this kind of materials, it is convenient to split the deformation into a *volumetric part* and an *isochoric part* because these two parts behave in a quite different way in bulk and shear [52]. As a result, the tensors $\mathbf{F}$ and $\mathbf{C}$ can be written as multiplicative decompositions into *volume-changing* (or *volumetric*) and *volume-preserving* (or *isochoric*) parts as follows:

$$\mathbf{F} = J^{1/3}\,\overline{\mathbf{F}}\,, \tag{3.183}$$

$$\mathbf{C} = J^{2/3}\,\overline{\mathbf{C}}\,. \tag{3.184}$$

In Eqs (3.183) and (3.184), $\overline{\mathbf{F}}$ and $\overline{\mathbf{C}}$ are called *modified deformation gradient tensor* and *modified right Cauchy–Green tensor*, respectively, and are both associated with volume-preserving deformations of the considered material. The factors $J^{1/3}$ [Eq. (3.183)] and $J^{2/3}$ [Eq. (3.184)] are related to volume-changing deformations of the material. Taking into account the kinematic assumption given by Eq. (3.184), the strain-energy, Ψ, can be postulated in a unique *decoupled* form as follows [51]:

$$\Psi = \Psi_{\mathrm{vol}}\left(J\right) + \Psi_{\mathrm{iso}}\left(\overline{\mathbf{C}}\right)\,, \tag{3.185}$$

Therefore, taking into account Eqs (3.173) and (3.185), the PK2 stress tensor is given by

$$\begin{aligned} \mathbf{S} &= 2\,\frac{\partial \Psi_{\mathrm{vol}}\left(J\right)}{\partial \mathbf{C}} + 2\,\frac{\partial \Psi_{\mathrm{iso}}\left(\overline{\mathbf{C}}\right)}{\partial \mathbf{C}} && (3.186)\\ &= \underbrace{J\,p\,\mathbf{C}^{-1}}_{\mathbf{S}_{\mathrm{vol}}} + \underbrace{J^{-2/3}\,\mathrm{Dev}\left(2\,\frac{\partial \Psi_{\mathrm{iso}}\left(\overline{\mathbf{C}}\right)}{\partial \overline{\mathbf{C}}}\right)}_{\mathbf{S}_{\mathrm{iso}}}\,, && (3.187) \end{aligned}$$

where $\mathbf{S}_{\mathrm{vol}}$ and $\mathbf{S}_{\mathrm{iso}}$ represent the purely volumetric and isochoric contributions to the PK2 stress tensor, respectively. Besides, the constitutive equation for the *hydrostatic pressure* p is defined by

$$p = \frac{\mathrm{d}\Psi_{\mathrm{vol}}\left(J\right)}{\mathrm{d}J} \tag{3.188}$$

and $\mathrm{Dev}\left(\bullet\right)$ is the *material deviator operator* defined by

$$\mathrm{Dev}\left(\mathbf{H}\right) = \mathbf{H} - \frac{1}{3}\left(\mathbf{H} : \mathbf{C}\right)\,\mathbf{C}^{-1}\,, \tag{3.189}$$

where $\mathbf{H}$ is an arbitrary second order tensor.

3.4.2.3 Compressible isotropic hyperelastic material

For a compressible isotropic hyperelastic material, in an analogous way to the decoupled representation given by Eq. (3.185), the strain-energy can be written as

$$\Psi = \Psi^{*}_{\mathrm{vol}}\left(J\right) + \Psi^{*}_{\mathrm{iso}}\left[\bar{I}_1\left(\overline{\mathbf{C}}\right), \bar{I}_2\left(\overline{\mathbf{C}}\right)\right] , \tag{3.190}$$

where $\bar{I}_1\left(\overline{\mathbf{C}}\right)$ and $\bar{I}_2\left(\overline{\mathbf{C}}\right)$ are the first two principal invariants of the modified right Cauchy–Green tensor, $\overline{\mathbf{C}}$. As previously mentioned in this section, this description is only valid for isotropic materials. In addition, considering the kinematic assumption described by Eq. (3.184), it can be shown that the relations between $\bar{I}_\alpha$ and I_α ($\alpha =$ 1, 2, 3) are given by [49, 51]

$$\bar{I}_1\left(\overline{\mathbf{C}}\right) = J^{-2/3}\, I_1\left(\mathbf{C}\right) , \tag{3.191}$$

$$\bar{I}_2\left(\overline{\mathbf{C}}\right) = J^{-4/3}\, I_2\left(\mathbf{C}\right) , \tag{3.192}$$

$$\bar{I}_3\left(\overline{\mathbf{C}}\right) = I_3\left(\mathbf{C}\right) . \tag{3.193}$$

Note that the first three modified invariants $\bar{I}_\alpha$ ($\alpha = 1$, 2, 3) are defined exactly in the same way as in Eqs (3.178)-(3.180) substituting $\overline{\mathbf{C}}$ for $\mathbf{C}$.

3.4.2.4 Mooney–Rivlin model

Assuming a compressible isotropic hyperelastic material and adopting the *Mooney–Rivlin model* [53, 54], the strain-energy is written in the decoupled representation as follows:

$$\Psi = \Psi^{*}_{\mathrm{vol}}\left(J\right) + \Psi^{*,\mathrm{MR}}_{\mathrm{iso}}\left[\bar{I}_1\left(\overline{\mathbf{C}}\right), \bar{I}_2\left(\overline{\mathbf{C}}\right)\right] , \tag{3.194}$$

with

$$\Psi^{*,\mathrm{MR}}_{\mathrm{iso}}\left[\bar{I}_1\left(\overline{\mathbf{C}}\right), \bar{I}_2\left(\overline{\mathbf{C}}\right)\right] = c_1\left(\bar{I}_1 - 3\right) + c_2\left(\bar{I}_2 - 3\right) , \tag{3.195}$$

where c_1 and c_2 are material constants which must satisfy certain restrictions. The strain-energy can also be written in the coupled representation as

$$\Psi \quad = \quad \Psi^{*,\mathrm{MR}}\left[J, I_1\left(\mathbf{C}\right), I_2\left(\mathbf{C}\right)\right] \ , \tag{3.196}$$

with for instance [51]

$$\begin{aligned} \Psi^{*,\mathrm{MR}}\left[J, I_1\left(\mathbf{C}\right), I_2\left(\mathbf{C}\right)\right] \quad &= \quad c\,\left(J-1\right)^2 - d\,\ln\left(J\right) \\ &\quad + c_1\,\left(I_1-3\right) + c_2\,\left(I_2-3\right)\ . \end{aligned} \tag{3.197}$$

Note that the first two terms on the RHS of Eq. (3.197) were initially proposed in [55] as $[c\,J^2 - d\,\ln\left(J\right)]$. In Eq. (3.197), c is a material constant and d is a parameter with certain restrictions. Assuming that the reference configuration is stress-free, $d = 2\left(c_1 + 2\,c_2\right)$ is deduced from Eq. (3.197). Using the decoupled representation of the strain-energy [Eq. (3.194)], the PK2 stress tensor can be written as

$$\mathbf{S} \quad = \quad J\,p\,\mathbf{C}^{-1} + J^{-2/3}\,\mathrm{Dev}\left[2\,c_1\,\mathbf{G} + 2\,c_2\,\left(\bar{I}_1\,\mathbf{G} - \overline{\mathbf{C}}\right)\right] \ , \tag{3.198}$$

where $p = \mathrm{d}\Psi^*_{\mathrm{vol}}\left(J\right)/\mathrm{d}J$. Note that $\Psi^*_{\mathrm{vol}}\left(J\right)$ may be written in several different ways [51]. For instance, the following form is proposed in [56]:

$$\Psi^*_{\mathrm{vol}}\left(J\right) \quad = \quad \kappa\,\beta^{-2}\,\left[\beta\,\ln\left(J\right) + J^{-\beta} - 1\right] \tag{3.199}$$

for $\beta > 0$. κ is the constant *bulk modulus* in the reference configuration and β represents an empirical coefficient that is strictly positive.

Now, considering the so-called *coupled* representation of the strain-energy [Eq. (3.197)], the PK2 stress tensor can be written as

$$\mathbf{S} \quad = \quad \left(2\,c_1 + 2\,c_2\,I_1\right)\,\mathbf{G} - 2\,c_2\,\mathbf{C} + \left[2\,c\,J\,\left(J-1\right) - d\right]\,\mathbf{C}^{-1}\,. \tag{3.200}$$

To establish Eqs (3.198) and (3.200), the following relations have been used [49, 51]:

$$\frac{\partial I_1}{\partial \mathbf{C}} = \mathbf{G}\,, \quad \frac{\partial \bar{I}_1}{\partial \overline{\mathbf{C}}} = \mathbf{G}, \tag{3.201}$$

$$\frac{\partial I_2}{\partial \mathbf{C}} = I_1\,\mathbf{G} - \mathbf{C}\,, \quad \frac{\partial \bar{I}_2}{\partial \overline{\mathbf{C}}} = \bar{I}_1\,\mathbf{G} - \overline{\mathbf{C}}, \tag{3.202}$$

$$\frac{\partial J}{\partial \mathbf{C}} = \frac{J}{2}\,\mathbf{C}^{-1}\,. \tag{3.203}$$

3.5 Implications of mechanical properties of cardiac tissue on modeling

The heart wall can be split into three different layers: the *endocardium* (the inner layer), the *myocardium* (the middle layer) and the *epicardium* (the outer layer). The endorcardium and epicardium are membranes with thickness of the order of 100μm. The first one consists mainly of *epimysial collagen*, *elastin* and a layer of *endothelial cells* which act as an interfacial layer between the wall and the blood [50].

In this work, mainly the functional tissue of the heart wall, namely the myocardium, is considered. The latter is characterized by a complex structure that is well represented in several quantitative studies [57, 58, 59, 60]. The most documented myocardial structure is that of the left ventricle. As a result, it is convenient to examine it to give some key elements explaining implications of microstructural architecture on the macroscopic mechanical modeling.

The left ventricular wall can be modeled reasonably well as a thick-walled ellipsoid of revolution that is truncated at the base, as shown in Fig. 3.2. This wall is a composite of discrete layers, called *sheets* or *laminæ*, of parallel cardiomyocytes (cardiac muscle fibers) occupying 70 % of the volume. The remaining part of the volume is composed of various interstitial components [61]. Note that only 2 % to 5 % of this interstitial volume is constituted of collagen, spatially arranged in a network that forms lateral connections between adjacent muscle fibers. In this context, the muscle fiber directions change through the wall thickness from the epicardium to the endocardium as shown in Fig. 3.2. In the equatorial region, the muscle fiber orientation changes from $+70^{\circ}$ to -70° with respect to the circumferential direction of the left ventricle when the wall from the sub-epicardial region (at 10 % of the wall thickness from the epicardium) to the sub-endorcardial region (at 90 % of the wall thickness from the epicardium) is crossed as depicted in Fig. 3.2.

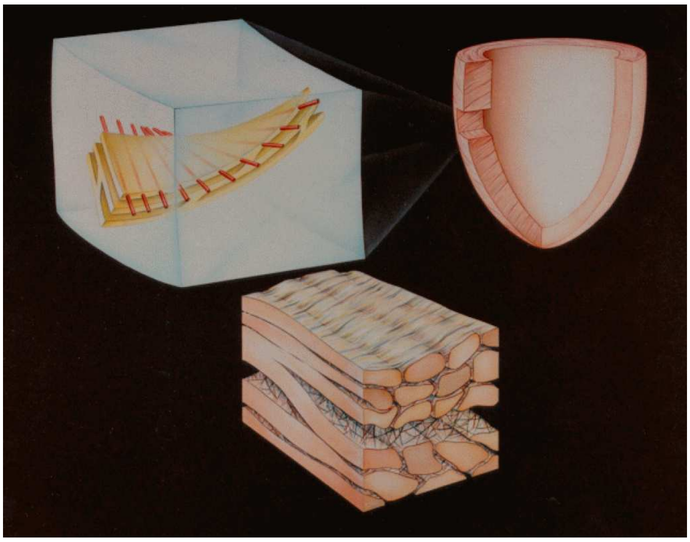

Fig. 3.2 – Microstructural organization of cardiac tissue shown by a transmural segment of tissue removed from the equatorial region of the left ventricular wall. The upper left schematic diagram depicts the transmural variation from the epicardium to the endocardium of the fiber orientation given by the red axes. The lower schematic diagram shows that fibers are bound tightly together in sheets 3 or 4 cardiomyocytes thick (by endomysial collagen), separated by cleavage planes (perimysial collagen) [57].

From a modeling point of view, for inhomogeneous and anisotropic materials such as the cardiac tissue, it is convenient to adopt a material coordinate system aligned with certain structural features of the material. To encapsulate the microstructural organization of the cardiac tissue, a microstructural orthogonal curvilinear material coordinate system Υ^M is introduced. A natural set of *material* covariant base vectors $\boldsymbol{\Upsilon}_M$ associated with the Υ^M-coordinate system is given by the *fiber axis* f which coincides with the muscle fiber orientation, the *sheet axis* s which is defined to be in the plane of the laminæ perpendicular to the fiber direction and the *sheet-normal axis* n which is defined to be orthogonal to the other two. Obviously, in the deformed configuration, these three particular directions are not orthogonal anymore. The covariant *spatial* base vectors are referred to as $\boldsymbol{\upsilon}_m$ and are associated with the microstructural curvilinear spatial coordinate system υ^m. As a result, in terms of these two coordinate systems, the motion is written as

$$\upsilon^m = \boldsymbol{\chi}^m\left(\Upsilon^M, t\right)\,, \quad m = \mathrm{f, s, n}\,, \quad M = \mathrm{f, s, n}\,. \tag{3.204}$$

The covariant components of the metric tensors $\mathbf{G}$ and $\mathbf{g}$ (with respect to the reference and current configurations) are, respectively, given by

$$G_{MN} = \boldsymbol{\Upsilon}_M \cdot \boldsymbol{\Upsilon}_N\,, \tag{3.205}$$

$$g_{mn} = \boldsymbol{\upsilon}_m \cdot \boldsymbol{\upsilon}_n\,. \tag{3.206}$$

The components of the deformation gradient tensor and the right Cauchy–Green deformation tensor are written as follows:

$$F^m_{\ M} = \frac{\partial \upsilon^m}{\partial \Upsilon^M}\,, \tag{3.207}$$

$$C_{MN} = g_{mn}\,\frac{\partial \upsilon^m}{\partial \Upsilon^M}\,\frac{\partial \upsilon^n}{\partial \Upsilon^N}\,, \tag{3.208}$$

$$C^{MN} = g^{mn}\,\frac{\partial \Upsilon^M}{\partial \upsilon^m}\,\frac{\partial \Upsilon^N}{\partial \upsilon^n}\,. \tag{3.209}$$

From different experimental *simple shear* tests on the passive ventricular myocardial tissue, the latter is known to behave as an *orthotropic* material having three mutually orthogonal planes, namely the plane built by the f-axis and the s-axis (fs-plane), the plane built by the f-axis and the n-axis (fn-plane) and the plane built by the s-axis and the n-axis (sn-plane), with distinct material responses [62]. From these shear stress-strain experiments, it is known that the ventricular myocardium is the least resistant to simple shear in the f-direction and s-direction in the fn-plane and the sn-plane, respectively, while the ventricular myocardium is the most resistant to shear deformations that induce extension in the f-direction in the fs-plane and the fn-plane. Note that for the fs-plane and the fn-plane, the shear responses in the s-direction and the n-direction are different. In a similar way, for the fs-plane and the ns-plane, the shear responses in the f-direction and the n-direction are also different. However, for the fn-plane and the sn-plane, the shear responses in the f-direction and the s-direction are the same for the specific sample used in [62]. Regarding the passive *biaxial* mechanical properties of the passive ventricular myocardial tissue, they are described in [63, 64, 65, 66]. As an example of these studies, Fig. 3.3 shows representative stress-strain data, extracted from [64].

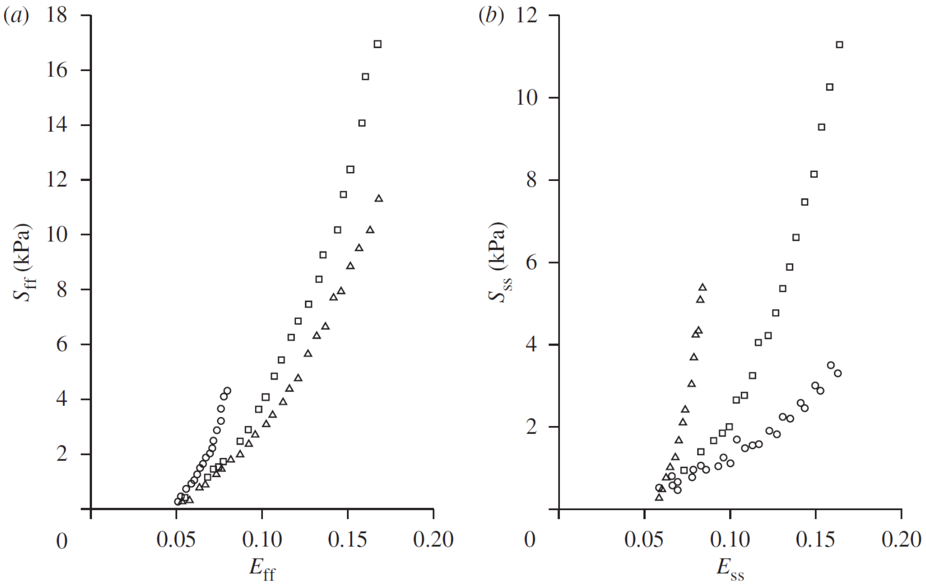

Fig. 3.3 – Stress-strain data obtained from a canine left ventricle myocardium for biaxial loading in the fs plane using three different loading protocols. Note that S_{ii} and E_{ii} ($i =$ f, s, where f and s are the fiber and sheet directions, respectively) are the components of the PK2 stress tensor and the Green–Lagrange strain tensor, respectively. S_{ff} as a function of E_{ff} (a) and S_{ss} as a function of E_{ss} for three different constant strain ratios E_{ff}/E_{ss} equal to 2.05 (triangles), 1.02 (squares), and 0.48 (circles) (b). From [50] using data from [64].

In a similar way to many other soft biological tissues, the myocardial tissue can be considered as an incompressible material. This has been established from experimental results in [67]. Moreover, the myocardium tissue appears to be viscoelastic but from a modeling point of view, it can be treated as elastic because the time scale of the cardiac cycle is long in comparison with the relaxation time of the viscoelastic response [50].

Previously in this section, a general theoretical framework, allowing to develop various detailed three-dimensional mechanical models accounting for more or less intrinsic features of cardiac tissue, has been introduced. However, using inhomogeneous and/or anisotropic properties is not suitable in the case of interest here because only the basic mechanisms related to the *mechano-electric feedback (MEF)* are examined. Thus, it is preferable to avoid inserting too much complexity because it can generate some additional effects that disturb the understanding of the basic physical processes regarding the MEF. Keeping this idea in mind, only essential mechanical properties of cardiac tissue needed to study the MEF issue are taken into account. As a first approach[12],

---

[12] For further modeling works, the general theoretical framework is already established.

the cardiac tissue is considered as a compressible[13] isotropic hyperelastic material and the Mooney–Rivlin model is used. As a result, a strain energy function given by an expression similar to Eq. (3.197) is adopted:

$$\widetilde{\Psi}^{*,\mathrm{MR}}\left[J, I_1\left(\mathbf{C}\right), I_2\left(\mathbf{C}\right)\right] = c_1\left(I_1-3\right)+c_2\left(I_2-3\right)-\frac{d}{2}\left(J-1\right) . \quad (3.210)$$

Therefore, the pure elastic part of the PK2 stress tensor is given by

$$\mathbf{S}_{\mathrm{elastic}} = \left(2\,c_1+2\,c_2\,I_1\right)\,\mathbf{G}-2\,c_2\,\mathbf{C}-J\,d\,\mathbf{C}^{-1} . \quad (3.211)$$

In addition, its contravariant components in terms of the microstructural curvilinear material coordinate system are given by

$$S^{MN}_{\mathrm{elastic}} = 2\,c_1\,G^{MN}+2\,c_2\,\Big(I_1\,G^{MN}-G^{MO}\,G^{NP}\,C_{OP}\Big)-J\,d\,C^{MN} , \quad (3.212)$$

where $I_1 = \mathrm{tr}\,\mathbf{C} = \mathbf{G} : \mathbf{C} = G_{OP}\,C^{OP}$ and $C^{MN} = C^{-1}_{MN}$.

Besides, contraction of the cardiac tissue is driven by an *active tension* that impacts the mechanical behavior of the tissue. Without caring about its physiological origin for the time being, the active tension is taken into account by linearly superimposing an active part to the pure elastic part (passive part), $\mathbf{S}_{\mathrm{elastic}}$, of the PK2 stress tensor, $\mathbf{S}$, as follows [21, 68, 69, 70]:

$$\mathbf{S} = \mathbf{S}_{\mathrm{elastic}}+\mathbf{S}_{\mathrm{active}} . \quad (3.213)$$

Obviously, $\mathbf{S}_{\mathrm{active}}$ must be in the form of a PK2 stress tensor to be consistent with the form used for the passive part. Note that $\mathbf{S}_{\mathrm{active}}$ may be superimposed to the pure elastic part of the PK2 stress tensor in several different ways. The most straightforward method of superimposition, which is used here, consists in adding a time-dependent active tension, σ_{active}, calculated from a cellular active tension model to the fiber component of the pure elastic Cauchy stress tensor if an anisotropic approach is used or to all the components if an isotropic approach is adopted. As a result, the following

---

[13] As shown in chapter 4, the assumption of compressibility is related to the formulation of SACs assuming an isotropic material.

relations can be written for the anisotropic and isotropic approaches, respectively:

$$S^{MN}_{\text{active}} \;=\; J\,\sigma_{\text{active}}\,C^{MN}\,\delta^{M}_{1}\,\delta^{N}_{1} \tag{3.214}$$

and

$$S^{MN}_{\text{active}} \;=\; J\,\sigma_{\text{active}}\,C^{MN}\,. \tag{3.215}$$

3.5.1 Mechanical equilibrium equation

The Cauchy's first equation of motion must be satisfied for all times. Assuming a quasi-static mechanical equilibrium[14] and no body force acting on cardiac tissue, Eq. (3.144) can be written, in terms of the microstructural curvilinear material coordinate system, as follows:

$$\left(F^{m}_{\;M}\,S^{MN}\right)\Big|_{N} \;=\; 0 \tag{3.216}$$

for $m =$ f, s, n. The assumption of quasi-static equilibrium comes from the fact that the time scale on which the elastic force balances the active tension is negligible in comparison with other time scales in the problem [71].

---

[14] A problem is called quasi-static if data depend on time and the acceleration is assumed to vanish [51].

CHAPTER 4

Electromechanics and thermo-electric coupling in cardiac tissue

Cardiac muscle is intrinsically a multiphysics and multiscale system. It involves subcellular and cellular processes (*e.g.* actin-myosin interaction) as well as mechanisms at the tissue level (*e.g.* propagation of *action potentials [APs]*). Both kinds of processes interplay in a strong way such that microscopic phenomena at the subcellular level generate properties at the macroscopic tissue level [72]. This work is mainly focused on the macroscopic electromechanical behavior of the heart. However, some key elements of electromechanical cell models are briefly discussed to give an overview of the microscopic modeling approach. The effects of a temperature variation on the electrical activity and the electromechanical behavior, *via* the coupling between electrical and mechanical phenomena, are also examined. For this purpose, modeling of these effects are presented.

Contents

4.1 Cardiomyocyte electromechanics: description

4.1.1 Active tension development

In a cardiomyocyte, the *active tension* development is physiologically initiated by the electrical excitation of the cardiomyocyte itself. Following this excitation (namely the depolarization of the cell membrane), the sarcolemmal[1] voltage-gated L-type calcium ion channels open and the resulting flow of calcium ions into the cell leads to a positive feedback mechanism consisting in a calcium ion release from the *sarcoplasmic reticulum (SR)* through sarcoplasmic calcium release channels gated by the cytoplasmic calcium concentration. This subcellular process is referred to as *Ca^{2+}-induced Ca^{2+} release (CICR)* [73]. Note that a small amount of calcium ions enter the cell through sarcolemmal sodium-calcium exchangers as well.

This combination of the influx and the release from SR of calcium ions increases the concentration of cytosolic calcium ions in a significant way. As a result, calcium ions

---

[1] Sarcolemma is an other word to refer to the cell membrane.

can bind to the myofilament protein troponin C resulting in a shift in the troponin-tropomyosin complex followed by structural changes of the tropomyosin-actin configuration [74]. These changes allow the binding of myosin heads to the actin filament, the so-called *cross-bridge cycling* [75], leading eventually to the active tension development in the cell. Collectively, this process is termed *excitation-contraction coupling (ECC)* [6, 75]. The relaxation then occurs when the concentration of cytosolic calcium ions declines. This requires calcium ion transport out of the cytosol by different pathways [28].

4.1.2 Mechano-electric feedback

As described in the previous section, the contraction of a cardiomyocyte is triggered by its electrical excitation *via* the ECC process. Furthermore, cardiac electrophysiological changes can also arise from mechanical changes *via* different processes collectively referred to as *mechano-electric feedback (MEF)* [76]. This MEF is a constituent part of the intrinsic electromechanical regulatory loop of the healthy heart. *A contrario* to the ECC, it has only recently begun to be appreciated [5] and modeled [77, 78].

The MEF can be viewed as made up of two distinct contributions: the *geometric* contribution and the *physiological* contribution. The geometric contribution is due to direct geometric effects of tissue deformations on depolarization wave propagation. Hitherto, two subcellular mechanisms are known to be the physiological contribution to the MEF:

i. *stretch-activated channels (SACs)*[2] [79]
ii. *mechanical modulation of cellular* Ca^{2+} *handling* [80]

These mechanisms are now more precisely discussed.

4.1.2.1 SACs

SACs have been recognized in cardiac cells [81] and respond to stretch by increasing the probability to be open. However, the underlying microscopic mechanisms leading to this increase in open probability induced by stretching (macroscopic stimulus) are

---

[2] SACs do not have to be confused with volume-activated channels (VACs). These channels are activated by changes in cell volume.

not yet completely understood. Note that two different kinds of SACs can be found: one is cation permeable [82] while the other is potassium-selective [83]. The potential pathophysiological role of cardiac SACs is huge and, as a result, there is a considerable number of clinical observations related to the cardiac MEF [84, 85], ranging from stretch-induced *ectopic excitation* to mechanical induction of *tachycardia* and *fibrillation*. From a physiological point of view, it is likely that cardiac SACs positively contribute to *chronotropic response* of the heart[3] to stretch [86].

4.1.2.2 Mechanical modulation of calcium handling

An increase in troponin C affinity for Ca^{2+} is mechanically induced when cardiac tissue is stretched leading to an initial rapid increase in twitch force [87]. This is followed by a slower rise in force production, which is related to an increase in Ca^{2+} transients induced by stretching [88, 89]. In addition, stretching of cardiac cells or tissues implies an increase in the diastolic free Ca^{2+} concentration [90] and a decrease in the apparent Ca^{2+} storage capacity of the sarcoplasmic reticulum [91].

4.2 Cardiac tissue electromechanics: modeling

A very nice general framework for the modeling of cardiomyocyte electromechanics has been described in [73] and is illustrated in Fig. 4.1. Actually, most models of cardiomyocyte electromechanics are combinations of previously published models describing specific mechanisms involved in the electromechanical behavior of cardiomyocytes. These subparts are coupled together *via* state variables including the membrane potential, calcium concentration, sarcomere length, power of hydrogen (pH) and concentration of *adenosine triphosphate (ATP)* (Fig. 4.1). Note that there is no single published model including all these mechanisms but the scheme shown in Fig. 4.1 demonstrates the feasibility of an integrated model of this type. Three main parts are needed for such a complete model: an *ECC model* that mimics cardiomyocyte electrophysioplogy and calcium handling, a *myofilament model* that accounts for actin-myosin interactions and calcium-based activation events (in cardiac myofilaments) and a *metabolic model* that describes metabolic processes.

---

[3] Chronotropic response of the heart is the fact that the heart rate over time may increase or decrease in response to stimuli.

At the tissue level, it is necessary to account for the propagation of APs by using a monodomain or bidomain model, described in sections 2.2.2 and 2.2.3, as well as mechanical deformations of the tissue controlled by the classical nonlinear theory of elasticity introduced in chapter 3. As a result, cardiac electromechanical models at the tissue level are essentially multiscale models: they incorporate some subcellular and cellular processes (*e.g.* ionic currents and active tension development in myofilaments) as well as some macroscopic mechanisms (*e.g.* propagation of APs and deformations of the tissue). However, mainly for computational cost reasons, it is not possible to account for all these subcellular and cellular processes when some numerical simulations at the tissue level are performed. As a result, only the key elements required for the purposes of this work will be retained.

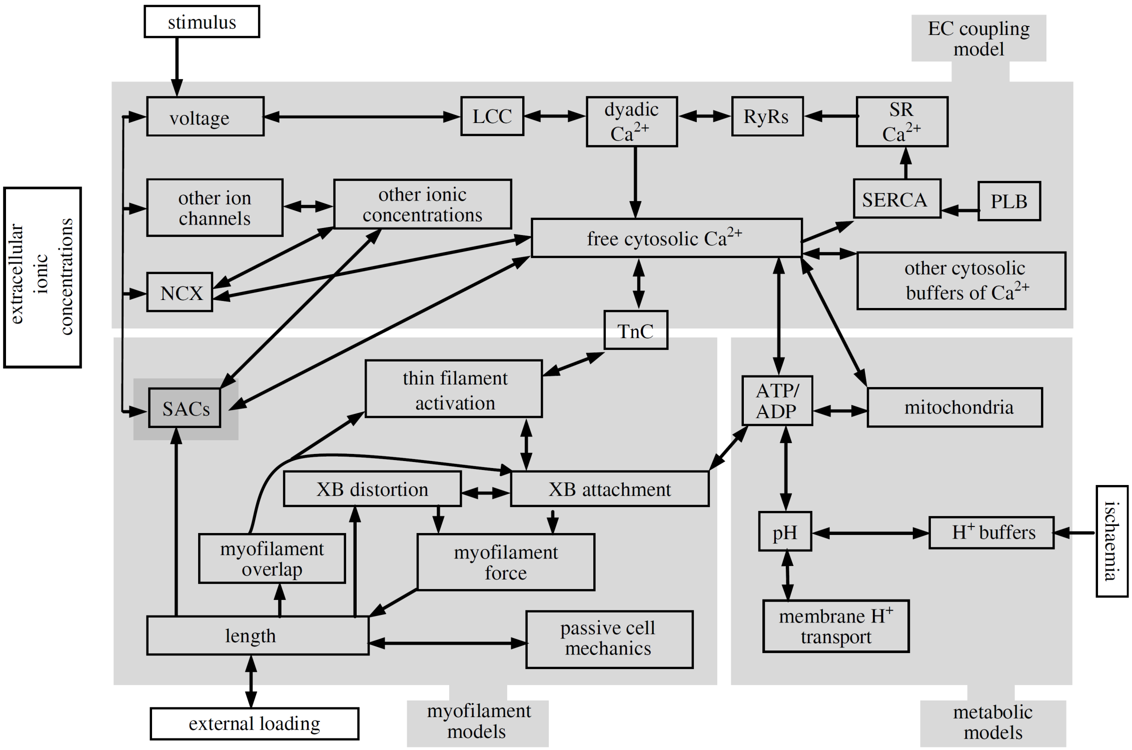

Fig. 4.1 – General framework for the modeling of cardiomyocyte electromechanics. Single arrows mean unidirectional couplings while double-headed arrows represent bidirectional couplings. Abbreviations: LCC is L-type Ca^{2+} channel, RyRs are ryanodine receptors, SERCA is sarcoplasmic reticulum Ca^{2+}-ATPase, PLB is phospholamban, NCX is Na^{+}/Ca^{2+} exchanger, SACs are stretch-activated channels, TnC is troponin C, XB is cross-bridge, ATP is adenosine triphosphate, ADP is adenosine diphosphate, and pH is power of hydrogen [73].

4.2.1 Active tension development

Section 3.5 described the way the active behavior of cardiac tissue is taken into account by linearly superimposing an additional component to the 'standard' PK2 stress tensor. The present section deals with the modeling of the scalar active tension, S_{active}, introduced on the right-hand side (RHS) of Eq. (3.214). There exists several approaches for active tension modeling accounting for more or less details. The first model of the active tension development that was specially designed for tissue-level electromechanical models is the *Hunter–McCulloch–ter Keurs (HMT) model* [21].

4.2.1.1 HMT model

The HMT model, consisting of four components, is able to reproduce a number of physiologically significant experimental observations. The four components are:

i. the passive elasticity of myocardial tissue
ii. the rapid binding of calcium ions to troponin C and the slower tension-dependent release of calcium ions from troponin C
iii. the kinetics of tropomyosin movement and availability of cross-bridge binding sites as well as the length dependence of this mechanism
iv. the kinetics of cross-bridge tension development under perturbations of myofilament length

The concentration of calcium, $\left[\mathrm{Ca}^{2+}\right]_{\mathrm{b}}$, bound to the calcium-specific binding site on troponin C, is assumed to be controlled by the following *ordinary differential equation (ODE)*:

$$\begin{aligned}\frac{\mathrm{d}\left[\mathrm{Ca}^{2+}\right]_{\mathrm{b}}}{\mathrm{d}t} &= \rho_0 \left[\mathrm{Ca}^{2+}\right]_{\mathrm{i}} \left(\left[\mathrm{Ca}^{2+}\right]_{\mathrm{b,max}} - \left[\mathrm{Ca}^{2+}\right]_{\mathrm{b}}\right) \\ &\quad -\rho_1 \left(1 - \frac{T}{\gamma T_0}\right) \left[\mathrm{Ca}^{2+}\right]_{\mathrm{b}} ,\end{aligned} \tag{4.1}$$

where ρ_0 and ρ_1 represent the rate constants for binding and unbinding, respectively, $\left[\mathrm{Ca}^{2+}\right]_{\mathrm{i}}$ is the concentration of free myoplasmic calcium, T is the tension, T_0 is the isometric tension, γT_0 is the maximum tension value, and $\left[\mathrm{Ca}^{2+}\right]_{\mathrm{b,max}}$ is the maximum value of $\left[\mathrm{Ca}^{2+}\right]_{\mathrm{b}}$ that is reached at equilibrium when $T = \gamma T_0$.

Tropomyosin movement resulting from calcium binding to troponin C controls the availabilty of actin sites for cross-bridge binding. The proportion of these sites available for cross-bridge binding is taken into account in the HMT model by a dimensionless parameter, z, ranging from 0 to 1. Based on the observation that tension increases exponentially with a first-order rate constant depending on the level of calcium activation, Hunter, McCulloch, and ter Keurs proposed to describe the behavior of z by a first-order kinetics mimicked by the following ODE:

$$\frac{\mathrm{d}z}{\mathrm{d}t} = \alpha_0 \left[\left(\frac{\left[\mathrm{Ca}^{2+}\right]_\mathrm{b}}{C_{50}} \right)^n (1-z) - z \right] , \tag{4.2}$$

where α_0 is the rate constant of tropomyosin movement, C_{50} and n are the Hill parameters. C_{50} corresponds to the value of $\left[\mathrm{Ca}^{2+}\right]_\mathrm{b}$ required to give $z_\mathrm{SS} = 0.5$ (z_SS denotes the value of z in steady state) and n governs the steepness of the curve. These two Hill parameters are stretch-dependent and given by the following relations:

$$n = n_\mathrm{ref} \left[1 + \beta_1 \left(\lambda - 1\right)\right] , \tag{4.3}$$

$$C_{50} = 10^{6 - pC_{50\mathrm{ref}} \left[1 + \beta_2 \left(\lambda - 1\right)\right]} . \tag{4.4}$$

In Eqs (4.3) and (4.4), λ is the stretch ratio, and β_1, β_2, and $pC_{50\mathrm{ref}}$ are other parameters. Under steady state conditions, namely $\mathrm{d}z/\mathrm{d}t = 0$ and $\left[\mathrm{Ca}^{2+}\right]_\mathrm{b} = \mathrm{const}$, Eq. (4.2) gives the proportion, z_SS, of actin sites available for cross-bridge binding:

$$z_\mathrm{SS} = \frac{\left[\mathrm{Ca}^{2+}\right]_\mathrm{b}^n}{\left[\mathrm{Ca}^{2+}\right]_\mathrm{b}^n + C_{50}^n} . \tag{4.5}$$

Assuming that all available actin sites are used for cross-bridge binding, the isometric tension, T_0, is defined by

$$T_0 = T_\mathrm{ref} \left[1 + \beta_0 \left(\lambda - 1\right)\right] z , \tag{4.6}$$

where T_ref is the reference tension at $\lambda = 1$ and $\beta_0 = T_\mathrm{ref}^{-1}\, \mathrm{d}T_0/\mathrm{d}\lambda$. Note that, if the increase in tension with length came about solely as a result of changing myofilament overlap, β_0 would be equal to 1. Therefore, $\beta_0 > 1$ reflects myofilament cooperativity [92, 93]. The developed tension, T, is determined by modulating the isometric tension,

T_0, by a nonlinear function of Q in the following way:

$$T = T_0 \frac{1 + a\,Q}{1 - Q}\,, \tag{4.7}$$

where a is a curvature parameter and Q is given by

$$Q\left(\frac{T}{T_0}\right) = \sum_{i=1}^{3} A_i \int_{-\infty}^{t} e^{-\alpha_i\,(t-\tau)}\,\frac{\mathrm{d}\lambda}{\mathrm{d}t}\,\mathrm{d}\tau\,, \tag{4.8}$$

where A_i and α_i are parameters determined by particular experiments [21].

4.2.1.2 Single ODE approach

The HMT model is too complex for the purposes of this work. In the present study, the onset of the active tension is modeled by using a single ODE as initially introduced in [69]. Using this approach, the biophysical details regarding the active tension development are not described and a direct dependence with respect to the membrane potential is assumed. Mathematically, it is modeled by the following ODE [69, 94, 95]:

$$\frac{\mathrm{d}\sigma_{\mathrm{active}}}{\mathrm{d}t} = \varepsilon\left(V_m\right)\,\left(\kappa_{\sigma_{\mathrm{active}}} V_m - \sigma_{\mathrm{active}}\right)\,, \tag{4.9}$$

where $\kappa_{\sigma_{\mathrm{active}}}$ is a parameter that controls the amplitude of the active stress twitch and $\varepsilon\left(V_m\right)$ is a function that accounts for the delay in the development and recovery of the active tension with respect to an AP. In the following, $\varepsilon\left(V_m\right) = \varepsilon_0$ if $V_m \geq V_{\mathrm{th}}$ (where V_{th} has been introduced in section 2.1.3) and $\varepsilon\left(V_m\right) = \varepsilon_1$, with $\varepsilon_1 > \varepsilon_0$, if $V_m < V_{\mathrm{th}}$.

4.2.2 Mechano-electric feedback

In this work, the physiological contribution to the MEF is taken into account only *via* SACs because these are the main physiological contribution to this MEF. Furthermore, as shown later in this section, the geometric contribution to the MEF is naturally embedded in the Laplacian operator when the monodomain equation is rewritten by taking into account cardiac tissue deformations.

In section 2.2.3, the 'standard' monodomain equation [Eq. 2.92] has been established assuming an undeformable cardiac tissue and, thus, without caring about deformation. However, the cardiac tissue is actually subjected to deformations due to the electromechanical coupling. When deformations are taken into account, new physical assumptions must be introduced to describe the spatio-temporal behavior of the membrane potential. A new monodomain equation which could be called the *deformable monodomain equation* must be established. To avoid any confusion in the following, two distinct functions, $V_m(\mathbf{X}, t)$ and $v_m(\mathbf{x}, t)$, are introduced to describe the same physical quantity, namely the membrane potential, but in terms of the material description and the spatial description, respectively. These two functions are related by the motion, $\boldsymbol{\chi}$, as follows:

$$V_m\left(\boldsymbol{\chi}^{-1}(\mathbf{x}, t), t\right) = v_m(\mathbf{x}, t). \tag{4.10}$$

As previously established in section 2.2.2.1, the total transmembrane current, made up of a capacitive current, different ionic currents, and a possible applied current is balanced by the diffusive current (Kirchhoff's first law). Consider that:

i. I_m and I_m^0 are the total transmembrane currents per unit deformed volume and per unit undeformed volume, respectively;

ii. I_{dif} and I_{dif}^0 are the diffusive currents per unit deformed volume and per unit undeformed volume, respectively.

In the current configuration, Ω, Kirchhoff's first law can then be written as

$$I_m = I_{\text{diff}} \tag{4.11}$$

In the present work, cellular mechanisms are assumed to be not altered by deformations excepted SACs which are induced by stretching. As a result, the total transmembrane current, $I_m \, \mathrm{d}\mathcal{V}$, for a given infinitesimal material volume element of cardiac tissue, $\mathrm{d}\mathcal{V} \in \Omega$, is identical to the total transmembrane current, $I_m^0 \, \mathrm{d}\mathcal{V}_0$, for the corresponding volume element, $\mathrm{d}\mathcal{V}_0 \in \Omega_0$:

$$\begin{aligned} I_m \, \mathrm{d}\mathcal{V} &= I_m^0 \, \mathrm{d}\mathcal{V}_0 && (4.12) \\ &= J^{-1} \, I_m^0 \, \mathrm{d}\mathcal{V}\,, && (4.13) \end{aligned}$$

where J is the volume ratio [Eq. (3.70)] that maps $\mathrm{d}\mathcal{V}_0$ in Ω_0 onto $\mathrm{d}\mathcal{V}$ in Ω. Therefore, from Eq. (4.13), I_m and I_m^0 are related by

$$I_m \;=\; J^{-1}\, I_m^0 \,. \tag{4.14}$$

Thus, substituting Eq. (4.14) into Eq. (4.11), the following relation is obtained:

$$J^{-1}\, I_m^0 \;=\; I_{\mathrm{dif}} \,. \tag{4.15}$$

Assuming that σ is the conductivity of the cardiac tissue per unit deformed length and is homogeneous, isotropic, and stretch-independent, the diffusive current per unit deformed volume is written, in terms of the spatial description, as

$$\begin{aligned} I_{\mathrm{dif}} &= \sigma \operatorname{div}\operatorname{grad} v_m && (4.16)\\ &= \frac{\sigma}{\sqrt{g}}\,\frac{\partial}{\partial x^m}\left(\sqrt{g}\, g^{mn}\,\frac{\partial v_m}{\partial x^n}\right) , && (4.17) \end{aligned}$$

where $g = \det \mathbf{g}$. In terms of the material description, this diffusive current is written in the form

$$\begin{aligned} I_{\mathrm{dif}} &= \frac{\sigma}{\sqrt{C}}\,\frac{\partial}{\partial X^M}\left(\sqrt{C}\, C^{MN}\,\frac{\partial V_m}{\partial X^N}\right) && (4.18)\\ &= \sigma\, C^{MN}\left(\frac{\partial^2 V_m}{\partial X^M\,\partial X^N} - \Gamma^L_{MN}\,\frac{\partial V_m}{\partial X^L}\right) , && (4.19) \end{aligned}$$

where $C = \det \mathbf{C} = J^2$ [Eq. (3.91)] and Γ^L_{MN} are the Christoffel symbols of the second kind (section 3.1.5). In Cartesian coordinates, all the Christoffel symbols are equal to zero and Eq. (4.19) becomes

$$I_{\mathrm{dif}} \;=\; \sigma\, C^{MN}\,\frac{\partial^2 V_m}{\partial X^M\,\partial X^N} \,. \tag{4.20}$$

Substituting Eq. (4.18) into Eq. (4.15), the deformable monodomain equation is obtained in the reference configuration, Ω_0. This is written as

$$I_m^0 \;=\; \sigma\,\frac{\partial}{\partial X^M}\left(\sqrt{C}\, C^{MN}\,\frac{\partial V_m}{\partial X^N}\right) , \tag{4.21}$$

where I_m^0 is given by

$$I_m^0 \;=\; \chi^0 \left(C_m^0 \, \frac{\partial V_m}{\partial t} + I_{\text{ion}}^0 + I_{\text{sac}}^0 + I_{\text{app}}^0 \right) , \tag{4.22}$$

where χ^0 is the undeformed surface to undeformed volume ratio, C_m^0 is the capacitance per unit undeformed surface area, I_{ion}^0 is the total ionic current per unit undeformed surface area, I_{sac}^0 represents the SACs per unit undeformed surface area[4], and I_{app}^0 is a possible applied current per unit undeformed surface area. The modeling of these SACs is described in section 4.2.2.2. Substituting Eq. (4.22) into Eq. (4.21), the deformable monodomain equation is eventually written as

$$\frac{\partial V_m}{\partial t} \;=\; D^0 \, \frac{\partial}{\partial X^M} \left(\sqrt{C} \, C^{MN} \, \frac{\partial V_m}{\partial X^N} \right) - \frac{I_{\text{ion}}^0}{C_m^0} - \frac{I_{\text{sac}}^0}{C_m^0} - \frac{I_{\text{app}}^0}{C_m^0} , \tag{4.23}$$

where $D^0 = \sigma \, (\chi^0 \, C_m^0)^{-1}$ is a diffusion coefficient often taken equal to $1\,\text{cm}^2\,\text{s}^{-1}$ [94]. In addition, typical values for χ^0 and C_m^0 are $2000\,\text{cm}^{-1}$ and $1\,\mu\text{F}\,\text{cm}^{-2}$, respectively. A typical value of σ is $2 \times 10^{-3}\,\text{S}\,\text{cm}^{-1}$ [96].

4.2.2.1 Geometric contribution to the MEF

The deformable monodomain equation naturally accounts for the geometric contribution to the MEF due to the first term on the RHS of Eq. (4.23). This term includes the information about cardiac tissue deformations *via* the right Cauchy–Green deformation tensor, $\mathbf{C}$.

4.2.2.2 SACs modeling

The first attempt to simulate the effect of SACs on the AP was realized in [77] and then used in [76, 81, 97]. The author of [77] proposed to model SACs by

$$I_{\text{sac}}^0 \;=\; \gamma \, \rho^0 \, \frac{V_m - E_{\text{sac}}}{1 + K \, e^{-\alpha^0 \, (L - L_0)}} , \tag{4.24}$$

where V_m is the membrane potential, E_{sac} is the SAC reversal potential, L is the length of sarcomere, L_0 is the reference length, α^0 is a parameter (per unit undeformed

---

[4] Note that these SACs only occur if the cardiac tissue is deformed. However, these SACs can be described either in terms of the current configuration, Ω, or the reference configuration, Ω_0.

length) controlling stretch sensitivity, K is an equilibrium constant (dimensionless) controlling the amount of current at L_0, γ is the single channel conductance (pS), and ρ^0 is the channel density (per unit undeformed surface area). As shown in Eq. (4.24), the sarcomere length was used as a measure of the strain. Note that Eq. (4.24) can be reformulated in terms of the fiber stretch ratio, λ_{11}, defined as the ratio of the current length of the sarcomere to the reference length:

$$\lambda_{11} \;=\; \frac{L}{L_0}\,. \tag{4.25}$$

As a result, substituting Eq. (4.25) into Eq. (4.24), the following relation is obtained:

$$I^0_{\mathrm{sac}} \;=\; \gamma\,\rho^0\,\frac{V_m - E_{\mathrm{sac}}}{1 + K\,e^{-\alpha^0\,L_0\,(\lambda_{11}-1)}}\,. \tag{4.26}$$

In this way, a subcellular mechanism (change in the length of sarcomere) can be taken into account at the tissue level. Finally, Eq. (4.26) can be written as

$$I^0_{\mathrm{sac}} \;=\; G^0_{\mathrm{sac}}\,\frac{V_m - E_{\mathrm{sac}}}{1 + K\,e^{-\alpha^0\,L_0\,(\lambda_{11}-1)}}\,, \tag{4.27}$$

where $G^0_{\mathrm{sac}} = \gamma\,\rho^0$ is the SAC conductance per unit undeformed surface area. As suggested in [98], SACs may also be modeled by the following relation:

$$I^0_{\mathrm{sac}} \;=\; G^0_{\mathrm{sac}}\,(V_m - E_{\mathrm{sac}})\left(\sqrt{C_{11}} - 1\right)\,\Theta\left(\sqrt{C_{11}} - 1\right)\,, \tag{4.28}$$

where C_{11} is related to λ_{11} by

$$C_{11} \;=\; \lambda^2_{11}. \tag{4.29}$$

Actually, Eq. (4.28) can be derived from Eq. (4.27) by making some assumptions and approximations. First, assume that $K = 1$ [76, 99] and there are only SACs when cardiac tissue is stretched [98, 100], namely $\lambda_{11} > 1$, Eq. (4.27) may be written as

$$I^0_{\mathrm{sac}} \;=\; G^0_{\mathrm{sac}}\,\frac{V_m - E_{\mathrm{sac}}}{1 + e^{-\alpha^0\,L_0\,(\lambda_{11}-1)}}\,\Theta\left(\lambda_{11} - 1\right)\,. \tag{4.30}$$

Given that L_0 and α^0 are positive, the exponential function has always a value ranging in $]0,\,1[$. The Taylor expansion of $\left(1+e^{-\alpha^0\,L_0\,(\lambda_{11}-1)}\right)^{-1}$ around $\lambda_{11}=1$ is given by

$$\begin{aligned}\left(1+e^{-\alpha^0\,L_0\,(\lambda_{11}-1)}\right)^{-1} &= 1-\alpha^0\,L_0\,(\lambda_{11}-1)+\frac{1}{2}\left(\alpha^0\right)^2\,L_0^2\,(\lambda_{11}-1)^2 \\ &\quad -\mathcal{O}\left[\frac{1}{6}\left(\alpha^0\right)^3\,L_0^3\,(\lambda_{11}-1)^3\right]\,.\end{aligned} \tag{4.31}$$

Assuming that $\alpha^0 = 1/L_0$ and neglecting the terms of higher order than the first in $(\lambda_{11}-1)$, Eq. (4.30) can be approximated by

$$I_{\text{sac}}^0 = G_{\text{sac}}^0\,(V_m - E_{\text{sac}})\,(\lambda_{11}-1)\,\Theta\,(\lambda_{11}-1)\,. \tag{4.32}$$

Note that the smaller the deformations, the better the approximation provided by Eq. (4.32). This formulation is valid for a mechanical model that accounts for the (real) anisotropic response of the cardiac tissue. Substituting Eq. (4.29) into Eq. (4.32), Eq. (4.28) is obtained.

In the present study, the material is considered isotropic for the reasons mentioned in chapter 3. As a result, Eq. (4.32) must be slightly modified to mimic SACs assuming an isotropic mechanical behavior. A measure of the stretching in such a case can be taken as the volume ratio J. Therefore, SACs are described in terms of J as [98, 100]

$$I_{\text{sac}}^0 = G_{\text{sac}}^0\,(V_m - E_{\text{sac}})\,(J-1)\,\Theta\,(J-1)\,. \tag{4.33}$$

4.3 Thermo-electric coupling in cardiomyocytes

As already mentioned in the introduction of this work, *therapeutic hypothermia (TH)* is the most efficient treatment for reducing brain damage during post-resuscitation from a cardiac arrest and has a protective effect on the myocardium as well. In this context, it is interesting to examine how the temperature modulates the electromechanical behavior of cardiac tissue in a qualitative way. For this purpose, two temperature-dependent functions mimicking the thermo-electric coupling are introduced in the electromechanical model.

First, the gating kinetics of ion channels is assumed to be temperature-dependent *via* temperature-dependent rates for the conformational transitions of the subunits constituting the ion channels. This exponential dependence is taken into account by multiplying the RHS of Eq. (2.36) in the FH model, Eq. (2.44) in the RM model, or Eq. (2.50) in the AlP model (section 2.1.3) by the following nonlinear temperature-dependent function [101, 102]:

$$\varphi(T) \;=\; Q_{10}^{\frac{T-T_0}{10}} \,, \tag{4.34}$$

where T is the absolute temperature, T_0 is a reference temperature, and Q_{10} represents the well-known 10-degree temperature coefficient that measures the change of rates due to a temperature increase of ten degrees[5] [25]. Due to the nature of Eq. (4.9), which describes the dynamics of the active tension development, this active tension development is also assumed to be modulated by a temperature change in a similar way as the gating kinetics of ion channels. Therefore, the RHS of Eq. (4.9) is also multiplied by $\varphi(T)$.

The second thermo-electric coupling is provided by a linear temperature dependence of ionic conductances. This mechanism is modeled by multiplying the term mimicking the total ionic current on the RHS of the monodomain equation by the linear temperature-dependent function [101, 102]

$$\eta(T) \;=\; 1 + B\,(T - T_0)\,, \tag{4.35}$$

where B is a constant parameter that describes the rate of change of conductance with temperature. As in [101, 102], $Q_{10} = 3$ and $B = 0.008\,^{\circ}\mathrm{C}^{-1}$.

4.4 Summary of the thermo-electro-mechanical model

This section summarizes the complete set of equations used to describe the strong (bidirectional) electromechanical coupling and the weak (unidirectional) thermo-electric coupling.

As suggested in [98], the model that describes electrophysiological processes is chosen

---

[5] Actually, this coefficient can be linked to the Arrhenius activation energy which allows a more physical description of temperature effects on rates.

as a 'combination' of the RM and AlP models. In terms of the dimensionless membrane potential[6], labeled $\bar{V}$, this model is given by

$$\frac{\mathrm{d}\bar{V}}{\mathrm{d}t} = \underbrace{\kappa_v \bar{V}\left(1-\bar{V}\right)\left(\bar{V}-a\right) - \bar{V}\,v}_{-\frac{I_{\text{ion}}^0}{V_{\text{a}}\,C_m^0}} - \underbrace{i_{\text{app}}}_{\frac{I_{\text{app}}^0}{V_{\text{a}}\,C_m^0}} \,, \tag{4.36}$$

$$\frac{\mathrm{d}v}{\mathrm{d}t} = \varepsilon\left(\bar{V}\right)\left(\kappa_v \bar{V} - v\right) , \tag{4.37}$$

where $\varepsilon\left(\bar{V}\right) = \varepsilon_0$ if $\bar{V} \geq a$ and $\varepsilon\left(\bar{V}\right) = \varepsilon_1$, with $\varepsilon_1 > \varepsilon_0$, if $\bar{V} < a$. Parameter κ_v is similar to parameter k in the AlP model [Eqs (2.49)-(2.51)]. The active tension development, initiated by the electrical excitation of cardiomyocytes, is provided by the single ODE approach [Eq. (4.9)].

From a mechanical point of view, the pure elastic (passive) behavior of the cardiac tissue is described by using a compressible Mooney–Rivlin model (thus, a hyperelastic isotropic material), leading to a PK2 stress tensor given by Eq. (3.212) in terms of components. The active behavior of the tissue is taken into account by linearly superimposing additional stresses, resulting from the active tension generated in cardiomyocytes, to the passive stresses induced by pure elastic deformations [Eq. (3.213)]. In terms of components, the active contribution to the PK2 stress tensor is given by Eq. (3.215). Obviously, the Cauchy's first equation of motion must be satisfied at any time. Assuming quasi-static conditions, this equation can be written as Eq. (3.216).

SACs, namely the physiological contribution to the MEF, generated by stretching of cardiac tissue are described by Eq. (4.33). Deformations also induce a geometric contribution to this MEF. These two effects are taken into account by using the deformable monodomain equation [Eq. (4.23)] to describe the spatio-temporal behavior of the membrane potential.

Finally, the thermo-electric coupling is introduced as mentioned in section 4.3. As a result, the complete model is given, in terms of the dimensionless membrane potential,

---

[6] The dimensionless membrane potential is given by $\bar{V} = \left(V_m - V_{\text{r}}\right)/V_{\text{a}}$, where V_{r} and V_{a} have already been introduced in section 2.1.3.

$\bar{V}$, by the following equations:

$$
\begin{aligned}
\frac{\partial \bar{V}}{\partial t} &= D^0 \frac{\partial}{\partial X^M} \left(\sqrt{C}\, C^{MN} \frac{\partial \bar{V}}{\partial X^N} \right) - f\left(\bar{V}, v, i_{\text{sac}}\right) \eta\left(T\right) - i_{\text{app}} \,, && (4.38) \\
f\left(\bar{V}, v, i_{\text{sac}}\right) &= \kappa_v \bar{V} \left(\bar{V} - 1\right) \left(\bar{V} - a\right) + \bar{V} v + i_{\text{sac}} \,, && (4.39) \\
\eta\left(T\right) &= 1 + B \left(T - T_0\right) \,, && (4.40) \\
\frac{\mathrm{d}v}{\mathrm{d}t} &= \varepsilon\left(\bar{V}\right) \left(\kappa_v \bar{V} - v\right) \varphi\left(T\right) \,, && (4.41) \\
\varepsilon\left(\bar{V}\right) &= \varepsilon_0 \,\Theta\left(\bar{V} - a\right) + \varepsilon_1 \,\Theta\left(a - \bar{V}\right) , && (4.42) \\
\varphi\left(T\right) &= Q_{10}^{\frac{T - T_0}{10}} \,, && (4.43) \\
\frac{\mathrm{d}\sigma_{\text{active}}}{\mathrm{d}t} &= \varepsilon\left(\bar{V}\right) \left(\kappa_{\sigma_{\text{active}}} \bar{V} - \sigma_{\text{active}}\right) \varphi\left(T\right) \,, && (4.44) \\
0 &= \left(F^m_{\ N} S^{MN} \right)\Big|_M \,, && (4.45) \\
S^{MN} &= S^{MN}_{\text{elastic}} + S^{MN}_{\text{active}} \,, && (4.46) \\
S^{MN}_{\text{elastic}} &= 2\, c_1 G^{MN} + 2\, c_2 \left(\operatorname{tr} \mathbf{C}\, G^{MN} - G^{MO} G^{NP} C_{OP} \right) \\
&\quad - J\, d\, C^{MN} \,, && (4.47) \\
S^{MN}_{\text{active}} &= J\, \sigma_{\text{active}} C^{MN} \,, && (4.48) \\
i_{\text{sac}} &= g_{\text{sac}} \left(\bar{V} - e_{\text{sac}}\right) \left(J - 1\right) \Theta\left(J - 1\right) \,, && (4.49) \\
g_{\text{sac}} &= \frac{G^0_{\text{sac}}}{C^0_m} \,, && (4.50) \\
e_{\text{sac}} &= \frac{1}{V_{\text{a}}} \left(E_{\text{sac}} - V_{\text{r}}\right) . && (4.51)
\end{aligned}
$$

As suggested in [98, 103], $e_{\text{sac}} = 1$.

CHAPTER 5

Methods, results, and discussion

Arrhythmias in ventricles and atria have been shown to be notably caused by mechanical changes inducing several electrophysiological alterations *via mechano-electric feedback (MEF)*. In this context, the characterization of the MEF and the study of the underlying mechanisms seem to be very important. For this purpose, the *time-dependent thermo-electro-mechanical model (time-dependent TEM model)*, which embeds the complexity and richness of the key mechanisms involved in the TEM activity of the cardiac muscle tissue, has been developed in chapter 4.

This model is particularly complex because it takes into account different coupled physical phenomena. Electrical and mechanical phenomena interplay in a bidirectional way, *via* the *excitation-contraction coupling (ECC)* and the MEF, while electrical and thermal phenomena are coupled in an unidirectional fashion. In this context, the role played by the MEF on the TEM behavior of the cardiac muscle tissue and the underlying fundamental mechanisms are not easy to characterize.

Due to the intrinsic complexity of this model, additional difficulties, arising from complex geometries or three-dimensional spatial configurations, must be avoided. In this spirit, the first part of this chapter presents the development of a *one-dimensional time-dependent TEM model*. The different assumptions regarding this one-dimensional time-dependent TEM model are introduced in sections 5.1.1 and 5.1.2. This model may correspond to different geometric situations such as a one-dimensional cardiac fiber, or a two- or three-dimensional patch of cardiac tissue limited to a one-dimensional deformation by using appropriate experimental conditions. Although these experimental angles are out of the scope of this work, it is practically conceivable to perform such experimental studies leading to a one-dimensional deformation for a patch of cardiac tissue.

A *modified global coupling minimal model (modified GC minimal model)* is then derived by adding new restrictions to the one-dimensional time-dependent TEM model. Key numerical elements needed to understand the methods used for solving the model equations are introduced. The spatial discretization is described as well as numerical schemes to perform time integrations. A comparison between the one-dimensional time-dependent TEM model and the modified GC minimal model is made before inspecting the differences between the *Euler-forward scheme* and the *Cash–Karp Runge–Kutta method* for temporal integrations by running simulations with the modified GC minimal model.

A general parametric study of the modified GC minimal model enabling to identify the role played by the model parameters is conducted. A more quantitative examination regarding the key parameters of the *mechano-electric feedback (MEF)* was also performed. An *autonomous electrical activity (AEA)* induced by cardiac tissue deformations *via* the MEF has been highlighted for particular conditions. This AEA has been characterized in detail. The effects of a temperature change on this AEA has also been studied.

The second part of this chapter consists in a *two-dimensional* study of the AEA induced by the MEF. This qualitative analysis must be viewed as a first extension of the one-dimensional time-dependent TEM study described in the first part of this chapter. This two-dimensional study is conducted in the spirit of paving the way for further more extensive and quantitative studies. For this purpose, the *finite-element method (FEM)* has been adopted.

Contents

5.1 Part 1: one-dimensional time-dependent TEM model

5.1.1 Mechanical assumptions

Consider cardiac tissue subject to deformation only in one dimension. Two different geometric cases (Fig. 5.1) may satisfy this assumption and are discussed below:

i. a patch of cardiac tissue subject to a one-dimensional deformation (displayed on the top of Fig. 5.1)

ii. an idealized one-dimensional cardiac fiber of length L (displayed on the bottom of Fig. 5.1)

5.1.1.1 Patch of cardiac tissue subject to a one-dimensional deformation

In this geometric situation (Fig. 5.1, top panel), the patch of cardiac tissue stands in a three-dimensional space.

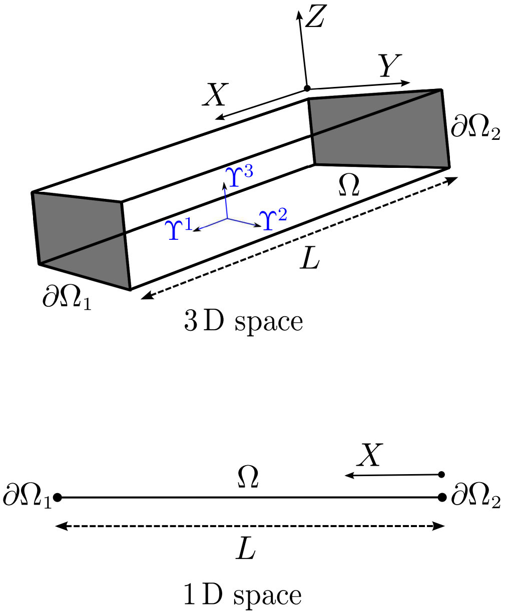

Fig. 5.1 – Two different cases leading to a one-dimensional deformation.

To restrict the deformation of this patch of cardiac tissue to one dimension (X-direction in Fig. 5.1, top panel) and thus prevent deformation in the other two dimensions (Y- and Z-directions) the borders of the three-dimensional patch parallel to the $X-Y$ and $X-Z$ planes must be held fixed in the Z-direction and Y-direction, respectively, so that no friction is generated at these borders.

As previously introduced in section 3.5, when the structural features of the cardiac tissue are taken into account, the mechanical behavior of this cardiac tissue is mathematically described using a microstructural orthogonal curvilinear material coordinate system (colored blue in Fig. 5.1, top panel), Υ^M, and a microstructural curvilinear spatial coordinate system, υ^m. However, in the present study, the cardiac tissue is assumed to be homogeneous and isotropic. Thus, a classical Cartesian coordinate system may be used.

Due to the configuration of the patch of cardiac tissue, the gradient deformation tensor, $\mathbf{F}$, and the right Cauchy–Green deformation tensor, $\mathbf{C}$, can be described, in terms of components, by the following two matrices:

$$[F] = \begin{pmatrix} {F^1}_1(X) & 0 & 0 \\ 0 & 1 & 0 \\ 0 & 0 & 1 \end{pmatrix} \tag{5.1}$$

and

$$[C] = \begin{pmatrix} \left[{F^1}_1(X)\right]^2 & 0 & 0 \\ 0 & 1 & 0 \\ 0 & 0 & 1 \end{pmatrix} . \tag{5.2}$$

In this case, the volume ratio is equal to ${F^1}_1 = \partial x / \partial X$ and the trace of $\mathbf{C}$ is equal to $\left([{F^1}_1]^2 + 2\right)$. Given that there is only one relevant direction in each configuration (X-direction and x-direction), superscripts and subscripts of components of vector and tensor may be omitted. As a result, ${F^1}_1$ may simply be rewritten as F.

5.1.1.2 One-dimensional cardiac fiber

If the fiber stands in a 'hypothetical' one-dimensional space (Fig. 5.1, bottom panel), the gradient deformation tensor, $\mathbf{F}$, and the right Cauchy–Green deformation tensor, $\mathbf{C}$, are reduced to single scalar quantities:

$$F \;=\; \frac{\partial x}{\partial X} \tag{5.3}$$

and

$$C \;=\; F^2\,. \tag{5.4}$$

In Eq. (5.3), x and X are the coordinates along the cardiac fiber with respect to the current configuration Ω and the reference configuration Ω_0. In such a case, the volume ratio, J, previously defined by Eq. (3.71), is identical to F, and the trace and the determinant of the right Cauchy–Green deformation tensor are reduced to F^2.

5.1.1.3 Boundary conditions

In the case of the patch of cardiac tissue subject to a one-dimensional deformation (top of Fig. 5.1), a no-displacement condition is applied to the gray-colored boundaries referred to as $\partial\Omega_1$ and $\partial\Omega_2$. The other boundaries of the patch, parallel to the $X-Y$ and $X-Z$ planes (non-colored on the top of Fig. 5.1), are held fixed without friction as previously mentioned. In the case of the one-dimensional cardiac fiber (bottom of Fig. 5.1), the same condition is applied to the left and right boundaries (also referred to as $\partial\Omega_1$ and $\partial\Omega_2$). Mathematically, the no-displacement condition is written, in terms of the displacement field, as follows:

$$\mathbf{u} = \mathbf{0} \quad \text{on } \partial\Omega_1 \cup \partial\Omega_2 \tag{5.5}$$

for any time t.

5.1.1.4 Initial conditions

The patch and the fiber of cardiac tissue are initially ($t = t_0$) assumed to be undeformed:

$$F\,(X,t)\big|_{t=t_0} = 1 \tag{5.6}$$

and

$$J\,(X,t)\big|_{t=t_0} = 1 \tag{5.7}$$

for any $X \in [0, L]$.

5.1.2 Electrical assumptions

5.1.2.1 Boundary conditions

The patch and the fiber of cardiac tissue are assumed to be surrounded by an electrical insulator. As a result, a no-flux boundary condition (BC) for the membrane potential is applied to all boundaries:

$$\widehat{\mathbf{N}} \cdot (\operatorname{Grad} V_m) = 0 \quad \text{on } \partial\Omega \,, \tag{5.8}$$

where $\widehat{\mathbf{N}}$ is the outward unit normal to the considered boundary and $\partial\Omega$ is the boundary of the solving domain, Ω.

5.1.2.2 Initial conditions

From one simulation to another, initial conditions (ICs) for electrical variables may be changed. For each simulation, the particular ICs used will be specified later on.

5.1.3 The modified global coupling minimal model

The modified global coupling minimal model (modified GC minimal model), which has been developed in this work, consists in a modification of the *global coupling minimal model (GC minimal model)* presented in [94]. The GC minimal model is a reduction of a more complicated model, similar to the *time-dependent thermo-electro-mechanical model (time-dependent TEM model)* (given by Eqs (4.38)-(4.49) without the thermal component), arising from specific BCs and the assumption of small deformations. The starting point of the modified GC minimal model is the time-dependent TEM model. Two differences between the modified GC minimal model and the GC minimal model may be underlined:

i. The modified GC minimal model includes the *thermo-electric coupling (TEC)* as opposed to the GC minimal model.
ii. The linear superposition of the active part, derived from the active tension developed in cardiac cells, to the passive part of the PK2 stress tensor is not performed in a similar way. The difference regarding this superposition will be detailed in

section 5.1.4.

5.1.3.1 Assumptions and modified GC minimal model equations

To establish the modified GC minimal model, cardiac tissue deformations must be assumed small and only occurring in one direction. Two different situations enable to satisfy these hypotheses: a one-dimensional cardiac fiber or a patch of cardiac tissue subject to a one-dimensional deformation as explained in section 5.1.1. The assumption of small deformations implies

$$F\,(X) \approx 1\,. \tag{5.9}$$

Using the relation

$$F \;=\; \frac{\partial U}{\partial X} + 1\,, \tag{5.10}$$

Eq. (5.9) can also be rewritten as

$$\left|\frac{\partial U}{\partial X}\right| \;<<\; 1\,. \tag{5.11}$$

In addition, due to Eq. (3.212) corresponding to the assumptions made in this section, the only relevant component, S^{11}_{elastic}, or more simply S_{elastic}, of the passive PK2 stress tensor, $\mathbf{S}_{\text{elastic}}$, is

$$\begin{aligned} S_{\text{elastic}} &= 2\,c_1 + 2\,c_2\left[F^2 + (\text{Dim} - 1)\right] - 2\,c_2\,F^2 - \frac{d}{F} && (5.12)\\ &= 2\,c_1 + 2\,c_2\,(\text{Dim} - 1) - \frac{d}{F}\,, && (5.13)\end{aligned}$$

where Dim is the dimension of the space where the problem is examined. As a result, in the case of the one-dimensional cardiac fiber, $\text{Dim}-1 = 0$ and for the three-dimensional patch of cardiac tissue subject to a one-dimensional deformation, $\text{Dim} - 1 = 2$.

Assuming that the reference configuration is initially stress-free, and taking into account the ICs relative to the mechanics [Eqs (5.6) and (5.7)], d is given by

$$d \;=\; 2\,\left[c_1 + c_2\,(\text{Dim} - 1)\right]\,. \tag{5.14}$$

Substituting Eq. (5.14) into Eq. (5.13), S_{elastic} may be written as

$$S_{\text{elastic}} \;=\; d\left(1-\frac{1}{F}\right). \tag{5.15}$$

Taking into account the active tension, σ_{active}, leading to the active part of the PK2 stress tensor, $\mathbf{S}_{\text{active}}$, described in terms of components by Eq. (4.48), the full relevant component, S^{11}, or more simply[1] S, of the PK2 stress tensor, $\mathbf{S}$, is then given by

$$S \;=\; d\left(1-\frac{1}{F}\right)+\frac{\sigma_{\text{active}}}{F}. \tag{5.16}$$

From Eq. (4.45), which can be written here as

$$\frac{\partial(F\,S)}{\partial X} \;=\; 0\,, \tag{5.17}$$

$F\,S$ is a constant, A. Therefore, Eq. (5.16) may be written as

$$d\,(F-1)+\sigma_{\text{active}} \;=\; A\,. \tag{5.18}$$

Thus, F is given by

$$F \;=\; 1+\frac{1}{d}\,(A-\sigma_{\text{active}})\,. \tag{5.19}$$

As mentioned previously, the fiber of length L is held fixed at its two extremities:

$$\int_0^L F\,(X)\;\mathrm{d}X \;=\; L\,. \tag{5.20}$$

As a result, substituting Eq. (5.19) into Eq. (5.20), the following relation is obtained:

$$\int_0^L \left[1+\frac{1}{d}\,(A-\sigma_{\text{active}})\right]\mathrm{d}X \;=\; L\,. \tag{5.21}$$

Performing the integration and solving the resulting algebraic equation gives

$$A \;=\; \overline{\sigma}_{\text{active}}=\frac{1}{L}\int_0^L \sigma_{\text{active}}\,\mathrm{d}X\,. \tag{5.22}$$

---

[1] Superscripts may be omitted here for similar reasons as those explained in section 5.1.1.1.

Taking into account Eq. (5.19), F becomes

$$F = 1 + \frac{1}{d} \left(\overline{\sigma}_{\mathrm{active}} - \sigma_{\mathrm{active}} \right) . \tag{5.23}$$

Due to Eq. (5.23), SACs modeled by Eq. (4.49) can be written, in terms of σ_{active}, as

$$\tilde{i}_{\mathrm{sac}} = \frac{g_{\mathrm{sac}}}{d} \left(\bar{V} - 1 \right) \left(\overline{\sigma}_{\mathrm{active}} - \sigma_{\mathrm{active}} \right) \Theta \left(\overline{\sigma}_{\mathrm{active}} - \sigma_{\mathrm{active}} \right) . \tag{5.24}$$

From Eq. (4.41) and Eq. (4.44), it can be seen that v/κ_v and $\sigma_{\mathrm{active}}/\kappa_{\sigma_{\mathrm{active}}}$ obey the same ODE. Assuming similar ICs for v and σ_{active}, the following algebraic relation between σ_{active} and v is then found:

$$\sigma_{\mathrm{active}} = \frac{\kappa_{\sigma_{\mathrm{active}}}}{\kappa_v} v . \tag{5.25}$$

Thus, Eq. (5.24) can be rewritten as

$$\tilde{i}_{\mathrm{sac}} = \tilde{g}_{\mathrm{sac}} \left(\bar{V} - 1 \right) \left(\bar{v} - v \right) \Theta \left(\bar{v} - v \right) , \tag{5.26}$$

with

$$\tilde{g}_{\mathrm{sac}} = \frac{g_{\mathrm{sac}}}{d} \frac{\kappa_{\sigma_{\mathrm{active}}}}{\kappa_v} \tag{5.27}$$

and

$$\bar{v} = \frac{1}{L} \int_0^L v \, \mathrm{d}X . \tag{5.28}$$

In the one-dimensional problem, Eq. (4.38) can be written in the following way:

$$\frac{\partial \bar{V}}{\partial t} = D \frac{\partial}{\partial X} \left(\frac{1}{F} \frac{\partial \bar{V}}{\partial X} \right) - f \left(\bar{V}, v, \tilde{i}_{\mathrm{sac}} \right) \eta \left(T \right) - i_{\mathrm{app}} . \tag{5.29}$$

Note that the first term on the right-hand side (RHS) of Eq. (5.29) (the diffusive term) can be expanded as follows:

$$\frac{\partial}{\partial X} \left(\frac{1}{F} \frac{\partial \bar{V}}{\partial X} \right) = \frac{1}{F} \left(\frac{\partial^2 \bar{V}}{\partial X^2} - \frac{1}{F} \frac{\partial F}{\partial X} \frac{\partial \bar{V}}{\partial X} \right) . \tag{5.30}$$

Due to Eq. (5.9), Eq. (5.29) can be written at the lowest order with respect to the difference between F and 1 as follows:

$$\frac{\partial \bar{V}}{\partial t} = D\,\frac{\partial^2 \bar{V}}{\partial X^2} - f\left(\bar{V}, v, \tilde{i}_{\text{sac}}\right)\, \eta\,(T) - i_{\text{app}}\,. \tag{5.31}$$

In summary, the simplified one-dimensional time-dependent TEM model, also called the modified GC minimal model, is given by the the following set of equations:

$$\begin{aligned}
\frac{\partial \bar{V}}{\partial t} &= D\,\frac{\partial^2 \bar{V}}{\partial X^2} - f\left(\bar{V}, v, \tilde{i}_{\text{sac}}\right)\, \eta\,(T) - i_{\text{app}}\,, && (5.32)\\
f\left(\bar{V}, v, \tilde{i}_{\text{sac}}\right) &= \kappa_v\, \bar{V}\, \left(\bar{V} - 1\right)\, \left(\bar{V} - a\right) + \bar{V}\, v + \tilde{i}_{\text{sac}}\,, && (5.33)\\
\tilde{i}_{\text{sac}} &= \tilde{g}_{\text{sac}}\, \left(\bar{V} - 1\right)\, (\bar{v} - v)\; \Theta\,(\bar{v} - v)\;, && (5.34)\\
\eta\,(T) &= 1 + B\; (T - T_0)\;, && (5.35)\\
\frac{\mathrm{d}v}{\mathrm{d}t} &= \varepsilon\left(\bar{V}\right)\, \left(\kappa_v\, \bar{V} - v\right)\, \varphi\,(T)\;, && (5.36)\\
\varepsilon\left(\bar{V}\right) &= \varepsilon_0\, \Theta\left(\bar{V} - a\right) + \varepsilon_1\, \Theta\left(a - \bar{V}\right), && (5.37)\\
\varphi\,(T) &= Q_{10}^{\frac{T-T_0}{10}}\;. && (5.38)
\end{aligned}$$

Instead of two PDEs and two ODEs to solve in the complete model [Eqs (4.38)-(4.51)], the modified GC minimal model requires the solution of only one PDE and one ODE. From now on, it is important to keep in mind that all information regarding cardiac tissue deformation is embedded in $(\bar{v} - v)$ in Eq. (5.34) due to the relation

$$\bar{v} - v = d\, \frac{\kappa_v}{\kappa_{\sigma_{\text{active}}}}\; (F - 1)\;. \tag{5.39}$$

This Eq. (5.39) enables to compute F for the modified GC minimal model from v and $\bar{v}$, *a posteriori*. In addition, note that the assumption of small deformations, $F \approx 1$, made to establish this modified GC minimal model, implies

$$\frac{1}{d}\, \frac{\kappa_{\sigma_{\text{active}}}}{\kappa_v}\; (\bar{v} - v) \ll 1\,. \tag{5.40}$$

5.1.4 Digression regarding differences between the GC minimal model and the modified GC minimal model

As already mentioned in section 5.1.3, two differences exist between the GC minimal model and the modified GC minimal model. The first difference between these two models is the TEC, introduced in section 4.3. The second difference is more delicate to introduce and is related to the way that the active part is linearly superimposed to the passive part of the PK2 stress tensor.

5.1.4.1 Formulation of the active PK2 stress tensor used in this work

The active tension arising from the initial depolarization of the cell membrane, must be considered as a physical quantity intrinsically defined on the current configuration, namely the configuration corresponding to the 'true' world. As a result, the scalar quantity σ_{active} controlled by the ODE given by Eq. (4.44) may be viewed quite naturally as a particular component of a Cauchy stress tensor (the 'true' stress tensor). Assuming that the cardiac tissue behaves like an isotropic material from a mechanical point of view, the active part, $\boldsymbol{\sigma}_{\text{active}}$, of the Chauchy stress tensor can be written as

$$\boldsymbol{\sigma}_{\text{active}} \quad = \quad \sigma_{\text{active}}\, \mathbf{g}\,, \tag{5.41}$$

where $\mathbf{g}$ is the metric tensor with respect to the current configuration. Therefore, using the relation given by Eq. (3.142), the corresponding active part, $\mathbf{S}_{\text{active}}$, of the PK2 stress tensor is written, in terms of $\boldsymbol{\sigma}_{\text{active}}$, as follows:

$$\mathbf{S}_{\text{active}} \quad = \quad J\, \sigma_{\text{active}}\, \mathbf{C}^{-1}\,. \tag{5.42}$$

This is the formulation used in Eq. (4.48).

5.1.4.2 Formulation of the active PK2 stress tensor used in the GC minimal model

In [94], the active part of the PK2 stress tensor is directly written as follows:

$$\mathbf{S}_{\text{active}} \quad = \quad \sigma_{\text{active}}\, \mathbf{C}^{-1} \tag{5.43}$$

without the volume ratio J as opposed to Eq. (5.42). This is not clearly explained but it seems that the active tension, controlled by the ODE given by Eq. (4.44), is considered as a quantity defined on the reference configuration. In such a case, from the point of view of this work, the active part of the PK2 stress tensor should be written as

$$\mathbf{S}_{\text{active}} = \sigma_{\text{active}}\,\mathbf{G}\,, \tag{5.44}$$

where $\mathbf{G}$ is the metric tensor with respect to the reference configuration, as previously introduced. Therefore, the formulation used in [94] seems to be ambiguous. Actually, the formulation used in [94] is more like the active tension is considered as a quantity defined in a similar way as a *Kirchhoff* stress tensor, $\boldsymbol{\kappa}$, related to the Cauchy stress tensor, $\boldsymbol{\sigma}$, by [50]

$$\boldsymbol{\kappa} = J\boldsymbol{\sigma}. \tag{5.45}$$

5.1.5 Numerical methods

This section introduces key elements of the numerical methods developed to solve both the one-dimensional time-dependent TEM model and the modified GC minimal model:

i. spatial discretization
ii. specific quadrature rule used in this study to numerically evaluate integrals
iii. discretization of the Laplacian operator
iv. two different schemes for the numerical temporal integrations

Note that the reader that is acquainted with these methods can safely skip this section 5.1.5 and directly proceed to section 5.1.6.

5.1.5.1 Spatial discretization and numerical evaluation of the spatial mean value of the gate variable

Spatial discretization

This section focuses on spatial discretization. Time is assumed to be continuous. The spatial domain of length L (size of the cardiac fiber) is divided into M regular spatial steps, ΔX. As a result, $X \in [0, L]$ is discretized as follows:

$$X_m = m\,\Delta X\,, \tag{5.46}$$

with $m = 0, 1, \ldots, M-1, M$. Thus, $X_M = L = M\,\Delta X$.

Simpson's rule

The modified GC minimal model involves the spatial mean of the gate variable, v, in the expression of SACs (Eq. 5.34). Mathematically, the mean value is given by

$$\bar{v}\,(t) \;=\; \frac{1}{L}\int_0^L v\,(X,t)\;\mathrm{d}X\,. \tag{5.47}$$

In terms of the discrete material points, Eq. (5.47) can be rewritten as

$$\bar{v}\,(t) \;=\; \frac{1}{L}\int_{X_0}^{X_M} v\,(X,t)\;\mathrm{d}X\,. \tag{5.48}$$

Simpson's rule enables numerical evaluation of the integral on the RHS of Eq. (5.48) as follows:

$$\begin{aligned}\int_{X_0}^{X_M} v\,(X,t)\;\mathrm{d}X \;=\; & \Delta X\,\left[\frac{1}{3}\,v_0\,(t) + \frac{4}{3}\,v_1\,(t) + \frac{2}{3}\,v_2\,(t) + \frac{4}{3}\,v_3\,(t) + \right. \\ & \left.\cdots + \frac{2}{3}\,v_{M-2}\,(t) + \frac{4}{3}\,v_{M-1}\,(t) + \frac{1}{3}\,v_M\,(t)\right] \\ & + \mathcal{O}\left(\Delta X^4\right)\,,\end{aligned} \tag{5.49}$$

where M is an even number.

5.1.5.2 Discretization of the Laplacian operator and numerical temporal integration

Discretization of the Laplacian operator

The Laplacian operator applied to $\bar{V}$ (second-order spatial derivative of $\bar{V}$) is discretized, at a given discrete material point, X_m, using a *second-order central difference scheme*:

$$\widetilde{\left(\frac{\partial^2\bar{V}}{\partial X^2}\right)}_m \;=\; \frac{\bar{V}_{m+1} + \bar{V}_{m-1} - 2\,\bar{V}_m}{\Delta X^2}\,. \tag{5.50}$$

The Taylor series expansions of $\bar{V}_{m+1} = \bar{V}\left(X_{m+1}\right)$ and $\bar{V}_{m-1} = \bar{V}\left(X_{m-1}\right)$ around the point X_m, are given by

$$\begin{aligned} \bar{V}_{m+1} &= \bar{V}_m + \Delta X \left(\frac{\partial \bar{V}}{\partial X}\right)_m + \frac{\Delta X^2}{2}\left(\frac{\partial^2 \bar{V}}{\partial X^2}\right)_m \\ &\quad + \frac{\Delta X^3}{6}\left(\frac{\partial^3 \bar{V}}{\partial X^3}\right)_m + \mathcal{O}\left[\frac{\Delta X^4}{24}\left(\frac{\partial^4 \bar{V}}{\partial X^4}\right)_m\right] \end{aligned} \tag{5.51}$$

and

$$\begin{aligned} \bar{V}_{m-1} &= \bar{V}_m - \Delta X \left(\frac{\partial \bar{V}}{\partial X}\right)_m + \frac{\Delta X^2}{2}\left(\frac{\partial^2 \bar{V}}{\partial X^2}\right)_m \\ &\quad - \frac{\Delta X^3}{6}\left(\frac{\partial^3 \bar{V}}{\partial X^3}\right)_m + \mathcal{O}\left[\frac{\Delta X^4}{24}\left(\frac{\partial^4 \bar{V}}{\partial X^4}\right)_m\right], \end{aligned} \tag{5.52}$$

respectively. Substituting Eqs (5.51) and (5.52) into Eq. (5.50) enables to emphasize the *truncation error* resulting from the approximation [Eq. (5.50)] used to numerically compute the Laplacian operator:

$$\widetilde{\left(\frac{\partial^2 \bar{V}}{\partial X^2}\right)}_m = \left(\frac{\partial^2 \bar{V}}{\partial X^2}\right)_m + \underbrace{\mathcal{O}\left[\frac{\Delta X^2}{12}\left(\frac{\partial^4 \bar{V}}{\partial X^4}\right)_m\right]}_{\text{truncation error}}. \tag{5.53}$$

Euler-forward scheme

This section focuses on time discretization. Therefore, space is supposed to be continuous. Assume that the time of a given simulation, t_{simu}, is divided into N regular time steps, Δt. In this case, current time $t \in [0, t_{\text{simu}}]$ is discretized as follows:

$$t_n = n\,\Delta t\,, \tag{5.54}$$

with $n = 0,\, 1,\, \ldots,\, N-1,\, N$. Thus, $t_N = t_{\text{simu}} = N\,\Delta t$. As a first approach to deal with basic implementation issues of the different models, time derivatives of dependent variables have been discretized using a classical *first-order Euler-forward scheme*. For instance, the time derivative of $\bar{V}$, at a given discrete temporal point, t_n, is discretized as follows:

$$\widetilde{\left(\frac{\partial \bar{V}}{\partial t}\right)}^n = \frac{\bar{V}^{n+1} - \bar{V}^n}{\Delta t}\,. \tag{5.55}$$

The Taylor series expansion of $\bar{V}^{n+1} = \bar{V}\left(t_{n+1}\right)$ around the point t_n, is given by

$$\bar{V}^{n+1} \;=\; \bar{V}^{n} + \Delta t \left(\frac{\partial \bar{V}}{\partial t}\right)^{n} + \mathcal{O}\left[\frac{\Delta t^2}{2}\left(\frac{\partial^2 \bar{V}}{\partial t^2}\right)^{n}\right]. \tag{5.56}$$

Substituting Eq. (5.56) into Eq. (5.55) enables to highlight the truncation error due to the approximation [Eq. (5.55)] used to numerically compute the time derivative:

$$\widetilde{\left(\frac{\partial \bar{V}}{\partial t}\right)}^{n} \;=\; \left(\frac{\partial \bar{V}}{\partial t}\right)^{n} + \underbrace{\mathcal{O}\left[\frac{\Delta t}{2}\left(\frac{\partial^2 \bar{V}}{\partial t^2}\right)^{n}\right]}_{\text{truncation error}}. \tag{5.57}$$

Spatio-temporal numerical scheme

Using Eqs (5.50) and (5.55), the resulting finite difference approximation to Eq. (5.31) is given by

$$\begin{aligned}\bar{V}_m^{n+1} \;=\; & \bar{V}_m^{n} + \frac{D\,\Delta t}{\Delta X^2}\left(\bar{V}_{m+1}^{n} + \bar{V}_{m-1}^{n} - 2\,\bar{V}_m^{n}\right) - \Delta t \left[f\left(\bar{V}_m^{n}, v_m^{n}, \bar{v}^{n}\right)\eta\left(T\right) + \left(i_{\text{app}}\right)_m^{n}\right] \\ & + \mathcal{O}\left[\frac{\Delta t}{2}\left(\frac{\partial^2 \bar{V}}{\partial t^2}\right)_m^{n}, \frac{\Delta X^2}{12}\left(\frac{\partial^4 \bar{V}}{\partial X^4}\right)_m^{n}\right],\end{aligned} \tag{5.58}$$

where

$$\begin{aligned} f\left(\bar{V}_m^{n}, v_m^{n}, \bar{v}^{n}\right) \;=\; & \kappa_v\,\bar{V}_m^{n}\left(\bar{V}_m^{n} - 1\right)\left(\bar{V}_m^{n} - a\right) + \bar{V}_m^{n}\,v_m^{n} \\ & + \tilde{g}_{\text{sac}}\left(\bar{V}_m^{n} - 1\right)\left(\bar{v}^{n} - v_m^{n}\right)\Theta\left(\bar{v}^{n} - v_m^{n}\right). \end{aligned} \tag{5.59}$$

Applying the Euler-forward scheme to numerically compute the time derivative of v at the discrete spatio-temporal point (X_m, t_n), the finite difference approximation to Eq. (5.36) is written as

$$v_m^{n+1} \;=\; v_m^{n} + \Delta t\,\varepsilon\left(\bar{V}_m^{n}\right)\left(\kappa_v\,\bar{V}_m^{n} - v_m^{n}\right)\varphi\left(T\right) + \mathcal{O}\left[\frac{\Delta t}{2}\left(\frac{\partial^2 v}{\partial t^2}\right)_m^{n}\right]. \tag{5.60}$$

Stability condition of the spatio-temporal numerical scheme

When an explicit Euler-forward scheme is used to perform the temporal integration, Δt cannot be chosen arbitrarily. The time step must satisfy a condition depending on ΔX. This condition can be determined by performing a stability analysis of the numerical scheme. For this purpose, the *Von Neumann stability analysis* is used. This method is based on *Fourier modes*. Rigorously, this analysis applies only to problems without BCs and with constant coefficients but in practice, it is also used when these restrictions are not satisfied. Regarding this heuristic approach, BCs are simply ignored and coefficients are *frozen* in the linear difference scheme [104]. In the case where the difference scheme is nonlinear, it is necessary to linearize it before applying the Von Neumann stability analysis. The method consists in substituting $\bar{V}_m^n$ with a single discrete Fourier mode:

$$\xi^n \, e^{i\,k\,m\,\Delta X}\,, \tag{5.61}$$

where $\xi^n = \xi^n\,(k)$ is called the *(complex) amplification factor* for the mode corresponding to the wave number k, into Eq. (5.58) after having neglected the last two terms on the RHS (the nonlinear terms). This yields

$$\begin{aligned} \xi^{n+1}\, e^{i\,k\,m\,\Delta X} &= \xi^n \, e^{i\,k\,m\,\Delta X} \\ &+ \frac{D\,\Delta t}{\Delta X^2}\,\xi^n\,\left[e^{i\,k\,(m+1)\,\Delta X} + e^{i\,k\,(m-1)\,\Delta X} - 2\,e^{i\,k\,m\,\Delta X}\right]\,. \end{aligned} \tag{5.62}$$

In addition, dividing Eq. (5.62) by $\xi^n \, e^{i\,k\,m\,\Delta X}$, Eq. (5.62) can be written as

$$\begin{aligned} \xi\,(k, \Delta t, \Delta X) &= 1 + \frac{D\,\Delta t}{\Delta X^2}\,\left(e^{i\,k\,\Delta X} + e^{-i\,k\,\Delta X} - 2\right) \\ &= 1 + 2\,\frac{D\,\Delta t}{\Delta X^2}\,\cos\,(k\,\Delta X) \\ &= 1 - 4\,\frac{D\,\Delta t}{\Delta X^2}\,\sin^2\left(\frac{1}{2}\,k\,\Delta X\right)\,. \end{aligned} \tag{5.63}$$

The *Von Neumann stability condition* is given as [104]

$$|\xi| \leq 1 + \mathcal{O}\,(\Delta t)\,. \tag{5.64}$$

Instead of Eq. (5.64), the simpler *strict Von Neumann condition* is often used:

$$|\xi| \leq 1\,. \tag{5.65}$$

Therefore, the condition given by Eq. (5.65) is verified if

$$\Delta t \;\leq\; \frac{1}{2\,D}\,\Delta X^2\,. \tag{5.66}$$

Runge–Kutta methods

As a second approach, without modifying the spatial discretization, temporal integration has been performed using a more accurate scheme from the explicit *Runge–Kutta methods (RKMs)* family. More precisely, the method used in this work is known as the *Cash–Karp Runge–Kutta method (CKRKM)* [105]. The method developed by Cash and Karp is very suitable for initial value problems (IVPs) having rapidly varying solutions. To introduce this method, assume a general system of ordinary differential equations (ODEs) given by

$$\frac{\mathrm{d}\,[y]}{\mathrm{d}t} = f\left(t, [y\left(t\right)]\right) , \tag{5.67}$$

where $[y\left(t\right)] = \left[y_1\left(t\right), y_2\left(t\right), \ldots, y_{m-1}\left(t\right), y_m\left(t\right)\right]^{\mathrm{T}}$ is a column matrix with m unknowns, t is the independent variable, and f is an arbitrary function of t and $[y]$ such that $f : \mathbb{R} \times \mathbb{R}^m \mapsto \mathbb{R}^m$. The IC, $[y\left(0\right)] = [y_0]$, of the system is known. Assume that t is discretized as in Eq. (5.54). Applying the explicit Euler-forward scheme to Eq. (5.67), $[y]^{n+1}$ can be written as

$$[y]^{n+1} = [y]^n + \Delta t\, f\left(t_n, [y]^n\right) . \tag{5.68}$$

As already mentioned, this scheme is a first-order scheme. To increase the accuracy of the temporal integration, one approach is to include extra function evaluations in the numerical procedure. In the case of explicit RKMs, the derivatives at several points within a given integration interval $[t_n, t_{n+1}]$ are evaluated and used to advance the integration from t_n to t_{n+1}. The general form of a standard explicit RKM to numerically solve Eq. (5.67) is written as follows:

$$[y]^{n+1} = [y]^n + \Delta t \sum_{j=1}^{s} b_j\, k_j\,, \tag{5.69}$$

$$k_i = f\left(t_n + c_i\,\Delta t, [y]^n + \Delta t \sum_{j=1}^{i-1} a_{ij}\, k_j\right) , \tag{5.70}$$

$$c_i = \sum_{j=1}^{i-1} a_{ij}\,, \tag{5.71}$$

where $i = 1, 2, \ldots, s-1, s$ with s that is the number of intermediate *'stages'* and k_j are the corresponding slopes. This method gives an approximation of $[y]$ at the discrete temporal point t_{n+1} by evaluating s intermediate stages in the interval $[t_n, t_{n+1}]$. To specify a particular RKM, it is necessary to provide:

i. the number of stages, s
ii. the coefficients c_i for $i = 2, 3, \dots, s-1, s$
iii. the coefficients a_{ij} for $1 \leq j < i \leq s$
iv. the coefficients b_j for $j = 1, 2, \dots, s-1, s$

A very convenient way to summarize data relative to a particular RKM is introduced in [106]: the *Butcher tableau*, depicted in Tab. 5.1. The CKRKM used in this work is a fifth-order method from the RKMs subfamily, called *embedded RKMs*. The Butcher tableau corresponding to the fifth-order CKRKM is shown in Tab. 5.2.

$$
\begin{array}{c|ccccc}
0 & 0 & & & & \\
c_2 & a_{21} & 0 & & & \\
c_3 & a_{31} & a_{32} & 0 & & \\
\vdots & \vdots & \vdots & \ddots & \ddots & \\
c_s & a_{s1} & a_{s2} & \cdots & a_{ss-1} & 0 \\
\hline
 & b_1 & b_2 & \cdots & b_{s-1} & b_s
\end{array}
$$

Tab. 5.1 – Typical Butcher tableau.

$$
\begin{array}{c|cccccc}
0 & 0 & & & & & \\
\frac{1}{5} & \frac{1}{5} & 0 & & & & \\
\frac{3}{10} & \frac{3}{40} & \frac{9}{40} & 0 & & & \\
\frac{3}{5} & \frac{3}{10} & -\frac{9}{10} & \frac{6}{5} & 0 & & \\
1 & -\frac{11}{54} & \frac{5}{2} & -\frac{70}{27} & \frac{35}{27} & 0 & \\
\frac{7}{8} & \frac{1631}{55\,296} & \frac{175}{512} & \frac{575}{13\,824} & \frac{44\,275}{110\,592} & \frac{253}{4096} & 0 \\
\hline
 & \frac{37}{398} & 0 & \frac{250}{621} & \frac{125}{594} & 0 & \frac{512}{1771}
\end{array}
$$

Tab. 5.2 – Butcher tableau for the fifth-order CKRKM [105].

5.1.6 One-dimensional time-dependent TEM model vs modified GC minimal model

This section aims at underlining differences and similarities between the one-dimensional time-dependent TEM model and the modified GC minimal model. In this context, the naive explicit Euler-forward scheme, with a time step, Δt, equal to $0.04\,\mathrm{ms}$, is used to perform the temporal integration. The second-order central difference scheme is adopted to discretize the Laplacian operator. As suggested in [107], a spatial step, ΔX, of $0.025\,\mathrm{cm}$ ($250\,\mu\mathrm{m}$) is required to fully mimic spatio-temporal characteristics of depolarization wave propagation. In this section, $\Delta X = 0.02\,\mathrm{cm}$.

First, assume that $g_{\mathrm{sac}} = 0\,\mathrm{ms}^{-1}$, meaning that the MEF is purely due to a geometric factor (remind that this geometric MEF is not present in the modified GC minimal model). With this assumption, SACs, which are the physiological contribution to the MEF, are not taken into account. It is interesting to examine how a depolarization wave (propagation of an *action potential [AP]*) behaves in such a case by running two similar simulations with the two different models. ICs, BCs, and parameter values, given in Tab. 5.3, are exactly the same for both simulations.

Parameter	Value	Units
a	0.05	dimensionless
D^0	10^{-3}	$\mathrm{cm}^2\,\mathrm{ms}^{-1}$
ε_0	3×10^{-3}	ms^{-1}
ε_1	90×10^{-3}	ms^{-1}
$\kappa_{\sigma_{\mathrm{active}}}$	1	$\mathrm{N\,cm}^{-2}$
κ_v	2	ms^{-1}
g_{sac}	0 or 0.08	ms^{-1}
d	0.8	$\mathrm{N\,cm}^{-2}$
L	5	cm

Tab. 5.3 – Parameter values for simulations with the one-dimensional time-dependent TEM model and the modified GC minimal model. Note that $g_{\mathrm{sac}} = 0\,\mathrm{ms}^{-1}$ if SACs are not taken into account and $g_{\mathrm{sac}} = 0.08\,\mathrm{ms}^{-1}$ otherwise.

Initially, an external current, i_{app}, is applied locally on a small region, which is $4 \times \Delta X$ wide, in a cardiac fiber of length $L = 5\,\mathrm{cm}$ and during a small time interval of $5\,\mathrm{ms}$. This current behaves with respect to the time (expressed in ms) as shown in Fig. 5.2.

Mathematically, this current is written as follows:

$$i_{\text{app}}(t) \quad = \quad i_{\text{app,max}}\,[\Theta(t) - \Theta(t-1)]\; t + i_{\text{app,max}}\,[\Theta(t-1) - \Theta(t-5)]\ , \quad (5.72)$$

where $i_{\text{app,max}} = 0.06\,\text{ms}^{-1}$ and Θ is the Heaviside function.

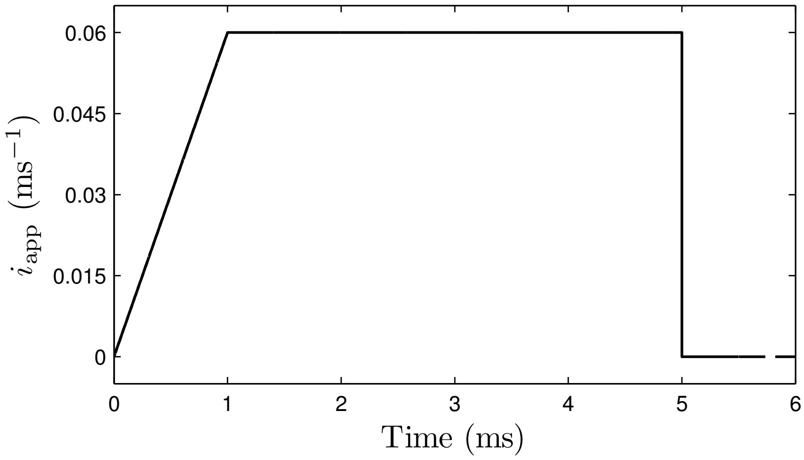

Fig. 5.2 – Time-dependent external current, $i_{\text{app}}(t)$, applied to the region from $X = 0.46\,\text{cm}$ to $X = 0.54\,\text{cm}$.

Figs 5.3a and 5.3b seem to be very similar. However, the propagating AP, shown in Fig. 5.3a, reaches the boundary of the fiber ($X = 5\,\text{cm}$) a bit later than the propagating AP in Fig. 5.3b.

To better visualize this behavior, the time course of both APs can be observed at some specific spatial positions. The time courses of the dimensionless membrane potential, $\bar{V}$, shown in Fig. 5.4, emphasize the rough observation already made on time-space plots (Fig. 5.3). The further from the region of initial excitation the time course of $\bar{V}$ is examined, the more significant the difference between the two models becomes. Red short dashed and solid lines are time-shifted, while black short dashed and solid lines overlap (Fig 5.4). This difference can be explained by looking at the gradient deformation, F, or the displacement gradient field, $\partial U/\partial X$, shown in Fig. 5.5. In the one-dimensional time-dependent TEM model, F is not assumed to be equal to one in the diffusive term, given by Eq. (5.30), as in the modified GC minimal model. As a result, it is not surprising that the spatio-temporal behavior of the dimensionless membrane potential is different from one model to another.

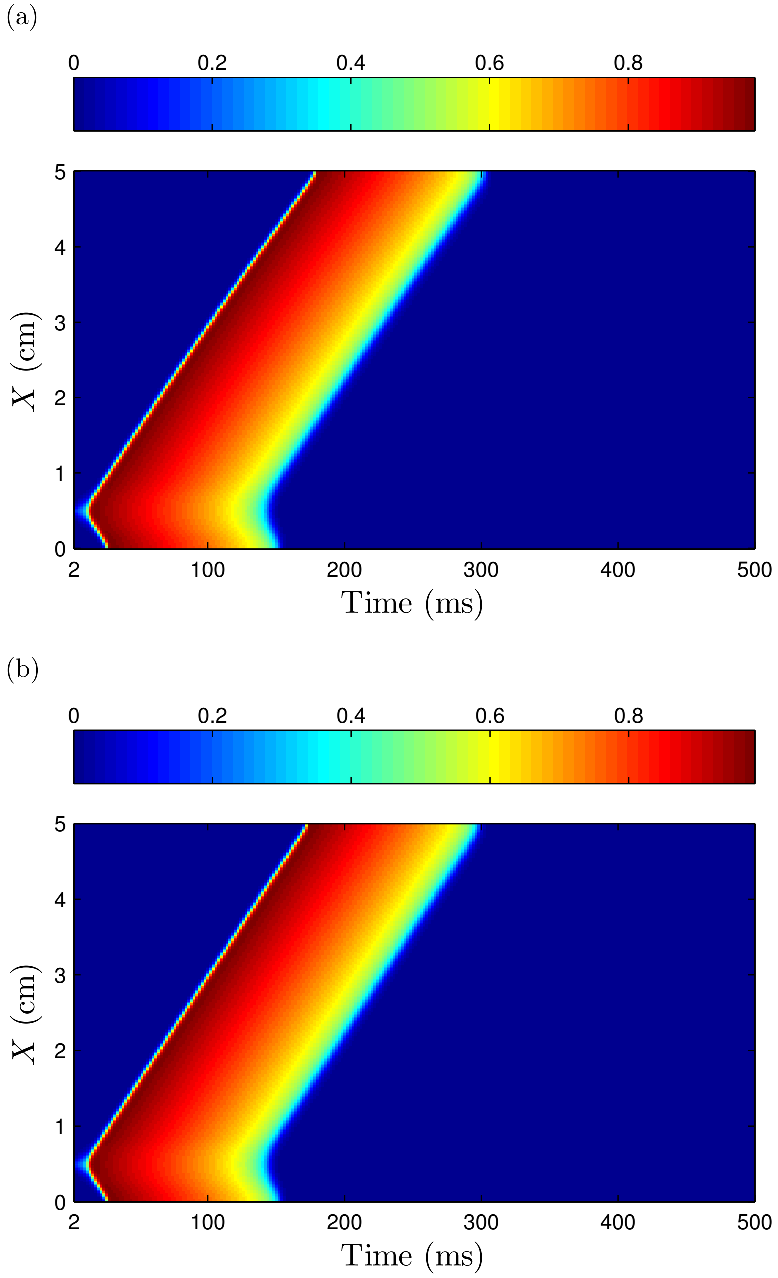

Fig. 5.3 – Time-space plots of the dimensionless membrane potential, $\bar{V}$, with the one-dimensional time-dependent TEM model (a) and the modified GC minimal model (b), without taking into account SACs.

The inspection of the time-space plot of the displacement gradient field, shown in Fig. 5.5, reveals that the wavefront of the AP propagates, from $X = 0.5\,\text{cm}$ to $X = 5\,\text{cm}$, on a stretched region of the fiber (colored red in Fig. 5.5). This stretching gradually increases when the AP moves toward the boundary, $X = 5\,\text{cm}$. As a result, the effect of the stretching (*via* F) on the diffusive term [Eq. (5.30)] gradually increases when the AP moves toward the boundary $X = 5\,\text{cm}$. This is the reason for that the time courses are more shifted for $X = 4\,\mathrm{cm}$ than for $X = 2\,\mathrm{cm}$. In the case when the changes of F are taken into account (one-dimensional time-dependent TEM model), the AP, initially generated close to $X = 0.5\,\mathrm{cm}$, propagates on a larger part of the fiber to reach the material point $X = 4\,\mathrm{cm}$ in comparison with the case where $F = 1$ (modified GC minimal model). Therefore, as shown in Fig. 5.4, the AP simulated by the one-dimensional time-dependent TEM model reaches $X = 4\,\mathrm{cm}$ just after the AP simulated by the modified GC minimal model.

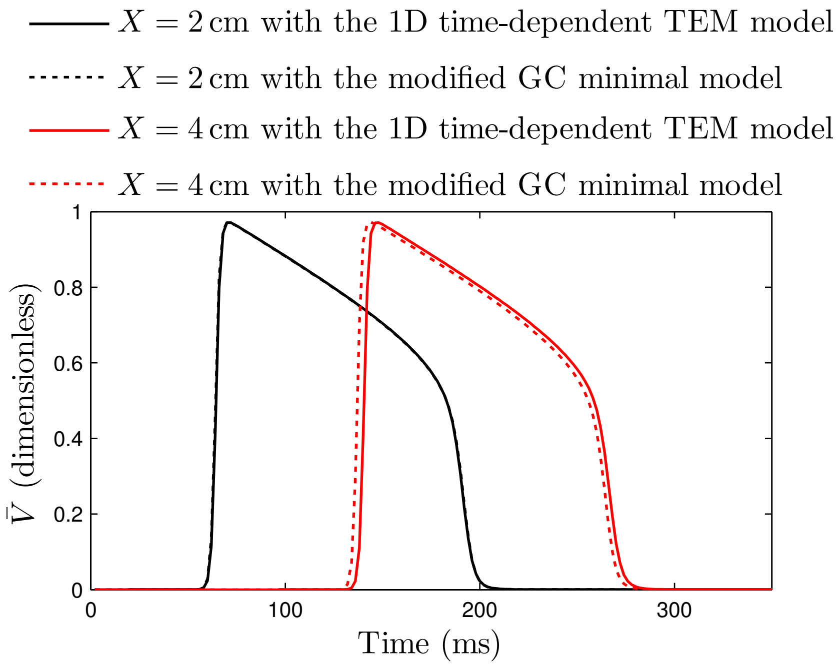

Fig. 5.4 – Time courses of the dimensionless membrane potential, $\bar{V}$, for two specific locations, $X = 2\,\mathrm{cm}$ and $X = 4\,\mathrm{cm}$, with the two different models. Parameter values are given in Tab. 5.3 with $g_{\mathrm{sac}} = 0\,\mathrm{ms}^{-1}$.

As shown in Fig. 5.5, it is interesting to underline that stretching and shortening in the fiber can reach more than 15 % and 20 %, respectively, with the set of parameter values given in Tab. 5.3. *A priori*, theoretically, it seems delicate to simulate large deformations with the modified GC minimal model, which assumes small deformations. That is precisely the reason for which results involving large deformations are emphasized with the one-dimensional time-dependent TEM model in Figs 5.5, 5.6, and 5.7. However, as shown further in this section, from a pragmatic point of view, the modified GC minimal model leads to results very similar to these obtained with the one-dimensional time-dependent TEM model using the parameter values given in Tab. 5.3, although rather large deformations are generated.

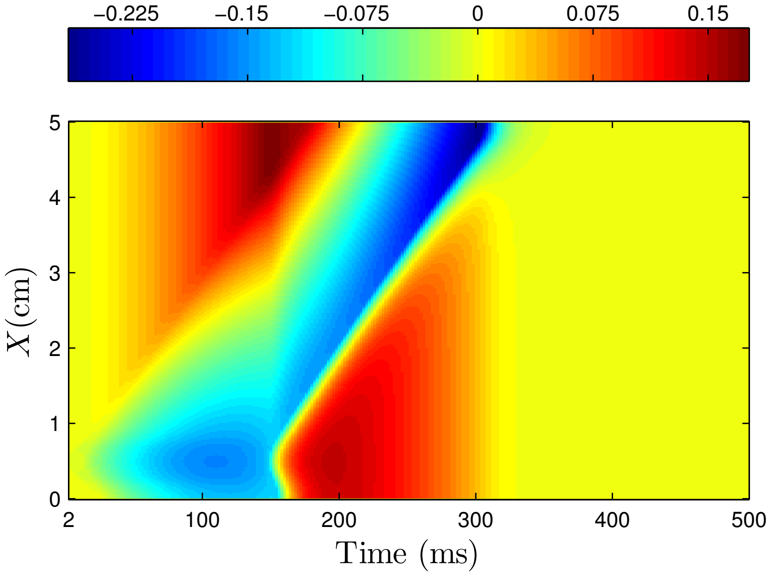

Fig. 5.5 – Time-space plot of the displacement gradient field, $\partial U/\partial X = F - 1$, simulating by the one-dimensional time-dependent TEM model. Stretched and shortened regions are colored red and blue, respectively.

Consider now the case for which g_{sac} is not equal to zero anymore and take $g_{\text{sac}} = 0.08\,\text{ms}^{-1}$. It means that the MEF is also taken into account *via* the physiological effect due to a mechanical deformation in addition to the geometric effect. For $g_{\text{sac}} \neq 0\,\text{ms}^{-1}$, SACs occur for stretched regions of the fiber. As a result, these SACs can locally trigger a new AP at a given material point, which is not in an ERS, if their accumulation (integration) over time provides a supra-threshold stimulus leading to the onset of an AP. It is very important to remind that the magnitude of the stimulus required to exceed the threshold potential depends on the state of the cardiac tissue. When the tissue is in a resting state, the stimulus required to exceed the threshold potential is weaker than the one required whether the tissue is in a *relative refractory state (RRS) and stronger than the one required whether the tissue is in a supernormal state (SS)*. If the cardiac tissue is in an *effective* or *absolute refractory state (ERS/ARS)*, no AP can be initiated, regardless of the strength of the stimulus (section 2.1.1).

As shown in Fig. 5.6a, an *autonomous electrical activity (AEA)* occurs in the fiber. Given that all parameter values are exactly the same as those used in the previous simulation except that $g_{\text{sac}} = 0.08\,\text{ms}^{-1}$ as opposed to $g_{\text{sac}} = 0\,\text{ms}^{-1}$ (Tab. 5.3), it can be stated that the physiological MEF is essential to generate an AEA in the present case. The propagation of the first AP toward the boundary $X = 5\,\text{cm}$, induced by the initial external current [Eq. (5.72)] applied close to $X = 0.5\,\text{cm}$, generates an active tension (Fig. 5.6b) where the fiber undergoes an AP, with a slight time delay with respect to the beginning of the local depolarization. As a result, these parts of the fiber, subject to an active tension, are shortened (Fig. 5.7). At the same time, these local shortenings gradually stretch the remaining part of the fiber that has not yet been reached by the propagating AP (Fig. 5.7).

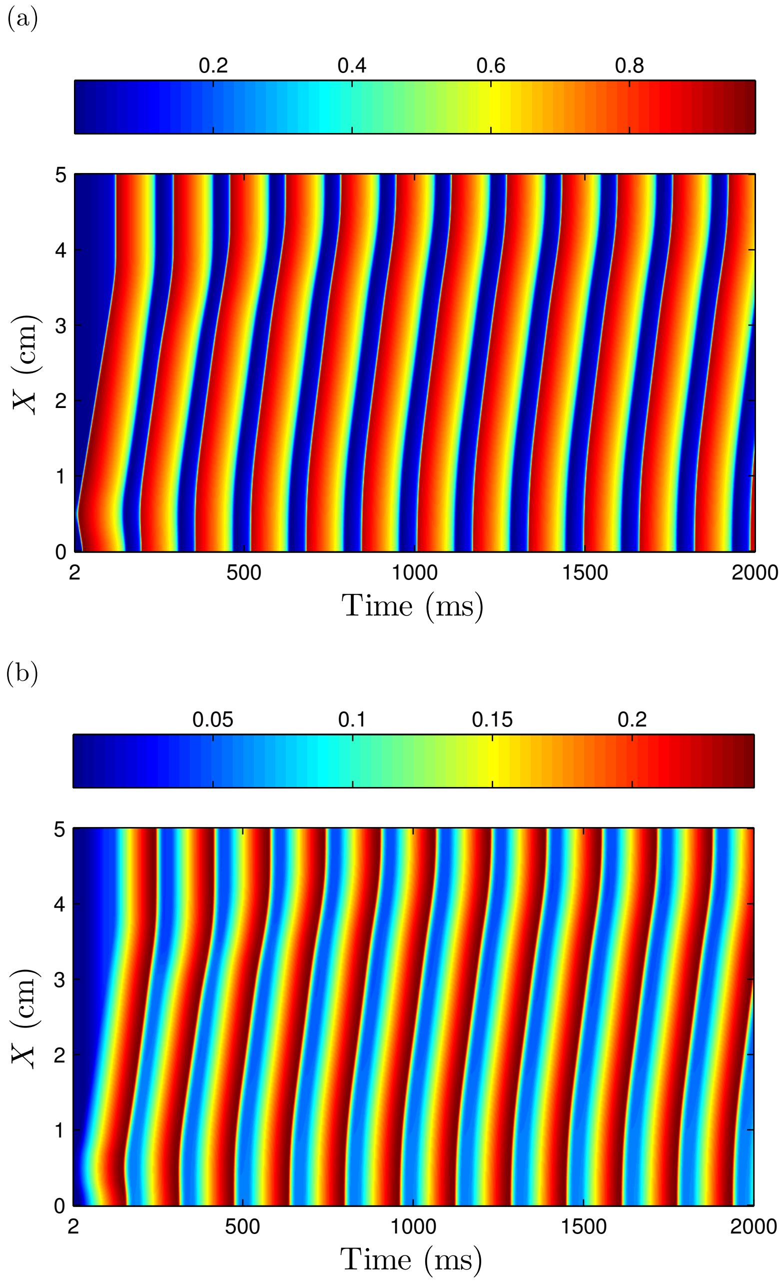

Fig. 5.6 – Time-space plots of the dimensionless membrane potential, $\bar{V}$ (a), and the active tension in $\mathrm{N\,cm^{-2}}$, σ_{active} (b), simulating by the one-dimensional time-dependent TEM model with $g_{\mathrm{sac}} = 0.08\,\mathrm{ms^{-1}}$.

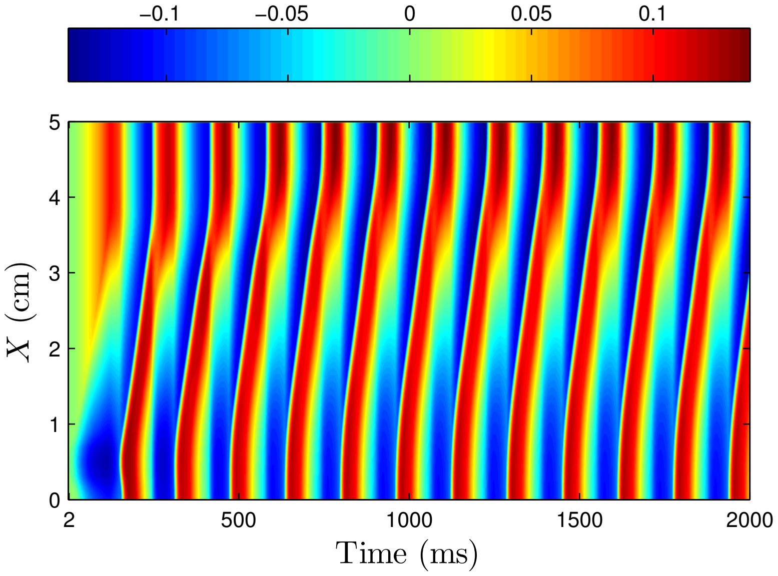

Fig. 5.7 – Time-space plot of the gradient displacement field, $\partial U/\partial X = F - 1$, simulating by the one-dimensional time-dependent TEM model with $g_{\text{sac}} = 0.08\,\text{ms}^{-1}$. Stretched and shortened regions are colored red and blue, respectively.

As shown in Fig. 5.6a, at a specific material point, the AP can be triggered by two different mechanisms:

i. As long as the AP propagates (part of the fiber characterized by a finite *conduction velocity [CV]*), the onset of the local AP occurs in a progressive way. This process is mainly due to diffusive currents. In this part of the fiber, the stretching generates SACs but these are not large enough to trigger an AP by themselves.
ii. On the other hand, the APs induced in the part of the fiber corresponding to a CV $\rightarrow \infty$ on the time-space plot shown in Fig. 5.6a, are generated by SACs. For all the material points of this part of the fiber, the integration of SACs over time results in a sufficient stimulus to exceed the threshold value enabling to trigger an AP. As a result, all the material points of this part of the fiber undergo an AP at once.

The onset of the second AP occurs close to $X = 0.5\,\text{cm}$, which corresponds to the part of the fiber that has undergone first the AP (and thus, the first active tension and shortening). Therefore, this part is also the first one to recover a non-ERS (Fig. 5.6a) and to undergo a decrease of the active tension (Fig. 5.6b).

Due to the slight time delay between the behavior of the active tension and the dimensionless membrane potential, the part of the fiber in question is still in a contracted state while the dimensionless membrane potential has already recovered its resting state for a few milliseconds. After this time delay, the active tension begins to decrease in a sharp way at this spatial location while the other parts of the fiber still undergo a significant active tension. As a consequence, this part of the fiber is locally strongly stretched and SACs are generated in a great amount enabling to trigger a new AP after the integration of these SACs over a few milliseconds.

Obviously, material points which are at some distance from this part of the fiber are also subject to the same mechanism (with a time delay) but the local stretching is less strong in comparison with the one close to $X = 0.5\,\mathrm{cm}$ and thus, SACs are generated in a smaller amount for these material points. The AP that propagates from $X = 0.5\,\mathrm{cm}$ toward $X = 5\,\mathrm{cm}$ reaches these points before the integration of local SACs over time results in a sufficient stimulus enabling to exceed the threshold value leading to an AP.

However, when the AP reaches the region corresponding approximately to the material point $X = 4\,\mathrm{cm}$, the SACs in the part of the fiber from $X = 4\,\mathrm{cm}$ to $X = 5\,\mathrm{cm}$ have been integrated over a sufficient time enabling to generate an AP by themselves. As for the first beat, these material points of the fiber undergo an AP at once. For the next beats, the mechanisms are similar to the ones just explained.

Finally, as already mentioned in this section, the modified GC minimal model is not originally designed to simulate cases involving large deformations. However, as shown in Fig. 5.8, although $\partial U/\partial X$ exceeds $12\,\%$, the time evolutions of the membrane potential and of the displacement gradient field, at a specific material point in the fiber, are very similar for both models. Note that $\partial U/\partial X$ for the modified GC minimal model is computed, *a posteriori*, using Eq. (5.39). These results underline that, from a pragmatic point of view, the modified GC minimal model may be used to simulate cases involving rather large deformations which can be of the order of magnitude as those obtained with the parameter values given in Tab. 5.3, even if Eq. (5.40) (assumption of small deformations) is not strictly satisfied. Due to this observation, assuming one-dimensional deformations, the modified GC minimal model can be considered as suitable for gaining insight into the arrhythmogenic consequences of the MEF.

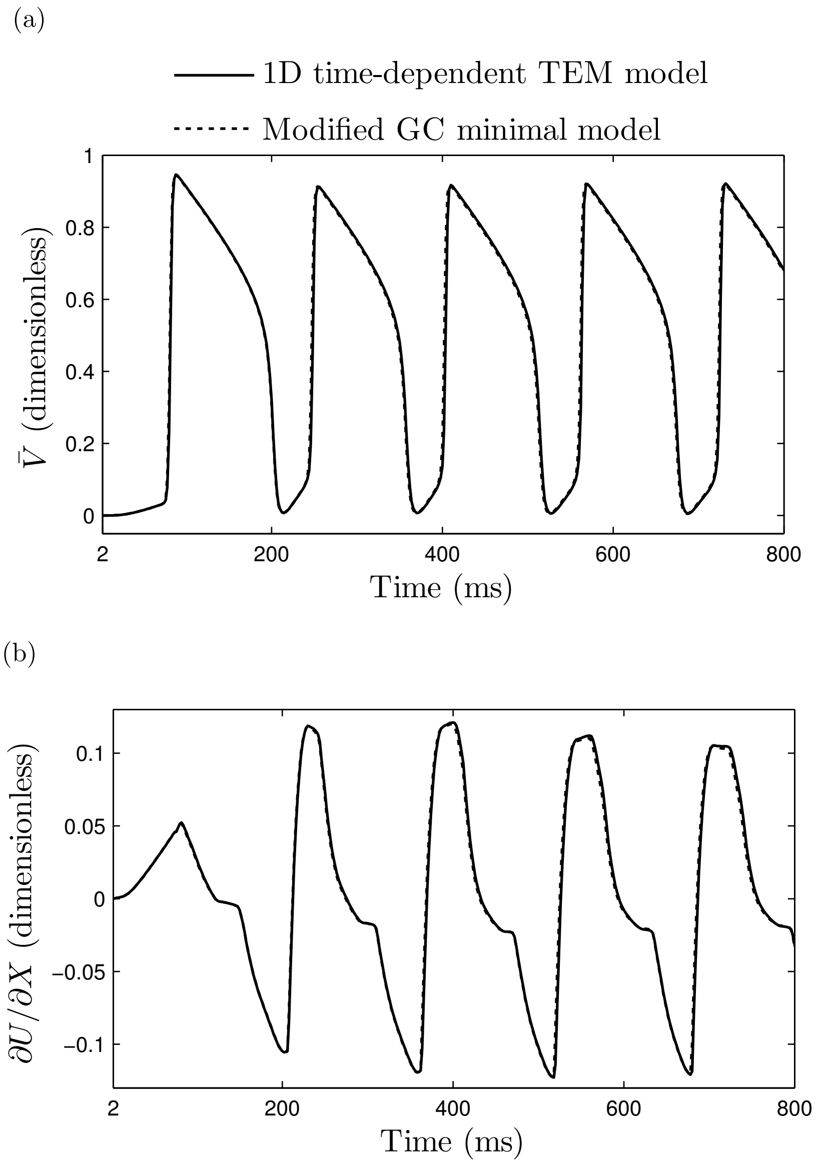

Fig. 5.8 – Time courses of the dimensionless membrane potential, $\bar{V}$ (a), and the displacement gradient field, $\partial U/\partial X$ (b), at $X = 2.5\,\mathrm{cm}$, simulating by the one-dimensional time-dependent TEM model (solid line) and the modified GC minimal model (short dashed line), with parameter values given in Tab. 5.3.

In the following, it will be interesting to characterize this AEA induced by the MEF in a quantitative way. Several questions arise from the first simulations. For instance, without being exhaustive at this point, some interesting questions could be:

i. Does the AEA carry on for a long time or just for a few seconds?
ii. Does the length of the cardiac fiber influence the spatio-temporal behavior of the AEA?
iii. Does the conductance of SACs influence the spatio-temporal properties of the

AEA?

iv. Does the temperature of the cardiac fiber affect the characteristics of the AEA?
v. Does the ICs impact the spatio-temporal behavior of the AEA?
vi. Do the magnitudes of the active tension and deformation remain similar with other ICs?

Before going deeper into the analysis of the model and answering to these questions, the two different methods of temporal integration are compared in the next section.

5.1.7 Comparison of the Euler-forward scheme and the CKRKM for temporal integration

This section aims at underlining the differences between the two methods developed to perform temporal integration. As already mentioned, the Euler-forward scheme is a first-order method while the CKRKM is a fifth-order method. The choice to use one or the other method is primarily controlled by the goals of the study and the constraints associated with it. In the present work, temporal accuracy is of a paramount importance, especially for the *Floquet stability analysis* conducted in section 5.1.12.

To compare the two methods, a simulation of the modified GC minimal model taking into account the physiological MEF ($g_{\text{sac}} = 0.08\,\text{ms}^{-1}$), and with the same parameter values as those given in Tab. 5.3, is performed by using the CKRKM and the Euler-forward scheme.

As shown in Fig. 5.9, 20 s from the beginning of the simulation, the time delay between the two time courses of the dimensionless membrane potentials is not negligible (10 ms and 12 ms in the beginning and the end of the time window shown in Fig. 5.9, respectively). As a consequence, the difference can become significant for a long simulation time. From this point forward, the CKRKM will be used for all simulations.

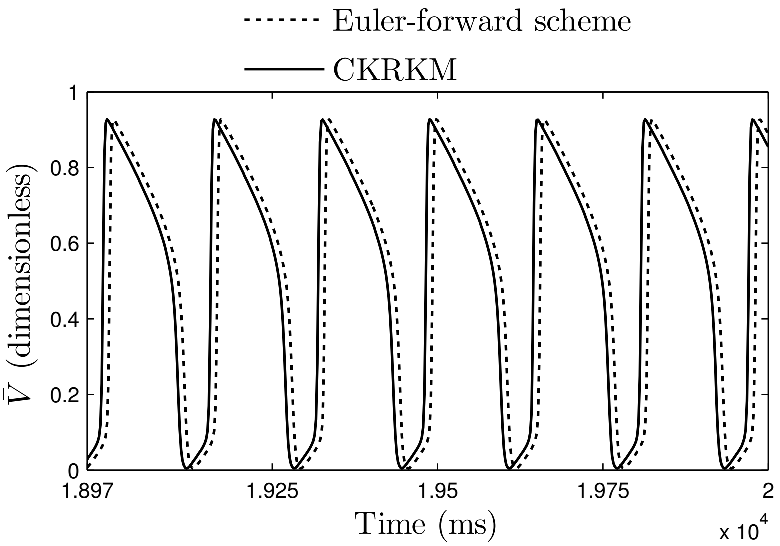

Fig. 5.9 – Time courses at $X = 4\,\text{cm}$, from $18970\,\text{ms}$ to $20000\,\text{ms}$, of the dimensionless membrane potential, $\bar{V}$, integrated over time with the Euler-forward scheme (short dashed line) and the CKRKM (solid line).

5.1.8 Parametric study of the modified GC minimal model

This section aims at identifying the main effects of each parameter of the modified GC minimal model on the one-dimensional physical system for $L = 5\,\text{cm}$ and $T = 37^{\circ}\text{C}$. For this purpose, each parameter value is changed while other parameter values are unchanged from values given in Tab. 5.3, taken as a reference for this parametric study. The role played by the length of the fiber and by the temperature value will be extensively discussed later on.

As shown in Eq. (5.27), $\tilde{g}_{\text{sac}}$ depends on g_{sac}, $\kappa_{\sigma_{\text{active}}}$, and d. These three parameters do not appear explicitly in the modified GC minimal model contrary to κ_v. Thus, the value of $\tilde{g}_{\text{sac}}$ can be modified by changing indifferently the values of g_{sac}, $\kappa_{\sigma_{\text{active}}}$, or d, though each of these parameters plays a particular role in the one-dimensional time-dependent TEM model from which the modified GC minimal model comes from. However, a given variation of one of these three parameters induces a logical effect on $\tilde{g}_{\text{sac}}$, which can be physically interpreted. For example, a decrease in the value of d physically results in an increase of the stiffness of the cardiac fiber. As a consequence, shortening and stretching generated by a given active tension are lower for high values of d than for small values. And thus, the higher the value of d, the lower the SACs, which is reflected by a decrease of the value of $\tilde{g}_{\text{sac}}$ in the modified GC minimal model.

5.1.8.1 Parameter D^0

The higher the value of D^0, the higher the CV of the AP (Fig. 5.10).

(a)

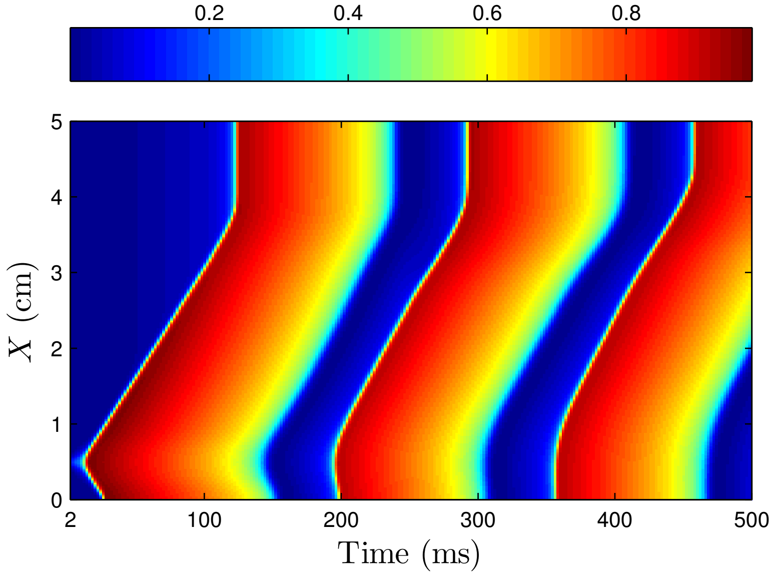

(b)

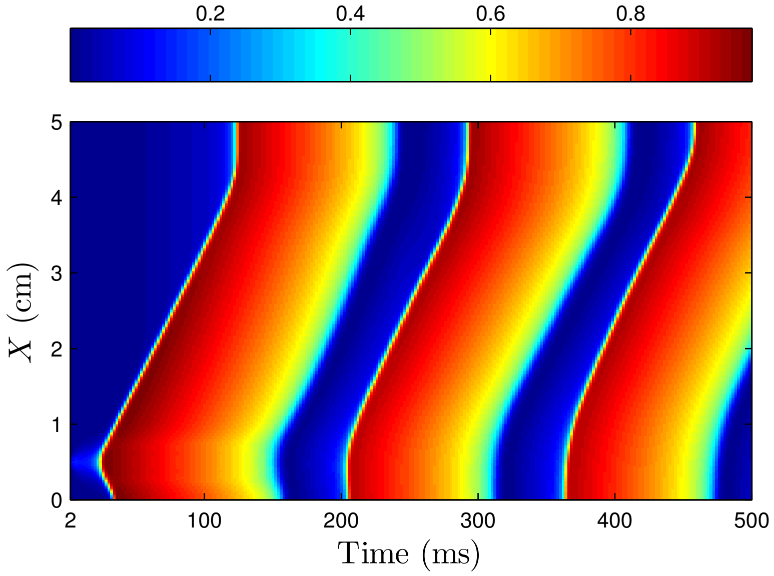

Fig. 5.10 – Time-space plots of the dimensionless membrane potential, $\bar{V}$, for $D = 1\,\mathrm{cm}^2\,\mathrm{s}^{-1}$ (a) and $D = 1.6\,\mathrm{cm}^2\,\mathrm{s}^{-1}$ (b).

In addition, the time period is also altered by a change of the value of D^0: the higher the diffusion coefficient, the higher the time period. This is barely visible in Fig. 5.10 but clearly shown by picking out the values of the time periods. These are equal to approximately 162.8 ms, 163.2 ms, 163.8 ms, and 167.3 ms for $D = 1\,\mathrm{cm}^2\,\mathrm{s}^{-1}$, $D = 1.2\,\mathrm{cm}^2\,\mathrm{s}^{-1}$,

$D = 1.4\,\mathrm{cm^2\,s^{-1}}$, and $D = 1.6\,\mathrm{cm^2\,s^{-1}}$, respectively. Besides, when $D = 1.8\,\mathrm{cm^2\,s^{-1}}$, the propagation of the initial depolarization does not occur and the electrical activity vanishes without even experiencing one AP (Fig. 5.11).

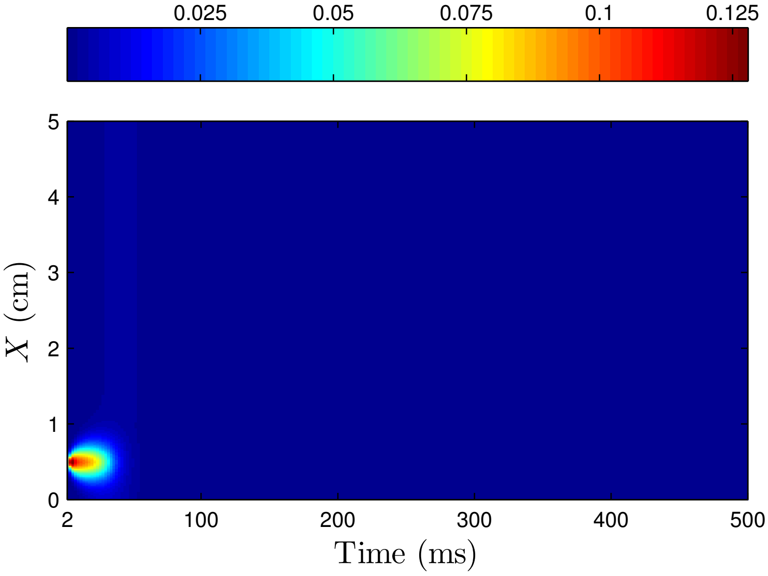

Fig. 5.11 – Time-space plot of the dimensionless membrane potential, $\bar{V}$, for $D = 1.8\,\mathrm{cm^2\,s^{-1}}$.

The increase of the CV of the AP resulting from an increase of the value of D^0 is due to the fact that the stimulus, necessary to trigger the excitation process, is provided earlier at a given site in an non-ERS close to a particular site undergoing an AP as this with a smaller value of D^0. Regarding the propagation block occurring when D^0 is too large (Fig. 5.11), it is due to the fact that the initial stimulus is too quickly diffused to adjacent regions leading to a local decrease of the initial stimulus. Therefore, the membrane potential does not reach the threshold value enabling the onset of an AP and the propagation is blocked.

5.1.8.2 Parameters ε_0 and ε_1

These two parameters appear in the function $\varepsilon\left(\bar{V}\right)$ [Eqs (4.41) and (4.44)]. When ε_0 is changed, the CV of the AP is very slightly altered: the higher the value of ε_0, the higher the CV of the AP (barely visible in Fig. 5.12a). When ε_1 is raised, the CV of the AP decreases (Fig. 5.12b). This variation is more significant as the variation of the CV due to a change of ε_0. From these observations, the CV of the AP is slightly decreased/increased if both ε_0 and ε_1 are increased/decreased at once by a factor two for instance.

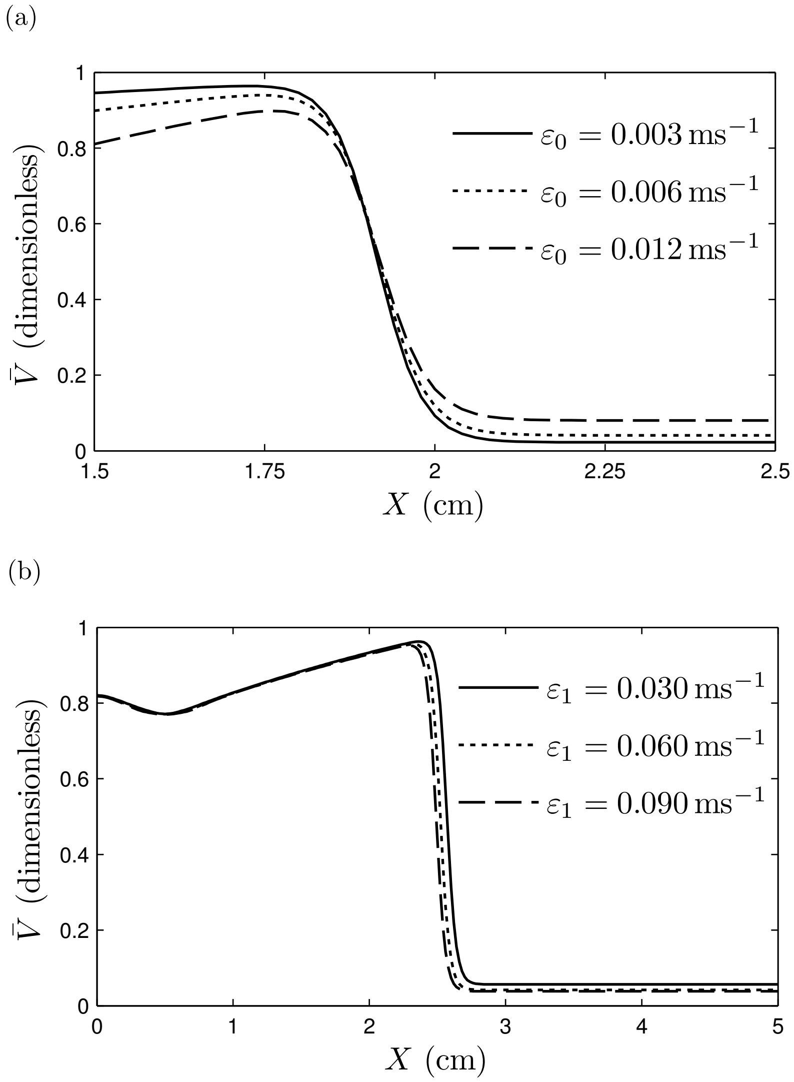

Fig. 5.12 – Spatial distribution in the cardiac fiber of the dimensionless membrane potential, $\bar{V}$, after $80\,\mathrm{ms}$ from the beginning of the simulation, for three different values of ε_0 with $\varepsilon_1 = 0.090\,\mathrm{ms}^{-1}$ (a) and for three different values of ε_1 with $\varepsilon_0 = 0.003\,\mathrm{ms}^{-1}$ (b).

Another important property of the AP, namely the *action potential duration (APD)*, is more significantly altered by a change of the values of ε_0 and ε_1. As shown in Fig. 5.13a, the APD is dramatically decreased when ε_0 is raised. A decrease of the APD resulting from an increase of ε_1 is also observed (Fig. 5.13b) but in a very weak way. As a consequence of these facts, the APD is terribly decreased/increased if both ε_0 and ε_1 are increased/decreased at once by a factor two for instance.

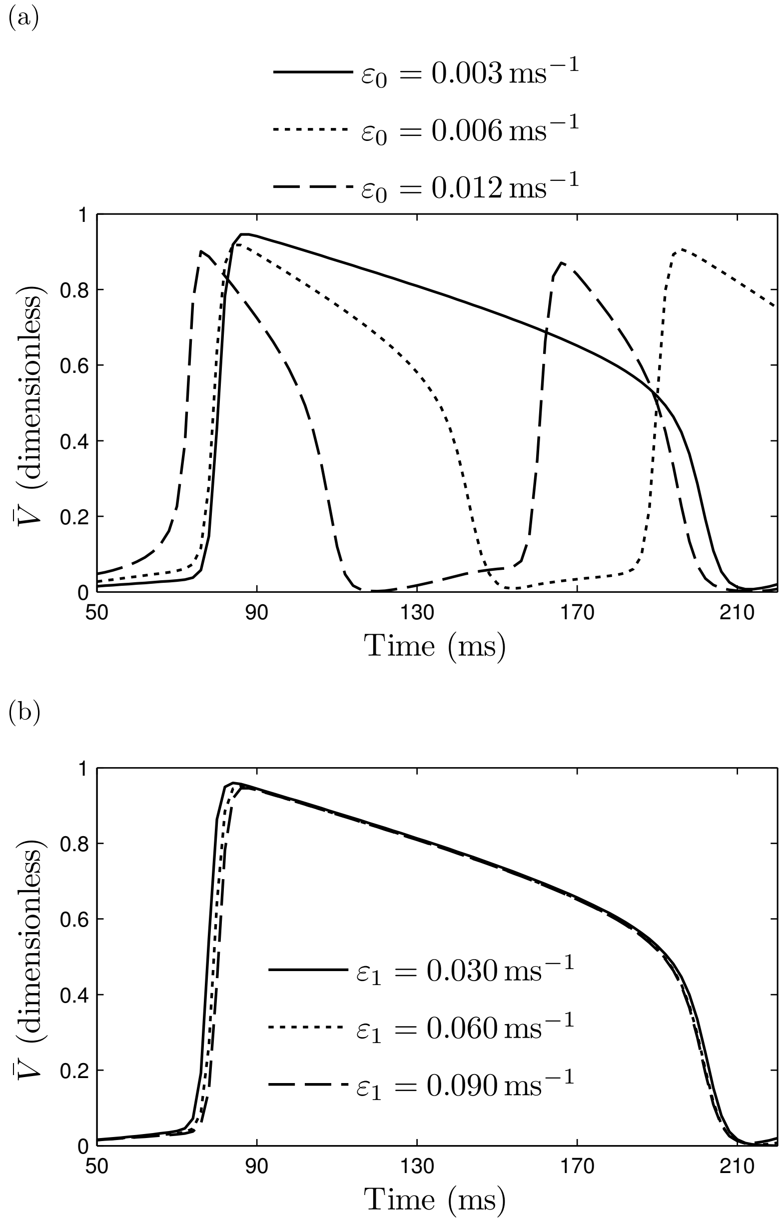

Fig. 5.13 – Time courses at $X = 2.5\,\mathrm{cm}$, from $50\,\mathrm{ms}$ to $220\,\mathrm{ms}$, of the dimensionless membrane potential, $\bar{V}$, for three different values of ε_0 with $\varepsilon_1 = 0.090\,\mathrm{ms}^{-1}$ (a) and three different values of ε_1 with $\varepsilon_0 = 0.003\,\mathrm{ms}^{-1}$ (b).

The lengthening of the APD can be physically explained by the fact that the dynamics of the gate variable, v, which controls the recovery process, is slower when the values of ε_0 and ε_1 are raised.

Thinking ahead, increasing the temperature, T, with respect to a reference temperature, T_0, is equivalent to increase the values of ε_0 and ε_1 by a given factor depending on the value of the function $\varphi(T)$ [Eq. 5.36], which itself depends on $(T - T_0)$. Although a temperature variation also affects ionic conductances *via* the function $\eta(T)$ [Eq. 5.32], similar effects on the dynamics of the system as those observed in Figs 5.12 and 5.13 should occur when the temperature is changed. This is due to the fact that ionic conductances are impacted by a temperature change in a linear way while the gating kinetics of ion channels are altered in an exponential way.

5.1.8.3 Parameter κ_v

As shown in Figs 5.14 and 5.15, the higher the value of κ_v, the higher the CV of the AP. This observation is not easy to interpret physically because κ_v explicitly appears both in Eqs (5.33) and (5.36) and is hidden in $\tilde{g}_{\text{sac}}$ [Eq.(5.27)]. However, each individual effect on the CV of the AP resulting from an increase of the value of κ_v can be examined:

i. In Eq. (5.33), from the one hand, an increase of the value of κ_v induces, at a given site in the fiber, a faster increase of the ionic currents, which are triggered by a perturbation arising from the AP that propagates toward this site. This leads to a faster excitation at this site. This behavior contributes to increase the CV of the AP. On the other hand, the increase of the value of κ_v yields a decrease of the value of $\tilde{g}_{\text{sac}}$ leading to a slower excitation at a given site in the fiber. This effect contributes to decrease the CV of the AP.
ii. In Eq. (5.36), an increase of the value of κ_v is almost similar to a rise in the values of ε_0 and ε_1. Due to the conclusions made in section 5.1.8.2, the increase of the value of κ_v in Eq. (5.36) should thus contribute to decrease the CV of the AP but in a very weak way.

From these three effects, the increase of the ionic currents seems to be the predominant phenomenon since the CV of the AP is increased when the value of κ_v is raised (Figs 5.14 and 5.15).

As shown in Fig. 5.14, by changing the value of κ_v from $2\,\text{ms}^{-1}$ (Fig. 5.14a) to $4\,\text{ms}^{-1}$ (Fig. 5.14b), the AEA does not occur anymore because SACs are not large enough to generate a supra-threshold stimulus enabling the onset of a new AP or the cardiac tissue is in an ERS. The time-space plot for $\kappa_v = 8\,\text{ms}^{-1}$ is similar to the one shown in Fig. 5.14b inasmuch as no AEA is induced by the initial excitation that propagates (from $X = 0.5\,\text{cm}$ toward the boundaries of the fiber) with a higher CV than for

$\kappa_v = 4\,\mathrm{ms}^{-1}$. On the other hand, for $\kappa_v = 1\,\mathrm{ms}^{-1}$, the membrane potential directly recovers its resting state without experiencing an AP.

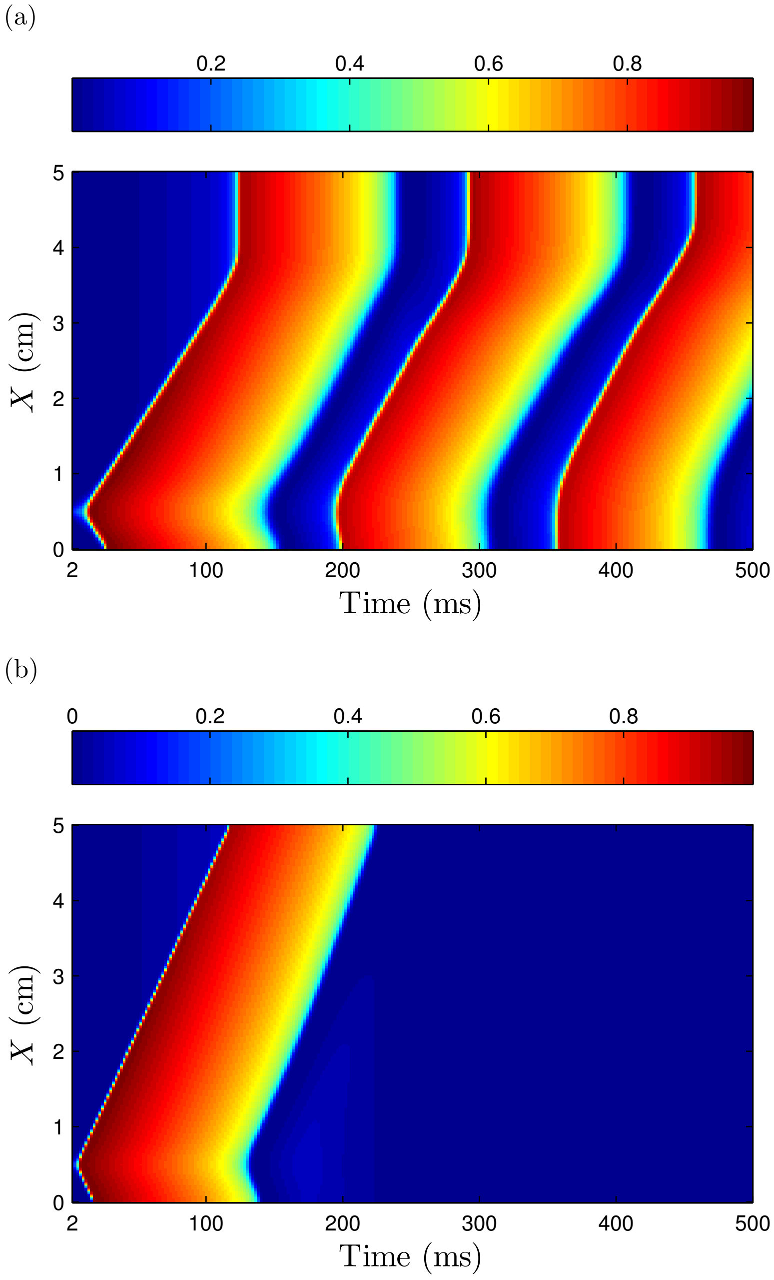

Fig. 5.14 – Time-space plots of the dimensionless membrane potential, $\bar{V}$, for $\kappa_v = 2\,\mathrm{ms}^{-1}$ (a) and $\kappa_v = 4\,\mathrm{ms}^{-1}$ (b).

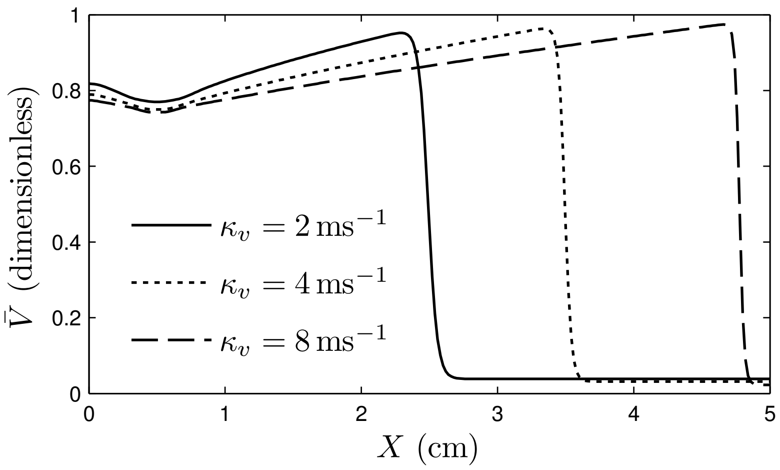

Fig. 5.15 – Spatial distribution in the cardiac fiber of the dimensionless membrane potential, $\bar{V}$, after $80\,\mathrm{ms}$ from the beginning of the simulation, for three different values of κ_v.

5.1.8.4 Parameter a

As shown in Fig. 5.16, the higher the value of a, the smaller the CV of the AP. Thus, the effect on the CV of the AP resulting from an increase of the value of a is opposite to this arising from an increase of the value of κ_v. Physically, increasing the value of a leads to a cardiac tissue that is less excitable. As a result, the excitation process at a given site in the fiber is slower and the CV of the AP is then decreased.

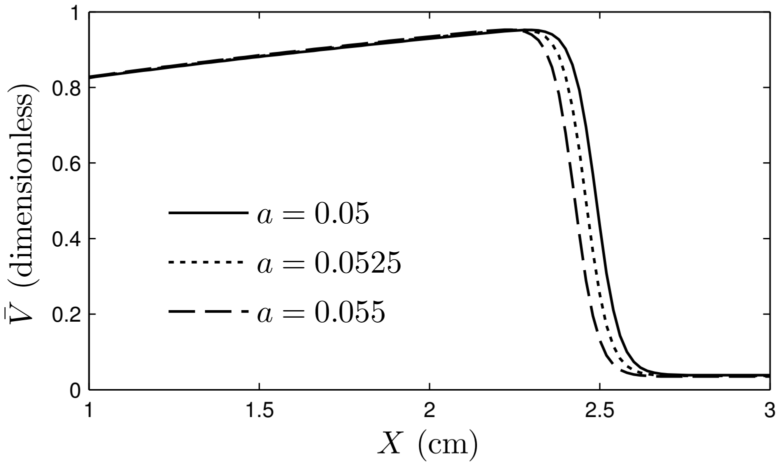

Fig. 5.16 – Spatial distribution in the cardiac fiber of the dimensionless membrane potential, $\bar{V}$, after $80\,\mathrm{ms}$ from the beginning of the simulation for three different values of a.

Before going deeper into the analysis of the role played by parameter a, some concepts must be introduced. First, when an AEA is induced by the MEF and lasts indefinitely, it is referred to as a *perpetual AEA*. In the case when the AEA occurs only for a finite time interval, it is referred to as a *finite AEA*. Due to computational cost reasons, it is important to underline that a criterion must be chosen to determine whether the AEA is perpetual or not. For this parametric study, the AEA is considered as perpetual if it persists after a time interval larger than 20 s. Otherwise, the AEA is not considered as perpetual. Second, in the case when a perpetual AEA occurs, the *penultimate* and *last* wavefronts will correspond in the entire section 5.1.8 to the penultimate and last wavefronts inside the 20 s time window. In the case when a finite AEA is observed, the penultimate and last wavefronts denote the penultimate and last wavefronts inside the time window for which the AEA occurs, namely just before the vanishing of the AEA.

With the set of parameter values given in Tab. 5.3, perpetual AEAs occur only for specific values of a (Fig. 5.17): a small region between boundaries 1 and 2 and a large region between boundaries 3 and 5. Note that:

i. a-boundary 1 is located at approximately[2] 0.047;
ii. a-boundary 2 is located at approximately $a = 0.047\,812\,5$;
iii. a-boundary 3 is located at approximately $a = 0.048\,062\,5$;
iv. a-boundary 4 is located at approximately $a = 0.0605$;
v. a-boundary 5 is located at approximately $a = 0.0615$.

For values of a smaller than approximately 0.0475 (on the left side of boundary 1, shown in Fig. 5.17) and for values of a larger than approximately 0.061 (on the right side of boundary 5, shown in Fig. 5.17), the AEAs are not indefinitely sustained (the AEAs vanish before 20 s).

To obtain a first information about the spatio-temporal behavior of the AEAs as functions of parameter a, the spatial average over all the material points of the fiber, $\bar{T}_\text{l}$, of the local time interval (namely at a specific material point, X_m, of the fiber) between the penultimate and last wavefronts, referred to as $T_\text{l}(X_m)$, is examined at the end of the simulations to avoid transitory solutions. The same physical quantities, referred to as $\bar{T}_\text{p}$ and $T_\text{p}(X_m)$, are noted between the antipenultimate and penultimate wavefronts. In addition, looking at the *spatial variances* of $T_\text{l}(X_m)$ and $T_\text{p}(X_m)$, referred to as $\sigma^2_\text{s,l}$ and $\sigma^2_\text{s,p}$, respectively, enables to get some information about the spatial dispersion of

---

[2] The term 'approximately' is used because the location of this boundary is not exactly known due to the a-step used to discretize a.

$T_\mathrm{l}\left(X_m\right)$ and $T_\mathrm{p}\left(X_m\right)$. Due to the chosen spatial discretization given by Eq. (5.46), $\sigma^2_\mathrm{s,l}$ and $\sigma^2_\mathrm{s,p}$ are given by

$$\begin{aligned}\sigma^2_\mathrm{s,l} &= \frac{1}{M+1}\sum_{m=0}^{M}\left[T_\mathrm{l}\left(X_m\right)\right]^2 - \bar{T}_\mathrm{l}^2\,, &(5.73)\\ \sigma^2_\mathrm{s,p} &= \frac{1}{M+1}\sum_{m=0}^{M}\left[T_\mathrm{p}\left(X_m\right)\right]^2 - \bar{T}_\mathrm{p}^2\,. &(5.74)\end{aligned}$$

The inspection of the *temporal variance* of $\bar{T}_\mathrm{l}$ and $\bar{T}_\mathrm{p}$, referred to as σ^2_t, enables to get some information about the temporal variation between $\bar{T}_\mathrm{l}$ and $\bar{T}_\mathrm{p}$. This variance is given by

$$\begin{aligned}\sigma^2_\mathrm{t} &= \frac{1}{2}\left(\bar{T}_\mathrm{l}^2 + \bar{T}_\mathrm{p}^2\right) - \left[\frac{1}{2}\left(\bar{T}_\mathrm{l} + \bar{T}_\mathrm{p}\right)\right]^2\\ &= \frac{1}{4}\left(\bar{T}_\mathrm{l} - \bar{T}_\mathrm{p}\right)^2. &(5.75)\end{aligned}$$

Combining Eqs (5.73)-(5.75), a *spatio-temporal variance* can be defined as

$$\sigma^2 = \sigma^2_\mathrm{s,l} + \sigma^2_\mathrm{s,p} + \sigma^2_\mathrm{t}\,. \tag{5.76}$$

The corresponding *standard deviation* is then given by

$$\sigma = \sqrt{\sigma^2_\mathrm{s,l} + \sigma^2_\mathrm{s,p} + \sigma^2_\mathrm{t}}\,. \tag{5.77}$$

The simultaneous examination of $\bar{T}_\mathrm{p}$, $\bar{T}_\mathrm{l}$, and σ, shown in Fig. 5.17, as functions of parameter a, enables to underline that the lack of perpetual AEAs (denoted by symbol '×' in Fig. 5.17) seems to be associated with two different mechanisms depending on the considered a-region:

i. For values of a smaller than approximately 0.0475 (on the left side of boundary 1) and larger than approximately 0.061 (on the right side of boundary 5), the lack of perpetual AEAs is characterized by two significantly different values of $\bar{T}_\mathrm{l}$ and $\bar{T}_\mathrm{p}$ and a large value of σ. For these two a-regions, σ_t/σ is close to one or, equivalently, $\sigma_\mathrm{s}/\sigma = \left(\sqrt{\sigma^2_\mathrm{s,l} + \sigma^2_\mathrm{s,p}}\right)/\sigma$ is close to zero. Thus, this information seems to reveal that the AEA essentially ends due to a *temporal* mechanism.

ii. For the small a-window between boundaries 2 and 3, close to 0.048 125, the lack of perpetual AEAs is characterized by two slightly different values of $\bar{T}_\mathrm{l}$ and $\bar{T}_\mathrm{p}$ and a large value of σ. For this a-region, σ_s/σ is close to one. Thus, this feature seems to reveal that the AEA mainly ends due to a *spatial* mechanism.

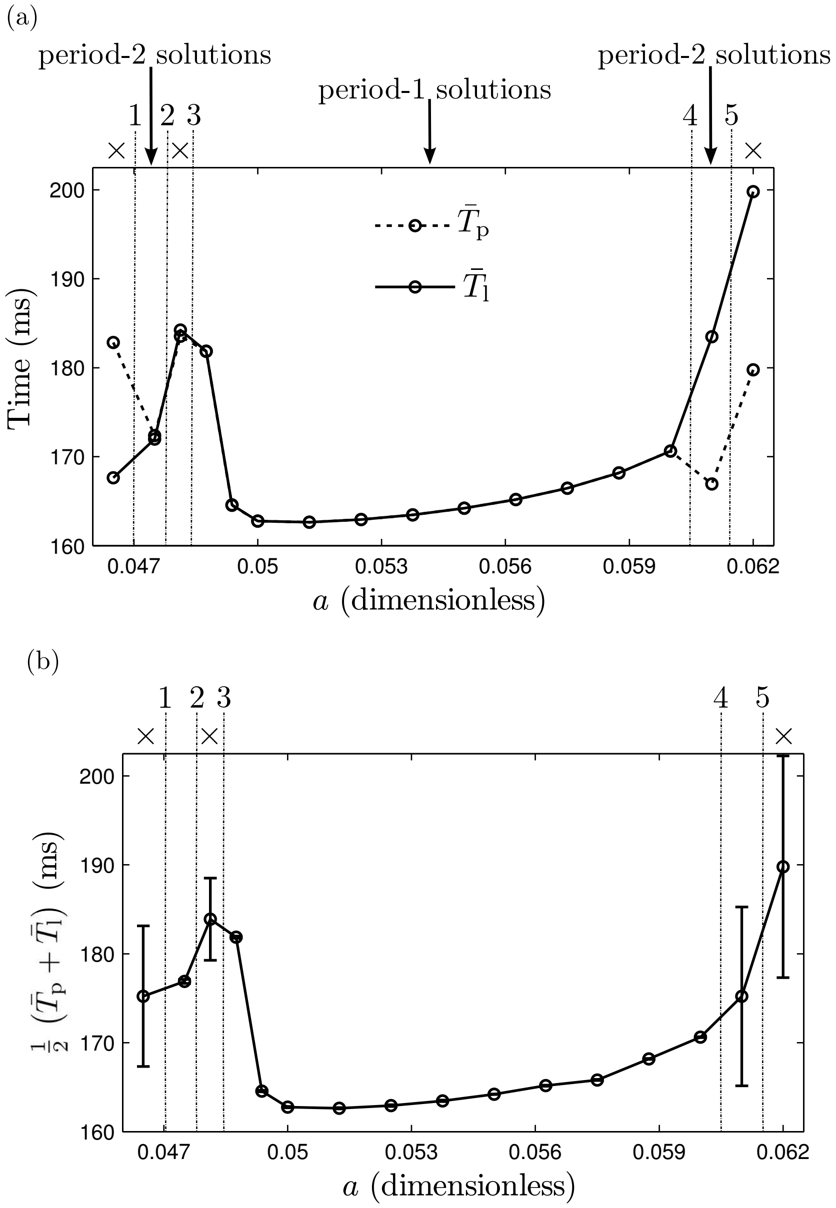

Fig. 5.17 – Spatial averages of the local time interval between the antipenultimate and penultimate wavefronts, $\bar{T}_\mathrm{p}$, and the penultimate and last wavefronts, $\bar{T}_\mathrm{l}$, as a function of a (a). Average (over time) of $\bar{T}_\mathrm{p}$ and $\bar{T}_\mathrm{l}$ with error bars in terms of the standard deviation σ (b). Symbol '×' denotes an a-region for which there are finite AEAs or no AEAs. Other regions correspond to different kinds of periodic AEAs. Vertical lines and corresponding labels 1 to 5 define boundaries which are discussed in the text.

For values of a leading to a perpetual AEA, three different cases, corresponding to three different a-regions, are clearly distinguishable as shown in Fig. 5.17:

i. The a-region between boundaries 3 and 4, ranging from approximately 0.048 75 to 0.06, is characterized by $\bar{T}_\mathrm{l} = \bar{T}_\mathrm{p}$ (Fig. 5.17a) and a very tiny spatial standard deviation[3] (Fig. 5.17b), which corresponds to *periodic* AEAs. These periodic AEAs are described by different solutions with period-1 cycles. Two time-space plots for two different values of a for which the AEA is characterized by a period-1 solution are shown in Fig. 5.18.

(a)

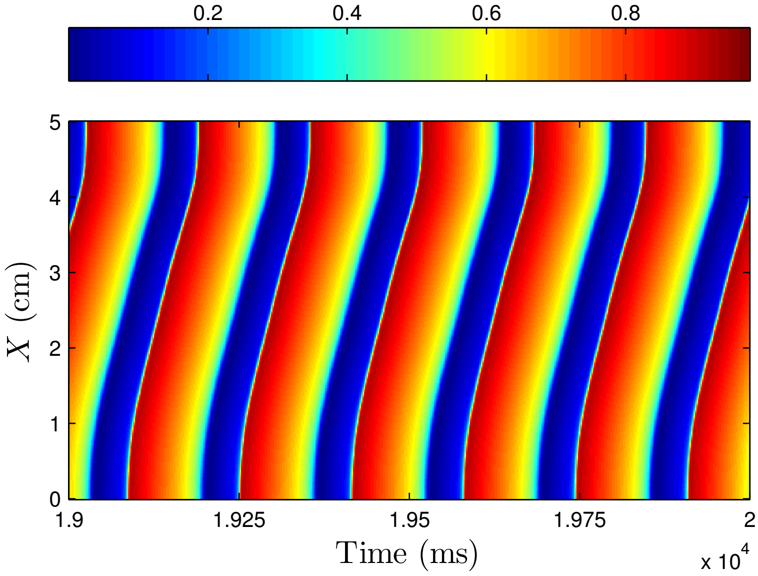

(b)

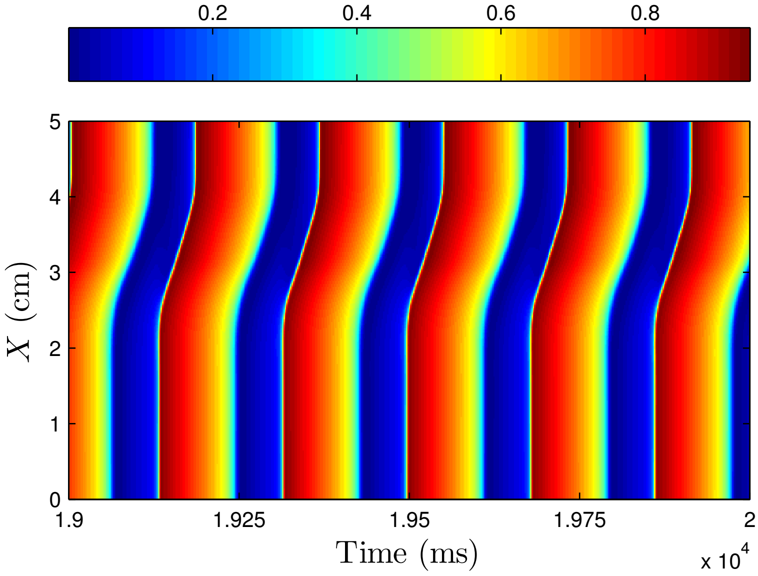

Fig. 5.18 – Time-space plots of the dimensionless membrane potential, $\bar{V}$, for $a = 0.055$ (a) and $a = 0.048\,75$ (b).

---

[3] Theoretically, this spatial standard deviation should be zero.

ii. The a-region between boundaries 1 and 2, close to 0.0475, corresponds to period-2 solutions, which are characterized by two slightly different values of $\bar{T}_\mathrm{l}$ and $\bar{T}_\mathrm{p}$ (Fig. 5.17a) and a small spatio-temporal standard deviation (Fig. 5.17b). In particular[4], $\bar{T}_\mathrm{l} = 171\,\mathrm{ms}$, $\bar{T}_\mathrm{p} = 172.3\,\mathrm{ms}$, and $\sigma = 0.22\,\mathrm{ms}$ for $a = 0.0475$. Given that $\sigma_\mathrm{t} = 0.20\,\mathrm{ms}$ and $\sigma_\mathrm{t}/\sigma = 0.90$, the main contribution to the spatio-temporal standard deviation is generated by a temporal phenomenon. This seems to correspond to *quasi-spatially synchronized alternans*[5]. A typical time-space plot of this behavior is shown in Fig. 5.19 (note that the phenomenon of alternans is not easily seen in Fig. 5.19 since the two period are very close to each other).

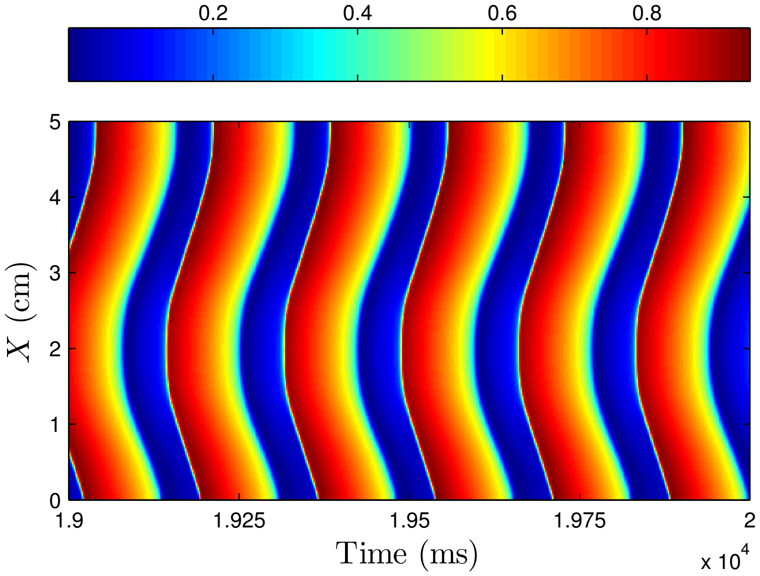

Fig. 5.19 – Time-space plot of the dimensionless membrane potential, $\bar{V}$, for $a = 0.0475$.

iii. The a-region between boundaries 4 and 5, close to 0.061, corresponds to period-2 solutions, which are characterized by two significant different values of $\bar{T}_\mathrm{l}$ and $\bar{T}_\mathrm{p}$ (Fig. 5.17a) and a large spatio-temporal standard deviation (Fig. 5.17b). In particular, $\bar{T}_\mathrm{l} = 183.5\,\mathrm{ms}$, $\bar{T}_\mathrm{p} = 166.9\,\mathrm{ms}$, and $\sigma = 10.05\,\mathrm{ms}$ for $a = 0.061$. Given that $\sigma_\mathrm{t} = 8.29\,\mathrm{ms}$ and $\sigma_\mathrm{t}/\sigma = 0.82$, the main contribution to the spatio-temporal standard deviation is still induced by a temporal phenomenon, namely the alternans. However, these alternans are less spatially synchronized than those described in the previous item. A Typical time-space plot of this phenomenon is

---

[4] In the whole of this work, the values of $\bar{T}_\mathrm{p}$ and $\bar{T}_\mathrm{l}$ are displayed with one significant decimal while the values of σ with two significant decimals.

[5] Cardiac alternans rhythms are characterized by an alternation of the timing or morphology of the electrical activity in cardiac tissue from one beat to the next [108].

shown in Fig. 5.20.

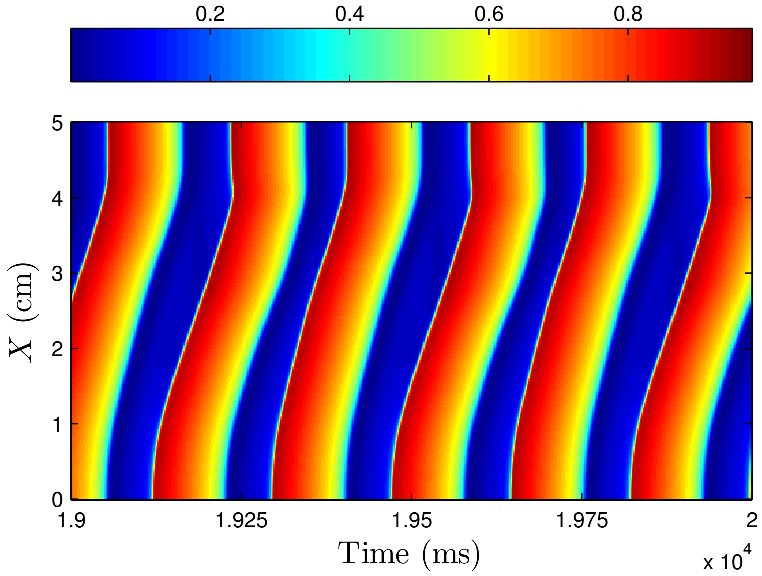

Fig. 5.20 – Time-space plots of the dimensionless membrane potential, $\bar{V}$, for $a = 0.061$.

The inspection of the time-space plot of the dimensionless membrane potential for $a = 0.048\,125$ (Fig. 5.21), namely in the region between boundaries 2 and 3 for which there are no perpetual AEAs, reveals that the end of the AEA corresponds to an abrupt change in the spatio-temporal pattern as expected due to the large value of the spatio-temporal standard deviation for this value of a (Fig. 5.17b).

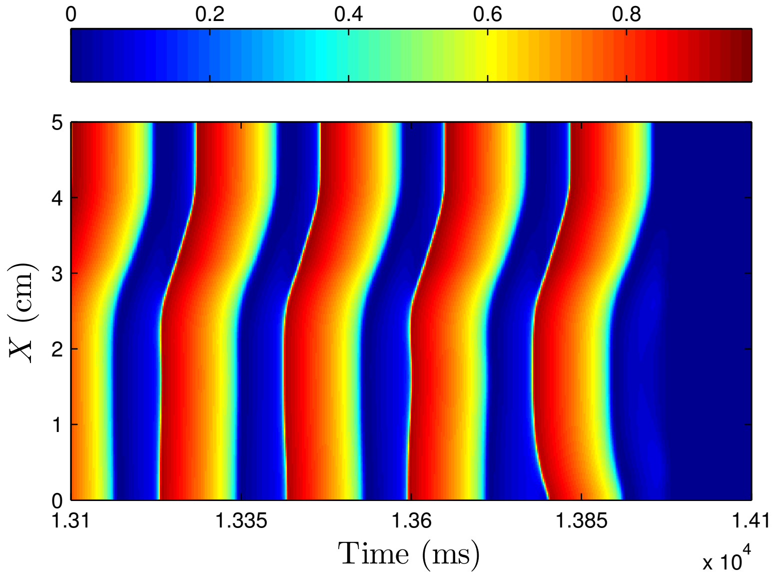

Fig. 5.21 – Time-space plots of the dimensionless membrane potential, $\bar{V}$, for $a = 0.048\,125$.

It is interesting to note that the spatio-temporal patterns before this abrupt change are similar to those for $a = 0.048\,75$ (Fig. 5.18b) while the spatio-temporal distribution of the last wavefront, after this abrupt change, looks like the spatio-temporal patterns observed for $a = 0.0475$ (Fig. 5.19).

From these results, different interesting phenomena can be emphasized:

i. Perpetual AEAs occur only for particular values of a.
ii. The spatial average of the time period significantly changes when the value of a is modified.
iii. The excitatory source seems to be attracted to a specific location in the fiber depending on the value of a.
iv. The spatial width of the excitatory source changes as a function of a.
v. Two different kinds of periodic solutions, namely period-1 solutions and period-2 solutions, are observed for different values of a.
vi. For the a-regions where there are no perpetual AEAs, the end of the AEA seems to be induced by two different kinds of mechanisms.

5.1.8.5 Parameter $\tilde{g}_{\text{sac}}$

This section aims at emphasizing the role played by $\tilde{g}_{\text{sac}}$ in the modified GC minimal model. As already mentioned, there are three possibilities to change the value of $\tilde{g}_{\text{sac}}$ while κ_v is held fixed [Eq. (5.27)] at the value given in Tab. 5.3:

i. change the value of g_{sac}
ii. change the value of $\kappa_{\sigma_{\text{active}}}$
iii. change the value of d

Here, the value of $\tilde{g}_{\text{sac}}$ is changed by modifying the value of g_{sac} around the reference value given in Tab. 5.3 ($g_{\text{sac}} = 0.08\,\text{ms}^{-1}$ corresponds to $\tilde{g}_{\text{sac}} = 0.05$ for parameter values in Tab. 5.3). The choice to change g_{sac} in place of $\kappa_{\sigma_{\text{active}}}$ or d is completely arbitrary.

As shown in Fig. 5.22, the higher the value of g_{sac}, the higher the CV of the propagating AP. This feature can be explained in the following way. When SACs occur in a particular site in the fiber, they generate a depolarization whose the magnitude is proportional to the magnitude of these SACs, which is also proportional to the value of g_{sac}. Therefore, the higher the value of g_{sac}, the weaker the required contribution from an external stimulus to reach the threshold membrane potential. In other words, the larger the SACs, the easier the tissue is excited. This behavior explains the increase of the CV of the propagating AP when the value of g_{sac} is raised.

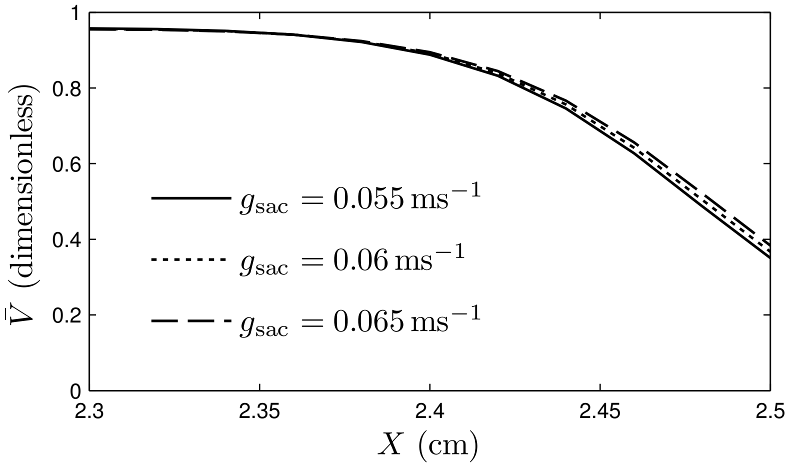

Fig. 5.22 – **Spatial distribution in the cardiac fiber of the dimensionless membrane potential, $\bar{V}$, after $80\,\mathrm{ms}$ from the beginning of the simulation, for three different values of g_{sac}.**

As shown in Fig. 5.23, perpetual AEAs occur only for specific values of g_{sac}: a large region between boundaries 1 and 4, a small region between boundaries 5 and 6, and a small region between boundaries 7 and 8. Note that:

i. g_{sac}-boundary 1 is located at approximately[6] $0.044\,25\,\mathrm{ms}^{-1}$;
ii. g_{sac}-boundary 2 is located at approximately $0.046\,625\,\mathrm{ms}^{-1}$;
iii. g_{sac}-boundary 3 is located at approximately $0.048\,15\,\mathrm{ms}^{-1}$;
iv. g_{sac}-boundary 4 is located at approximately $0.084\,25\,\mathrm{ms}^{-1}$;
v. g_{sac}-boundary 5 is located at approximately $0.086\,325\,\mathrm{ms}^{-1}$;
vi. g_{sac}-boundary 6 is located at approximately $0.086\,375\,\mathrm{ms}^{-1}$;
vii. g_{sac}-boundary 7 is located at approximately $0.086\,925\,\mathrm{ms}^{-1}$;
viii. g_{sac}-boundary 8 is located at approximately $0.086\,975\,\mathrm{ms}^{-1}$.

---

[6] The term 'approximately' is used because the location of this boundary is not exactly known due to the g_{sac}-step used to discretize g_{sac}.

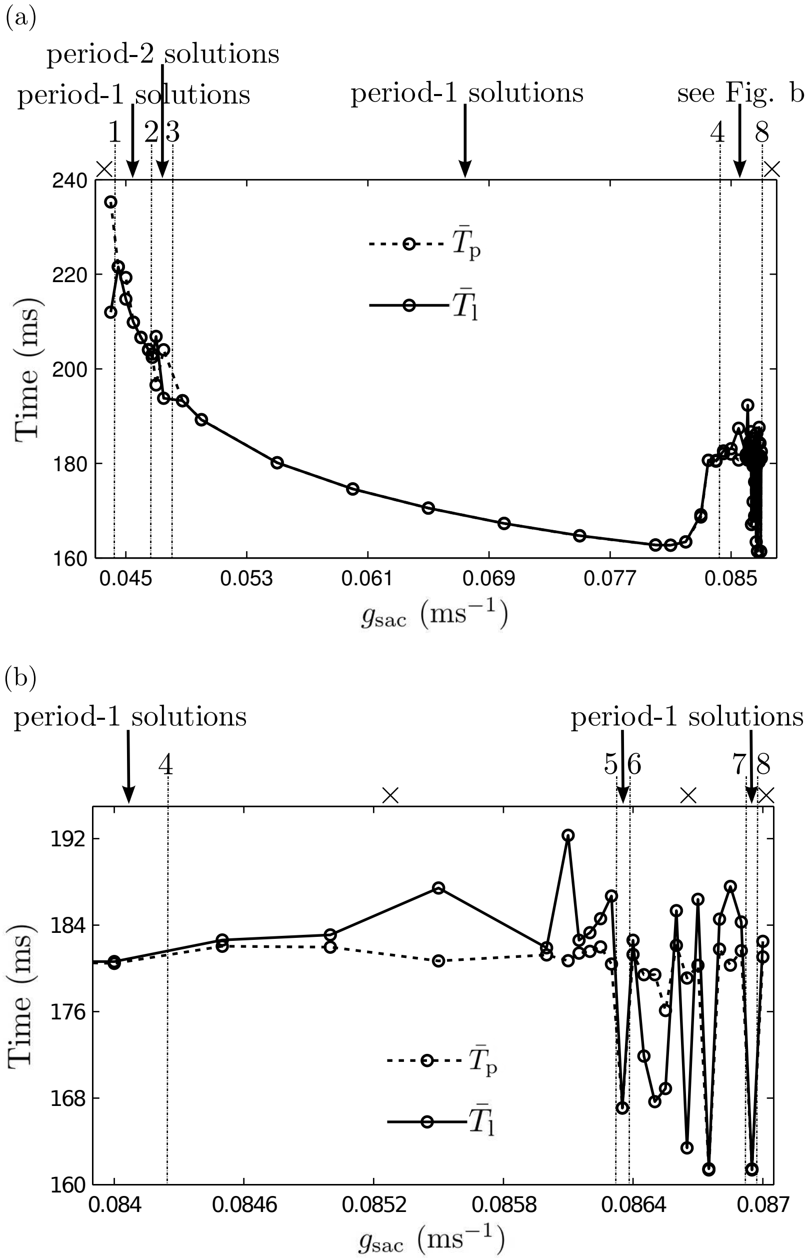

Fig. 5.23 – Spatial averages of the local time interval between the antipenultimate and penultimate wavefronts, $\bar{T}_{\rm p}$, and the penultimate and last wavefronts, $\bar{T}_{\rm l}$, as a function of $g_{\rm sac}$. General behavior (a) and local behavior for large values of $g_{\rm sac}$ (b). Symbol '×' denotes a $g_{\rm sac}$-region for which there are finite AEAs or no AEAs. Other regions correspond to different kinds of periodic AEAs. Vertical lines and corresponding labels 1 to 5 define boundaries which are discussed in the text.

For the following values of $g_{\rm sac}$, there are no perpetual AEAs (the AEAs vanish before 20 s):

i. values smaller than approximately 0.0445 ms^{-1} (on the left side of boundary 1);
ii. values ranging from approximately 0.084 ms^{-1} to 0.0863 ms^{-1} (between bound-

aries 4 and 5);

iii. values ranging from approximately $0.086\,35\,\mathrm{ms^{-1}}$ to $0.0869\,\mathrm{ms^{-1}}$ (between boundaries 6 and 7);

iv. values larger than approximately $0.086\,95\,\mathrm{ms^{-1}}$ (on the right side of boundary 8).

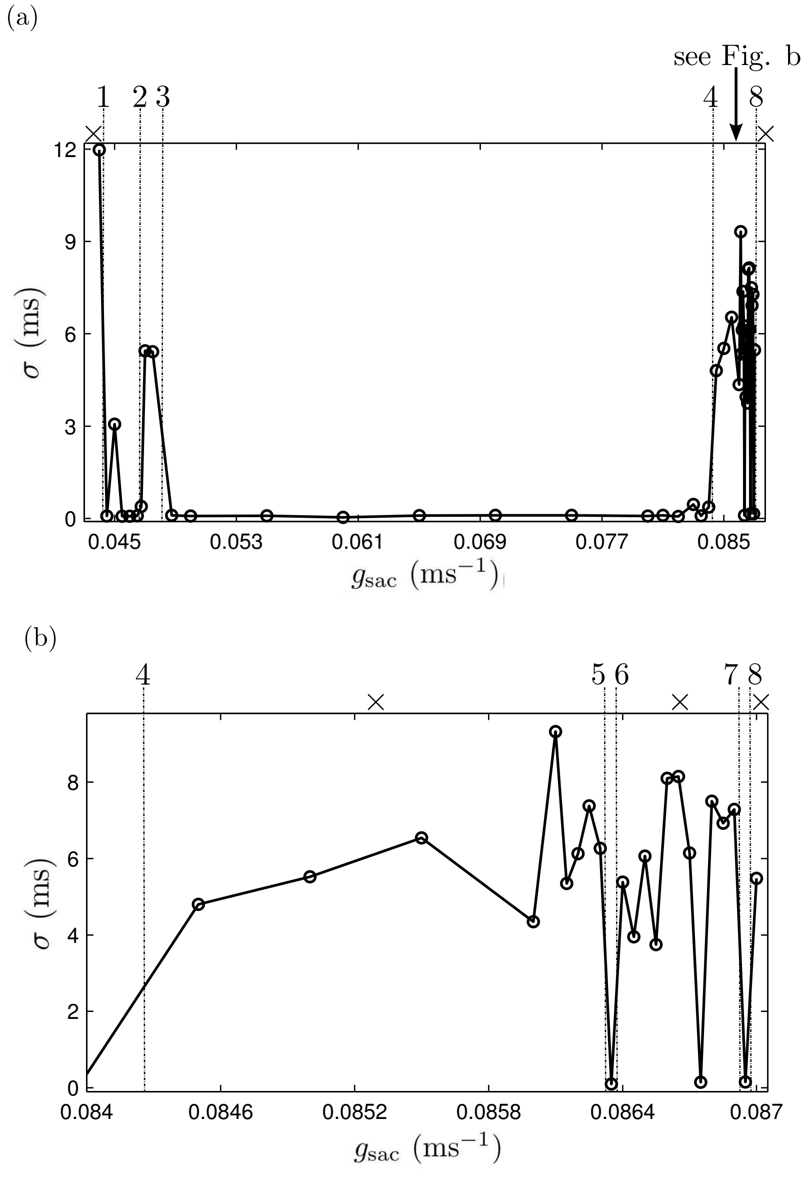

Fig. 5.24 – General behavior of the spatio-temporal standard deviation, σ, as a function of g_{sac} (a) and local behavior of σ for large values of g_{sac} (b). Symbol '×' denotes a g_{sac}-region for which there are finite AEAs or no AEAs. Other regions correspond to different kinds of periodic AEAs.

The simultaneous inspection of $\bar{T}_{\mathrm{p}}$, $\bar{T}_{\mathrm{l}}$, and σ, shown in Figs 5.23 and 5.24, as functions of parameter g_{sac}, enables to emphasize that the lack of perpetual AEAs (denoted by symbol '×' in Figs 5.23 and 5.24) seems to be characterized by three different mechanisms depending on the considered g_{sac}-region:

i. For values of g_{sac} smaller than approximately $0.0445\,\mathrm{ms}^{-1}$ (on the left side of boundary 1), the lack of perpetual AEAs is characterized by two significantly different values of $\bar{T}_{\mathrm{l}}$ (211 ms) and $\bar{T}_{\mathrm{p}}$ (235.3 ms) and a large value of σ (11.98 ms). In addition, the ratio $\sigma_{\mathrm{t}}/\sigma$ is close to one meaning that the AEA mainly ends due to a temporal mechanism.

ii. For values of g_{sac} larger than approximately $0.084\,\mathrm{ms}^{-1}$ (on the right side of boundary 4), for values of g_{sac} larger than approximately $0.086\,35\,\mathrm{ms}^{-1}$ (on the right side of boundary 6), for values smaller than approximately $0.086\,95\,\mathrm{ms}^{-1}$ (on the left side of boundary 7), and for values of g_{sac} larger than approximately $0.086\,95\,\mathrm{ms}^{-1}$ (on the right side of boundary 8), the lack of perpetual AEAs is characterized by two slightly different values of $\bar{T}_{\mathrm{l}}$ (182.6 ms, 182.6 ms, 184.3 ms, and 182.5 ms, respectively) and $\bar{T}_{\mathrm{p}}$ (182.1 ms, 181.3 ms, 181.7 ms, and 181.1 ms, respectively) and a large value of σ (4.80 ms, 5.38 ms, 7.29 ms, and 5.48 ms, respectively). In these four cases, the ratio $\sigma_{\mathrm{s}}/\sigma$ is close to one. Thus, the AEA seems to essentially vanish due to a spatial mechanism.

iii. For values of g_{sac} smaller than approximately $0.08635\,\mathrm{ms}^{-1}$ (on the left side of boundary 5), the lack of perpetual AEAs is characterized by two different values of $\bar{T}_{\mathrm{l}}$ (186.7 ms) and $\bar{T}_{\mathrm{p}}$ (180.4 ms) and a large value of σ (6.26 ms). In this case, the ratio $\sigma_{\mathrm{t}}/\sigma$ is close to 1/2. Therefore, it seems that the AEA mainly vanishes due to a *spatio-temporal* mechanism.

For values of g_{sac} leading to a perpetual AEA, different kinds of solution, corresponding to different g_{sac}-regions, can be highlighted as shown in Figs 5.23 and 5.24:

i. The g_{sac}-region between boundaries 1 and 2, ranging from approximately 0.0445 ms^{-1} to $0.0465\,\mathrm{ms}^{-1}$, is mainly characterized by $\bar{T}_{\mathrm{l}} = \bar{T}_{\mathrm{p}}$ and σ close to zero. The time-space plot of the dimensionless membrane potential for $g_{\mathrm{sac}} = 0.0445\,\mathrm{ms}^{-1}$, shown in Fig. 5.25, enables to observe the period-1 phenomenon. However, by scanning this region, a point ($g_{\mathrm{sac}} = 0.045\,\mathrm{ms}^{-1}$) leading to a different behavior has been observed. This point seems to be associated with a non-periodic solution as depicted in Fig. 5.26 and a quite large value of σ, namely $\sigma = 3.06\,\mathrm{ms}$ (Fig. 5.24a). The corresponding time-space plot of the dimensionless membrane potential is shown in Fig. 5.26. Note that no satisfactory explanation has been found to interpret this singular behavior.

ii. The g_{sac}-region between boundaries 2 and 3, ranging from approximately 0.046 75 ms^{-1} to $0.0475\,\mathrm{ms}^{-1}$, is characterized by two different values of $\bar{T}_{\mathrm{l}}$ and $\bar{T}_{\mathrm{p}}$ and a relatively large value of σ depending on the considered point in this region. For instance, for $g_{\mathrm{sac}} = 0.047\,\mathrm{ms}^{-1}$, $\bar{T}_{\mathrm{l}} = 206.8\,\mathrm{ms}$, $\bar{T}_{\mathrm{p}} = 196.6\,\mathrm{ms}$, and $\sigma = 5.44\,\mathrm{ms}$. Since $\sigma_{\mathrm{t}} = 2.56\,\mathrm{ms}$ and $\sigma_{\mathrm{t}}/\sigma = 0.47$, the period-2 phenomenon seems to correspond to *spatially desynchronized alternans*. The spatio-temporal behavior of the dimensionless membrane potential is depicted as a time-space plot in Fig. 5.27.

iii. The g_{sac}-region between boundaries 3 and 4, ranging from approximately 0.048 75 ms^{-1} to $0.084\,\mathrm{ms}^{-1}$, is characterized by $\bar{T}_{\mathrm{l}} = \bar{T}_{\mathrm{p}}$ and σ close to zero. This g_{sac}-region correspond to different types of period-1 solutions. The time-space plot of the dimensionless membrane potential is shown in Fig. 5.28 for $g_{\mathrm{sac}} = 0.06\,\mathrm{ms}^{-1}$.

iv. The g_{sac}-region between boundaries 5 and 6, close to $0.086\,35\,\mathrm{ms}^{-1}$, leads to period-1 phenomenons, characterized by $\bar{T}_{\mathrm{l}} = \bar{T}_{\mathrm{p}}$ and σ close to zero. The time-space plot of the dimensionless membrane potential for $g_{\mathrm{sac}} = 0.086\,35\,\mathrm{ms}^{-1}$ is depicted in Fig. 5.29.

v. The g_{sac}-region between boundaries 7 and 8, close to $0.086\,95\,\mathrm{ms}^{-1}$, also leads to period-1 phenomenons (Fig 5.30). However, the spatio-temporal patterns of these solutions are very different from those observed for $g_{\mathrm{sac}} = 0.086\,35\,\mathrm{ms}^{-1}$.

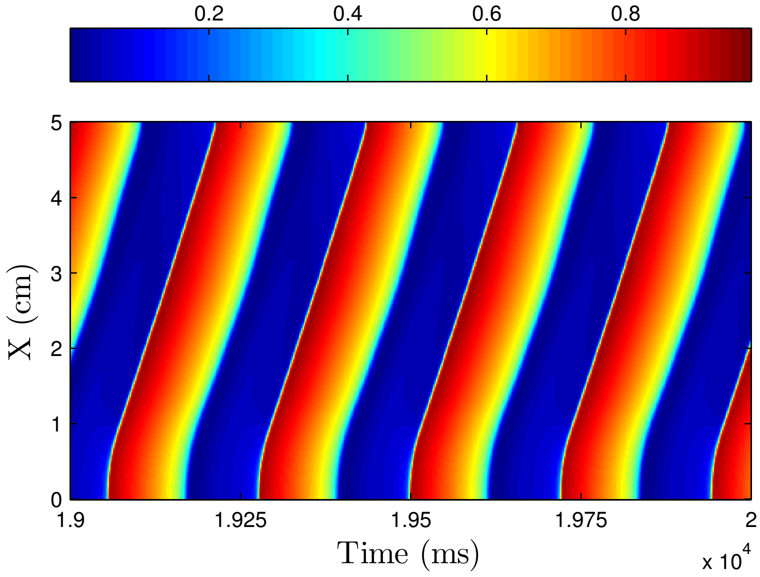

Fig. 5.25 – Time-space plot of the dimensionless membrane potential, $\bar{V}$, for $g_{\mathrm{sac}} = 0.0445\,\mathrm{ms}^{-1}$.

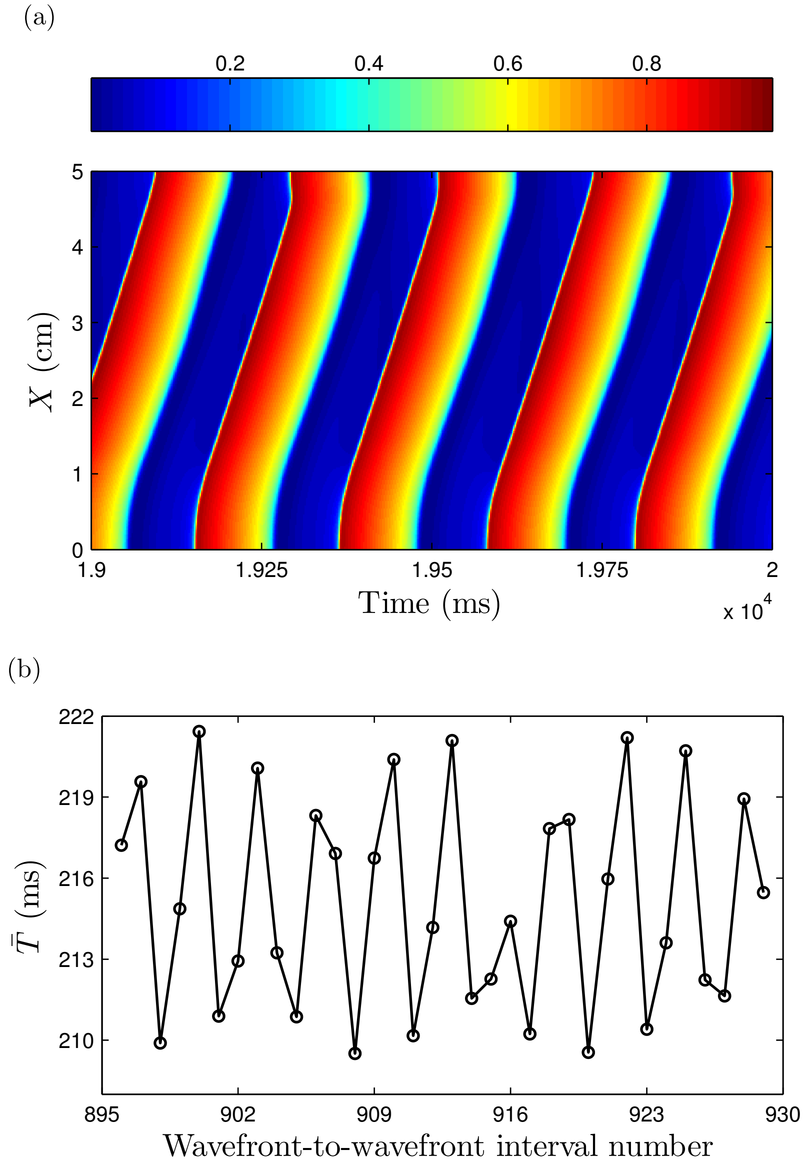

Fig. 5.26 – **Time-space plot of the dimensionless membrane potential (a) and spatial average, $\bar{T}$, of the local time interval between two wavefronts as a function of the wavefront-to-wavefront interval number (b), for $g_{\mathrm{sac}} = 0.045\,\mathrm{ms}^{-1}$.**

From these results, similar interesting phenomena as those emphasized in section 5.1.8.4 relative to the parameter a can be highlighted:

i. Perpetual AEAs occur only for particular values of g_{sac}.

ii. The spatial average of the time period significantly changes when the value of g_{sac} is modified.

iii. The excitatory source seems to be attracted to a specific location in the fiber depending on the value of g_{sac}.

iv. The spatial width of the excitatory source changes as a function of g_{sac}.

v. Two different kinds of periodic solutions, namely period-1 solutions and period-2 solutions, are observed for different values of g_{sac}.

vi. For the g_{sac}-regions where there are no perpetual AEAs, the end of the AEA seems to be induced by two different kinds of mechanisms.

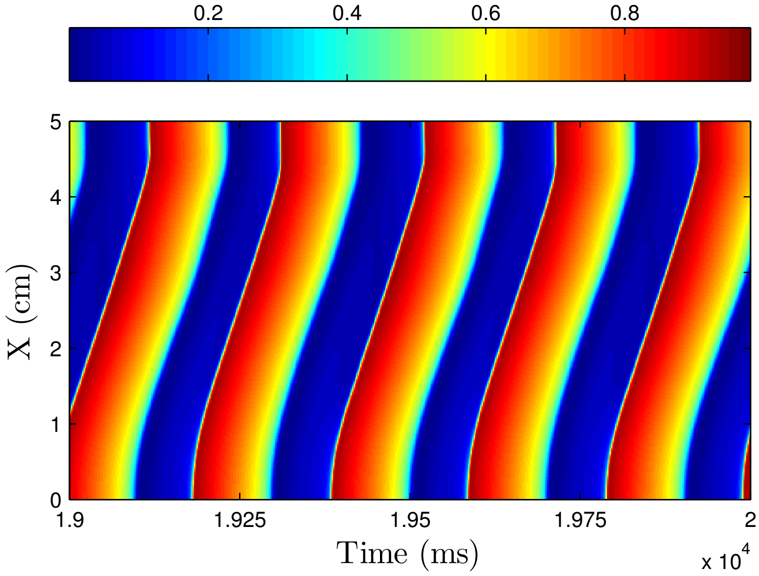

Fig. 5.27 – Time-space plot of the dimensionless membrane potential, $\bar{V}$, for $g_{\text{sac}} = 0.047\,\text{ms}^{-1}$.

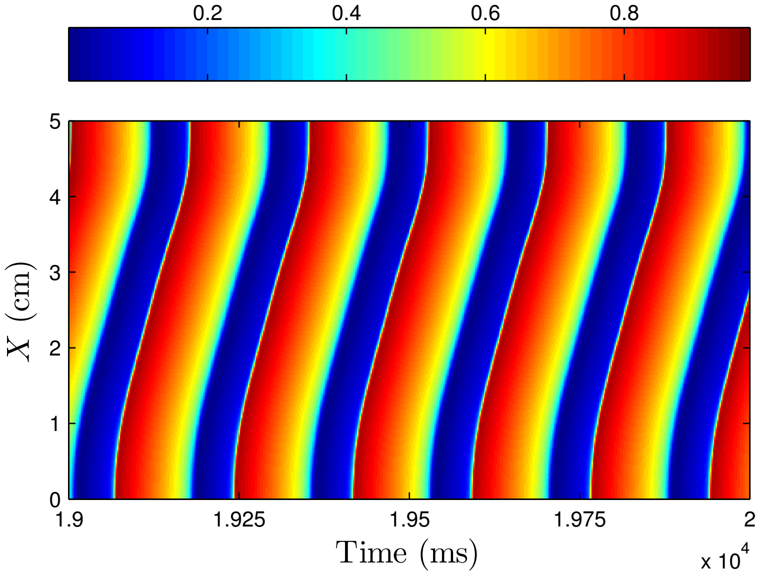

Fig. 5.28 – Time-space plot of the dimensionless membrane potential, $\bar{V}$, for $g_{\text{sac}} = 0.06\,\text{ms}^{-1}$.

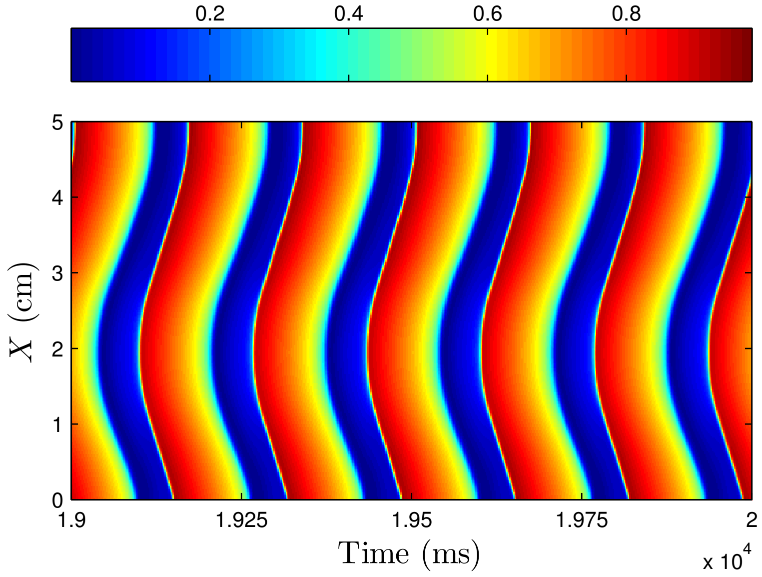

Fig. 5.29 – Time-space plot of the dimensionless membrane potential, $\bar{V}$, for $g_{\mathrm{sac}} = 0.086\,35\,\mathrm{ms}^{-1}$.

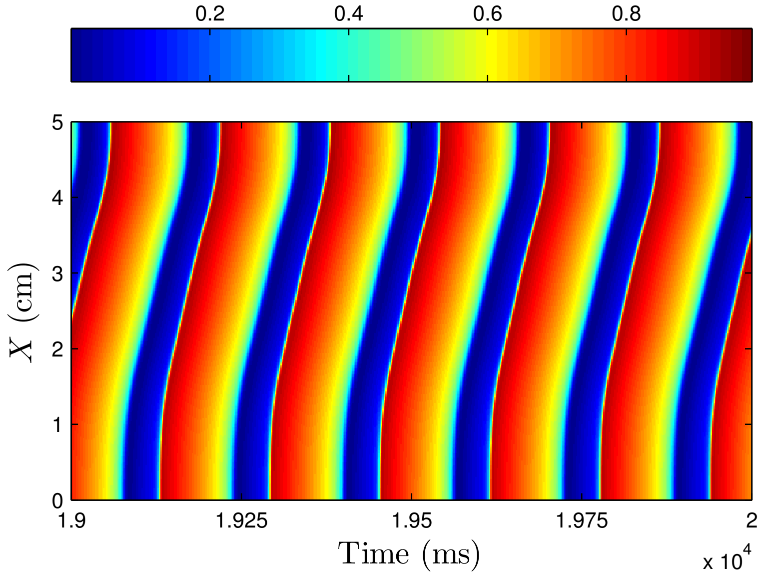

Fig. 5.30 – Time-space plot of the dimensionless membrane potential, $\bar{V}$, for $g_{\mathrm{sac}} = 0.086\,95\,\mathrm{ms}^{-1}$.

5.1.9 Map in the $(L, \tilde{g}_{\mathrm{sac}})$ space of the persistence of the AEA induced by the MEF

In essence, the cardiac MEF is a spatio-temporal phenomenon. It needs a spatially extended system to occur because it is induced by stretchings in the cardiac tissue. From a geometrical point of view, these stretchings affect the propagation of APs in the tissue. This is the geometric MEF. In addition to this geometric effect, these stretchings can generate additional currents, namely stretch-activated currents, when stretch-activated channels are found in the tissue. This is the physiological MEF. From a modeling point of view, the existence of these channels is intrinsically related to the parameter $\tilde{g}_{\text{sac}}$: setting the SAC conductance to zero is similar to consider that there are no SACs in the tissue. From these facts, it is obvious that L and $\tilde{g}_{\text{sac}}$ are the key parameters regarding the MEF phenomenon.

As a consequence, this section aims at examining in great detail the influence of L and $\tilde{g}_{\text{sac}}$ on the AEA for a given temperature value. All other parameter values used in this section are given in Tab. 5.4.

Parameter	Value	Units
a	0.05	dimensionless
D^0	10^{-3}	$\text{cm}^2\,\text{ms}^{-1}$
ε_0	3×10^{-3}	ms^{-1}
ε_1	90×10^{-3}	ms^{-1}
$\kappa_{\sigma_{\text{active}}}$	0.5	$\text{N}\,\text{cm}^{-2}$
κ_v	2	ms^{-1}
d	1.6	$\text{N}\,\text{cm}^{-2}$

Tab. 5.4 – Parameter values used for systematic scanning of the $(L, \tilde{g}_{\text{sac}})$ space with the modified GC minimal model.

For this purpose, the $(L, \tilde{g}_{\text{sac}})$ space is scanned in a systematic way for L ranging from 2 cm to 13.96 cm and $\tilde{g}_{\text{sac}}$ ranging from 0 to 0.12 with increment steps of 0.04 cm and 0.0005, respectively. As a result, 72 300 numerical simulations have to be performed to scan all the $(L, \tilde{g}_{\text{sac}})$ space. Moreover, six different temperature values (31°C, 33°C, 35°C, 37°C, 39°C, and 41°C) have been studied and five different ICs have been tested (time-dependent external current, shown in Fig. 5.2, is applied to the fiber regions centered on $X = L/10$, $X = L/5$, $X = L/3$, $X = 2\,L/5$, and $X = L/2$). As a consequence, 2 169 000 different numerical simulations have been run for this systematic parametric study[7].

---

[7] To run this huge amount of simulations, the *divide-and-conquer strategy* has been adopted as needed for this kind of time-consuming study. For a given IC and a given temperature value, the (L, g_{sac}) space has been split into four parts:

i. part 1 is constituted by the 'parametric area' that is spanned by $\tilde{g}_{\text{sac}} \in [0, 0.12]$ and $L \in [2\,\text{cm}, 4.96\,\text{cm}]$
ii. part 2 is constituted by the 'parametric area' that is spanned by $\tilde{g}_{\text{sac}} \in [0, 0.12]$ and $L \in [5\,\text{cm}, 7.96\,\text{cm}]$

In addition, several points of the computational code have been adapted to enable the further Floquet stability analysis (section 5.1.12):

i. The Heaviside functions have been substituted by appropriate hyperbolic tangent functions. These functions are less tricky to handle numerically than Heaviside functions.
ii. The hyperbolic tangent functions have been substituted by suitable *lookup table functions* to reduce the computational time.

For the interested reader, these two technical points are discussed in some detail below.

Hyperbolic tangent functions substitute Heaviside functions

The first adaptation consists in the substitution of $\varepsilon\left(\bar{V}\right)$ into Eq. (5.36) by

$$f^1\left(\bar{V}\right) \;=\; \varepsilon_0 + (\varepsilon_1 - \varepsilon_0)\left[\frac{1}{2}\left(1 + \tanh\left[\xi_1\left(a - \bar{V}\right)\right]\right)\right], \tag{5.78}$$

where ξ_1 is a parameter that enables to control the width of the transition region between the two asymptotic values (-1 and $+1$) of the hyperbolic tangent function. The second adaptation consists in the substitution of $\Theta\left(\bar{v} - v\right)$ into Eq. (5.26) by

$$f^2\left(\bar{v}, v\right) \;=\; \frac{1}{2}\left(1 + \tanh\left[\xi_2\left(\bar{v} - v\right)\right]\right), \tag{5.79}$$

where ξ_2 is a parameter that plays a similar role as ξ_1. These two functions, given by Eqs (5.78) and (5.79), are continuous contrary to those, which involve Heaviside functions, used previously. In the case where $\xi_1 \to \infty$ and $\xi_2 \to \infty$, Eqs (5.78) and (5.79) behave as the original functions, which involve Heaviside functions.

The values of ξ_1 and ξ_2 have been chosen by comparing several results from simulations performed with Heaviside functions and hyperbolic tangent functions for different val-

---

iii. part 3 is constituted by the ‘parametric area’ that is spanned by $\tilde{g}_{\mathrm{sac}} \in [0, 0.12]$ and $L \in [8\,\mathrm{cm}, 10.96\,\mathrm{cm}]$
iv. part 4 is constituted by the ‘parametric area’ that is spanned by $\tilde{g}_{\mathrm{sac}} \in [0, 0.12]$ and $L \in [11\,\mathrm{cm}, 13.96\,\mathrm{cm}]$

Each part has been run either on a specific core from the computer cluster of the department of physics and applied mathematics from the University of Navarra (Spain) or on a specific core from the computing server (32 cores) of the laboratory of thermodynamics of irreversible processes from the University of Liège (Belgium). Four nodes are needed to scan the whole $(L, \tilde{g}_{\mathrm{sac}})$ space for a given temperature value and a given IC. Proceeding in this way significantly reduces the computational time.

ues of ξ_1 and ξ_2. From that comparison, the values of ξ_1 and ξ_2 have been set to 5000 and 500, respectively. Note that the role played by ξ_1 and ξ_2 is emphasized in Fig. 5.31.

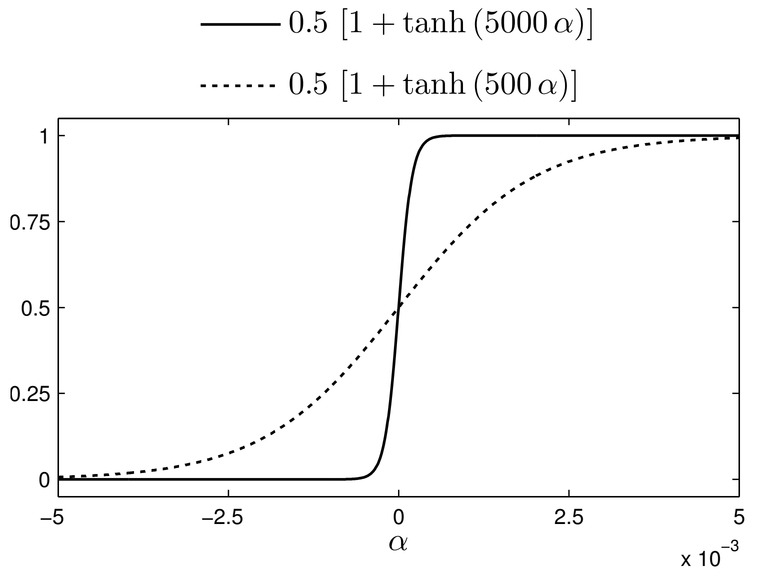

Fig. 5.31 – **Heaviside functions are mimicked by using hyperbolic tangent functions; α represents the value of the argument of a given Heaviside function.**

Lookup table functions

To reduce the computational time, the functions defined by Eqs (5.78) and (5.79) are approximated by using two lookup table functions, which consist of the couples (α_i, f_i^1) and $\left(\beta_j, f_j^2\right)$ where $f_i^1 = \varepsilon_0 + (\varepsilon_1 - \varepsilon_0)\,[0.5\ (1 + \tanh\alpha_i)]$ and $f_j^2 = 0.5\ (1 + \tanh\beta_j)$, with α_i and β_j represent the available discretized values (in the two lookup tables) of the arguments of the hyperbolic functions from Eqs (5.78) and (5.79), respectively.

From a practical point of view, $\left(a - \bar{V}\right)$ is assumed to range from -1.5 to 0.5 and $(\bar{v} - v)$ is assumed to range from -1 to 1. Therefore, $\xi_1\left(a - \bar{V}\right) \in [-7500, 2500]$ and $\xi_2\ (\bar{v} - v) \in [-500, 500]$. The two lookup table functions are built with 100 001 and 10 001 breakpoints. Therefore, $\alpha_i = -7500 + 0.1\,i$ and $\beta_j = -500 + 0.1\,j$, with $i = 0,\ 1,\ \ldots,\ 100\,000$ and $j = 0,\ 1,\ \ldots,\ 10\,000$.

The values of the two ideal functions (hyperbolic tangent functions) at a given point (which does not match a point of the lookup tables) are approximated by linearly interpolating between the two breakpoints closest to the point. Mathematically, considering the hyperbolic tangent function f^1 and assuming that the value of the argument is $\alpha^\star \in [\alpha_i, \alpha_{i+1}]$, $f^1(\alpha^\star)$ is approximated by the following expression:

$$\hat{f}^1(\alpha^\star) \;=\; f_i^1 + \frac{f_{i+1}^1 - f_i^1}{\alpha_{i+1} - \alpha_i}\,(\alpha^\star - \alpha_i)\ . \tag{5.80}$$

Criterion used to determine the perpetual persistence of the AEA

For computational cost reasons, a similar criterion as the one used in section 5.1.8.4 has been adopted in this section to determine whether the AEA lasts indefinitely or not: the AEA is considered as perpetual if it lasts more than 200 s. Otherwise, the AEA only occurs for a finite time interval.

Physiological case: $T = 37\,^\circ\mathrm{C}$

The first case for which the persistence is examined corresponds to a temperature value of 37 °C (physiological value) with an initial excitation (external current shown in Fig. 5.2), applied to the region of the fiber ranging from $L/10 - 0.04\,\mathrm{cm}$ to $L/10 + 0.04\,\mathrm{cm}$.

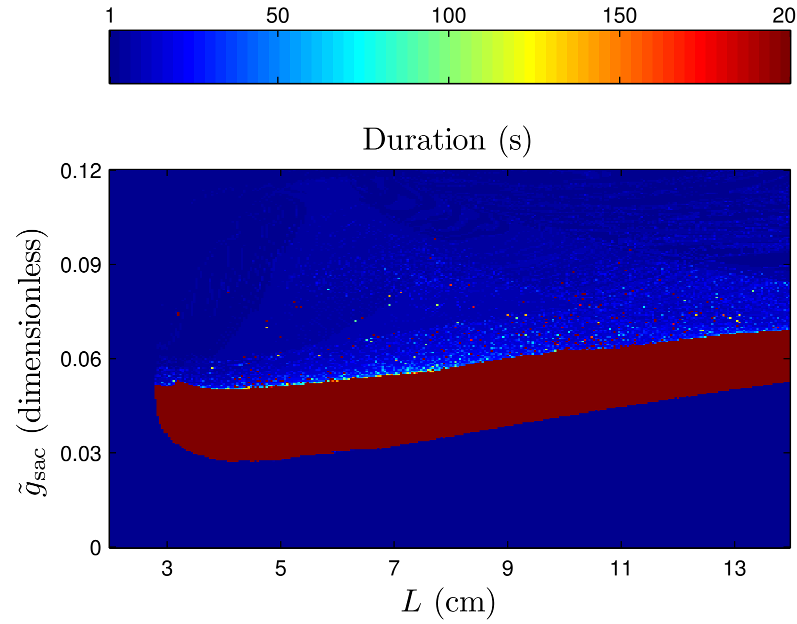

Fig. 5.32 – Persistence of the AEA induced by the MEF as a function of parameters L and $\tilde{g}_{\mathrm{sac}}$ for $T = 37\,^\circ\mathrm{C}$.

As shown in Fig. 5.32, the area in which the AEA is perpetual, which is referred to as the *main dark red spot (main DRS)* in this work, is surrounded by regions in which the AEA is not sustained even for a short time interval (dark blue regions) and by regions in which the AEA is sustained for a finite time interval (all other colored regions). The transitions between the regions in which the AEA is indefinitely sustained and those in which the AEA does not occur at all are very sharp on the left and lower boundaries of the main DRS in Fig. 5.32. The end of the AEA on the left side of the main DRS and below the main DRS can be explained quite readily as follows:

i. For values of L smaller than those corresponding to the left boundary of the main DRS, the APD is too long to enable the SACs to generate an AP. After the propagation of the first AP due to the initial excitation, all the fiber is in an ERS; therefore, even if the SACs are very large (large value of $\tilde{g}_{\text{sac}}$), the electrical activity ends.
ii. For values of $\tilde{g}_{\text{sac}}$ smaller than those corresponding to the lower boundary of the main DRS, SACs are not large enough to trigger a new AP after the propagation of the first one induced by initial excitation applied to the fiber. Thus, no AEA occurs in this region.

For the upper boundary of the main DRS, the transitions are different. These transitions are defined by switches from a perpetual AEA to a finite AEA. Further in this work, the Floquet stability analysis, conducted in section 5.1.12, will corroborate that the transitions at the lower and upper boundaries of the main DRS are intrinsically different. The underlying spatio-temporal mechanisms associated with these transitions will also be highlighted in the aforesaid section.

As depicted in Fig. 5.32, the AEA is sustained above the main DRS for different finite time intervals depending on the values of $\tilde{g}_{\text{sac}}$ and L. Fig. 5.32 also shows that the persistence of the AEA does not have a monotonic behavior with respect to $\tilde{g}_{\text{sac}}$ for a given L. There are even a few dark red isolated points above the main DRS.

The inspection of time-space plots of the AEA occurring in the main DRS, not ‘too’ close to its boundaries, reveals that the AEA behaves in a periodic way with period-1 cycles. A typical spatio-temporal pattern, corresponding to $L = 3.2\,\text{cm}$ and $\tilde{g}_{\text{sac}} = 0.0435$, is depicted in Fig. 5.33. Other points $(L, \tilde{g}_{\text{sac}})$ inside the main DRS, not ‘too’ close to its boundaries, also correspond to similar periodic AEAs.

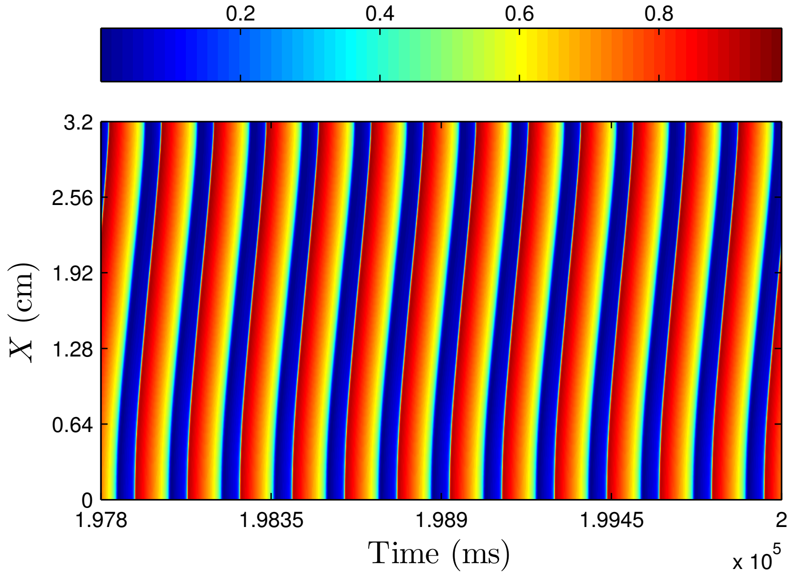

Fig. 5.33 – Time-space plot of the dimensionless membrane potential, $\bar{V}$, for $L = 3.2\,\mathrm{cm}$ and $\tilde{g}_{\mathrm{sac}} = 0.0435$, and with $T = 37\,^{\circ}\mathrm{C}$.

Quite far from the upper boundary of the main DRS, with for instance $\tilde{g}_{\mathrm{sac}} = 0.0680$ and $L = 3.2\,\mathrm{cm}$, Fig. 5.34 shows that the AEA occurs only for a finite time interval while no AEA occurs for $L = 3.2\,\mathrm{cm}$ and for values of $\tilde{g}_{\mathrm{sac}}$ slightly below or above 0.0680 (in the blue area in Fig. 5.32).

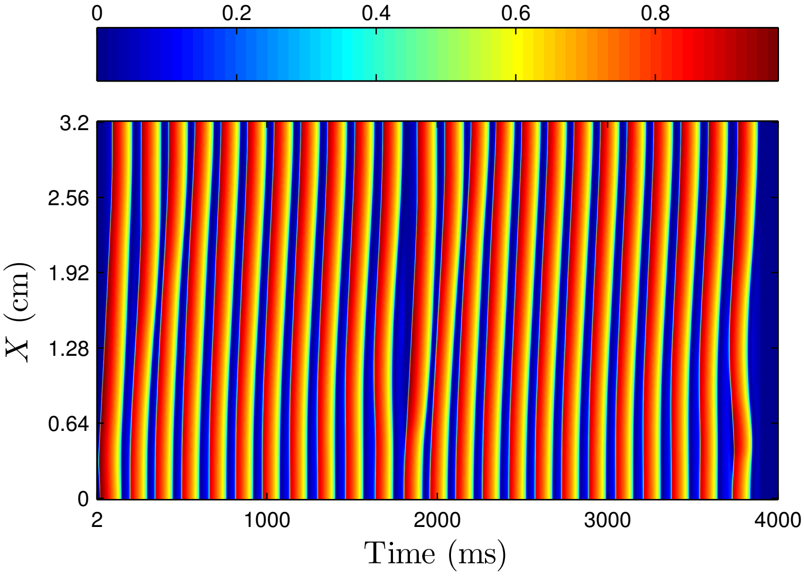

Fig. 5.34 – Time-space plot of the dimensionless membrane potential, $\bar{V}$, for $L = 3.2\,\mathrm{cm}$ and $\tilde{g}_{\mathrm{sac}} = 0.0680$, and with $T = 37\,^{\circ}\mathrm{C}$.

Continuing to increase the value of $\tilde{g}_{\mathrm{sac}}$ for the same length of the fiber, $L = 3.2\,\mathrm{cm}$, the AEA disappears for a large window of values regarding $\tilde{g}_{\mathrm{sac}}$ before occurring again in a perpetual way for $\tilde{g}_{\text{sac}} = 0.0745$. The spatio-temporal behavior of the dimensionless membrane potential, corresponding to the point $(3.2\,\text{cm}, 0.0745)$ in the $(L, \tilde{g}_{\text{sac}})$ space, is shown in Fig. 5.35. This Fig. 5.35 indicates that the AEA is periodic with a period-11 cycle. Shortly after this point toward larger values of $\tilde{g}_{\text{sac}}$, the AEA disappears again.

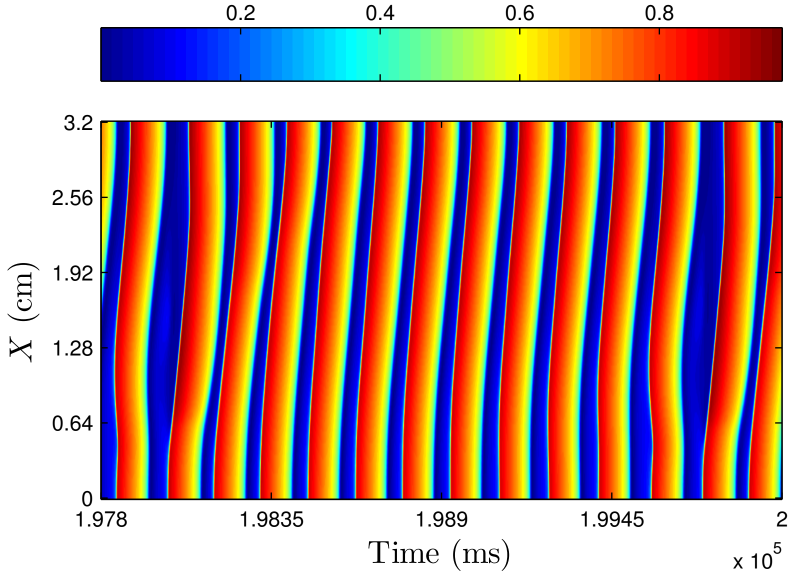

Fig. 5.35 – Time-space plot of the dimensionless membrane potential, $\bar{V}$, for $L = 3.2\,\text{cm}$ and $\tilde{g}_{\text{sac}} = 0.0745$, and with $T = 37\,^{\circ}\text{C}$.

The non-monotonic behavior with respect to a *control parameter* (in the present case, the parameter $\tilde{g}_{\text{sac}}$) is reminiscent of particular phenomena, observed in dynamical systems, which consist in different *regular solutions* existing in different small windows of values of the control parameter, interspersed with *chaotic solutions* [109, 110]. However, this analogy must be handle very carefully because the spatial component, intrinsic to the modified GC minimal model, adds an additional ingredient to the problems examined with dynamical systems. By the way, the spatial component could be the reason for which the AEA disappears above the main DRS in large windows of the control parameter value before occurring again in short windows. Contrary to dynamical systems for which a chaotic solution is able to survive, it seems that the AEA needs to be spatially structured to be sustained.

Effects of an increase in the temperature value

When the temperature is raised by 2 °C, the AEA is significantly affected. The effect on the persistence of AEA as a function of parameters L and $\tilde{g}_{\text{sac}}$ can be observed by comparing Figs 5.32 and 5.36.

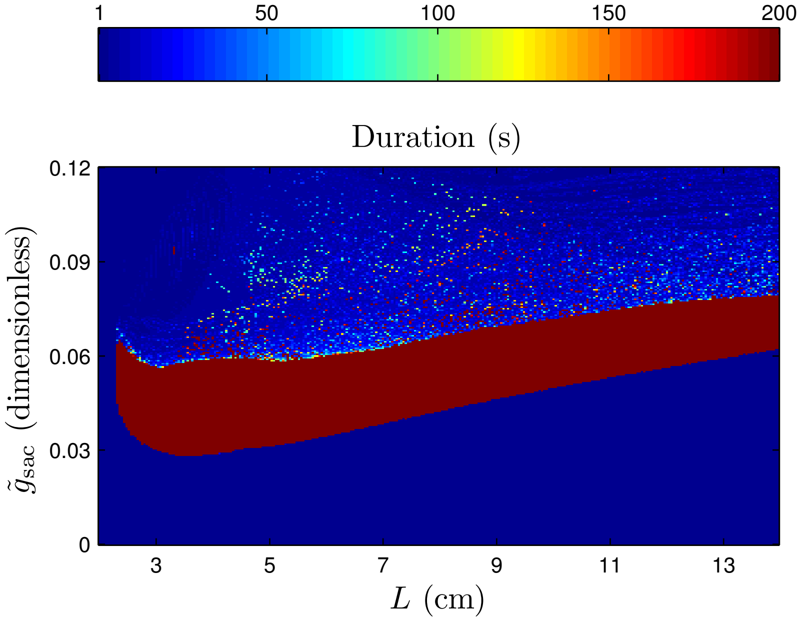

Fig. 5.36 – Persistence of the AEA induced by the MEF as a function of parameters L and $\tilde{g}_{\mathrm{sac}}$ for $T = 39\,^{\circ}\mathrm{C}$.

The main differences between Figs 5.32 and 5.36 are:

i. The area in which the AEA is indefinitely sustained is larger for $T = 39\,^{\circ}\mathrm{C}$ than for $T = 37\,^{\circ}\mathrm{C}$.
ii. There are more dark red regions and points above the main DRS for $T = 39\,^{\circ}\mathrm{C}$ than for $T = 37\,^{\circ}\mathrm{C}$.
iii. There are more non dark blue regions and points in which the AEA is sustained for a finite time interval above the main DRS for $T = 39\,^{\circ}\mathrm{C}$ than for $T = 37\,^{\circ}\mathrm{C}$.
iv. The left boundary of the main DRS is shifted left.
v. The global slopes of the lower and upper boundaries of the main DRS are larger for $T = 39\,^{\circ}\mathrm{C}$ than for $T = 37\,^{\circ}\mathrm{C}$.

Some similarities can also be noted:

i. The transitions between the regions in which the AEA is indefinitely sustained and those in which the AEA does not occur at all are still very sharp for $T = 39\,^{\circ}\mathrm{C}$ (left and lower boundaries of the main DRS in Fig. 5.36).
ii. The lower critical value of $\tilde{g}_{\mathrm{sac}}$ for which the AEA is indefinitely sustained is very similar for $T = 37\,^{\circ}\mathrm{C}$ and $T = 39\,^{\circ}\mathrm{C}$.

Before physically interpreting these observations, some features already highlighted must be reminded and developed:

i. A temperature increase induces a linear increase of ionic conductances (section 4.3). This effect is taken into account in the modified GC minimal model by multiplying the reaction term in Eq. (5.32) with the linear function $\eta\left(T\right)$ [Eq. (5.35)]. Regarding $\tilde{g}_{\mathrm{sac}}$, this multiplication is equivalent to slightly increase its value and leads to particular effects described previously in detail in section 5.1.8.5.

ii. A temperature increase also affects the dynamics of the two-dependent variables, $\bar{V}$ and v. This effect is taken into account in the modified GC minimal model by multiplying the RHS of Eq. (5.36) by the exponential function $\varphi\left(T\right)$ [Eq. (5.38)]. This multiplication is equivalent to increase the values of ε_0 and ε_1 involved in the function $\varepsilon\left(\bar{V}\right)$, which controls directly the dynamics of v and indirectly the one of $\bar{V}$ due to the coupling between these two variables. The effects resulting from an increase in the values of ε_0 and ε_1 have been shown and discussed in detail in section 5.1.8.2: the APD and the time period (if an AEA occurs) are shortened when the values of ε_0 and ε_1 are raised; as a consequence, increasing the temperature shortens the APD and the time period (if an AEA occurs).

The left shift of the left boundary, which corresponds to a smaller value of the length of the fiber, on the main DRS induced by a temperature increase of 2 °C (Fig. 5.36) can be mainly explained by the shortening of the APD induced by the temperature increase of 2 °C (ε_0 and ε_1 are multiplied by a factor of approximately 1.25). In these conditions, the part of the fiber in which the first AP has been triggered has recovered a non-ERS, enabling the onset of a new AP, when a supra-threshold stimulus is generated by the accumulation of the SACs induced by the propagation of the first AP.

The increase of the global slope of the lower boundary of the main DRS arising from a temperature increase can be physically explained by breaking down the phenomenon into two phenomena:

i. the shift towards larger $\tilde{g}_{\mathrm{sac}}$ of the lower boundary for a given length of the fiber
ii. the higher the length of the fiber, the larger the magnitude of the shift of the lower boundary

The first item can be explained by the shortening of the APD and its consequences on the magnitude of the SACs. By examining Eq. (5.34), describing the SACs in the modified GC minimal model, these ones can be seen to be proportional to $\tilde{g}_{\text{sac}}$ and $(\bar{v} - v)$, where $\bar{v}$ is given by Eq. (5.28). In the following, it is important to remind that, in the modified GC minimal model, the quantity $\bar{v} - v$ essentially represents the gradient displacement field, $\partial U / \partial X = F - 1$, in the cardiac tissue: $\bar{v} - v > 0$ represents a stretching whereas $\bar{v} - v < 0$ means that the cardiac tissue is tightened. From Eqs (5.23) and (5.25), the relation between $\bar{v} - v$ and $F - 1$ can be written as

$$\bar{v} - v \;=\; d \, \frac{\kappa_v}{\kappa_{\sigma_{\text{active}}}} \, (F - 1) \, . \tag{5.81}$$

Given that v locally follows the behavior of $\bar{V}$ with a time delay [Eq. (5.36)], the shortening of the APD (thus, the shortening of the spatial extension of the depolarization wave) induces a decrease of the value of the integral on the RHS of Eq. (5.28). Therefore, the contribution to the SACs of $(\bar{v} - v)$ at $T = 39\,^{\circ}\mathrm{C}$ is weaker than the one in the case where $T = 37\,^{\circ}\mathrm{C}$. Therefore, the value of $\tilde{g}_{\text{sac}}$ must be larger to counterbalance the effect on $\bar{v}$ and enabling to induce a supra-threshold stimulus leading to the onset of an AP.

The second item can be explained in the following way. Assume a first case in which an AP characterized by a spatial extension, W_{AP}, propagates in a fiber of length $L^{\star}$ such that $W_{\text{AP}} < L^{\star}$. Assume then a second case where the same AP (with the same spatial extension) propagates in a fiber of length $L^{\star\star} = S\, L^{\star}$ where $S > 1$ represents a given factor. In both situations, the value of the integral on the RHS of Eq. (5.28) is mainly driven by the spatial extension of the AP. In other words, the value of the aforesaid integral increases less than linearly with the length of the fiber. Thus, the following relation may be written:

$$\frac{L^{\star\star}}{L^{\star}} >> \frac{\displaystyle\int_0^{L^{\star\star}} v \, \mathrm{d}X}{\displaystyle\int_0^{L^{\star}} v \, \mathrm{d}X} \tag{5.82}$$

or, similarly,

$$\frac{1}{L^{\star}} \int_0^{L^{\star}} v \, \mathrm{d}X \quad >> \quad \frac{1}{L^{\star\star}} \int_0^{L^{\star\star}} v \, \mathrm{d}X \, . \tag{5.83}$$

Due to the relation given by Eqs (5.34) and (5.83), it is obvious that the magnitude of $\tilde{g}_{\mathrm{sac}}$ must be larger for $L = L^{\star\star}$ than the one for $L = L^{\star}$ to get a supra-threshold stimulus with the same magnitude enabling the onset of an AP. This explains why the global slope of the lower boundary of the main DRS is increased when the temperature is raised. Note that similar arguments may be used to explain the increase of the global slope of the upper boundary of the main DRS induced by a temperature increase.

Effects of a decrease in the temperature value

The effect of a temperature decrease of 2 °C is then examined. As shown in Fig. 5.37, some differences and similarities with the physiological case can be underlined. As expected, the differences that can be noted are exactly opposite to those for $T = 39\,^{\circ}\mathrm{C}$ in comparison with the physiological case:

i. The area in which the AEA is indefinitely sustained is smaller for $T = 35\,^{\circ}\mathrm{C}$ than for $T = 37\,^{\circ}\mathrm{C}$.
ii. There are less dark red regions and points above the main DRS for $T = 35\,^{\circ}\mathrm{C}$ than for $T = 37\,^{\circ}\mathrm{C}$.
iii. There are less regions in which the AEA is sustained for a finite time interval above the main DRS for $T = 35\,^{\circ}\mathrm{C}$ than for $T = 37\,^{\circ}\mathrm{C}$.
iv. The global slopes of the lower and upper boundaries of the main DRS are smaller for $T = 35\,^{\circ}\mathrm{C}$ than for $T = 37\,^{\circ}\mathrm{C}$.

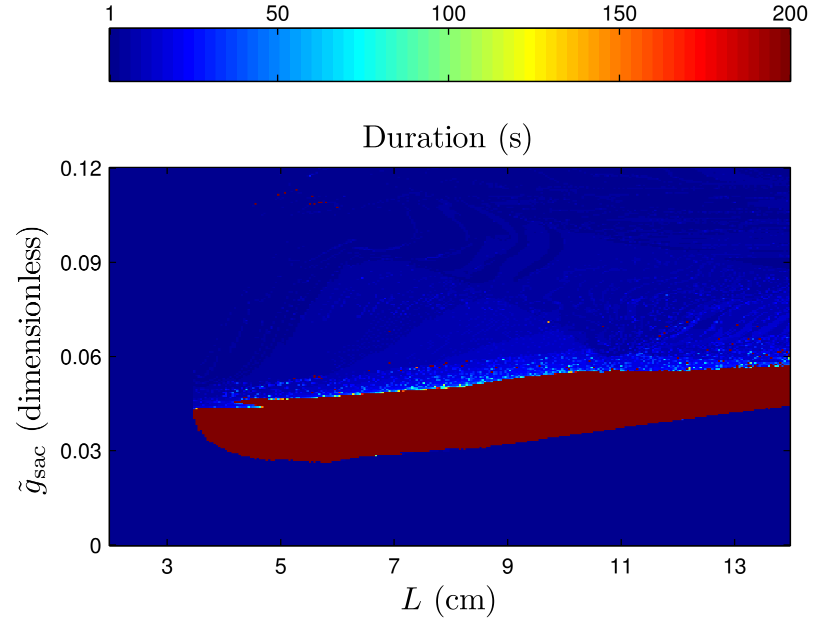

Fig. 5.37 – Persistence of the AEA induced by the MEF as a function of parameters L and $\tilde{g}_{\mathrm{sac}}$ for $T = 35\,^{\circ}\mathrm{C}$.

Therapeutic hypothermia and hyperthermia

The target temperature value for therapeutic hypothermia is close to 33 °C. The representation of the persistence of the AEA induced by the MEF for $T = 33\,^\circ\mathrm{C}$ is shown in Fig. 5.38. For $T = 41\,^\circ\mathrm{C}$ (hyperthermia), the corresponding plot is shown in Fig. 5.39.

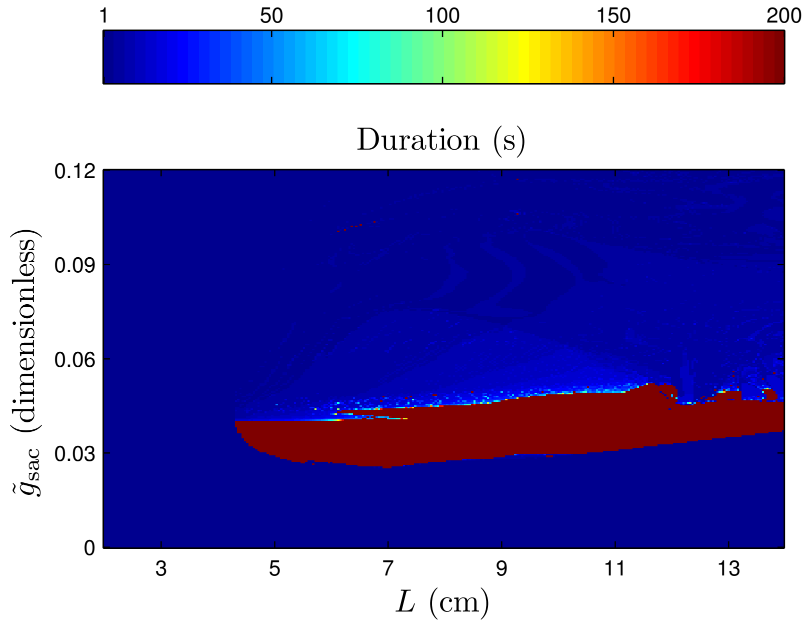

Fig. 5.38 – **Persistence of the AEA induced by the MEF as a function of parameters L and $\tilde{g}_{\mathrm{sac}}$ for $T = 33\,^\circ\mathrm{C}$.**

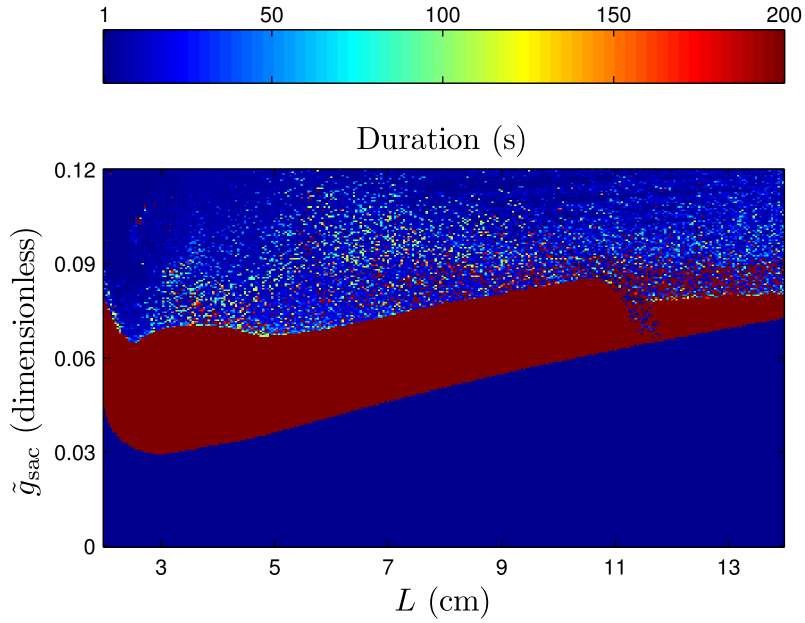

Fig. 5.39 – **Persistence of the AEA induced by the MEF as a function of parameters L and $\tilde{g}_{\mathrm{sac}}$ for $T = 41\,^\circ\mathrm{C}$.**

As expected, comparing Figs 5.37 and 5.38, the phenomena induced by a temperature decrease of 2 °C from the physiological case are even more accentuated for the therapeutic hypothermia.

Looking at the hyperthermia case, the same conclusions can be made in the opposite direction. Without physically interpreting, it can be underline that for these later two extreme cases, the upper boundary of the main DRS is less smooth than the ones for the other cases. This observation can be made mainly for large values of L.

5.1.10 Effects of the spatial location of the initial excitation: qualitative and systematic approaches

5.1.10.1 Qualitative approach

As a first approach, the influence of the spatial location of the initial excitation on the persistence of the AEA induced by the MEF by testing five different ICs for $T = 39\,°\mathrm{C}$. The initial excitation is successively applied to the regions of the fiber ranging from:

i. $L/10 - 0.04\,\mathrm{cm}$ to $L/10 + 0.04\,\mathrm{cm}$;
ii. $L/5 - 0.04\,\mathrm{cm}$ to $L/5 + 0.04\,\mathrm{cm}$;
iii. $L/3 - 0.04\,\mathrm{cm}$ to $L/3 + 0.04\,\mathrm{cm}$;
iv. $2\,L/5 - 0.04\,\mathrm{cm}$ to $2\,L/5 + 0.04\,\mathrm{cm}$;
v. $L/2 - 0.04\,\mathrm{cm}$ to $L/2 + 0.04\,\mathrm{cm}$.

The first case, for which the external current is applied to the region of the fiber ranging from $L/10 - 0.04\,\mathrm{cm}$ to $L/10 + 0.04\,\mathrm{cm}$, has already been depicted in Fig. 5.36. The four other plots of the persistence of the AEA, corresponding to the four other ICs, are shown in Figs 5.40, 5.41, 5.42, and 5.43.

The five plots of the persistence of the AEA are heavily dependent on ICs as observed by comparing Figs 5.36, 5.40, 5.41, 5.42, and 5.43:

i. The five main DRSs are significantly different. The lower critical value relative to L, under which the AEA is not indefinitely sustained, is larger when the initial excitation is applied close to the boundaries of the fiber. The closer to the boundary the initial excitation, the smaller the lower critical value.

ii. The left and the lower boundaries of the main DRSs are very sharp for all the different ICs except the upper part of the left boundary of the main DRS for the case corresponding to Fig. 5.41.

iii. For all the different ICs, the transitions relative to the upper boundary of the main DRS correspond to switches from a perpetual AEA to a finite AEA. For all the ICs, there are different regions above the main DRS for which the AEA is indefinitely sustained. However, the number, the size, and the distribution of these regions are very different.

iv. From the five different cases regarding the influence of the ICs on the persistence of the AEA, one of them is very singular. This is the case for which the external current is applied to the region of the fiber ranging from $L/3 - 0.04\,\mathrm{cm}$ to $L/3 + 0.04\,\mathrm{cm}$, corresponding to Fig. 5.41. The main DRS is significantly larger than those for the other cases. In addition, a large region for which the AEA is sustained for a finite time interval occurs close to the 'north-west' part of the main DRS.

Contrary to the effects of a change of temperature on the key features of the persistence on the AEA, the influence of the ICs is less readily established. Therefore, it is quite reasonable to perform a systematic scanning for all the possible locations of the initial excitation to go further into the role played by the ICs.

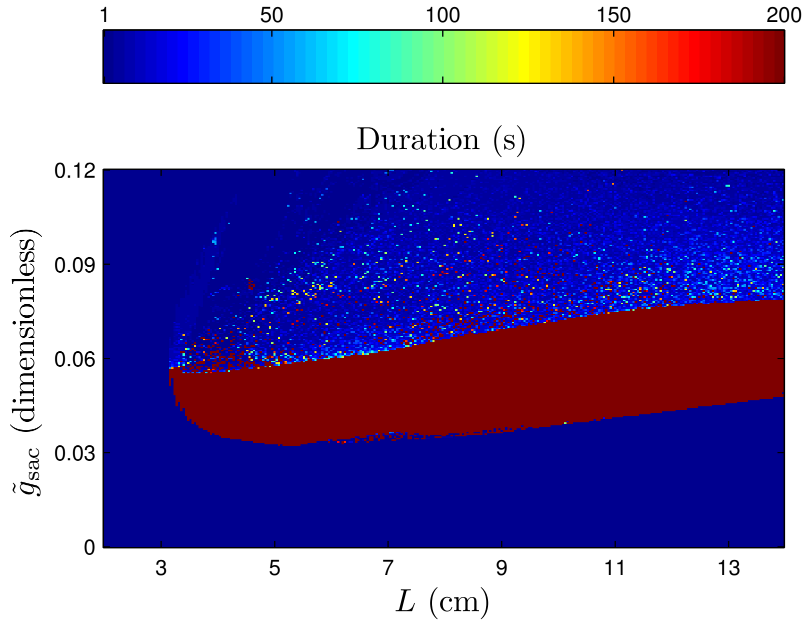

Fig. 5.40 – Persistence of the AEA induced by the MEF as a function of parameters L and $\tilde{g}_{\mathrm{sac}}$ for $T = 39\,^{\circ}\mathrm{C}$ and an initial excitation applied to $X \in [L/5 - 0.04\,\mathrm{cm}, L/5 + 0.04\,\mathrm{cm}]$.

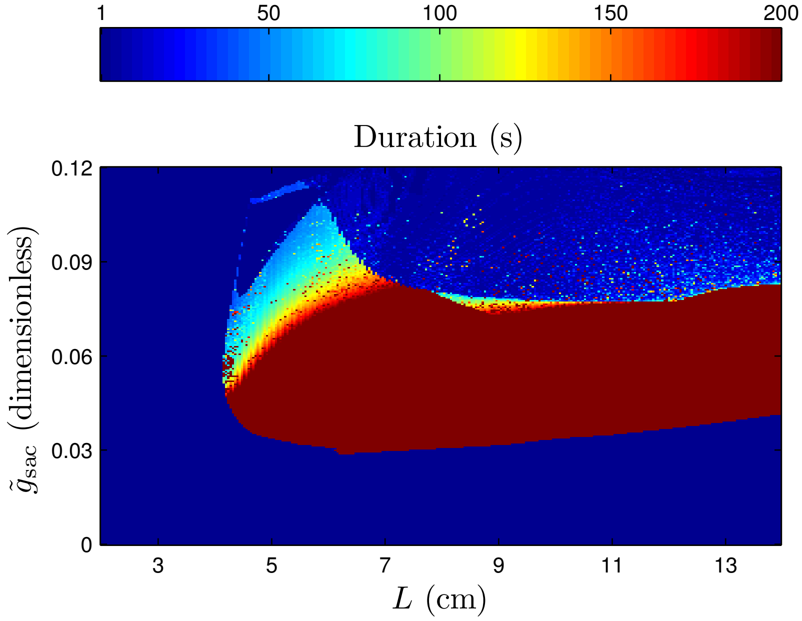

Fig. 5.41 – **Persistence of the AEA induced by the MEF as a function of parameters L and $\tilde{g}_{\mathrm{sac}}$ for $T = 39\,^\circ\mathrm{C}$ and an initial excitation applied to $X \in [L/3 - 0.04\,\mathrm{cm}, L/3 + 0.04\,\mathrm{cm}]$.**

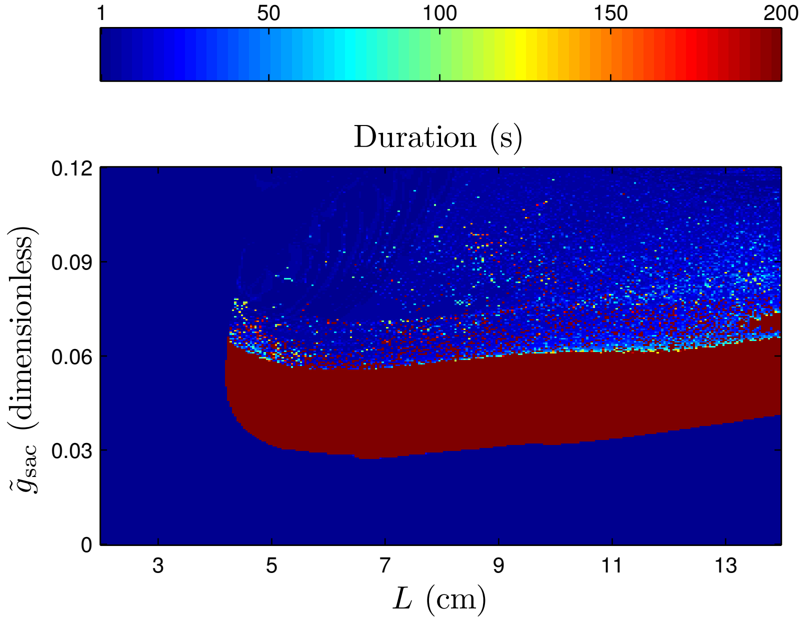

Fig. 5.42 – **Persistence of the AEA induced by the MEF as a function of parameters L and $\tilde{g}_{\mathrm{sac}}$ for $T = 39\,^\circ\mathrm{C}$ and an initial excitation applied to $X \in [2\,L/5 - 0.04\,\mathrm{cm}, 2\,L/5 + 0.04\,\mathrm{cm}]$.**

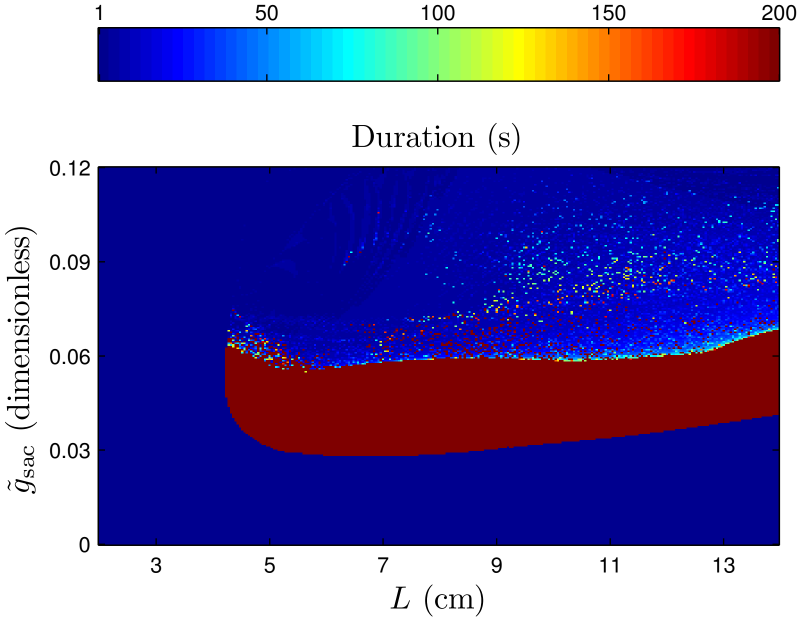

Fig. 5.43 – Persistence of the AEA induced by the MEF as a function of parameters L and $\tilde{g}_{\mathrm{sac}}$ for $T = 39\,^{\circ}\mathrm{C}$ and an initial excitation applied to $X \in [L/2 - 0.04\,\mathrm{cm}, L/2 + 0.04\,\mathrm{cm}]$.

5.1.10.2 Systematic approach

To perform this systematic scanning, the length of the fiber is chosen equal to 7 cm. All other model parameters are held fixed except the temperature value that ranges from 36.5 °C to 39 °C with a step of 0.5 °C. In this way, the influence of a temperature change on the AEA will be highlighted. The model parameter values have been chosen to generate an AEA indefinitely sustained by the MEF for the six different temperature values: $D^0 = 0.001\,\mathrm{cm}^2\,\mathrm{ms}^{-1}$, $\varepsilon_0 = 0.003\,\mathrm{ms}^{-1}$, $\varepsilon_1 = 0.090\,\mathrm{ms}^{-1}$, $\tilde{g}_{\mathrm{sac}} = 0.045$, $a = 0.05$, and $\kappa_v = 2\,\mathrm{ms}^{-1}$. With the chosen parameter values, only period-1 solutions occur: $\bar{T}_{\mathrm{l}} = \bar{T}_{\mathrm{p}}$ and the spatio-temporal variance [Eq. (5.76)] is equal to zero. In this case, $\bar{T}_{\mathrm{l}} = T_{\mathrm{l}}\,(X_m)\ \forall\ X_m \in [0, L]$.

In addition to $\bar{T}_{\mathrm{l}}$, other features may be interesting to observe to characterize the AEA:

i. the spatial width of the excitatory source
ii. the final location, X_{end}, of the center of the excitatory source

In the following, the influence of the location of the initial excitation, whose the center is referred to as X_{ini}, on the following three features of the AEA occurring in a fiber of 7 cm long is examined in a systematic way:

i. the time period, $\bar{T}_l$

ii. X_{end} (after 200 s of simulation)

iii. the spatial width of the excitatory source

Using the spatial discretization introduced in section 5.1.5.1, with $\Delta X = 0.02$ cm, and the symmetry of the problem with respect to the middle of the fiber, 176 different locations (nodes) are possible for the center of the initial excitation with a fiber of 7 cm long. Since six different temperature values are examined, 1056 (176×6) simulations must be performed to scan all the possible locations and temperature values.

Due to the aforesaid symmetry, results are presented from 0 cm (or 0 with a normalized length) to 3.5 cm (or 0.5 with a normalized length). In addition, for the clarity of the plots, the results are depicted only for three temperatures. However, these three values encapsulate all the possible cases[8] observed for the six temperature values actually tested.

Final location of the excitatory source

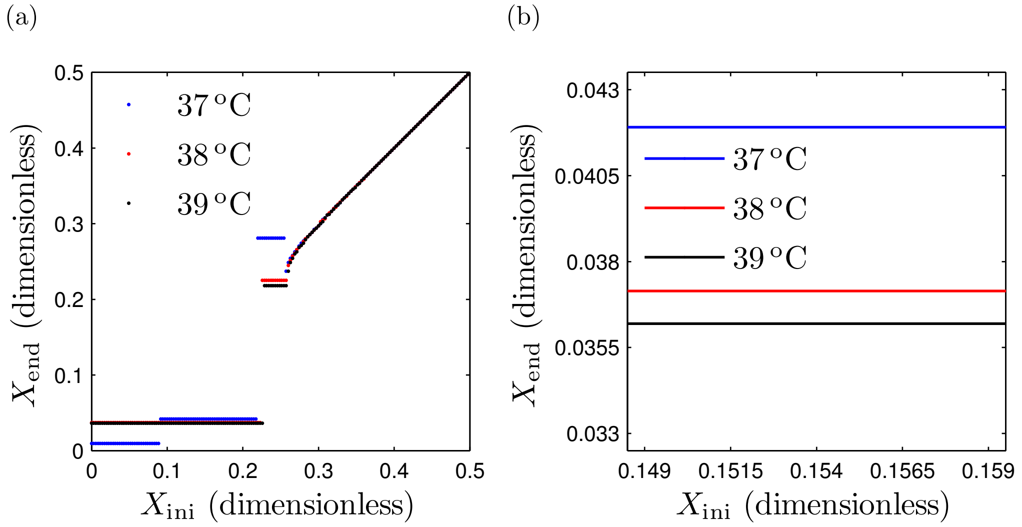

Fig. 5.44 – Location of the center of the excitatory source as a function of the location of the center of the initial excitation in terms of the normalized length of the fiber for three different temperature values (37 °C, 38 °C, and 39 °C). General behavior (a) and local behavior for X_{ini} ranging from 0.1485 to 0.1595 (b).

---

[8] From a qualitative point of view, two different behaviors are observed. For 36.5 °C and 37 °C, three attractors are found whereas for T ranging from 37.5 °C to 39 °C, only two attractors are found.

As shown in Fig. 5.44, for a given temperature value, X_{end} is very dependent on the location of the initial excitation in the fiber. Different *attractors* are observed in the fiber. The number of attractors depends on the temperature value. Their locations and the sizes of their *basins of attraction* also change (in a very slight way for the sizes) due to a temperature variation.

For $T = 37\,^{\circ}\mathrm{C}$, three attractors are found. In terms of the normalized length, the first attractor is close to the boundary, at 9.52×10^{-3}, and the size of its basin of attraction is 8.86×10^{-2} (region of the fiber ranging from 0 to 8.86×10^{-2}, referred to as *'region* 1a*'* for $T = 37\,^{\circ}\mathrm{C}$). The second attractor is found at 4.19×10^{-2} and its basin of attraction has a size of 1.26×10^{-1} (region of the fiber ranging from 9.14×10^{-2} to 2.17×10^{-1}, referred to as *'region* 1b*'* for $T = 37\,^{\circ}\mathrm{C}$). The third attractor is observed at 2.81×10^{-1} and the size of its basin of attraction is equal to 3.43×10^{-2} (region of the fiber ranging from 2.20×10^{-1} to 2.54×10^{-1}, referred to as *'region* 2*'* for $T = 37\,^{\circ}\mathrm{C}$). For X_{ini} ranging from 2.57×10^{-1} to 5×10^{-1}, referred to as *'region* 3*'* for $T = 37\,^{\circ}\mathrm{C}$, there is no attractor since the excitatory source stays at the location of the initial excitation.

For $T = 38\,^{\circ}\mathrm{C}$, only two attractors are found (red lines depicted in Fig. 5.44). The first one is located at 3.71×10^{-2} (red line shown in Fig. 5.44b) with a large basin of attraction, characterized by a size of 2.23×10^{-2} (*'region* 1*'*, ranging from 0 to 2.23×10^{-1} for $T = 38\,^{\circ}\mathrm{C}$). The second one is located at 2.252×10^{-1} and has a size of 3.14×10^{-2} (*'region* 2*'*, ranging from 2.26×10^{-1} to 2.57×10^{-1} for $T = 38\,^{\circ}\mathrm{C}$). From 2.6×10^{-1} to 5×10^{-1}, referred to as *'region* 3*'* for $T = 38\,^{\circ}\mathrm{C}$, the excitatory source stays at the location of the initial excitation.

For $T = 39\,^{\circ}\mathrm{C}$, two attractors are found as for $T = 38\,^{\circ}\mathrm{C}$. The first one is located at 3.62×10^{-2} with a basin of attraction characterized by a size of 2.26×10^{-2} (*'region* 1*'*, ranging from 0 to 2.26×10^{-1} for $T = 39\,^{\circ}\mathrm{C}$). This is a bit larger than the corresponding attractor for $T = 38\,^{\circ}\mathrm{C}$. The second one is located at 2.18×10^{-1} and has a size of 2.85×10^{-2} (*'region* 2*'*, ranging from 2.29×10^{-1} to 2.57×10^{-1} for $T = 39\,^{\circ}\mathrm{C}$). From 2.6×10^{-1} to 5×10^{-1}, referred to as *'region* 3*'* for $T = 39\,^{\circ}\mathrm{C}$ (as for $T = 38\,^{\circ}\mathrm{C}$), no attractor is found and the excitatory source stays at the location of the initial excitation.

Finally, three remarks may be added to the previous comments:

i. Whether the number of attractor is the same (*e.g.* for $T = 38\,^{\circ}\mathrm{C}$ and $T = 39\,^{\circ}\mathrm{C}$), the location of the attractor close to the boundary of the fiber is very similar for different temperatures while the location of the attractor characterized by the smallest basin of attraction and corresponding to region 2 is different.

ii. Whether the number of attractor is different (*e.g.* for $T = 37\,^{\circ}\mathrm{C}$ and $T = 38\,^{\circ}\mathrm{C}$), the location of the attractor with the smallest basin of attraction is different. By comparing the cases corresponding to $T = 37\,^{\circ}\mathrm{C}$ and $T = 38\,^{\circ}\mathrm{C}$, the two basins of attraction (regions 1a and 1b) relative to the two attractors close to the boundary for $T = 37\,^{\circ}\mathrm{C}$ can be seen to merge due to a temperature increase ($T = 38\,^{\circ}\mathrm{C}$). This merging leads to a new single attractor with a larger basin of attraction, which is located very close to the second attractor (by scanning the fiber from the boundary toward the center) of the case corresponding to $T = 37\,^{\circ}\mathrm{C}$.

iii. The size of the different basins of attraction is very similar for all the temperature values. In other words, the size of these basins of attraction is not very sensitive to a temperature change. Note that for $T = 37\,^{\circ}\mathrm{C}$, the size of the sum of region 1a and region 1b is similar (a tiny bit smaller) to the size of region 1 for $T = 38\,^{\circ}\mathrm{C}$ and $T = 39\,^{\circ}\mathrm{C}$.

Time period

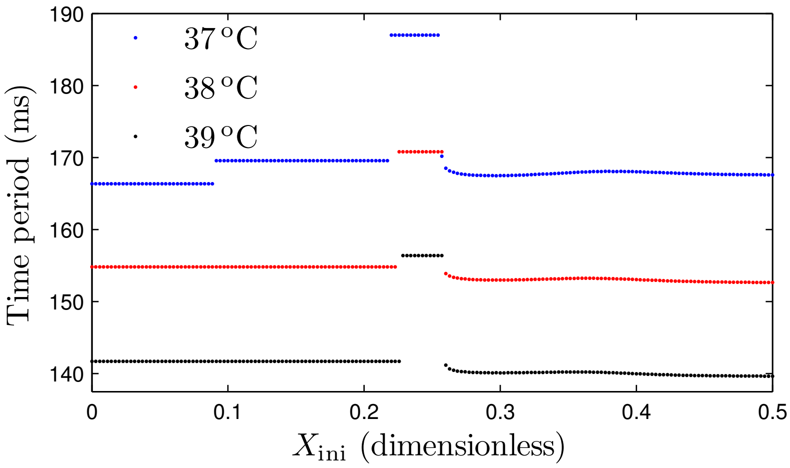

Fig. 5.45 – Time period as a function of the location of the center of the initial excitation in terms of the normalized length of the fiber for three different temperature values (37 °C, 38 °C, and 39 °C).

As shown in Fig. 5.45, for a given temperature value, the time period significantly depends on the location of the initial excitation. For $T = 37\,°\mathrm{C}$, the time periods corresponding to an initial excitation applied to regions 1a and 1b are equal to 166.3 ms and 169.6 ms, respectively. The largest time period of 187 ms characterizes an initial excitation applied to region 2. Finally, the time period corresponding to an initial excitation applied to region 3 ranges from 167.5 ms to 170.2 ms. Regarding this region 3, the time period is non-monotonic with respect to X_{ini}.

For $T = 38\,°\mathrm{C}$ the time periods relative to an initial excitation applied to regions 1 and 2 are equal to 154.8 ms and 170.8 ms, respectively. The time period corresponding to an initial excitation applied to region 3 ranges from 152.7 ms to 153.9 ms. Anew, the behavior of the time period with respect to X_{ini} for this region is non-monotonic.

For $T = 39\,°\mathrm{C}$, the time periods regarding initial excitations applied to regions 1 and 2 are equal to 141.7 ms and 156.4 ms, respectively. An initial excitation applied to region 3 is characterized by a time period that ranges from 139.7 ms to 141.2 ms and this time period behaves in a non-monotonic fashion with respect to X_{ini}.

Several key elements may be underlined from theses simulations:

i. The time period significantly decreases when the temperature increases everywhere in the fiber.
ii. The time period, for a given X_{ini}, behaves as a nonlinear function of the temperature. The variations of the time period, for a given X_{ini}, resulting from an increment (decrement) of 1 °C, are not similar depending on whether the increment (decrement) is performed from 38 °C (39 °C) to 39 °C (38 °C) or from 37 °C (38 °C) to 38 °C (37 °C).
iii. The largest variation of the time period, arising from an increment or a decrement of 1 °C from any temperature value tested, is found in the ‘same’ region, namely region 2.
iv. The larger the temperature value, the flatter the time period with respect to X_{ini} in region 3 for $T = 37\,°\mathrm{C}$, $T = 38\,°\mathrm{C}$, and $T = 39\,°\mathrm{C}$.

Spatial width of the excitatory source

This section shows the dependence of the spatial width of the excitatory source with respect to X_{ini}.

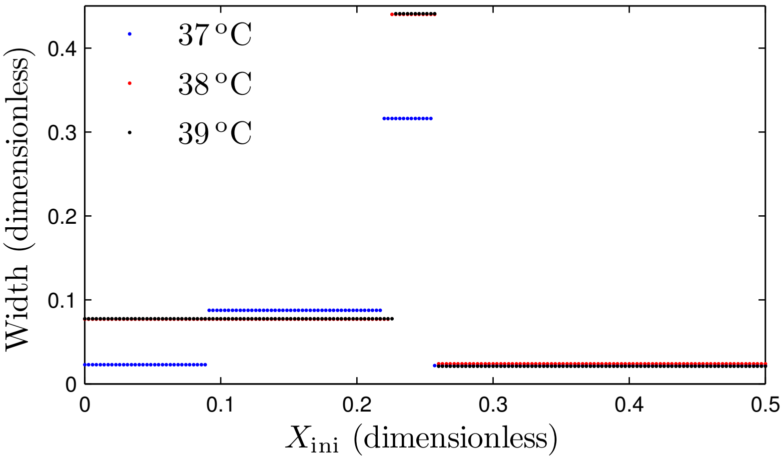

Fig. 5.46 – Spatial width of the excitatory source as a function of the location of the center of the initial excitation in terms of the normalized length of the fiber for three different temperature values (37 °C, 38 °C, and 39 °C).

As shown in Fig. 5.46, for $T = 37\,^{\circ}\mathrm{C}$, the excitatory source has a width of 2.29×10^{-2} (approximately 0.16 cm) when the initial excitation is applied to region 1. For an initial excitation applied to region 2, the width of the excitatory source is approximately equal to 8.76×10^{-2} (approximately 0.61 cm). The largest width, 3.16×10^{-1} (approximately 2.21 cm), occurs for an initial excitation applied to region 3. By contrast, the smallest width of the excitatory source, 2.19×10^{-2} (approximately 0.15 cm), occurs for an initial excitation applied to region 4.

For $T = 38\,^{\circ}\mathrm{C}$, the width of the excitatory source is equal to 7.71×10^{-2} (approximately 0.54 cm) for an initial excitation applied to region 1. The largest width of the excitatory source is equal to 4.4×10^{-1} (approximately 3.08 cm) and is shown for an initial excitation applied to region 2. Regarding the smallest width of the excitatory source, 2.38×10^{-2} (approximately 0.17 cm), it is observed for an initial excitation applied to region 3.

For $T = 39\,^{\circ}\mathrm{C}$, the widths of the excitatory source corresponding to the three different regions are very similar as for $T = 38\,^{\circ}\mathrm{C}$. For an initial excitation applied to region 1, the width is equal to 7.76×10^{-2} (approximately 0.54 cm). The largest and smallest widths of the excitatory source are equal to 4.41×10^{-1} (approximately 3.09 cm) and 2.10×10^{-2} (approximately 0.15 cm), respectively.

5.1.11 Effects of the magnitude of the initial excitation: a systematic approach

This section deals with the dependence of the behavior of the AEA with respect to the magnitude of the external current applied initially for triggering the first action potential in the fiber. For this purpose, the magnitude of this current is changed from $0.06\,\mathrm{ms}^{-1}$ to $0.1\,\mathrm{ms}^{-1}$ with an increment step of $0.005\,\mathrm{ms}^{-1}$. Its time-dependence is the same as the one depicted in Fig. 5.2. Results with different magnitudes are compared with the results from the previous section for the same parameter values and the specific case corresponding to a temperature value of $37\,^{\circ}\mathrm{C}$. As in the previous section and for similar reasons, results for only three different values of the magnitude are depicted in figures.

5.1.11.1 Final location of the excitatory source

First, as shown in Fig 5.47a, the maximal magnitude of the external current, $I_{\mathrm{s,max}}$, applied initially to the fiber does not influence the size of the four different regions. Second, X_{end} does not change for region 1a and region 3 whether $I_{\mathrm{s,max}}$ is increased. On the other hand, X_{end} for region 1b is slightly altered while X_{end} for region 2 is very different for $I_{\mathrm{s,max}} = 0.1\,\mathrm{ms}^{-1}$.

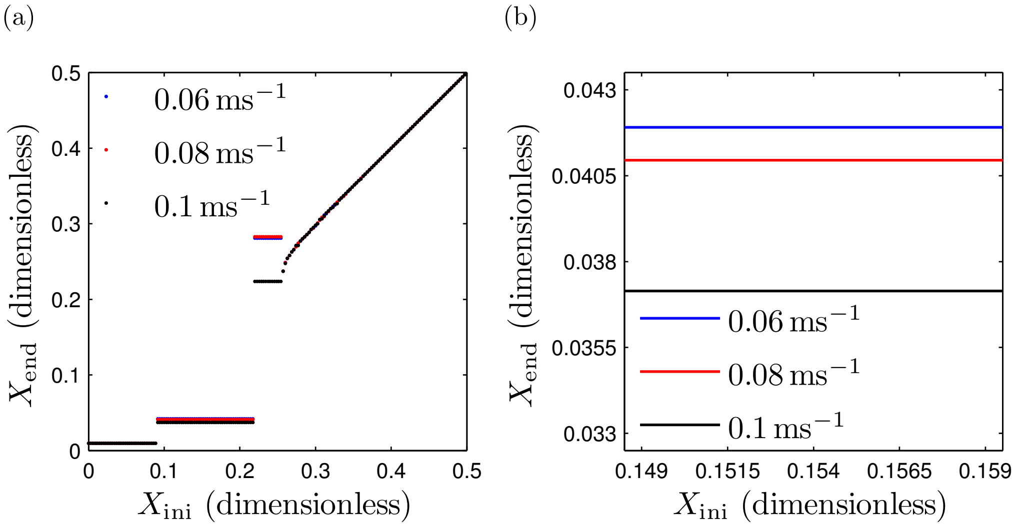

Fig. 5.47 – Location of the center of the excitatory source as a function of the location of the center of the initial excitation in terms of the normalized length of the fiber for three different magnitude values ($0.06\,\mathrm{ms}^{-1}$, $0.08\,\mathrm{ms}^{-1}$, and $0.1\,\mathrm{ms}^{-1}$). General behavior (a) and local behavior for X_{ini} ranging from 0.1485 to 0.1595 (b).

5.1.11.2 Time period

The time period seems to be not dependent on the maximal magnitude of the external current. As shown in Fig. 5.48, all the lines are similar.

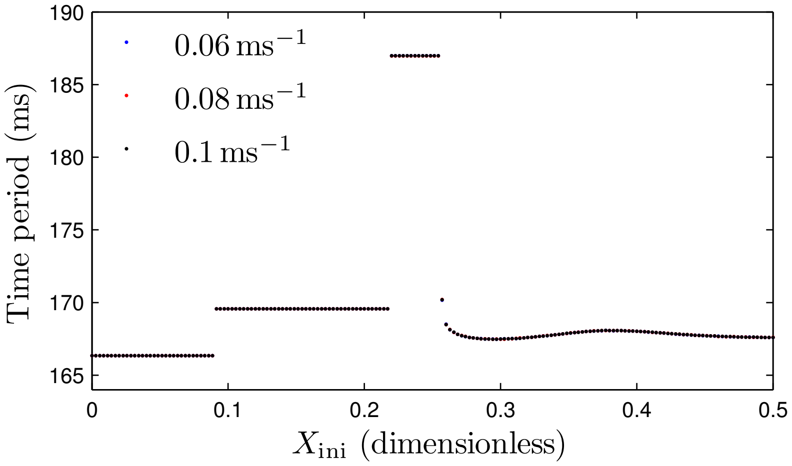

Fig. 5.48 – Time period as a function of the location of the initial excitation in terms of the normalized length of the fiber for three different magnitude values ($0.06\,\mathrm{ms}^{-1}$, $0.08\,\mathrm{ms}^{-1}$, and $0.1\,\mathrm{ms}^{-1}$).

5.1.11.3 Spatial width of the excitatory source

Finally, as shown in Fig. 5.49, the spatial width of the excitatory source is similar for $I_{\mathrm{s,max}} = 0.06\,\mathrm{ms}^{-1}$ and $I_{\mathrm{s,max}} = 0.08\,\mathrm{ms}^{-1}$ while a significant change is observed for $I_{\mathrm{s,max}} = 0.1\,\mathrm{ms}^{-1}$ in region 2 and region 3 (for $T = 37\,^{\circ}\mathrm{C}$).

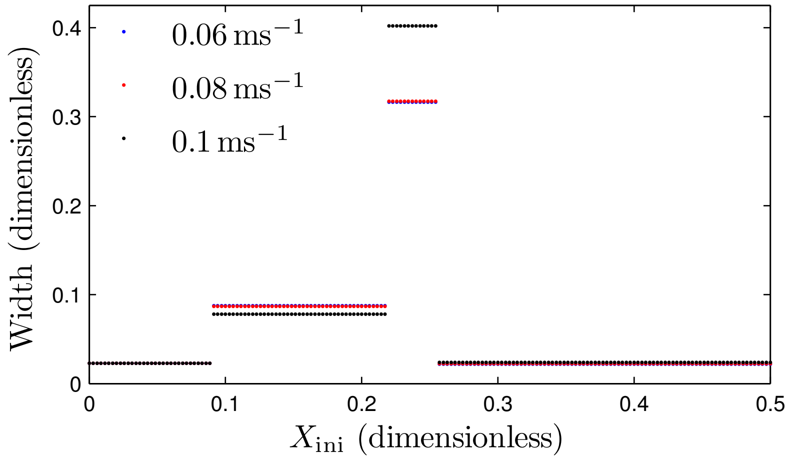

Fig. 5.49 – Spatial width of the excitatory source as a function of the location of the initial excitation in terms of the normalized length of the fiber for three different magnitude values ($0.06\,\mathrm{ms}^{-1}$, $0.08\,\mathrm{ms}^{-1}$, and $0.1\,\mathrm{ms}^{-1}$).

5.1.12 Floquet stability analysis

The Floquet theory consists in a linear stability analysis of periodic phenomena. This theory enables to determine how a periodic solution of a dynamical system becomes unstable. Assume an autonomous system

$$\dot{\mathbf{x}}(t) \quad = \quad \mathbf{f}\left(\mathbf{x}(t)\right) \ , \tag{5.84}$$

where $\mathbf{x} \in \mathbb{R}^n$ and $\mathbf{f} \in \mathbb{R}^n$. The latter is a time-independent vector-valued vector function. Eq. (5.84) has a reference periodic solution, $\mathbf{x}_r\left(t\right)$, with

$$\mathbf{x}_r\left(t+T\right) \quad = \quad \mathbf{x}_r\left(t\right) \ . \tag{5.85}$$

To examine the stability of the periodic solution $\mathbf{x}_r\left(t\right)$, the time evolution of a small perturbation, $\tilde{\mathbf{x}}\left(t\right)$, is studied. Consider $\mathbf{x}\left(t\right) = \mathbf{x}_r\left(t\right) + \tilde{\mathbf{x}}\left(t\right)$. Therefore, inserting the latter relation into Eq. (5.84), the following relation may be written:

$$\begin{aligned} \dot{\tilde{\mathbf{x}}}\left(t\right) &= \dot{\mathbf{x}}\left(t\right) - \mathbf{x}_r\left(t\right) \\ &= \mathbf{f}\left(\mathbf{x}_r\left(t\right) + \tilde{\mathbf{x}}\left(t\right)\right) - \mathbf{f}\left(\mathbf{x}_r\left(t\right)\right) \ . \end{aligned} \tag{5.86}$$

Moreover, $f\left(\mathbf{x}_r\left(t\right) + \tilde{\mathbf{x}}\left(t\right)\right)$ may be expanded in a Taylor series around $\mathbf{x}_r\left(t\right)$:

$$f\left(\mathbf{x}_r\left(t\right) + \tilde{\mathbf{x}}\left(t\right)\right) \quad = \quad \mathbf{f}\left(\mathbf{x}_r\left(t\right)\right) + \left.\frac{\partial \mathbf{f}}{\partial \mathbf{x}}\right|_{\mathbf{x}_r(t)} \cdot \tilde{\mathbf{x}}\left(t\right) + \mathcal{O}\left(\tilde{\mathbf{x}}\left(t\right)^2\right) \ . \tag{5.87}$$

As a result, substituting Eq. (5.87) into Eq. (5.86), the following relation may be written:

$$\dot{\tilde{\mathbf{x}}}\left(t\right) \quad = \quad \left.\frac{\partial \mathbf{f}}{\partial \mathbf{x}}\right|_{\mathbf{x}_r(t)} \cdot \tilde{\mathbf{x}}\left(t\right) \ . \tag{5.88}$$

Thus, the perturbation $\tilde{\mathbf{x}}\left(t\right)$ satisfies the relation

$$\dot{\tilde{\mathbf{x}}}\left(t\right) \quad = \quad \mathbf{D}\left(t\right) \cdot \tilde{\mathbf{x}}\left(t\right) \ , \tag{5.89}$$

with

$$\mathbf{D}\,(t) \;=\; \left.\frac{\partial \mathbf{f}}{\partial \mathbf{x}}\right|_{\mathbf{x}_r(t)} \; . \tag{5.90}$$

$\mathbf{D}\,(t)$ is periodic due to the periodicity of $\mathbf{x}_r\,(t)$. The basic idea of the Floquet stability theory is the assumption that the periodicity of $\mathbf{D}\,(t)$ enables to reduce the system given by Eq. (5.89) to a system with constant coefficients if the system is observed at discrete points in time $t = 0,\, T,\, 2\,T,\, 3\,T, \ldots$ From a geometric point of view, this corresponds to a *Poincarré section* [110].

The system given by Eq. (5.89) is characterized by the n linearly independent solutions $\boldsymbol{\varphi}_1\,(t)$, $\boldsymbol{\varphi}_2\,(t)$, $\ldots$, $\boldsymbol{\varphi}_n\,(t)$ which can be represented by $n \times 1$ matrices[9] $[\varphi_1\,(t)]$, $[\varphi_2\,(t)]$, $\ldots$, $[\varphi_n\,(t)]$. The *fundamental matrix*, $[\Phi\,(t)]$, of the system [Eq. (5.89)] is obtained by assembling $[\varphi_1\,(t)]$, $[\varphi_2\,(t)]$, $\ldots$, $[\varphi_n\,(t)]$, with $[\Phi\,(0)] = [I]$. As a result, $\left[\dot{\Phi}\right] = [D\,(t)]\;[\Phi\,(t)]$. Using the fundamental matrix, any solution $[\tilde{x}\,(t)]$ of Eq. (5.89) may be written in the following form:

$$[\tilde{x}\,(t)] \;=\; [\Phi\,(t)]\;[\tilde{x}_0]\;, \tag{5.91}$$

where $[\tilde{x}_0]$ represents the IC. As $[D\,(t)]$ is a periodic matrix, $[\tilde{x}\,(t+T)]$ is also a solution of Eq. (5.89) and, thus,

$$[\tilde{x}\,(t+T)] \;=\; [\Phi\,(t)]\;[\tilde{x}\,(T)]\;. \tag{5.92}$$

Due to Eq. (5.91), the following relation may be written:

$$[\tilde{x}\,(T)] \;=\; [\Phi\,(T)]\;[\tilde{x}_0]\;, \tag{5.93}$$

$$[\tilde{x}\,(t+T)] \;=\; [\Phi\,(t+T)]\;[\tilde{x}_0]\;. \tag{5.94}$$

Substituting Eq. (5.93) into Eq. (5.92), $[\tilde{x}\,(t+T)]$ may be written as

$$[\tilde{x}\,(t+T)] \;=\; [\Phi\,(t)]\;[\Phi\,(T)]\;[\tilde{x}_0]\;. \tag{5.95}$$

---

[9] Any quantity written as $[\bullet]$ describes a matrix.

Comparing Eqs (5.94) and (5.95), it can be observed that

$$\begin{aligned}[\Phi(t+T)] &= [\Phi(t)]\,[\Phi(T)] \\ &= [\Phi(T)]\,[\Phi(t)]\ . \end{aligned} \tag{5.96}$$

The matrix $[\Phi(T)]$ is called the *monodromy matrix.* The eigenvalues, λ_j, of this matrix are known as the *Floquet multipliers.* It can be shown that the monodromy matrix always has one eigenvalue equal to one, associated with the eigenvector $[\dot{x}_r(0)]$ [110]. This Floquet multiplier is also called the *trivial Floquet multiplier.* The eigenvalues of $[\Phi(T)]$, different from one, determine the stability of the periodic solution (also called limit cycle), $[x_r(t)]$. A periodic solution is stable if all the Floquet multipliers except the trivial Floquet multiplier are strictly smaller than one in modulus. When one or more Floquet multipliers cross the unit circle in the complex plane, bifurcations occur. In other words, if $\lambda_1 = 1$, the limit cycle will be stable if $|\lambda_j| < 1$ for $j \geq 2$ and unstable if $|\lambda_j| > 1$ at least for one value of $j \geq 2$.

In addition, a periodic orbit can lose its stability in three different ways:

i. $\lambda_j = 1$ and $\mathrm{Im}(\lambda_j) = 0$
ii. $\lambda_j = -1$ and $\mathrm{Im}(\lambda_j) = 0$
iii. $|\lambda_j| = 1$ and $\mathrm{Im}(\lambda_j) \neq 0$ (a pair of complex conjugate eigenvalues)

Each of these three cases is the sign of a particular type of bifurcation. The case (i), which corresponds to a crossing of the unit circle in the complex plane at +1, is associated with a *saddle-node bifurcation*, a *transcritical bifurcation*, or a *pitchfork bifurcation* (subcritical or supercritical). The case (ii), which corresponds to a crossing of the unit circle at −1, is associated with a *flip bifurcation* (subcritical or supercritical), also called *period-doubling bifurcation.* The case (iii), which corresponds to a crossing of the unit circle in the complex plane at $\exp(i\,\theta)$ ($i = \sqrt{-1}$ and θ is the argument of the complex number), is associated with a *Neimark–Sacker bifurcation* (subcritical or supercritical) [110].

Shortly after a saddle-node bifurcation, a subcritical Neimark–Sacker bifurcation, or a subcritical flip bifurcation, the system can undergo an *intermittency phenomenon.* As mentioned in [110], there is no precise standard definition of the concept of intermittency. A signal is generally designated intermittent if its temporal evolution appears regular (laminar) over long periods of time, yet is interrupted now and again by short irregular (turbulent) intervals with amplitudes of higher intensity [110]. In accordance with the path the eigenvalues take when crossing the unit circle, intermittency is classified in three groups:

i. *Type I intermittency* is generated by a saddle-node bifurcation corresponding to a Floquet multiplier crossing the unit circle at $+1$.
ii. *Type II intermittency* is generated by a subcritical Neimark–Sacker bifurcation corresponding to a pair of complex conjugate Floquet multipliers crossing the unit circle at $\exp(i\,\theta)$.
iii. *Type III intermittency* is generated by a subcritical flip bifurcation corresponding to a Floquet multiplier crossing the unit circle at -1.

In addition, shortly after a supercritical Neimark–Sacker bifurcation and shortly after a supercritical flip bifurcation, the system can be characterized by a quasi-periodic solution and by period-2 solution, respectively. These different phenomena which may be observed shortly after these particular bifurcations are summarized in Tab. 5.5.

Crossing	Bifurcation	Phenomenon
$+1$	saddle-node	type I intermittency
$\exp(i\,\theta)$	subcritical Neimark–Sacker	type II intermittency
$\exp(i\,\theta)$	supercritical Neimark–Sacker	quasi-periodicity
-1	subcritical flip	type III intermittency
-1	supercritical flip	periodicity

Tab. 5.5 – Behavior of dynamical systems as a function of the type of bifurcation.

The Floquet theory, briefly discussed above, is suitable for studying the linear stability of dynamical systems describing periodic phenomena (systems of ODEs). In this work, the system relative to the modified GC minimal model, constituted by one PDE and one ODE [Eqs (5.32)-(5.38)], is a spatially extended dynamical system. The dependent variables, $\bar{V}$ and v, of the modified GC minimal model are time- and space-dependent.

However, the spatial discretization of the problem leads to a dynamical system of dimension $2 \times (M+1)$, which corresponds to twice the number of spatial points (two ODEs for each spatial point). Therefore, as a first approach, it can be reasonably assumed that the study of the linear stability of the dynamical system, resulting from the discretization of the real spatially extended system examined in this work, can provide significant information about the linear stability of this real spatially extended system.

It is important to keep in mind that the conclusions summarized in Tab. 5.5 are theoretically valid for (non-spatially extended) dynamical systems. As a consequence, the conclusions established in the following must be handled with care and taken as a first characterization of the real spatially extended system.

5.1.12.1 Computation of the eigenvalues of the monodromy matrix

From a numerical point of view, there are different algorithms enabling to compute the eigenvalues of a matrix. The monodromy matrix is characterized by a dimension of $(2\,M+2)\times(2\,M+2)$. For instance, assuming that the cardiac fiber has a length of $7\,\mathrm{cm}$, the spatial discretization described in section 5.1.5.1, with $\Delta X = 0.02\,\mathrm{cm}$, leads to $M = 350$. Thus, the monodromy matrix has a dimension of 702×702.

A first approach would be to compute the entire eigenspectrum of the monodromy matrix with a direct approach. However, the Floquet stability analysis enables to know how the periodic solution becomes unstable only with the eigenvalues of the monodromy matrix with the largest magnitudes. For this particular case, a suitable approach, which reduces the computational cost, is used: the *Arnoldi iteration* [111]. This method is based on an iterative procedure that relies on *Krylov subspaces.*

Krylov subspaces

Assume a nonsingular matrix $[A] \in \mathbb{C}^{n\times n}$ and $[v] \neq [0] \in \mathbb{C}^{n\times 1}$. The *Krylov subspace* of order p, $\mathcal{K}_p$, generated by $[A]$ from $[v]$ is

$$\mathcal{K}_p\left([A]\,,[v]\right) \;=\; \operatorname{span}\left\{[v]\,,\,[A]\,[v]\,,\,[A]^2\,[v]\,,\,\ldots,\,[A]^{p-1}\,[v]\right\}\,. \tag{5.97}$$

Basically, the Arnoldi iteration is an orthonormal projection of $[A]$ onto a Krylov subspace of order p, $\mathcal{K}_p\left([A]\,,[v]\right)$, usually with $p \ll n$ [112]. In other words, the Arnoldi iteration is the *standard Gram-Schmidt orthonormalization procedure* [112] applied to the Krylov subspace $\mathcal{K}_p\left([A]\,,[v]\right)$. As a result, the Arnoldi iteration reduces the initial matrix $[A] \in \mathbb{C}^{n\times n}$ to a smaller *upper Hessenberg matrix* $[H] \in \mathbb{C}^{p\times p}$. The Arnoldi method is very useful because it enables to generate accurate eigenvalue approximations from a partial rather than a full upper Hessenberg factorization of the matrix $[A]$.

From a pragmatic point of view, p is taken equal to 40 to approximate the 20 eigenvalues of the monodromy matrix with the largest magnitudes: $|\lambda_1| \geq |\lambda_2| \geq \ldots \geq |\lambda_{19}| \geq |\lambda_{20}| \geq \ldots \geq |\lambda_{n-1}| \geq |\lambda_n|$. The determination of the value of p has been performed by a *trial-and-error method* to obtain the 20 eigenvalues with the largest magnitudes in an accurate way. The computation of the 20 eigenvalues with the largest magnitudes from the upper Hessenberg matrix $[H_{40}] \in \mathbb{C}^{40\times 40}$ is performed by using the *QZ eigensolver* implemented in the MATLAB® environment.

5.1.13 Tracking of the solution with respect to $\tilde{g}_{\text{sac}}$

The purpose of this section is to determine, for a given length of fiber, the values of $\tilde{g}_{\text{sac}}$ for which the branch of period-1 solutions is stable and unstable. Moreover, when the aforesaid branch becomes unstable, the Floquet multipliers enable to know the type of instability that occurs.

As shown in section 5.1.9, the simulations have highlighted that for a given IC and a specific temperature value, the AEA induced by the MEF occurs only for specific values of $\tilde{g}_{\text{sac}}$ and L, and is sustained either for a finite time interval or in a perpetual fashion.

The solution has been tracked with respect to $\tilde{g}_{\text{sac}}$ for six different length of the fiber: 3.5 cm, 5 cm, 6.5 cm, 8 cm, 9.5 cm, and 11 cm. Following the length of the fiber, the starting solution (depicted by a white point in Fig. 5.68), is characterized by different values of $\tilde{g}_{\text{sac}}$:

i. for $L = 3.5\,\text{cm}$, $L = 5\,\text{cm}$, or $L = 6.5\,\text{cm}$, $\tilde{g}_{\text{sac}} = 0.04$
ii. for $L = 8\,\text{cm}$, $\tilde{g}_{\text{sac}} = 0.045$
iii. for $L = 9.5\,\text{cm}$, $\tilde{g}_{\text{sac}} = 0.05$
iv. for $L = 11\,\text{cm}$, $\tilde{g}_{\text{sac}} = 0.055$

Note that these particular period-1 solutions have been obtained with $T = 37\,^\circ\text{C}$ and an initial excitation applied to the region of the fiber ranging from $L/10 - 0.04\,\text{cm}$ to $L/10 + 0.04\,\text{cm}$.

The tracking is performed in both directions (as depicted by doubleheaded arrows in Fig. 5.68) by progressively increasing and decreasing the value of $\tilde{g}_{\text{sac}}$. The increment and decrement steps are similar and equal to 10^{-6}. After each increment (or decrement) of the value of $\tilde{g}_{\text{sac}}$, the new solution is obtained by a *continuation method* (*simple shooting approach*) [113]. For computational cost reasons, rather than computing the Floquet multipliers (time-consuming) for each increment (or decrement) step of the value of $\tilde{g}_{\text{sac}}$, the computation is performed every 50 increment (or decrement) steps.

The computational code developed for tracking the period-1 solutions and studying the stability of the solution is robust until the solution becomes unstable. It does not enable to track the unstable solutions (after an eigenvalue of the monodromy matrix has crossed the unit circle in the complex plane). In other words, the computational code ends a bit before an eigenvalue crosses the unit circle in the complex plane. This is due to some stopping criteria used by the continuation method developed in this work. Nevertheless, the computational code enables to determine the way the Floquet multipliers cross the unit circle in the complex plane.

5.1.13.1 Type of bifurcation as a function of L

Different types of bifurcations may be associated with each length of the fiber. The purpose of this section is precisely to highlight these bifurcations. Moreover, this section also determines, for each L, the range of $\tilde{g}_{\text{sac}}$ for which the branch of period-1 solutions is stable. Note that the size of this range is slightly underestimated due to stopping criteria used by the continuation method as already mentioned. To visualize the state of the system, the Floquet multiplier with the largest magnitude, $\lambda_{\text{max}} = |\lambda_{\text{max}}| \exp(i\,\theta_{\text{max}})$, is depicted in terms of its magnitude, $|\lambda|_{\text{max}}$, and its phase, θ_{max}, as a function of $\tilde{g}_{\text{sac}}$. If $\theta_{\text{max}} = 0$, when the Floquet multiplier crosses the unit circle in the complex plane, this means that the crossing occurs at $+1$. When $\theta_{\text{max}} = \pi$, the Floquet multiplier crosses the unit circle at -1. And finally, when $\theta \neq 0$ and $\theta \neq \pi$, the two complex conjugate Floquet multipliers cross the unit circle at $\exp(\pm i\,\theta_{\text{max}})$.

Length of the fiber: $3.5\,\text{cm}$**,** $5\,\text{cm}$**, and** $6.5\,\text{cm}$

For $L = 3.5\,\text{cm}$, the value of $\tilde{g}_{\text{sac}}$ is decreased from 4×10^{-2} to 3.255×10^{-2} (lower critical value of the stability window of $\tilde{g}_{\text{sac}}$ with respect to the branch of period-1 solutions) and increased from 4×10^{-2} to 4.845×10^{-2} (upper critical value of the stability window of $\tilde{g}_{\mathrm{sac}}$ with respect to the branch of period-1 solutions). Fig. 5.50 shows the magnitude, $|\lambda|_{\mathrm{max}}$, and the phase, θ_{max}, of the Floquet multiplier with the largest magnitude with respect to $\tilde{g}_{\mathrm{sac}}$. The Floquet multiplier λ_{max} crosses the unit circle at -1 for the lower critical value of $\tilde{g}_{\mathrm{sac}}$ and at $+1$ for the upper critical value of $\tilde{g}_{\mathrm{sac}}$ (Fig. 5.50). Therefore, this result highlights that the type of bifurcation leading to the loss of stability, for $L = 3.5\,\mathrm{cm}$, is different depending on whether the system leaves the stability range of $\tilde{g}_{\mathrm{sac}}$ with respect to the branch of period-1 solutions at the bottom or top.

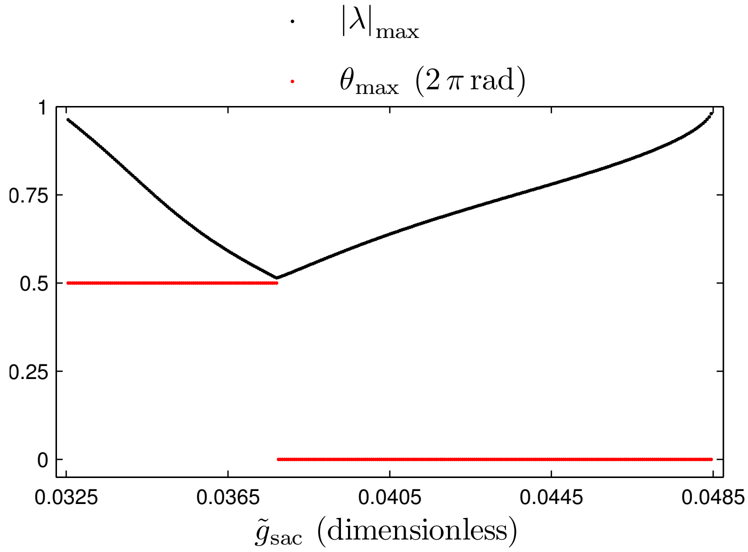

Fig. 5.50 – Magnitude and phase of the Floquet multiplier with the largest magnitude, in terms of $\tilde{g}_{\mathrm{sac}}$ and for $L = 3.5\,\mathrm{cm}$.

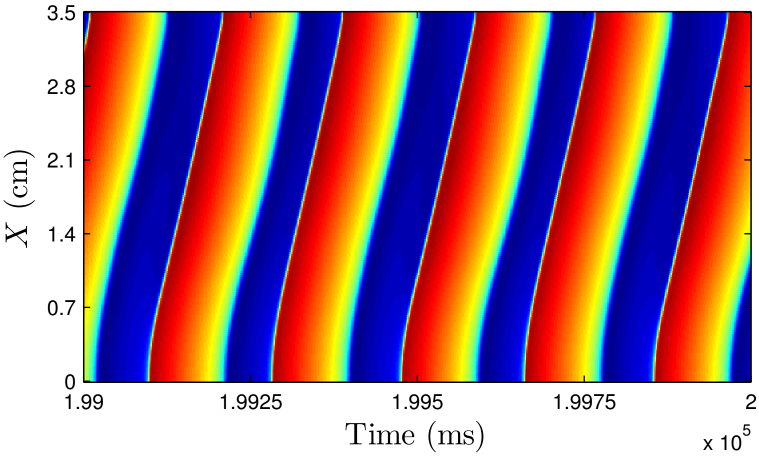

Fig. 5.51 – Time-space plot of the dimensionless membrane potential, $\bar{V}$, for $\tilde{g}_{\mathrm{sac}} = 0.0305$ and $L = 3.5\,\mathrm{cm}$, showing a period-2 cycle.

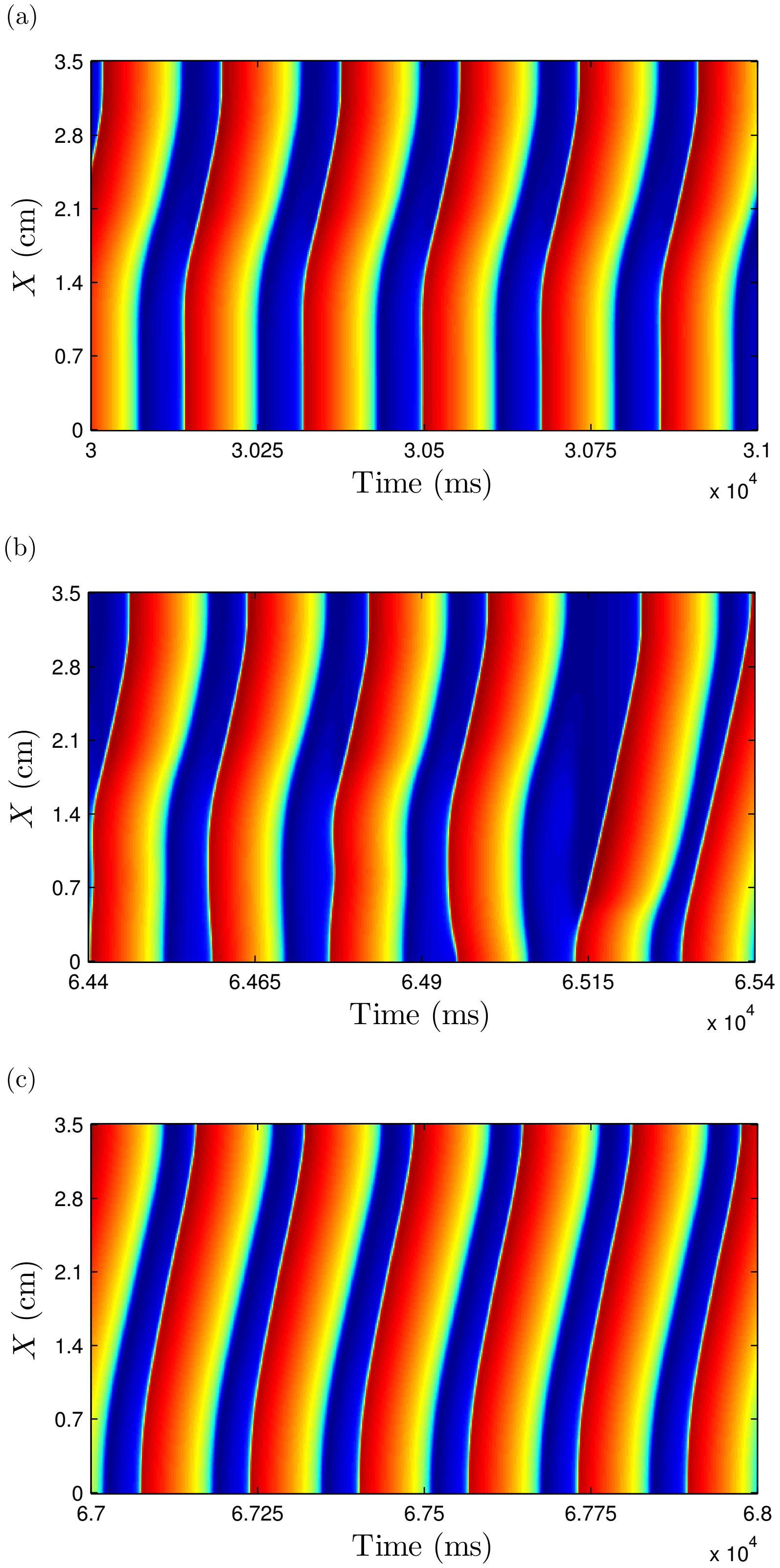

Fig. 5.52 – Time-space plots of the dimensionless membrane potential, $\bar{V}$, for $\tilde{g}_{\mathrm{sac}} = 0.05195$ and $L = 3.5\,\mathrm{cm}$. Regular spatio-temporal behaviors [(a) and (c)] are interrupted by irregular spatio-temporal behaviors during short time intervals (b).

Shortly after the bifurcation corresponding to λ_{max} crossing the unit circle at -1, the AEA is characterized by a periodic spatio-temporal pattern with a period-2 cycle (Fig. 5.51). The spatially averaged time periods of these alternans are equal to 197.3 ms and 180.8 ms. As a result, the loss of stability of the branch of period-1 solutions is induced by a supercritical flip bifurcation.

Shortly after the bifurcation corresponding to λ_{max} crossing the unit circle at $+1$, the AEA is characterized by a regular spatio-temporal pattern (Figs 5.52a and 5.52c) interrupted by irregular spatio-temporal patterns during short time intervals (Fig. 5.52b). This type of phenomenon is typical of intermittency. Due to the path λ_{max} takes when crossing the unit circle, the intermittency is probably a type I intermittency induced by a saddle-node bifurcation.

For $L = 5\,\mathrm{cm}$, as shown in Fig. 5.53, the loss of stability of the branch of period-1 solutions at the lower critical value of the stability range of $\tilde{g}_{\mathrm{sac}}$ is associated with λ_{max} that crosses the unit circle at -1. Therefore, the destabilization of this branch is induced by a flip bifurcation. Regarding the upper critical value of the stability range of $\tilde{g}_{\mathrm{sac}}$, the loss of stability of the branch of period-1 solutions corresponds to λ_{max} that crosses the unit circle at $+1$. Thus, the destabilization of this branch is generated by a saddle-node bifurcation.

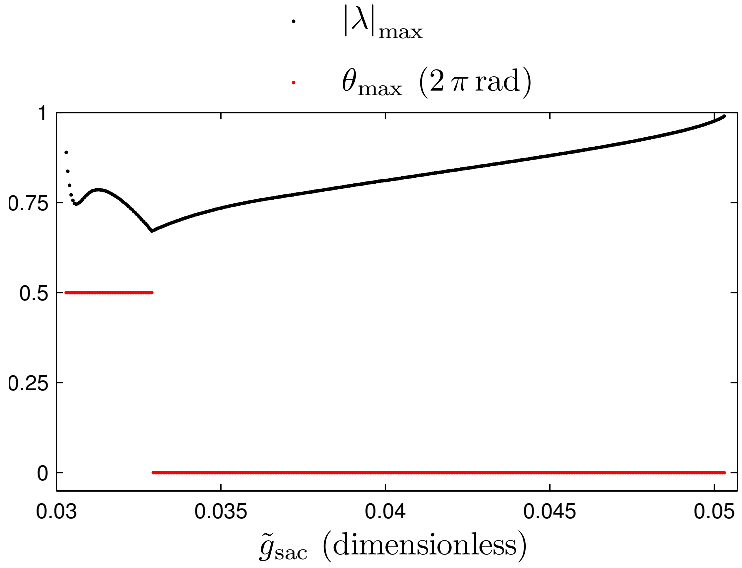

Fig. 5.53 – Magnitude and phase of the Floquet multiplier with the largest magnitude, with respect to $\tilde{g}_{\mathrm{sac}}$ and for $L = 5\,\mathrm{cm}$.

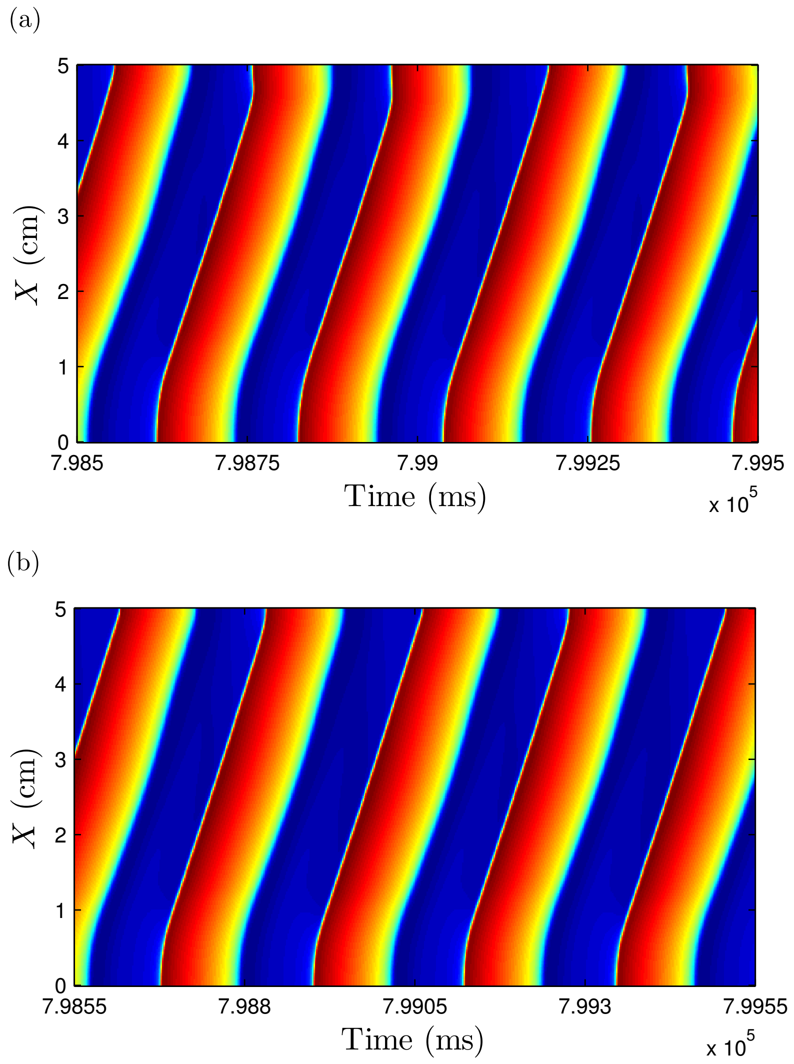

Fig. 5.54 – Time-space plots of the dimensionless membrane potential, $\bar{V}$, for $L = 5\,\mathrm{cm}$. Period-3 cycle for $\tilde{g}_{\mathrm{sac}} = 0.02830$ (a) and period-2 cycle for $\tilde{g}_{\mathrm{sac}} = 0.02775$ (b).

Shortly after the bifurcation ($\tilde{g}_{\mathrm{sac}} = 0.02830$) corresponding to $\lambda_{\max}$ that crosses the unit circle at -1, the AEA is characterized by a spatio-temporal behavior with a period-3 cycle (Fig. 5.54a). The characteristic spatially averaged time periods are approximately equal to 216.5 ms, 214.6 ms, and 206.3 ms. Continuing to decrease the value of $\tilde{g}_{\mathrm{sac}}$, the AEA is then characterized by a period-2 solution as shown in Fig. 5.54b ($\tilde{g}_{\mathrm{sac}} = 0.02775$). The spatially averaged time periods of these alternans are equal to 225.2 ms and 219.2 ms.

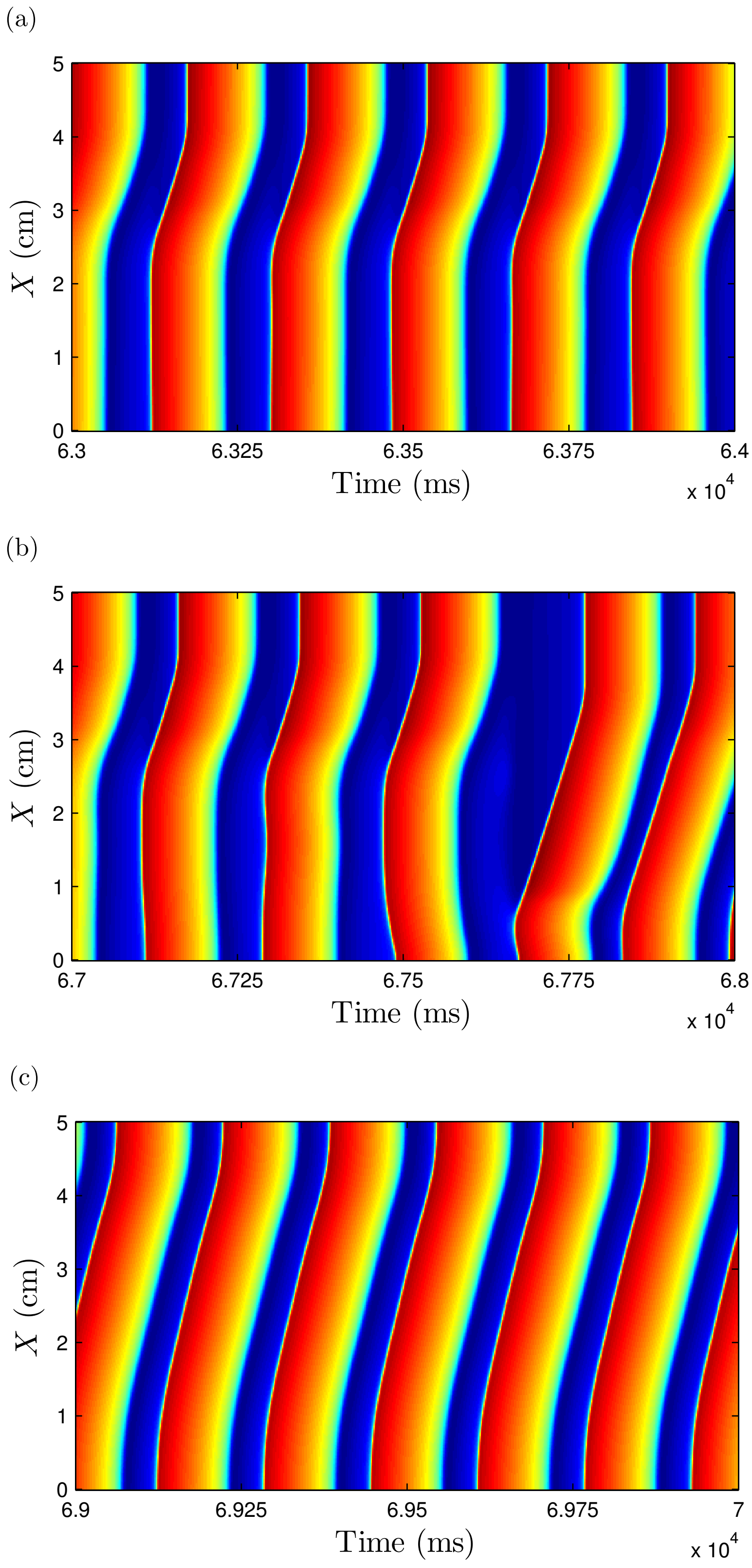

Fig. 5.55 – Time-space plots of the dimensionless membrane potential, $\bar{V}$, for $\tilde{g}_{\text{sac}} = 0.0514$ and $L = 5\,\text{cm}$. Regular spatio-temporal behaviors [(a) and (c)] are interrupted by irregular spatio-temporal behaviors during short time intervals (b).

Due to the path λ_{max} takes when crossing the unit circle, the loss of stability of the branch of period-1 solutions is associated with a flip bifurcation. However, it is tricky to determine whether this flip bifurcation is subcritical or supercritical because typical phenomena induced by such bifurcations (intermittency and period doubling) are not directly observed in the present case.

The inspection of the AEA, shortly after the saddle-node bifurcation (λ_{max} crossing the unit circle at $+1$), highlights regular spatio-temporal patterns (Figs 5.55a and 5.55c) interrupted by irregular patterns during short time intervals (Fig. 5.55b). This intermittency phenomenon, seems again to be a type I intermittency induced by a saddle-node bifurcation.

Finally, it can be noted that the stability window of $\tilde{g}_{\mathrm{sac}}$ with respect to the branch of period-1 solutions is a bit larger than this for $L = 3.5\,\mathrm{cm}$, and it ranges from 3.03×10^{-2} to 5.03×10^{-2} (Fig. 5.53).

For $L = 6.5\,\mathrm{cm}$, the stability window of $\tilde{g}_{\mathrm{sac}}$ with respect to the branch of period-1 solutions ranges from 3.215×10^{-2} to 4.91×10^{-2}. As shown in Fig. 5.56, the destabilization of the branch of period-1 solutions at the lower and upper critical values of the stability range of $\tilde{g}_{\mathrm{sac}}$ is associated with a flip bifurcation and a saddle-node bifurcation, respectively.

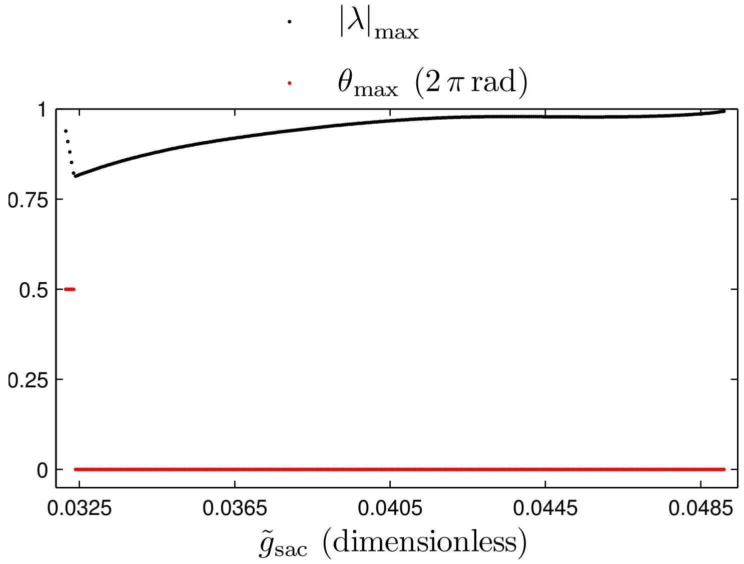

Fig. 5.56 – Magnitude and phase of the Floquet multiplier with the largest magnitude, in terms of $\tilde{g}_{\mathrm{sac}}$ and for $L = 6.5\,\mathrm{cm}$.

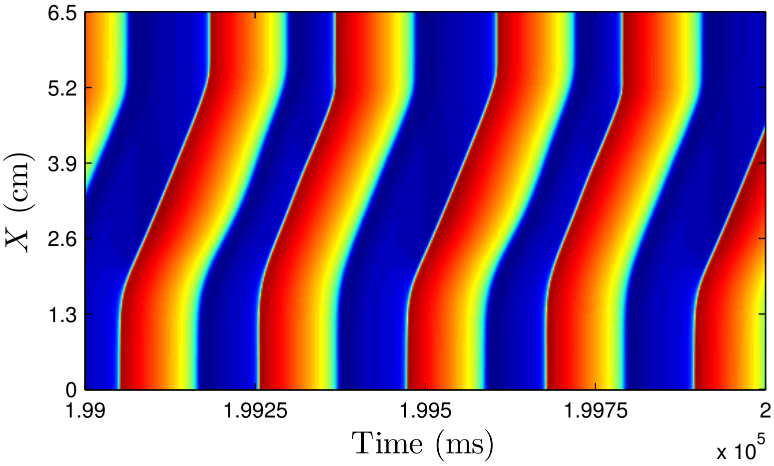

Fig. 5.57 – **Time-space plot of the dimensionless membrane potential, $\bar{V}$, for $\tilde{g}_{\text{sac}} = 0.0315$ and $L = 6.5\,\text{cm}$, showing a period-2 cycle.**

Shortly after the flip bifurcation, corresponding to λ_{max} crossing the unit circle at -1, the AEA appears to be characterized by a period-2 cycle (Fig. 5.57). Thus, the flip bifurcation is supercritical. The spatially averaged time periods of these alternans are equal to 227.3 ms and 194.5 ms.

Shortly after the saddle-node bifurcation, corresponding to λ_{max} crossing the unit circle at $+1$, the AEA is characterized by regular spatio-temporal patterns (Figs 5.58a and 5.58c) interrupted by irregular patterns during short time intervals (Fig. 5.58b). Therefore, the AEA seems to undergo an intermittency phenomenon, which is probably a type I intermittency due to the nature of the bifurcation.

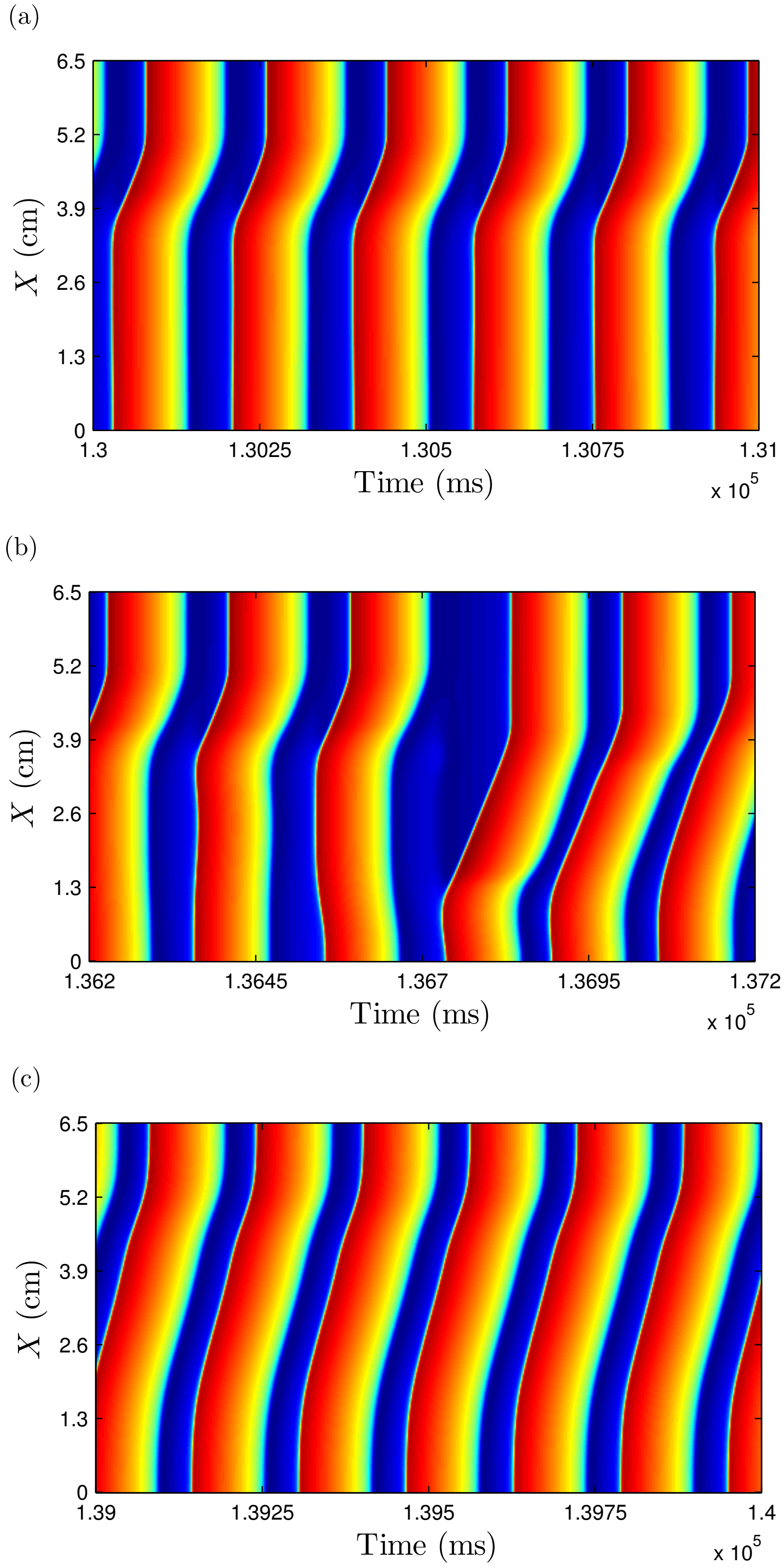

Fig. 5.58 – Time-space plots of the dimensionless membrane potential, $\bar{V}$, for $\tilde{g}_{\rm sac} = 0.0542125$ and $L = 6.5\,{\rm cm}$. Regular spatio-temporal behaviors [(a) and (c)] are interrupted by irregular spatio-temporal behaviors during short time intervals (b).

Length of the fiber: $8\,\mathrm{cm}$ **and** $9.5\,\mathrm{cm}$

For $L = 8\,\mathrm{cm}$, the stability window of $\tilde{g}_{\mathrm{sac}}$ with respect to the branch of period-1 solutions ranges from 3.205×10^{-2} to 5.69×10^{-2} (Fig. 5.59). The loss of stability of the branch of period-1 solutions is induced by a flip bifurcation at the lower critical value of the stability range of $\tilde{g}_{\mathrm{sac}}$ ($\lambda_{\max}$ crossing the unit circle at -1). At the upper critical value of the stability range of $\tilde{g}_{\mathrm{sac}}$, the destabilization of the branch of period-1 solutions corresponds to a Neimark–Sacker bifurcation (two complex conjugate Floquet multipliers cross the unit circle at $\exp(\pm i\,\theta)$ with $\theta \approx 6.58°$).

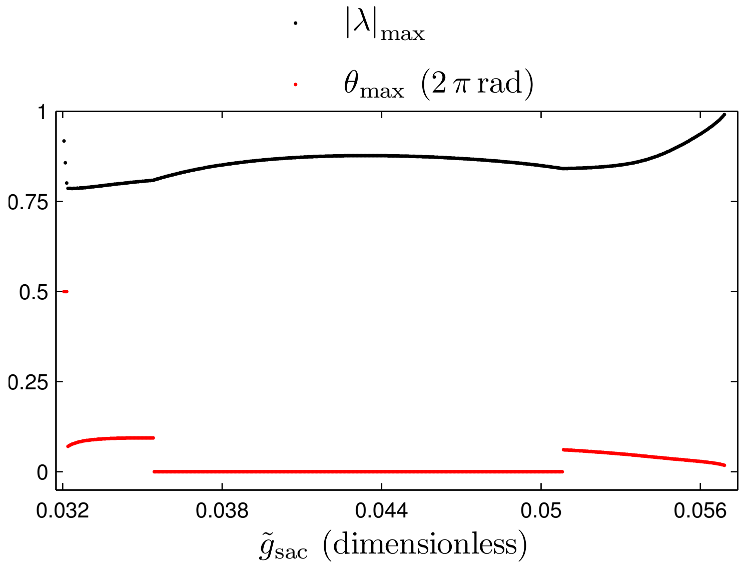

Fig. 5.59 – Magnitude and phase of the Floquet multiplier with the largest magnitude, with respect to $\tilde{g}_{\mathrm{sac}}$ **and for** $L = 8\,\mathrm{cm}$**.**

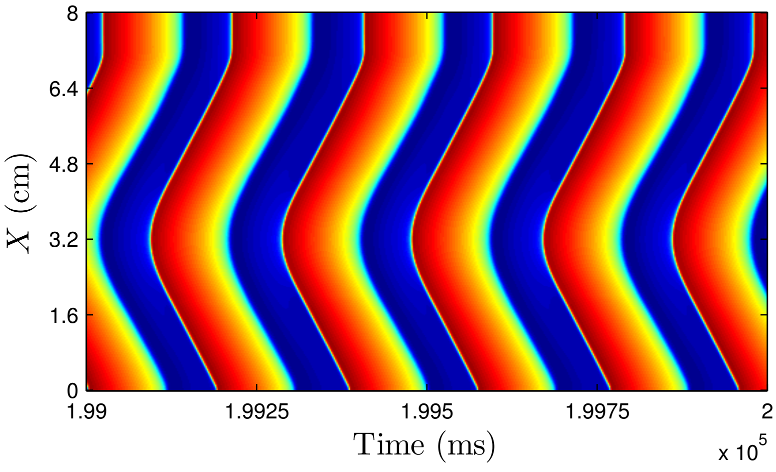

Fig. 5.60 – Time-space plot of the dimensionless membrane potential, $\bar{V}$**, for** $\tilde{g}_{\mathrm{sac}} = 0.03005$ **and** $L = 8\,\mathrm{cm}$**, showing a period-2 cycle.**

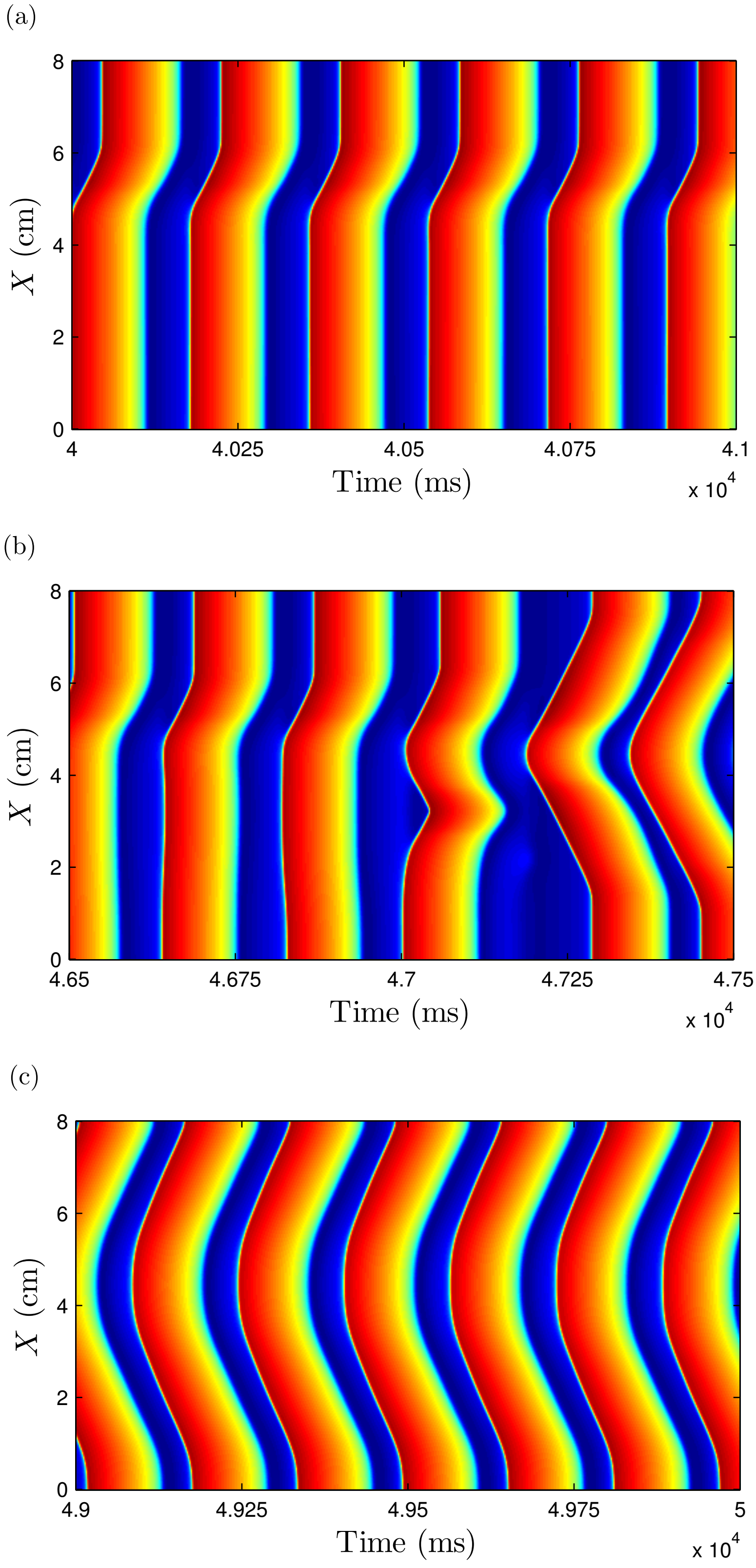

Fig. 5.61 – Time-space plots of the dimensionless membrane potential, $\bar{V}$, for $\tilde{g}_{\text{sac}} = 0.057105$ and $L = 8\,\text{cm}$. Regular spatio-temporal behaviors [(a) and (c)] are interrupted by irregular spatio-temporal behaviors during short time intervals (b).

Shortly after the flip bifurcation, an AEA characterized by a period-2 cycle (Fig. 5.60) is generated. As a result, this flip bifurcation is supercritical. The spatially averaged time periods of these alternans are equal to 194.3 ms and 188.6 ms.

Shortly after the Neimark–Sacker bifurcation, the AEA is characterized by regular spatio-temporal patterns interrupted by irregular patterns during short time intervals (Fig. 5.61). In other words, an intermittency phenomenon seems to occur. Since this phenomenon is induced by a Neimark–Sacker bifurcation, a type II intermittency can be assumed and, thus, the bifurcation is subcritical.

For $L = 9.5\,\mathrm{cm}$, the stability window of $\tilde{g}_{\mathrm{sac}}$ relative to the period-1 solution ranges from 3.145×10^{-2} to 6.105×10^{-2}. As shown in Fig. 5.62, the destabilization of the branch of period-1 solutions is characterized by a Floquet multiplier that crosses the unit circle at -1 at the lower critical value of the stability range of $\tilde{g}_{\mathrm{sac}}$. Therefore, a flip bifurcation occurs. At the upper critical value of the stability range of $\tilde{g}_{\mathrm{sac}}$, the loss of stability of the branch of period-1 solutions is associated with a Neimark–Sacker bifurcation because two complex conjugate Floquet multipliers cross the unit circle at $\exp(\pm i\,\theta)$ with $\theta \approx 10.71^{\circ}$.

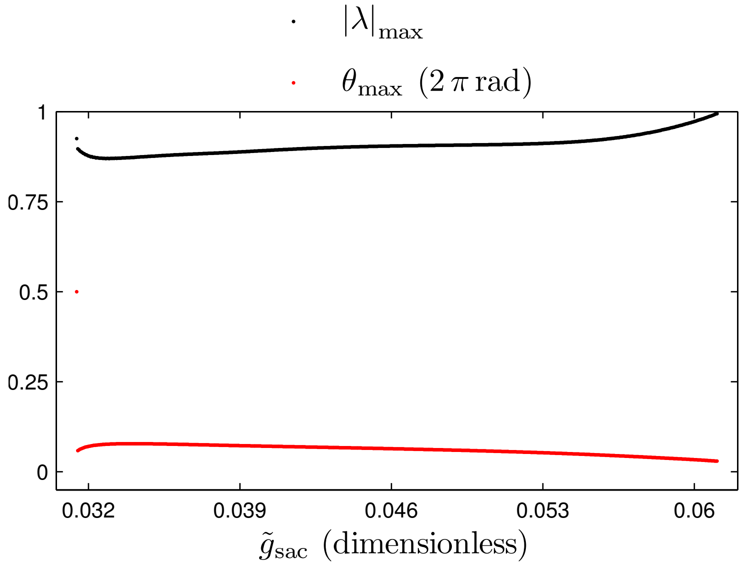

Fig. 5.62 – Magnitude and phase of the Floquet multiplier with the largest magnitude, with respect to $\tilde{g}_{\mathrm{sac}}$ and for $L = 9.5\,\mathrm{cm}$.

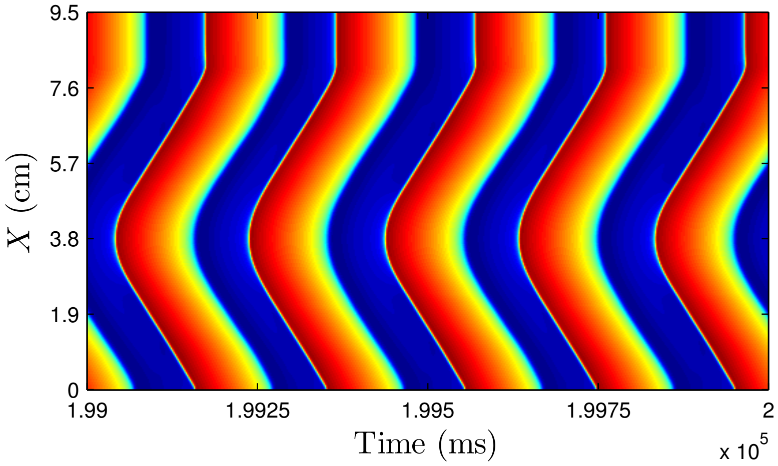

Fig. 5.63 – Time-space plot of the dimensionless membrane potential, $\bar{V}$, for $\tilde{g}_{\mathrm{sac}} = 0.0296$ and $L = 9.5\,\mathrm{cm}$, showing a period-2 cycle.

As shown in Fig. 5.63, shortly after the flip bifurcation ($\lambda_{\max}$ crossing the unit circle at -1), the AEA behaves in a periodic way with a period-2 cycle. The spatially averaged time periods of these alternans are equal to 202.7 ms and 193 ms. Due to this phenomenon, the flip bifurcation can be assumed to be supercritical.

Shortly after the Neimark–Sacker bifurcation, an intermittency phenomenon seems to occur. Regular spatio-temporal patterns (Figs 5.64a, 5.64c, and 5.64f) are interrupted by irregular patterns (Figs 5.64b, 5.64d, and 5.64e) during short time periods. Due to the path the two complex conjugate Floquet multipliers take when crossing the unit circle, the phenomenon is probably a type II intermittency and, thus, the Neimark–Sacker bifurcation is subcritical.

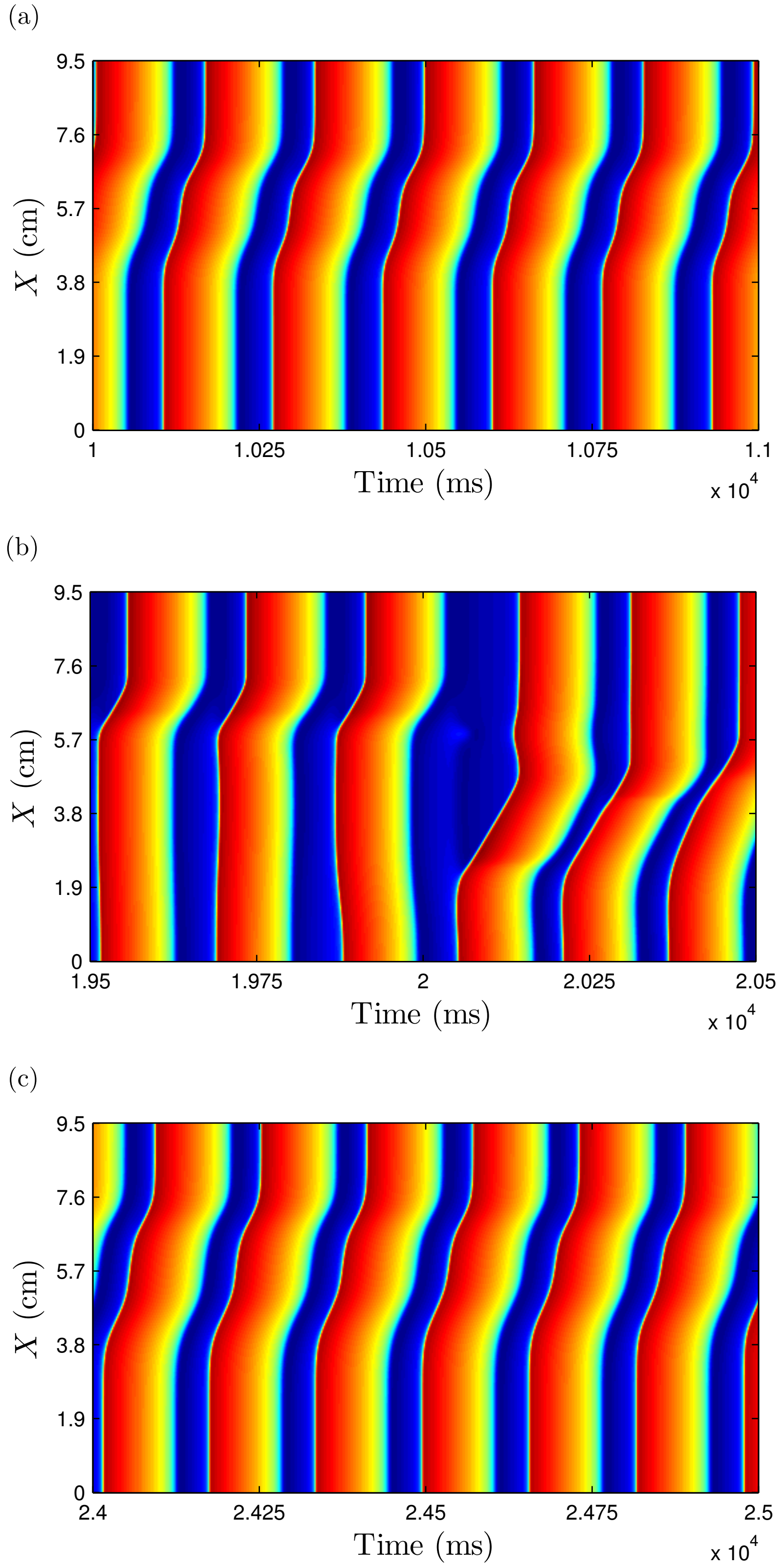

Fig. 5.64 – Time-space plots of the dimensionless membrane potential, $\bar{V}$, for $\tilde{g}_{\mathrm{sac}} = 0.06170$ and $L = 9.5\,\mathrm{cm}$. Regular spatio-temporal behaviors [(a), (c), and (f)] are interrupted by irregular spatio-temporal behaviors during short time intervals [(b), (d), and (e)].

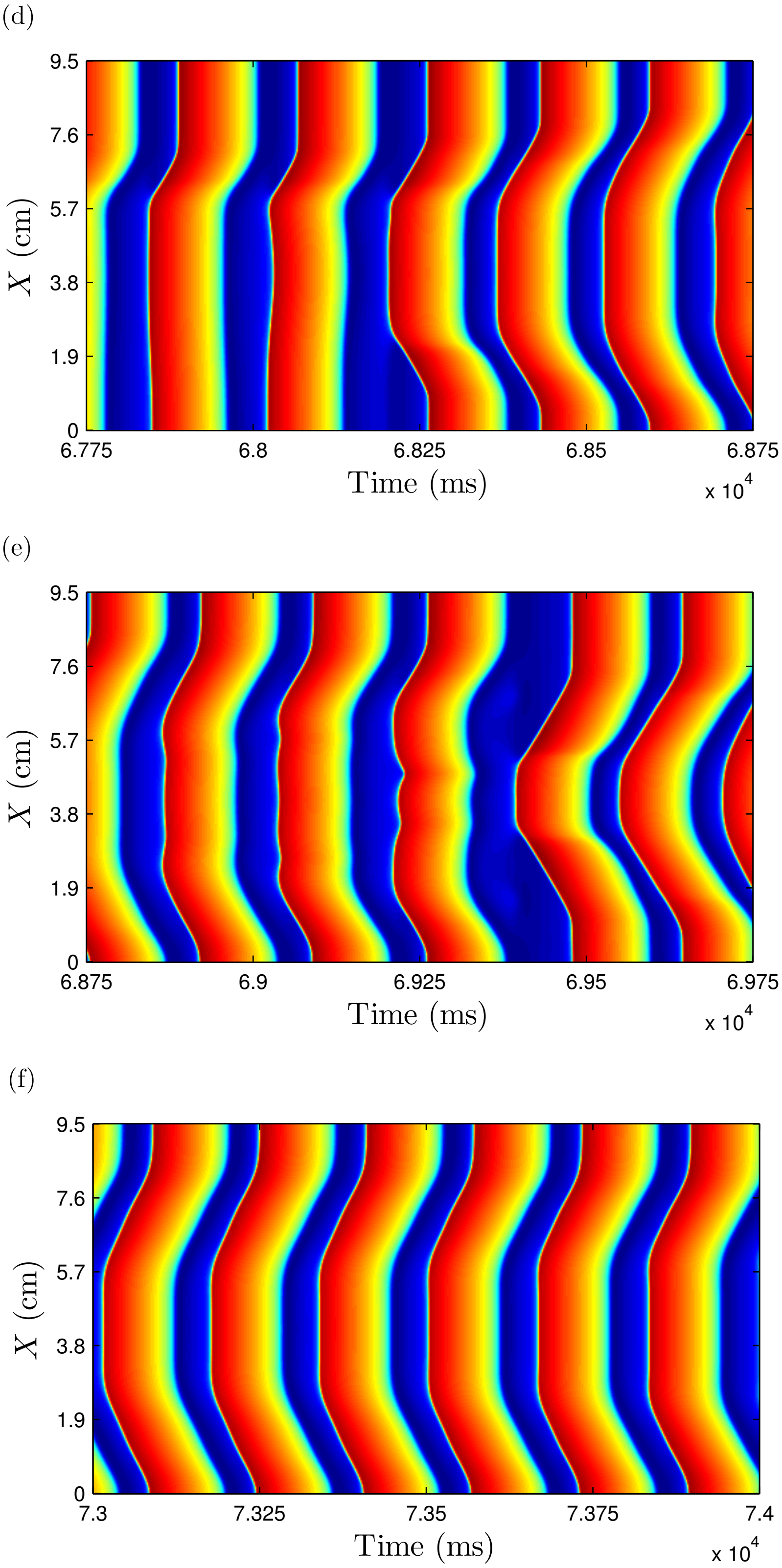

Fig. 5.64 – Time-space plots of the dimensionless membrane potential, $\bar{V}$, for $\tilde{g}_{\mathrm{sac}} = 0.06170$ and $L = 9.5\,\mathrm{cm}$. Regular spatio-temporal behaviors [(a), (c), and (f)] are interrupted by irregular spatio-temporal behaviors during short time intervals [(b), (d), and (e)].

Length of the fiber: 11 cm

The stability window of $\tilde{g}_{\mathrm{sac}}$ with respect to the branch of period-1 solutions ranges from 3.5×10^{-2} to 6.405×10^{-2}. Contrary to all previous cases, the loss of stability of the branch of period-1 solutions seems to be characterized by a Neimark–Sacker bifurcation (two complex conjugate Floquet multipliers cross the unit circle) both at the lower and upper critical values of the stability range of $\tilde{g}_{\mathrm{sac}}$. As shown in Fig. 5.65, the two pairs cross the unit circle at $\exp(\pm i\,\theta)$ with $\theta \approx 24.55^{\circ}$ and $\theta \approx 11.33^{\circ}$, respectively.

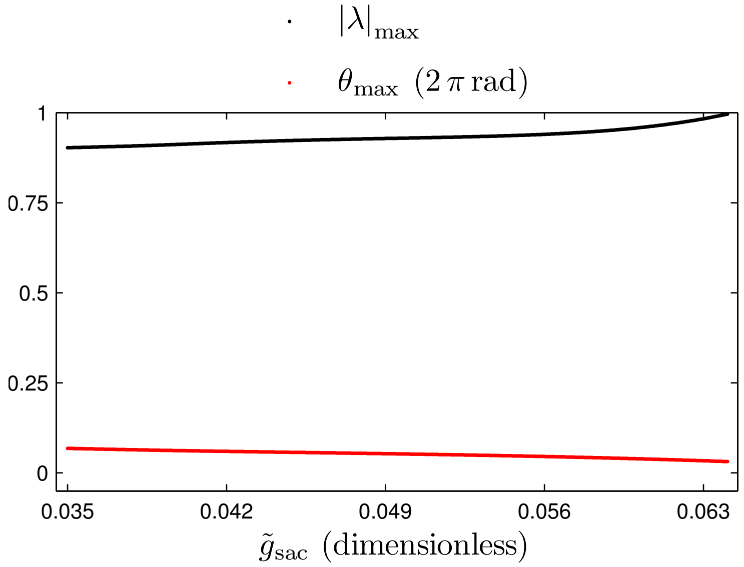

Fig. 5.65 – Magnitude and phase of the Floquet multiplier with the largest magnitude, with respect to $\tilde{g}_{\mathrm{sac}}$ and for $L = 11\,\mathrm{cm}$.

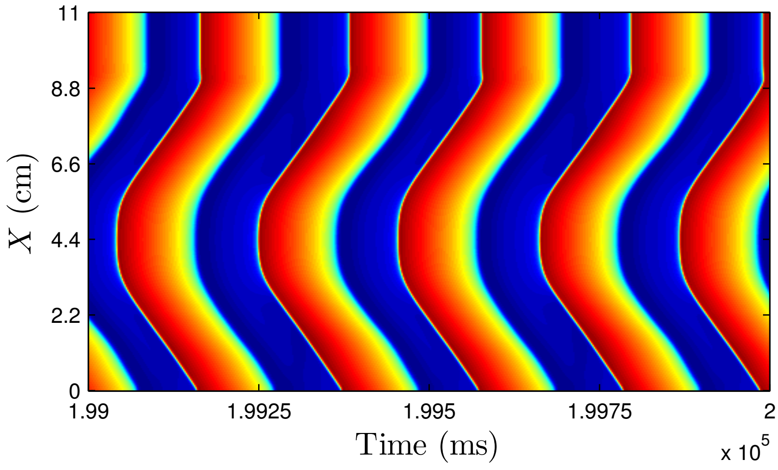

Fig. 5.66 – Time-space plot of the dimensionless membrane potential, $\bar{V}$, for $\tilde{g}_{\mathrm{sac}} = 0.03015$ and $L = 11\,\mathrm{cm}$, characterized by a periodic or a quasi-periodic solution with a period-2 cycle.

Shortly after the Neimark–Sacker bifurcation at the lower critical value of $\tilde{g}_{\mathrm{sac}}$ (pair of complex conjugate Floquet multipliers crossing the unit circle at $\exp\left(\pm i\,\theta_{\max}\right)$ with $\theta_{\max} \approx 24.55^{\mathrm{o}}$), the AEA is characterized by a period-2 solution (Fig. 5.66). This type of phenomenon is not expected to be induced by a Neimark–Sacker bifurcation.

A very plausible explanation is that the loss of stability of the branch of period-1 solutions is actually associated with a supercritical flip bifurcation leading to a new periodic solution with a period-2 cycle. In this case, $\lambda_{\max}$ should cross the unit circle at -1. As shown in Fig. 5.65, the tracking algorithm has ended quite far from $|\lambda_{\max}| = 1$. If the tracking algorithm had not ended so far from $|\lambda_{\max}| = 1$, the phase of $\lambda_{\max}$ would likely have switched to π rad as in the situation depicted in Fig. 5.62.

Shortly after the Neimark–Sacker bifurcation at the upper critical value of $\tilde{g}_{\mathrm{sac}}$ (pair of complex conjugate Floquet multipliers crossing the unit circle at $\exp\left(\pm i\,\theta_{\max}\right)$ with $\theta_{\max} \approx 11.33^{\mathrm{o}}$), the AEA is characterized by an intermittency as shown in Fig. 5.67. Due to the path the two complex conjugate Floquet multipliers cross the unit circle, this phenomenon is probably a type II intermittency and, thus, the Neimark–Sacker bifurcation is probably subcritical.

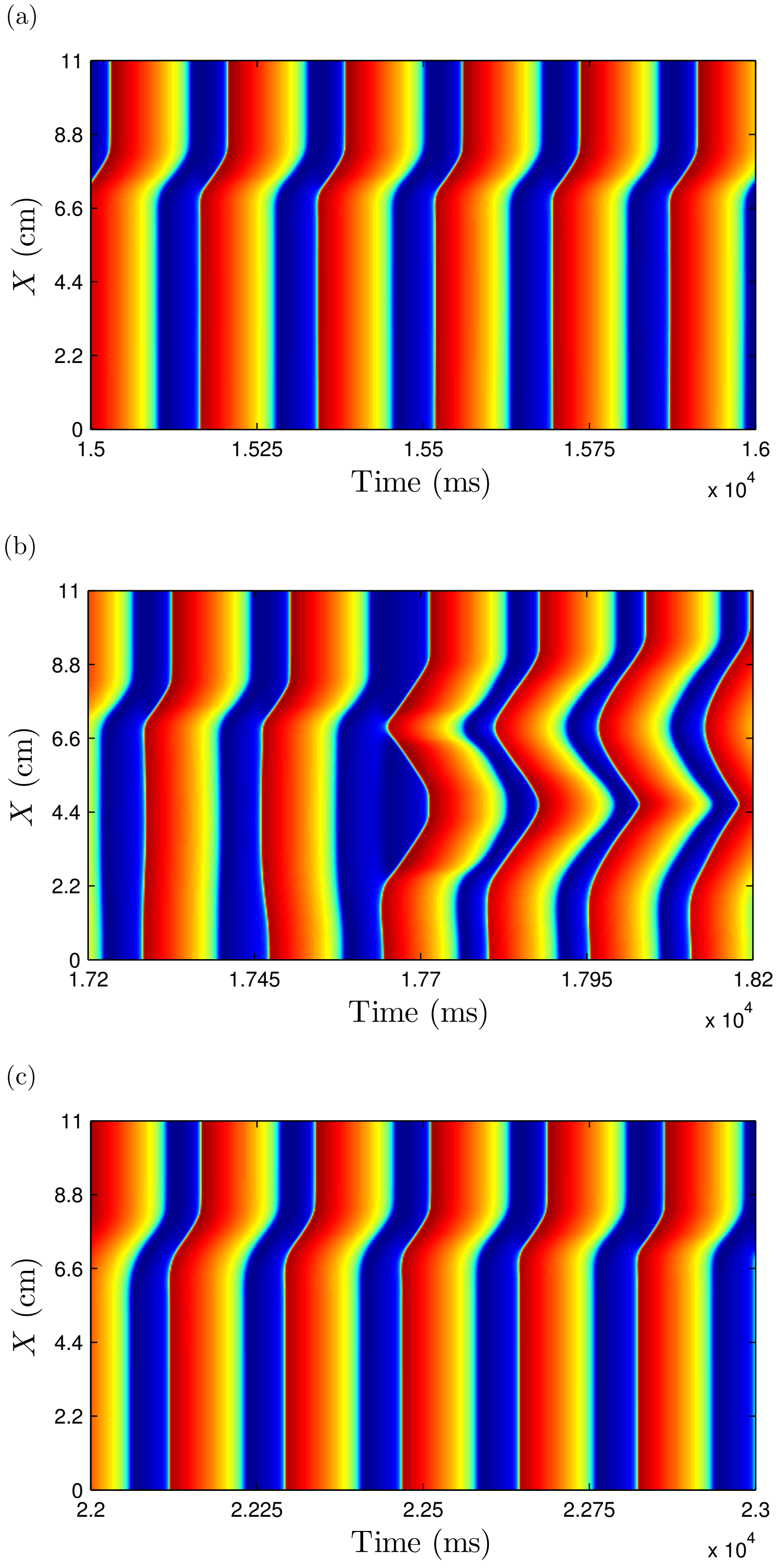

Fig. 5.67 – Time-space plots of the dimensionless membrane potential, $\bar{V}$, for $\tilde{g}_{\mathrm{sac}} = 0.06405$ and $L = 11\,\mathrm{cm}$. Regular spatio-temporal behaviors [(a) and (c)] are interrupted by irregular spatio-temporal behaviors during short time intervals [(b), (d), (e), and (f)].

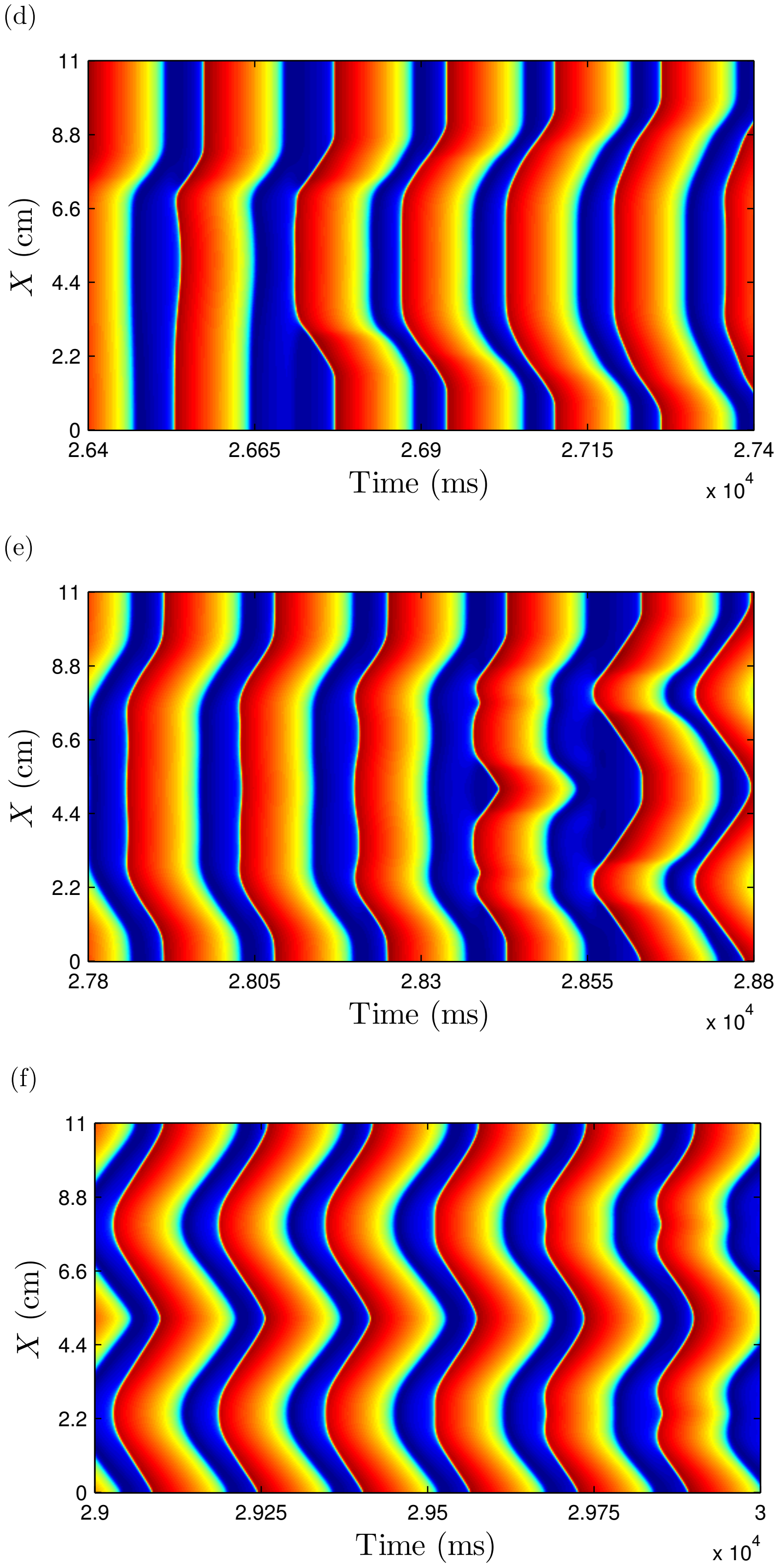

Fig. 5.67 – Time-space plots of the dimensionless membrane potential, $\bar{V}$, for $\tilde{g}_{\text{sac}} = 0.06405$ and $L = 11\,\text{cm}$. Regular spatio-temporal behaviors [(a) and (c)] are interrupted by irregular spatio-temporal behaviors during short time intervals [(b), (d), (e), and (f)].

5.1.13.2 Summary of the Floquet stability analysis

In summary, this Floquet stability analysis has emphasized that the loss of stability of the branch of period-1 solutions is induced by different types of bifurcations depending on the length of the fiber and whether the system leaves the stability range of $\tilde{g}_{\mathrm{sac}}$ with respect to the branch of period-1 solutions at the bottom or top (Fig. 5.68).

In addition, the analysis of the spatio-temporal behavior of the AEA, shortly after a particular type of bifurcation, has highlighted that specific spatio-temporal patterns are induced by specific types of bifurcations.

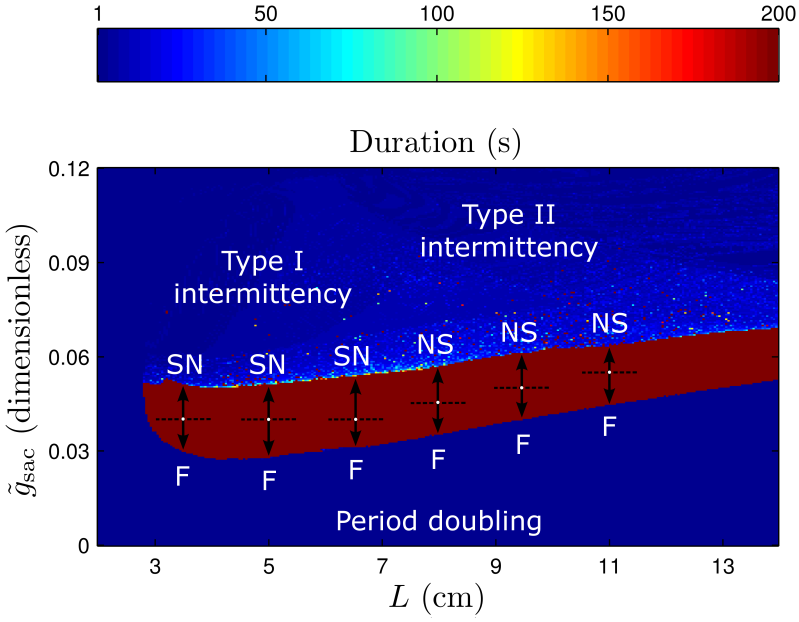

Fig. 5.68 – **Bifurcations leading to the loss of stability of the branches of period-1 solutions at the upper and lower boundaries of the main DRS for six different length of the fiber, L: 3.5 cm, 5 cm, 6.5 cm, 8 cm, 9.5 cm, and 11 cm. A flip bifurcation is denoted by F, a saddle-node bifurcation is denoted by SN, and a Neimark–Sacker bifurcation is denoted by NS. The white points correspond to the initial solutions used to track the branches of period-1 solutions and the doubleheaded arrows mean that the branches are tracked in both directions.**

In particular, for all the examined lengths of the fiber, the following observations can be made:

i. Shortly after the bifurcation occurring at the upper critical value of the stability range of $\tilde{g}_{\mathrm{sac}}$ with respect to the branch of period-1 solutions, an intermittency phenomenon (type I resulting from a saddle-node bifurcation and type II resulting from a Neimark–Sacker bifurcation) is induced and eventually leads to the end of the AEA, which corresponds to the region above the main DRS in Fig. 5.68.

ii. Shortly after the bifurcation occurring at the lower critical value of the stability range of $\tilde{g}_{\mathrm{sac}}$ with respect to the branch of period-1 solutions, a period doubling, namely a new periodic solution with a period-2 cycle (and period-3 cycle for $L = 5\,\mathrm{cm}$), is induced by a flip bifurcation and eventually leads to the end of the AEA (region under the main DRS in Fig. 5.68).

To go further into the understanding of the destabilization mechanisms and to corroborate the conclusions drawn from this work about the linear stability of the spatially extended system relative to the modified GC minimal model, a Floquet theory specially designed for PDEs should be used [114]. It could also be interesting to develop a tracking algorithm able to follow the solutions after that Floquet multipliers have crossed the unit circle. However, these two extensions have not been considered in this work.

5.2 Part 2: two-dimensional time-dependent TEM model

This section aims at studying the arrhythmogenic effects of the MEF within a TEM framework considering a two-dimensional geometry. This study must be thought as a first extension of the quantitative examination of the consequences of the MEF on arrhythmogenesis conducted in the one-dimensional case. In particular, it can be interesting to inspect whether the AEA induced by the MEF is characterized by similar features as those regarding the one-dimensional case:

i. Does the AEA depend on the SAC conductance and the size of the solving domain?
ii. Does the AEA depend on the location of the initial excitation applied to the cardiac muscle tissue?
iii. Does the temperature influence the spatio-temporal behavior of the AEA?

In addition, in a two-dimensional configuration, *re-entrant spiral waves* may occur[10]. In cardiac muscle tissue, these waves are life-threatening because they act as high frequency sources of waves that generate *tachycardia*, an abnormal rapid heart beat that is not controlled by the sino-atrial node. In ventricular tissue, tachycardia usually decays within a few seconds into *ventricular fibrillation (VF)* [119], which consists in an electrical activity which is completely spatio-temporally disorganized. This phenomenon leads to sudden cardiac death. In many cases, VF has been shown to be a consequence of several wandering spiral waves [120, 119, 121, 122, 123, 124]. As a result, it has been suggested that VF can be associated with the break of a spiral wave into multiple offsprings [125, 126].

In this context, it is interesting to qualitatively examine such phenomena within a TEM framework.

5.2.1 Mechanical assumptions

The two-dimensional configuration adopted in this work consists in a square-shaped slice of cardiac muscle tissue of side length L subject to the well-known *plane strain state* assumption. Mathematically, it means that the deformation gradient tensor, $\mathbf{F}$, can be represented in a given system of coordinates by a matrix, $[F]$, with a form

$$[F] = \begin{pmatrix} F^1_{\ 1} & F^1_{\ 2} & 0 \\ F^2_{\ 1} & F^2_{\ 2} & 0 \\ 0 & 0 & 1 \end{pmatrix} . \tag{5.98}$$

---

[10] A *re-entry* can be defined as a depolarization wave that repeatedly travels along a closed path. Re-entries are approximately periodic phenomena with respect to time and their frequencies exceed by far that of the sino-atrial node. In a two-dimensional context, re-entrant waves take the form of *spiral waves* [115]. These may be induced by both *anatomical* and *functional* causes.

Anatomical re-entry can occur when a depolarization wave is blocked by an obstacle in the tissue which is not able to conduct the depolarization wave. For instance, this obstacle may be made up of the orifice of a blood vessel, a region of unexcitable scar tissue, or a poorly excitable region induced by previous myocardial infarctions. The depolarization wave breaks when it strikes the aforesaid obstacle [116]. This wave then propagates around the obstacle and remains pinned to it. Note that the period of the spiral wave is defined by the CV and the size of the obstacle [117].

Functional re-entry does not need anatomic obstacles or local inhomogeneities to occur. This kind of phenomenon may be induced in a healthy cardiac tissue by functional conduction blocks. These can be generated by two causes:

i. a non-uniform dispersion of repolarization
ii. unidirectional blocks caused by stimuli at different sites [118]

Considering this assumption, the volume ratio, previously defined in Eq. (3.71), is now given by

$$J = F^1_{\ 1} F^2_{\ 2} - F^2_{\ 1} F^1_{\ 2} . \tag{5.99}$$

Assuming a plane strain state, the material constitutive laws in a two-dimensional case are provided by three-dimensional models, introduced in section 3.4, in which strains are simply set to zero in the third (irrelevant) direction, which is the direction normal to the plane of deformation. In addition, the cardiac tissue is assumed to passively behave like a compressible isotropic hyperelastic material. In particular, the strain-energy, Ψ, is described by a function, $\Psi_{\star}^{*,\mathrm{MR}}$, of $I_1(\mathbf{C})$ and $I_2(\mathbf{C})$ [69, 98]:

$$\begin{aligned} \Psi &= \Psi_{\star}^{*,\mathrm{MR}} \left[I_1(\mathbf{C}), I_2(\mathbf{C}) \right] \\ &= c_1 \left(I_1 - 3 \right) + c_2 \left(I_2 - 3 \right) . \end{aligned} \tag{5.100}$$

5.2.1.1 Boundary conditions

A no-displacement is applied on each boundary of the square-shaped slice of cardiac muscle tissue (the solving domain, Ω), respectively referred as to $\partial\Omega_1$, $\partial\Omega_2$, $\partial\Omega_3$, and $\partial\Omega_4$ to mechanically fix it. Mathematically, this condition is written as

$$\mathbf{u} = \mathbf{0} \quad \text{on } \partial\Omega_1 \cup \partial\Omega_2 \cup \partial\Omega_3 \cup \partial\Omega_4 \tag{5.101}$$

for any time t.

5.2.1.2 Initial conditions

Cardiac tissue is assumed to be initially ($t = t_0$) undeformed:

$$F^1_{\ 1} \left(X^1, X^2, t \right) \Big|_{t=t_0} = 1 , \tag{5.102}$$

$$F^1_{\ 2} \left(X^1, X^2, t \right) \Big|_{t=t_0} = 0 , \tag{5.103}$$

$$F^2_{\ 1} \left(X^1, X^2, t \right) \Big|_{t=t_0} = 0 , \tag{5.104}$$

$$F^2_{\ 2} \left(X^1, X^2, t \right) \Big|_{t=t_0} = 1 , \tag{5.105}$$

and

$$J\left(X^1, X^2, t\right)\Big|_{t=t_0} \;=\; 1 \qquad (5.106)$$

for any $(X^1, X^2) \in [0, L] \times [0, L]$.

5.2.2 Electrical assumptions

5.2.2.1 Boundary conditions

In a similar way as in the one-dimensional time-dependent TEM model, the domain Ω is assumed to be surrounded by an electrical insulator. Therefore, a no-flux boundary condition is applied on each boundary of the domain for the membrane potential. Mathematically, this condition is written as

$$\widehat{\mathbf{N}} \cdot (\mathrm{Grad}\, V_m) = 0 \quad \text{on } \partial\Omega\,, \qquad (5.107)$$

where $\widehat{\mathbf{N}}$ is the outward unit normal to the considered boundary and $\partial\Omega$ is the boundary of the solving domain, Ω (the square-shaped slice of cardiac muscle tissue).

5.2.2.2 Initial conditions

From one simulation to another, ICs for electrical variables may be changed. Consequently, the particular ICs used will be specified for each simulation.

5.2.3 Weak forms of the Cauchy's first equation of motion and the monodomain equation

Some numerical methods for solving *partial differential equations (PDEs)* require the formulation of these PDEs in a *weak form*. The *finite-element method (FEM)*, based on the weak form of PDEs, is a convenient, powerful, and popular numerical method to solve multi-dimensional problems. In the present work, this method has been used to solve the equations of the two-dimensional time-dependent TEM model. Therefore, the weak forms of the Cauchy's first equation of motion and the monodomain equation, involved in this model, must be established. This is precisely the purpose of this section.

5.2.3.1 Weak form of the Cauchy's first equation of motion

The well-known *principle of virtual work (PVW)* is a particular weak form of the Cauchy's first equation of motion. Assuming a *quasi-static case* (appendix A.2.1), the PVW is written, in the current configuration, Ω, as

$$\int_{\Omega} [\boldsymbol{\sigma} : \delta \mathbf{e}] \, \mathrm{d}\mathcal{V} \;=\; \int_{\Omega} \rho \, \mathbf{b} \cdot \delta \mathbf{u} \, \mathrm{d}\mathcal{V} + \int_{\partial \Omega_{\boldsymbol{\sigma}}} \bar{\mathbf{t}} \cdot \delta \mathbf{u} \, \mathrm{d}\mathcal{S} \,, \tag{5.108}$$

with

$$\delta \mathbf{e} \;=\; \frac{1}{2} \left(\mathrm{grad}^{\mathrm{T}} \, \delta \mathbf{u} + \mathrm{grad} \, \delta \mathbf{u} \right) . \tag{5.109}$$

Note that all details relative to the PVW are presented in appendix A.2.1. In Eq. (5.108), $\rho \, \mathbf{b}$, $\bar{\mathbf{t}}$, and $\boldsymbol{\sigma}$ represent the body force, the prescribed Cauchy traction vector, and the Cauchy stress tensor, previously introduced in Eqs (3.119) and (3.122). $\delta \mathbf{e}$ and $\delta \mathbf{u}$ represent the first variation of the Euler–Almansi strain tensor, $\mathbf{e}$ (section 3.2.6), and the *virtual displacement*, which satisfies some specific assumptions detailed in appendix A.2.1.1, respectively.

The weak form given by Eq. (5.108) can also be written in terms of the PK2 stress tensor, $\mathbf{S}$, introduced in section 3.3.2 and related to the Cauchy stress tensor by Eq. (3.142). In the reference configuration, Ω_0, the PVW is written as

$$\int_{\Omega_0} \mathbf{S} : \delta \mathbf{E} \, \mathrm{d}\mathcal{V}_0 \;=\; \int_{\Omega_0} \rho_0 \, \mathbf{B} \cdot \delta \mathbf{U} \, \mathrm{d}\mathcal{V}_0 + \int_{\partial \Omega_{0\,\boldsymbol{\sigma}}} \bar{\mathbf{T}}^{\star} \cdot \delta \mathbf{U} \, \mathrm{d}\mathcal{S}_0 \,, \tag{5.110}$$

with

$$\delta \mathbf{E} \;=\; \frac{1}{2} \left[\left(\mathbf{F}^{\mathrm{T}} \cdot \mathrm{Grad} \, \delta \mathbf{U} \right)^{\mathrm{T}} + \mathbf{F}^{\mathrm{T}} \cdot \mathrm{Grad} \, \delta \mathbf{U} \right] . \tag{5.111}$$

Note that $\delta \mathbf{E}$ is related to $\delta \mathbf{e}$ by the following relation:

$$\delta \mathbf{E} \;=\; \mathbf{F}^{\mathrm{T}} \cdot \delta \mathbf{e} \cdot \mathbf{F} \,. \tag{5.112}$$

In terms of components, Eq. (5.110) can be written as

$$\begin{aligned}\int_{\Omega_0} S^{MN}\, {F_N}^m \;\; \delta U_m|_M \, \mathrm{d}\mathcal{V}_0 \;\; &= \;\; \int_{\Omega_0} B^m \, \delta U_m \, \mathrm{d}\mathcal{V}_0 \\ &\quad + \int_{\partial\Omega_{0\,\sigma}} S^{MN}\, {F_N}^m \, N_M \, \delta U_m \, \mathrm{d}\mathcal{A}_0 \,, \qquad (5.113)\end{aligned}$$

where $\delta U_m|_M$ represents the covariant derivative (section 3.1.6) with respect to the X^M-coordinate. In addition, the last term on the RHS in Eq. (5.113) can be rewritten in terms of a volume integral by using the divergence theorem:

$$\begin{aligned}\int_{\partial\Omega_{0\,\sigma}} S^{MN}\, {F_N}^m \, N_M \, \delta U_m \, \mathrm{d}\mathcal{A}_0 \;\; &= \;\; \int_{\Omega_0} \left(S^{MN}\, {F_N}^m\right)\Big|_M \, \delta U_m \, \mathrm{d}\mathcal{V}_0 \\ &\quad + \int_{\Omega_0} S^{MN}\, {F_N}^m \;\; \delta U_m|_M \, \mathrm{d}\mathcal{V}_0 \,. \qquad (5.114)\end{aligned}$$

Substituting Eq. (5.114) into Eq. (5.113), the weak form of the Cauchy's first equation of motion can be rewritten, in terms of the reference configuration, Ω_0, as follows:

$$\int_{\Omega_0} \left[\frac{\partial}{\partial X^M}\left(S^{MN}\, {F_N}^m\right) - \Gamma^m_{kM}\left(S^{MN}\, {F_N}^k\right) + B^m\right] \delta U_m \, \mathrm{d}\mathcal{V}_0 \;\; = \;\; 0 \,, \qquad (5.115)$$

where Γ^m_{kM} represent the Christoffel symbols of the second kind (section 3.1.5).

5.2.3.2 Weak form of the monodomain equation

The strong form of the monodomain equation has been firstly established in section 2.2.3. Taking into account cardiac muscle tissue deformations, the monodomain equation has been rewritten in the reference configuration, Ω_0, as shown in Eq. (4.23).

As already mentioned, the FEM approach requires the weak form of PDEs. As a result, the corresponding weak form to Eq. (4.23) must be established. Adopting a weighted residual form to describe the membrane potential, V_m, over the reference configuration, Ω_0, and using an arbitrary weighting function, λ, the weak form of the monodomain equation may be written as

$$\int_{\Omega_0} \left[\frac{\partial V_m}{\partial t} + \frac{1}{C_m^0}\left(I^0_{\text{ion}} + I^0_{\text{sac}} + I^0_{\text{app}}\right) - D^0 \frac{\partial}{\partial X^M}\left(\sqrt{C}\, C^{MN} \frac{\partial V_m}{\partial X^N}\right)\right] \lambda \, \mathrm{d}\mathcal{V}_0 \;\; = \;\; 0 \,. \qquad (5.116)$$

5.2.4 Two-dimensional time-dependent simulations

The two-dimensional time-dependent simulations conducted in this work have been performed by using the finite-element software COMSOL Multiphysics® to solve the complete model given by Eqs (4.38)-(4.51). In these two-dimensional studies, all the model parameters (Tab. 5.6) and variables are made dimensionless in a similar way as in [98, 103] except the parameters relative to the temperature effects. The characteristic time, the characteristic length, and the characteristic pressure used here are equal to 10 ms, 0.1 cm, and 1 kPa, respectively. These values are consistent with those suggested in [23, 50].

Parameter	Value	Units
a	0.05	dimensionless
$\bar{D}^0$	1	dimensionless
$\bar{\varepsilon}_0$	0.1	dimensionless
$\bar{\varepsilon}_1$	1	dimensionless
$\bar{\kappa}_{\sigma_{\text{active}}}$	simulation-dependent	dimensionless
$\bar{\kappa}_v$	8	dimensionless
$\bar{g}_{\text{sac}}$	simulation-dependent	dimensionless
$\bar{c}_1$	2	dimensionless
$\bar{c}_2$	6	dimensionless
T_0	37	°C
T	simulation-dependent	°C
Q_{10}	3	dimensionless
B	0.008	$^{\circ}\mathrm{C}^{-1}$
$\bar{L}$	simulation-dependent	dimensionless

Tab. 5.6 – Parameter values for simulations with the two-dimensional time-dependent TEM model. All the parameters written as $(\bar{\bullet})$ are the parameters made dimensionless for the two-dimensional simulations.

5.2.4.1 Numerical aspects

The two-dimensional geometry is discretized by using a mapped mesh of *linear quadrilateral finite elements*. Quantities characterized by large spatial gradients are approximated by using *Bicubic Hermite shape functions* (appendix B.2.5) whereas *bilinear Lagrange shape functions* (appendix B.2.4) are used to approximate quantities that do not vary spatially in an abrupt way.

It is well known that many biological fields are characterized by nonlinear and C^1-

continuous variations with respect to space. Therefore, bicubic Hermite shape functions seem to be suitable for representing this kind of fields [127, 128]. In this work, all the electrophysiological variables ($\bar{V}$, v, σ_{active}) are represented by using bicubic Hermite shape functions and the displacement field is represented by using bilinear Lagrange shape functions.

The time-dependent solver used to solve the *nonlinear differential-algebraic system* resulting from the FE disretization is the *IDA solver* [129], a modernized implementation of the *DAE solver DASPK* [130], which uses *variable-order variable-step-size backward differentiation formulas* (first-order to fifth-order formulas are allowed). The IDA solver includes a *Newton solver* to solve the nonlinear system of equations. This Newton solver uses a particular linear solver for the resulting linear systems. Here, a direct solver is adopted: the *PARDISO solver*[131, 132]. Note that all these methods correspond to the versions implemented in COMSOL Multiphysics®.

5.2.4.2 Map in the $\left(\bar{L}, \bar{g}_{\text{sac}}\right)$ space of the persistence of the AEA induced by the MEF

The purpose of this section is essentially twofold:

i. Examine whether an AEA can be induced by the MEF in a two-dimensional configuration as observed in the previous one-dimensional study.
ii. Examine the conditions in terms of the values of $\bar{L}$ and $\bar{g}_{\text{sac}}$ under which the AEA may be perpetual.

Existence of an AEA induced by the MEF in a two-dimensional configuration

To examine this issue, the following parameter values are adopted: $\bar{L} = 28.8$, $\bar{g}_{\text{sac}} = 1$, $\bar{\kappa}_{\sigma_{\text{active}}} = 20$, and $T = 37\,°\text{C}$. All the other parameter values are given in Tab. 5.6. The initial excitation consists in a depolarization applied to a circular region at the center of the square with a radius length equal to 2.4 (dimensionless space units).

As shown in Fig. 5.69, there is a finite AEA induced by the MEF. After a few oscillations, the AEA vanishes: no electrical activity survives shortly after the instant $\bar{t} = 59$ (Fig. 5.69l).

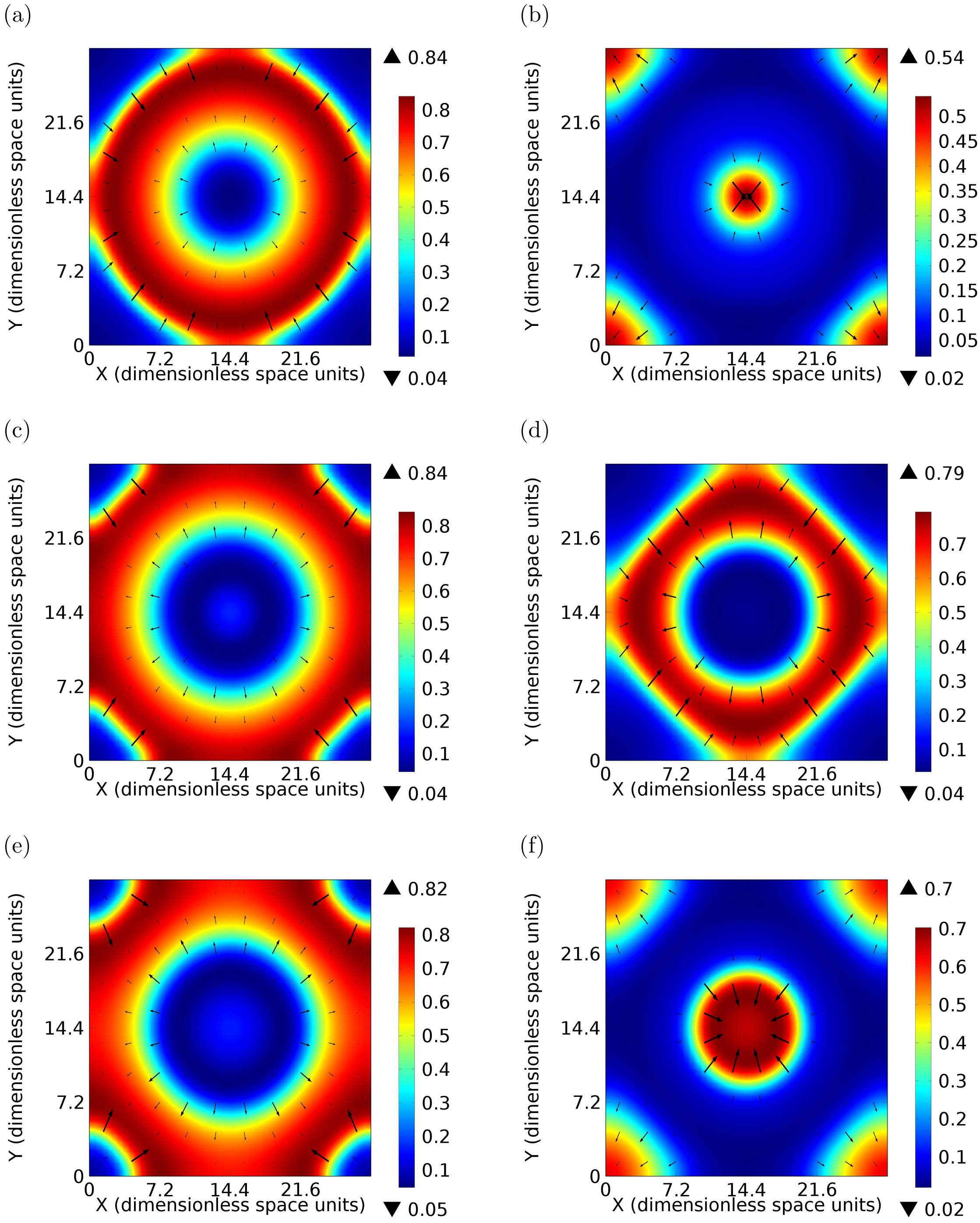

Fig. 5.69 – **Snapshots of the spatial distribution of the dimensionless membrane potential, $\bar{V}$, at $\bar{t} = 7$ (a), $\bar{t} = 13$ (b), $\bar{t} = 25$ (c), $\bar{t} = 37$ (d), $\bar{t} = 39$ (e), $\bar{t} = 43$ (f), $\bar{t} = 48$ (g), $\bar{t} = 51$ (h), $\bar{t} = 53$ (i), $\bar{t} = 55$ (j), $\bar{t} = 57$ (k), and $\bar{t} = 59$ (l). The black arrows depict the direction of the gradient of $\bar{V}$ and are proportional to its magnitude. Parameter values: Tab. 5.6 with $\bar{L} = 28.8$, $\bar{g}_{\text{sac}} = 1$, $\bar{\kappa}_{\sigma_{\text{active}}} = 20$, and $T = 37\,^{\circ}\text{C}$.**

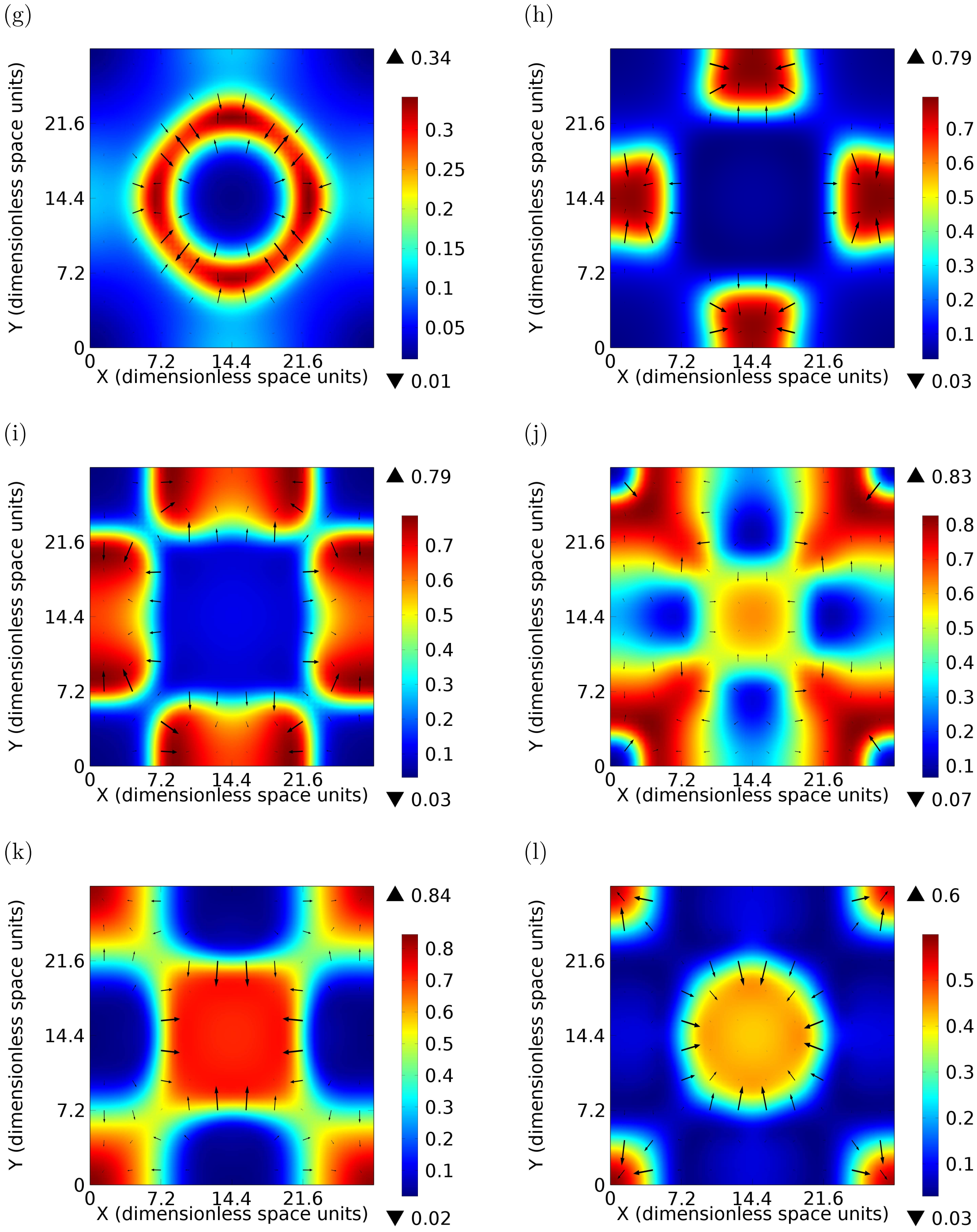

Fig. 5.69 – Snapshots of the spatial distribution of the dimensionless membrane potential, $\bar{V}$, at $\bar{t} = 7$ (a), $\bar{t} = 13$ (b), $\bar{t} = 25$ (c), $\bar{t} = 37$ (d), $\bar{t} = 39$ (e), $\bar{t} = 43$ (f), $\bar{t} = 48$ (g), $\bar{t} = 51$ (h), $\bar{t} = 53$ (i), $\bar{t} = 55$ (j), $\bar{t} = 57$ (k), and $\bar{t} = 59$ (l). The black arrows depict the direction of the gradient of $\bar{V}$ and are proportional to its magnitude. Parameter values: Tab. 5.6 with $\bar{L} = 28.8$, $\bar{g}_{\text{sac}} = 1$, $\bar{\kappa}_{\sigma_{\text{active}}} = 20$, and $T = 37\,^{\circ}\text{C}$.

In the beginning of the simulation, the AEA is induced by a single excitatory source, namely at the center of the square-shaped slice of cardiac tissue. This situation, characterized by a single excitatory source, lasts until the oscillation corresponding to $\bar{t} = 43$ (Fig. 5.69f). Then, the excitatory source is split into multiple excitatory sources due to the break of the propagating wave (Fig. 5.69g) as shown in Figs 5.69h and 5.69i. These multiple excitatory sources are actually spiral waves. These spirals are barely visible because they are not able to spatially develop in this situation but their tip can be clearly observed in Fig. 5.69i. Shortly after the onset of these spirals, they collide two by two while an AP is triggered at the center of the square-shaped slice of cardiac tissue (Fig. 5.69j). The propagation of this AP is quickly blocked because the tissue is still in an ERS; thus, the AEA ends (Figs 5.69k and 5.69l).

It is also interesting to note that, in the beginning of the simulation, the AP propagates from the center to the boundaries as a circular-like wave (Fig. 5.69a). This is due to the deformations occurring in the cardiac tissue. Without taking into account these deformations, the AP would propagate in a circular way (Fig. 5.70).

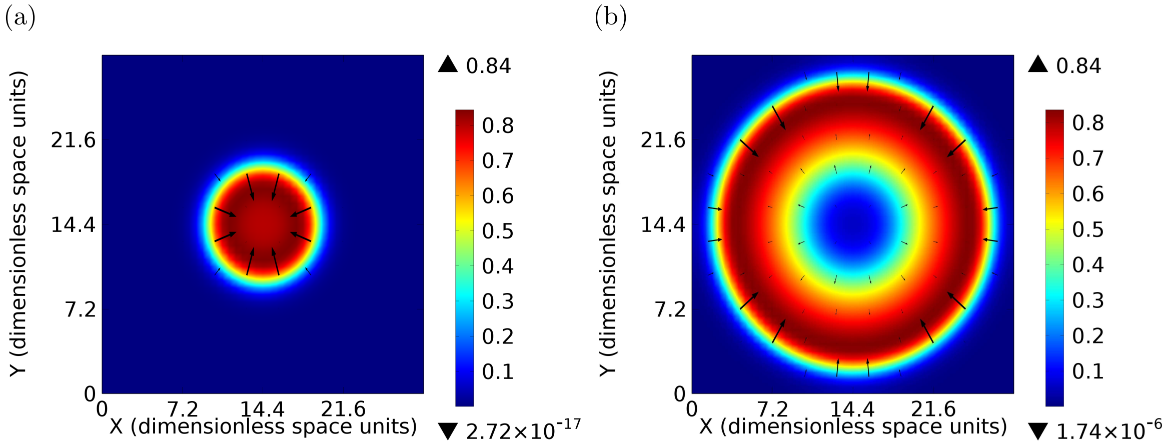

Fig. 5.70 – Snapshots of the spatial distribution of the dimensionless membrane potential, $\bar{V}$, at $\bar{t} = 2$ (a) and $\bar{t} = 7$ (b) for a purely electrical simulation. The black arrows depict the direction of the gradient of $\bar{V}$ and are proportional to its magnitude. The situation at $\bar{t} = 7$ (b) must be compared to Fig. 5.69a, which corresponds to the same instant.

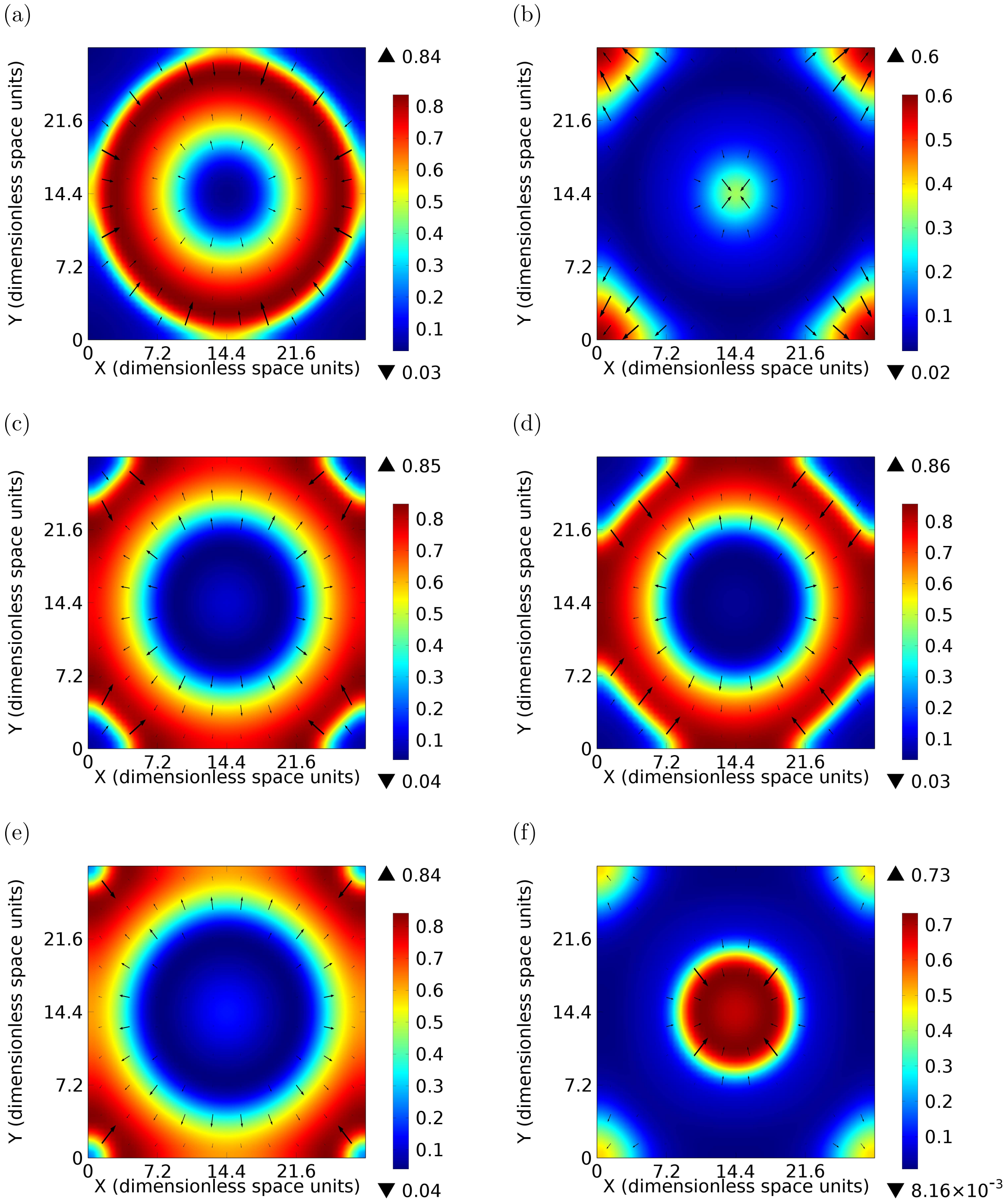

Fig. 5.71 – Snapshots of the spatial distribution of the dimensionless membrane potential, $\bar{V}$, at $\bar{t} = 7$ (a), $\bar{t} = 13$ (b), $\bar{t} = 25$ (c), $\bar{t} = 37$ (d), $\bar{t} = 39$ (e), $\bar{t} = 43$ (f), $\bar{t} = 48$ (g), $\bar{t} = 51$ (h), $\bar{t} = 53$ (i), $\bar{t} = 55$ (j), $\bar{t} = 168$ (k), and $\bar{t} = 172$ (l). The black arrows depict the direction of the gradient of $\bar{V}$ and are proportional to its magnitude. Parameter values: Tab. 5.6 with $\bar{L} = 28.8$, $\bar{g}_{\text{sac}} = 1$, $\bar{\kappa}_{\sigma_{\text{active}}} = 15$, and $T = 37\,^{\circ}\text{C}$.

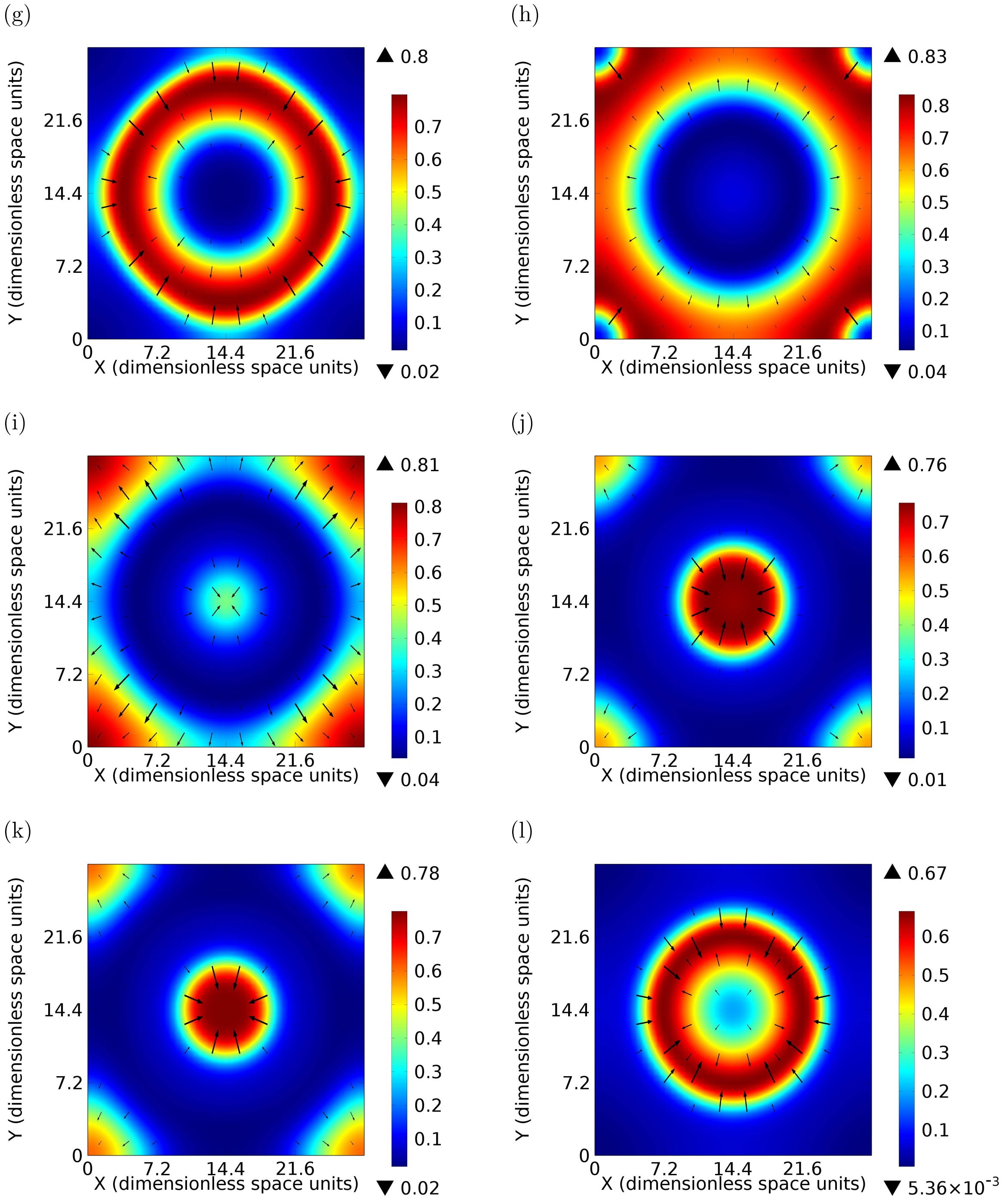

Fig. 5.71 – Snapshots of the spatial distribution of the dimensionless membrane potential, $\bar{V}$, at $\bar{t} = 7$ (a), $\bar{t} = 13$ (b), $\bar{t} = 25$ (c), $\bar{t} = 37$ (d), $\bar{t} = 39$ (e), $\bar{t} = 43$ (f), $\bar{t} = 48$ (g), $\bar{t} = 51$ (h), $\bar{t} = 53$ (i), $\bar{t} = 55$ (j), $\bar{t} = 168$ (k), and $\bar{t} = 172$ (l). The black arrows depict the direction of the gradient of $\bar{V}$ and are proportional to its magnitude. Parameter values: Tab. 5.6 with $\bar{L} = 28.8$, $\bar{g}_{\text{sac}} = 1$, $\bar{\kappa}_{\sigma_{\text{active}}} = 15$, and $T = 37\,^{\circ}\text{C}$.

Decreasing the value of $\bar{g}_{\mathrm{sac}}$ or $\bar{\kappa}_{\sigma_{\mathrm{active}}}$ should slow down the excitation process triggered by the SACs in the center of the square-shaped slice of cardiac tissue. For instance, assume that all the parameters are unchanged except that $\bar{\kappa}_{\sigma_{\mathrm{active}}}$ is set to 15. This means that the local active tension induced by the propagating wave will be smaller as the one occurring for $\bar{\kappa}_{\sigma_{\mathrm{active}}} = 20$. Thus, local stretchings will be smaller leading to smaller SACs [Eq. (4.49)].

Fig. 5.71 shows that an AEA occurs and is still sustained by the MEF in these conditions after more than 172 dimensionless time units. The spatio-temporal behavior of the dimensionless membrane potential depicted in Figs 5.71a-5.71j must be compared with the one depicted in Figs 5.69a-5.69j, which correspond exactly to the same moments.

The main difference between these two behaviors can be observed after approximately 48 dimensionless time units by comparing Fig. 5.69g with Fig. 5.71g. In the first situation (Fig. 5.69g), the depolarization wave is broken and multiple excitatory sources are induced by this phenomenon leading to complex spatial patterns and eventually to the end of the AEA. In the second situation (Fig. 5.71g), the depolarization wave does not break, which enables the excitatory source to remain single and the AEA to be sustained by the MEF for a longer period than the one observed in the first situation.

Conditions leading to a perpetual AEA

For reasons similar to those described in the one-dimensional study, a criterion must be chosen to determine whether the AEA is indefinitely sustained by the MEF or not. In this two-dimensional framework, the AEA will be considered as perpetual if the latter still occurs after 200 dimensionless time units. To determine the conditions in terms of $\bar{L}$ and $\bar{g}_{\mathrm{sac}}$ under which the AEA is perpetual, the $\left(\bar{L}, \bar{g}_{\mathrm{sac}}\right)$ space is scanned for $\bar{L} \in [28.8, 72]$ and $\bar{g}_{\mathrm{sac}} \in [0, 1.5]$ with increment steps of 7.2 and 0.125, respectively. For all the simulations, the same ICs as those introduced previously are used.

From these simulations, a qualitative map in the $\left(\bar{L}, \bar{g}_{\mathrm{sac}}\right)$ space of the persistence of the AEA induced by the MEF can be drawn (Fig. 5.72).

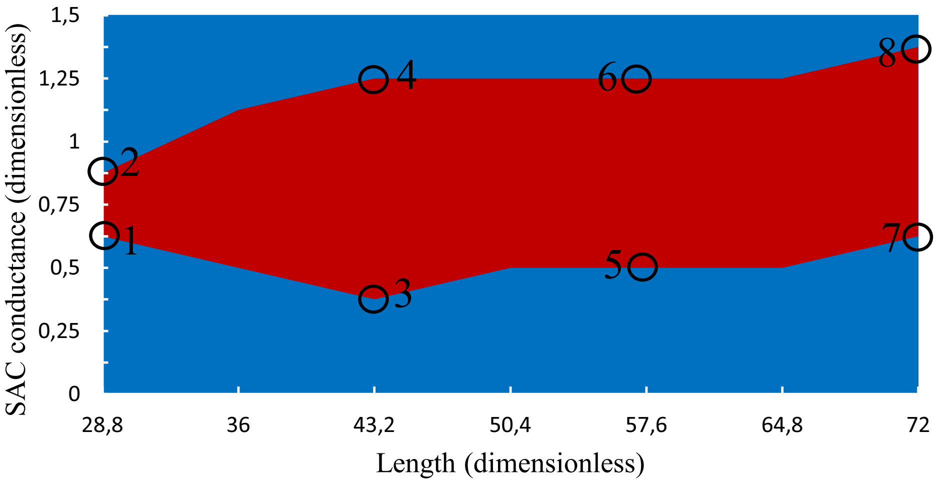

Fig. 5.72 – **Qualitative map in the $(\bar{L}, \bar{g}_{\text{sac}})$ space of the persistence of the AEA induced by the MEF for $T = 37\,^{\circ}\text{C}$. The dark red spot encapsulates all the situations corresponding to perpetual AEAs. The blue region encapsulates all the situations different from perpetual AEAs (no AEA at all or an AEA vanishing before 200 dimensionless time units).**

Contrary to the one-dimensional case studied before, this map (Fig. 5.72) does not show the duration of the persistence of the AEA for each particular points in the $\left(\bar{L}, \bar{g}_{\text{sac}}\right)$ space. This map consists in a dichotomy between the points $\left(\bar{L}, \bar{g}_{\text{sac}}\right)$ corresponding to perpetual AEAs (red region) and the points which do not correspond to such behaviors (blue region). In other words, the blue region in Fig. 5.72 encapsulates all the situations different from perpetual AEAs. It means that some points in this region correspond to finite AEAs vanishing before 200 dimensionless time units or no AEA at all.

Spatio-temporal patterns of perpetual AEAs

In Fig. 5.72, the red region highlights the points in the $\left(\bar{L}, \bar{g}_{\text{sac}}\right)$ space corresponding to AEAs. It could be interesting to examine the spatio-temporal patterns of the dimensionless membrane potential associated with these points. Typical spatio-temporal patterns of particular points in the $\left(\bar{L}, \bar{g}_{\text{sac}}\right)$ space are shown successively below (see labeled black circles in Fig. 5.72):

i. point 1 $(\bar{L} = 28.8, \bar{g}_{\text{sac}} = 0.625)$ and point 2 $(\bar{L} = 28.8, \bar{g}_{\text{sac}} = 0.875)$
ii. point 3 $(\bar{L} = 43.2, \bar{g}_{\text{sac}} = 0.375)$ and point 4 $(\bar{L} = 43.2, \bar{g}_{\text{sac}} = 1.25)$
iii. point 5 $(\bar{L} = 57.6, \bar{g}_{\text{sac}} = 0.5)$ and point 6 $(\bar{L} = 57.6, \bar{g}_{\text{sac}} = 1.25)$
iv. point 7 $(\bar{L} = 72, \bar{g}_{\text{sac}} = 0.625)$ and point 8 $(\bar{L} = 72, \bar{g}_{\text{sac}} = 1.375)$

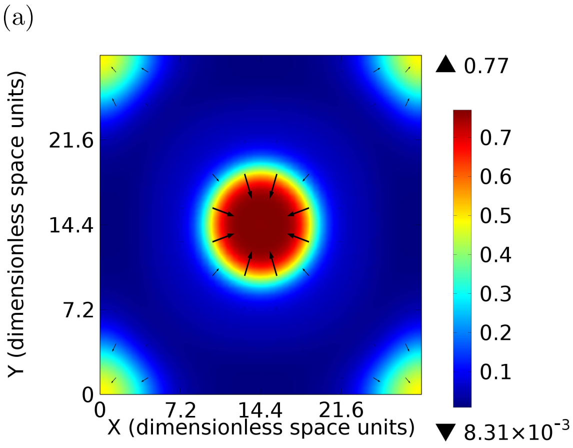

Fig. 5.73 – **Point** 1. **Snapshots of the spatial distribution of the dimensionless membrane potential,** $\bar{V}$**, at** $\bar{t} = 192$ **(a) and** $\bar{t} = 200$ **(b). Parameter values: Tab. 5.6 with** $\bar{L} = 28.8$**,** $\bar{g}_{\text{sac}} = 0.625$**,** $\bar{\kappa}_{\sigma_{\text{active}}} = 20$**, and** $T = 37\,^{\circ}\text{C}$**.**

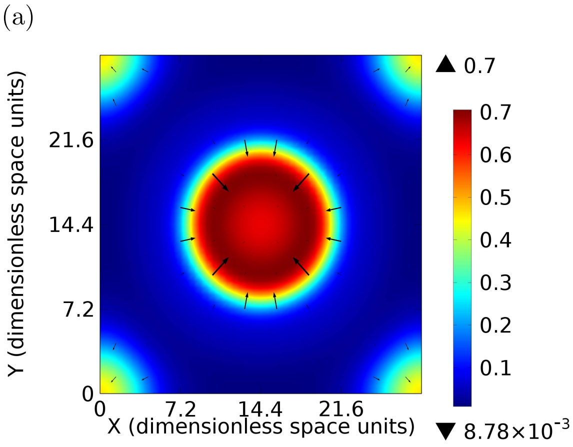

Fig. 5.74 – **Point** 2. **Snapshots of the spatial distribution of the dimensionless membrane potential,** $\bar{V}$**, at** $\bar{t} = 188$ **(a) and** $\bar{t} = 194$ **(b). Parameter values: Tab. 5.6 with** $\bar{L} = 28.8$**,** $\bar{g}_{\text{sac}} = 0.875$**,** $\bar{\kappa}_{\sigma_{\text{active}}} = 20$**, and** $T = 37\,^{\circ}\text{C}$**.**

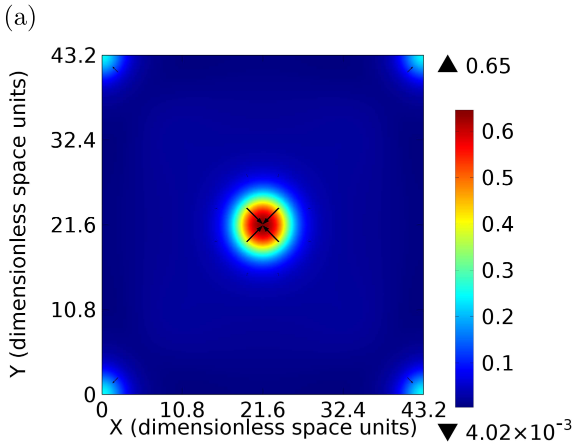

Fig. 5.75 – Point 3. **Snapshots of the spatial distribution of the dimensionless membrane potential,** $\bar{V}$**, at** $\bar{t} = 175$ **(a) and** $\bar{t} = 186$ **(b). Parameter values: Tab. 5.6 with** $\bar{L} = 43.2$**,** $\bar{g}_{\mathrm{sac}} = 0.375$**,** $\bar{\kappa}_{\sigma_{\mathrm{active}}} = 20$**, and** $T = 37\,^{\circ}\mathrm{C}$**.**

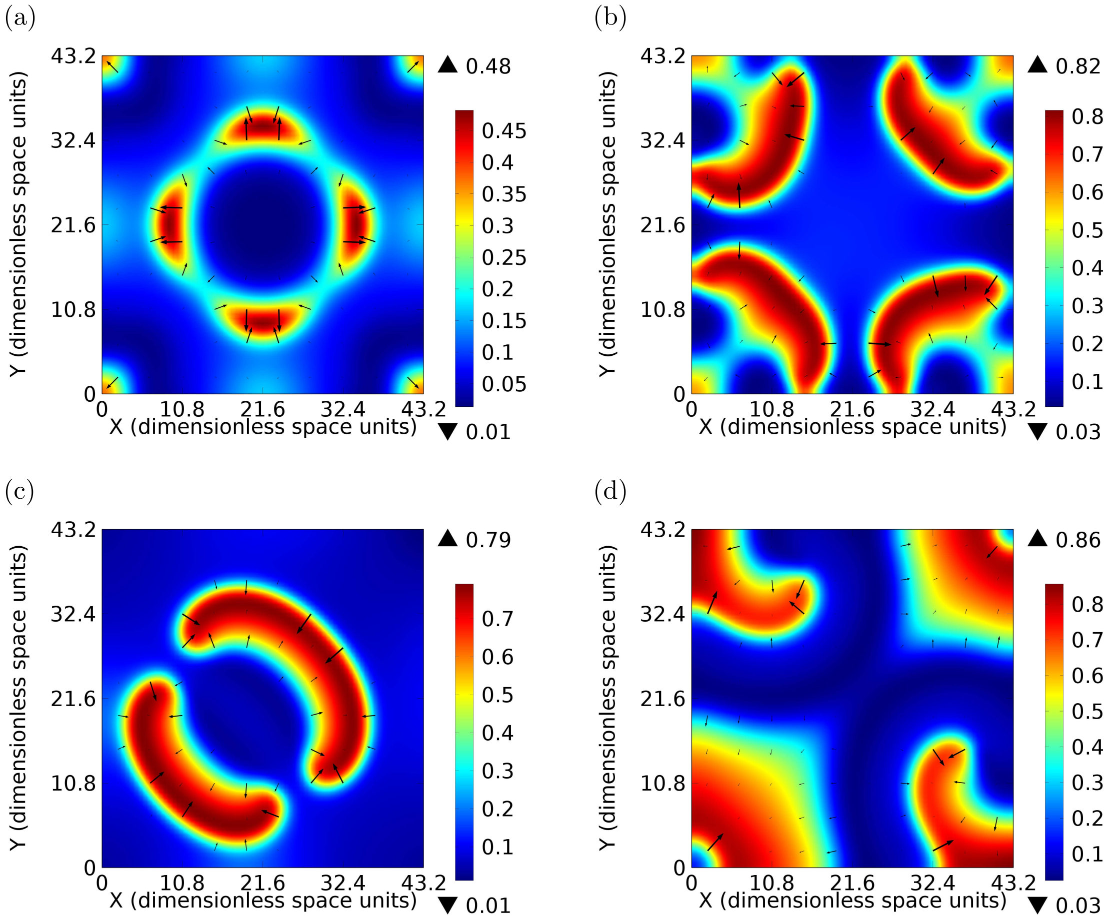

Fig. 5.76 – Point 4. **Snapshots of the spatial distribution of the dimensionless membrane potential,** $\bar{V}$**, at** $\bar{t} = 32$ **(a),** $\bar{t} = 64$ **(b),** $\bar{t} = 136$ **(c), and** $\bar{t} = 189$ **(d). Parameter values: Tab. 5.6 with** $\bar{L} = 43.2$**,** $\bar{g}_{\mathrm{sac}} = 1.25$**,** $\bar{\kappa}_{\sigma_{\mathrm{active}}} = 20$**, and** $T = 37\,^{\circ}\mathrm{C}$**.**

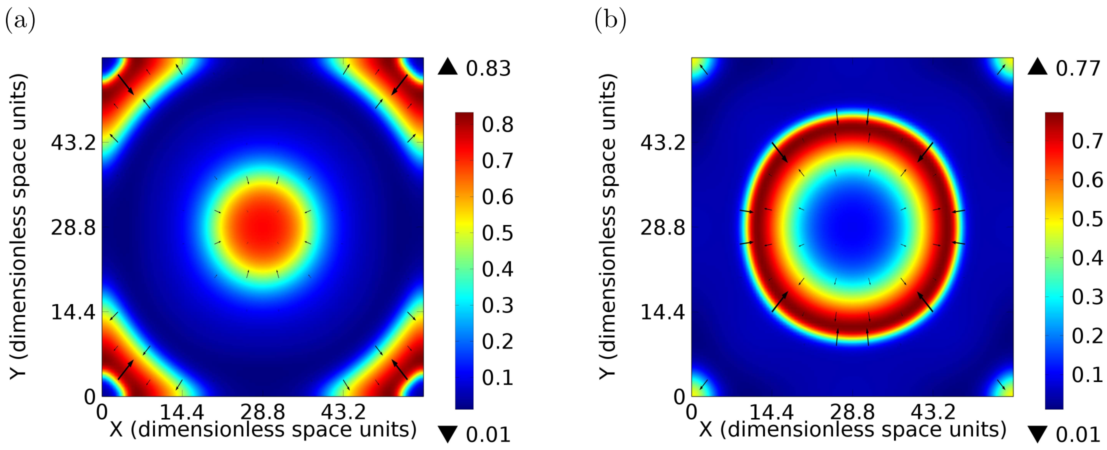

Fig. 5.77 – Point 5. **Snapshots of the spatial distribution of the dimensionless membrane potential,** $\bar{V}$**, at** $\bar{t} = 180$ **(a) and** $\bar{t} = 185$ **(b). Parameter values: Tab. 5.6 with** $\bar{L} = 57.6$**,** $\bar{g}_{\mathrm{sac}} = 0.5$**,** $\bar{\kappa}_{\sigma_{\mathrm{active}}} = 20$**, and** $T = 37\,^{\circ}\mathrm{C}$**.**

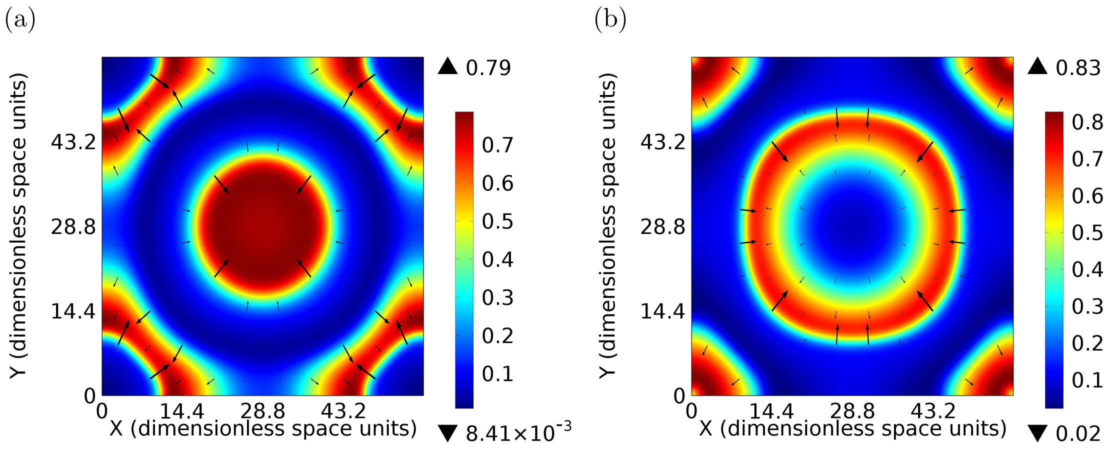

Fig. 5.78 – Point 6. **Snapshots of the spatial distribution of the dimensionless membrane potential,** $\bar{V}$**, at** $\bar{t} = 196$ **(a) and** $\bar{t} = 200$ **(b). Parameter values: Tab. 5.6 with** $\bar{L} = 57.6$**,** $\bar{g}_{\mathrm{sac}} = 1.25$**,** $\bar{\kappa}_{\sigma_{\mathrm{active}}} = 20$**, and** $T = 37\,^{\circ}\mathrm{C}$**.**

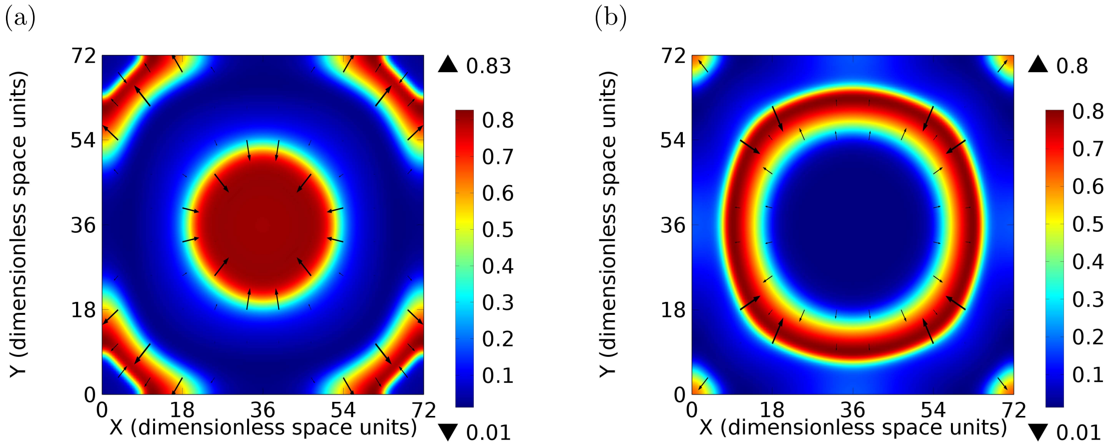

Fig. 5.79 – **Point** 7. **Snapshots of the spatial distribution of the dimensionless membrane potential,** $\bar{V}$**, at** $\bar{t} = 189$ **(a) and** $\bar{t} = 195$ **(b). Parameter values: Tab. 5.6 with** $\bar{L} = 72$, $\bar{g}_{\text{sac}} = 0.625$, $\bar{\kappa}_{\sigma_{\text{active}}} = 20$, **and** $T = 37\,^{\circ}\text{C}$.

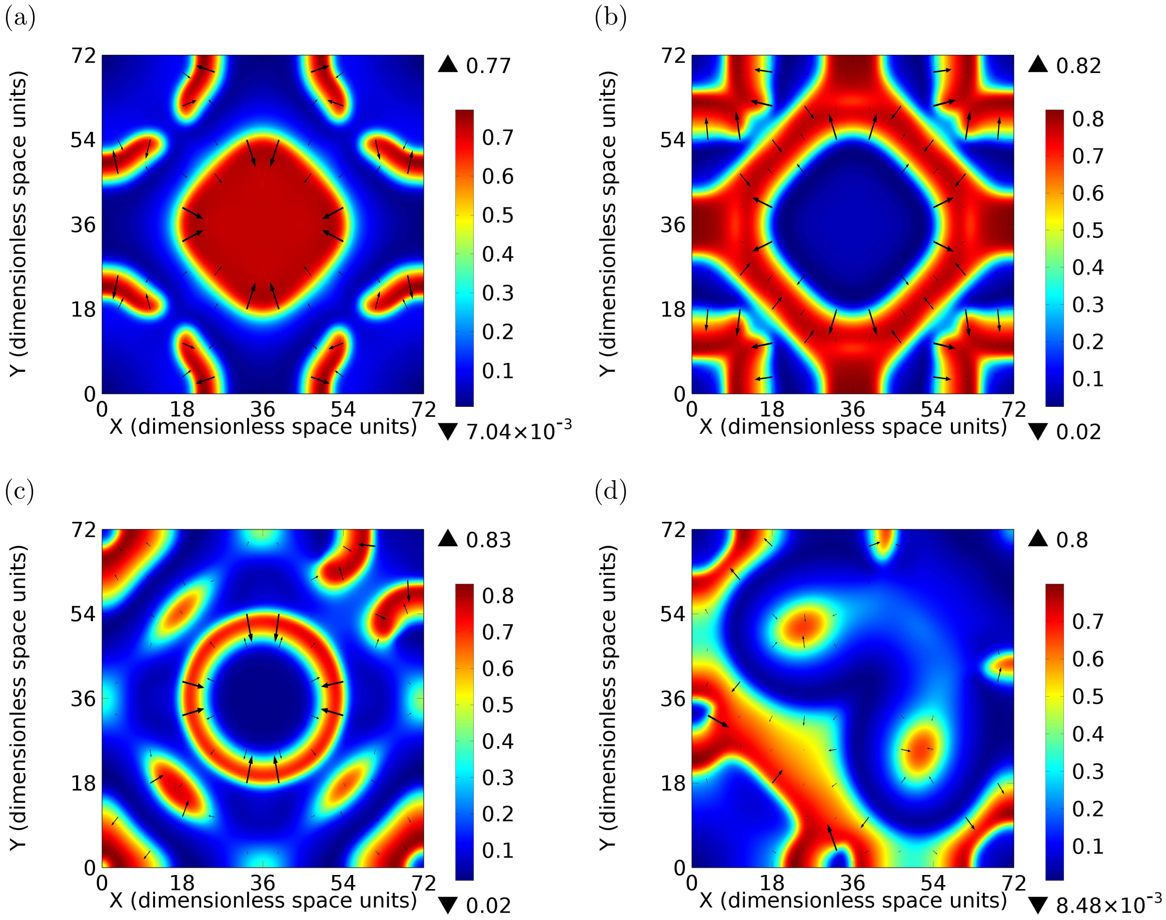

Fig. 5.80 – **Point** 8. **Snapshots of the spatial distribution of the dimensionless membrane potential,** $\bar{V}$**, at** $\bar{t} = 45$ **(a),** $\bar{t} = 62$ **(b),** $\bar{t} = 114$ **(c), and** $\bar{t} = 189$ **(d). Parameter values: Tab. 5.6 with** $\bar{L} = 72$, $\bar{g}_{\text{sac}} = 1.375$, $\bar{\kappa}_{\sigma_{\text{active}}} = 20$, **and** $T = 37\,^{\circ}\text{C}$.

As shown in Figs 5.73-5.80, the perpetual AEAs are characterized by different spatio-temporal patterns. These seem to be dependent on the values of $\bar{L}$ and $\bar{g}_{\text{sac}}$. For small values of $\bar{g}_{\text{sac}}$ and $\bar{L} \in [28.8, 72]$, the AEAs seem to be associated with circular-like waves (Figs 5.73, 5.75, 5.77, and 5.79). However, it seems that the larger the value of $\bar{L}$, the lesser circular the depolarization wave. Similar patterns are also observed for larger values of $\bar{g}_{\text{sac}}$ when $\bar{L} = 28.8$ and $\bar{L} = 57.6$ (Figs 5.74 and 5.78, respectively).

For larger values of $\bar{g}_{\text{sac}}$ when $\bar{L} = 43.2$ and $\bar{L} = 72$ (Figs 5.76 and 5.80, respectively), the AEAs correspond to spatio-temporal patterns characterized by multiple excitatory sources (concomitant spiral waves and circular-like waves). In the beginning of the simulation, these patterns seem to be spatially organized. Then, this organization is progressively broken and fibrillation-like patterns seem to occur.

5.2.4.3 Effects of the spatial location of the initial excitation

So far, all the simulations have been performed by applying an initial depolarization to the center of the square-shaped slice of cardiac tissue. Now, the influence of the spatial location of the initial excitation is examined.

As shown previously in Fig. 5.69, for $\bar{L} = 28.8$, $\bar{g}_{\text{sac}} = 1$, $\bar{\kappa}_{\sigma_{\text{active}}} = 20$, and $T = 37\,^{\circ}\text{C}$, an initial excitation applied to the center of the square-shaped slice of cardiac tissue leads to a finite AEA which vanishes shortly after 59 dimensionless time units.

Now, the initial depolarization is applied to a similar circular region (radius length equal to 2.4 dimensionless space units) but centered at $X = \bar{L}/4$ and $Y = \bar{L}/4$. In this case, the AEA is perpetual. Thus, the spatial location of the initial excitation is clearly a determining factor in the appearance of AEAs as in the one-dimensional study.

In addition, the excitatory source seems to drift in the direction of the center of the square-shaped slice and stay at a particular site on the diagonal as shown in Fig. 5.81. Therefore, the two-dimensional configuration seems to be characterized by attractors as in the one-dimensional case. The corresponding spatio-temporal pattern to the green line depicted in Fig. 5.81 is shown in Fig. 5.82a. The spatio-temporal pattern a few dimensionless time units after is displayed in Fig. 5.82b.

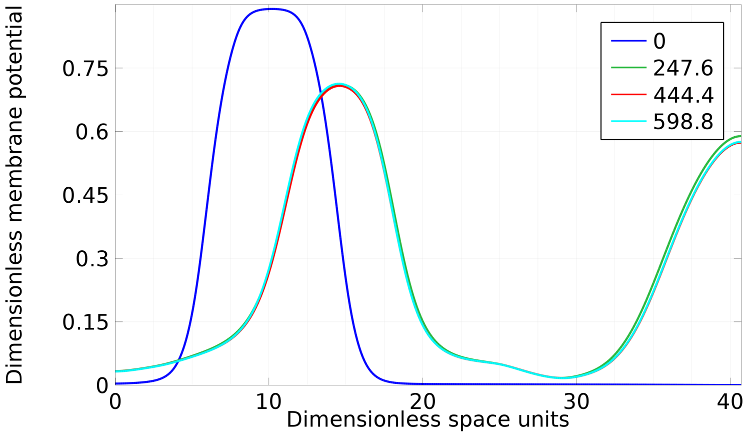

Fig. 5.81 – Spatial distribution along the diagonal of the square of the dimensionless membrane potential, $\bar{V}$, with $\bar{L} = 28.8$, $\bar{g}_{\text{sac}} = 1$, $\bar{\kappa}_{\sigma_{\text{active}}} = 20$, and $T = 37\,^{\circ}\text{C}$ at four different instants expressed in terms of dimensionless time units.

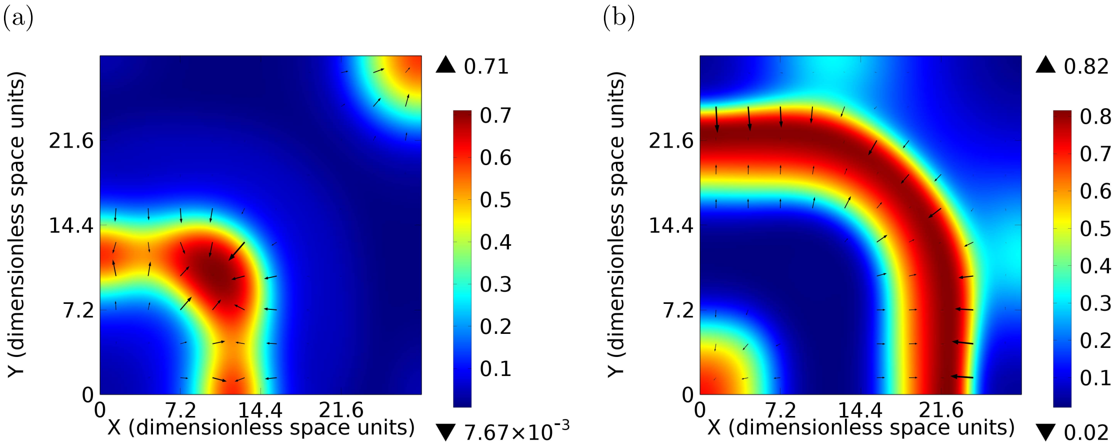

Fig. 5.82 – Spatial distribution of the dimensionless membrane potential, $\bar{V}$, with $\bar{L} = 28.8$, $\bar{g}_{\text{sac}} = 1$, $\bar{\kappa}_{\sigma_{\text{active}}} = 20$, and $T = 37\,^{\circ}\text{C}$ at $\bar{t} = 247.6$ (a) and $\bar{t} = 254$ (b).

It could be interesting to examine how this drift phenomenon behaves as a function of the length of the square. For this purpose, the same parameter values as those used in the previous simulation are adopted except that $\bar{L}$ is equal to 43.2 instead of 28.8. As shown in Fig. 5.83, there is also a drift phenomenon for $\bar{L} = 43.2$. In this case, the attractor corresponds to the center of the square-shaped slice of cardiac tissue (magenta line in Fig. 5.83). Note that the drift of the excitatory source seems to slow down as the latter moves to the center (Fig. 5.83).

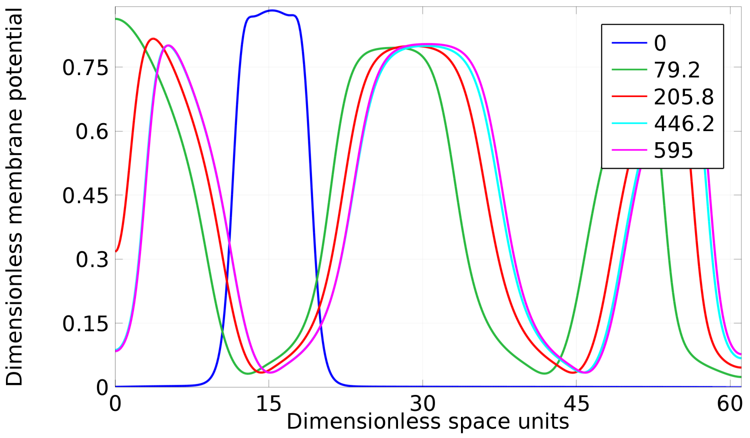

Fig. 5.83 – Spatial distribution along the diagonal of the square of the dimensionless membrane potential, $\bar{V}$, with $\bar{L} = 43.2$, $\bar{g}_{\mathrm{sac}} = 1$, $\bar{\kappa}_{\sigma_{\mathrm{active}}} = 20$, and $T = 37\,^{\circ}\mathrm{C}$ at five different instants expressed in terms of dimensionless time units.

The corresponding spatial pattern to the green line and the magenta line depicted in Fig. 5.83 are shown in Figs 5.84a and 5.84b, respectively.

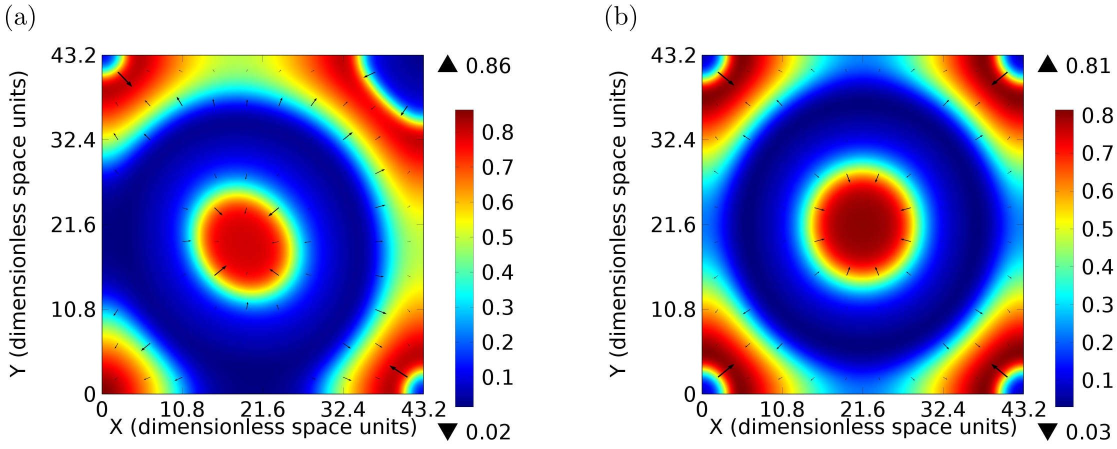

Fig. 5.84 – Spatial distribution in the square-shaped slice of cardiac tissue of the dimensionless membrane potential, $\bar{V}$, with $\bar{L} = 43.2$, $\bar{g}_{\mathrm{sac}} = 1$, $\bar{\kappa}_{\sigma_{\mathrm{active}}} = 20$, and $T = 37\,^{\circ}\mathrm{C}$ at $\bar{t} = 79.2$ (a) and $\bar{t} = 595$ (b).

Two other values of $\bar{L}$ have also been examined: a value slightly smaller than 28.8 and a value slightly larger than 28.8, namely 27.36 (95 % of 28.8) and 31.68 (110 % of 28.8), respectively. For $\bar{L} = 27.36$, there is no AEA whereas for $\bar{L} = 31.68$, a drift phenomenon similar to the one observed for $\bar{L} = 43.2$ occurs: the excitatory source moves along the diagonal towards the center of the square-shaped slice of cardiac tissue.

From these last four results, it can be stated that the drift phenomenon depends on $\bar{L}$, for all the other parameter values hold fixed. A similar phenomenon was also observed in [98]. In fact, for a given set of parameter values, it seems that there exists a critical length, $\bar{L}_{\mathrm{uc}}$, above which the excitatory source moves along the diagonal towards the center of the square. Slightly below this critical value (see results for $\bar{L} = 27.36$ and $\bar{L} = 28.8$), there is probably a small range of values of $\bar{L}$ for which the attractor is located at a particular site along the diagonal of the square.

Note that another critical length, $\bar{L}_{\mathrm{dc}}$, could also exist under which the excitatory source would drift in the direction of the corner of the square. For instance, in this situation, this critical length could be somewhere between 27.36 and 28.8. To better characterize and to corroborate this first analysis of the drift phenomenon, a systematic approach for scanning a large number of values of $\bar{L}$, as the one used in the one-dimensional study, should be used.

5.2.4.4 Effects of a temperature change

In the one-dimensional study, AEA has been observed to be significantly influenced by a temperature change. *A priori*, the temperature must also play a significant role in the spatio-temporal behavior of AEAs in a two-dimensional configuration. To corroborate the influence of a temperature change on AEA, several simulations for different temperature values are performed with the same parameter values and the same IC.

For all the simulations, the IC consists in a depolarization applied to a circular region, characterized by a radius length equal to 2.4 dimensionless space units, centered at $X = 15$ and $Y = 15$. The side length of the square-shaped slice of cardiac tissue is equal to 28.8. All the other parameter values are given in Tab. 5.6 with $\bar{g}_{\mathrm{sac}} = 1$ and $\bar{\kappa}_{\sigma_{\mathrm{active}}} = 20$.

Physiological case: $T = 37\,^{\circ}\mathrm{C}$

First, the temperature value is set to $37\,^{\circ}\mathrm{C}$. After a small transitory phase, the AEA is characterized by a periodic phenomenon with a period approximately equal to 12.4 dimensionless time units. As shown in Fig. 5.85, two concomitant spiral waves are implied in this periodic phenomenon. Note that the spatial pattern of the dimensionless membrane potential corresponding to $\bar{t} = 545.2$, which is not represented, is exactly the same as the one depicted in Fig. 5.85a.

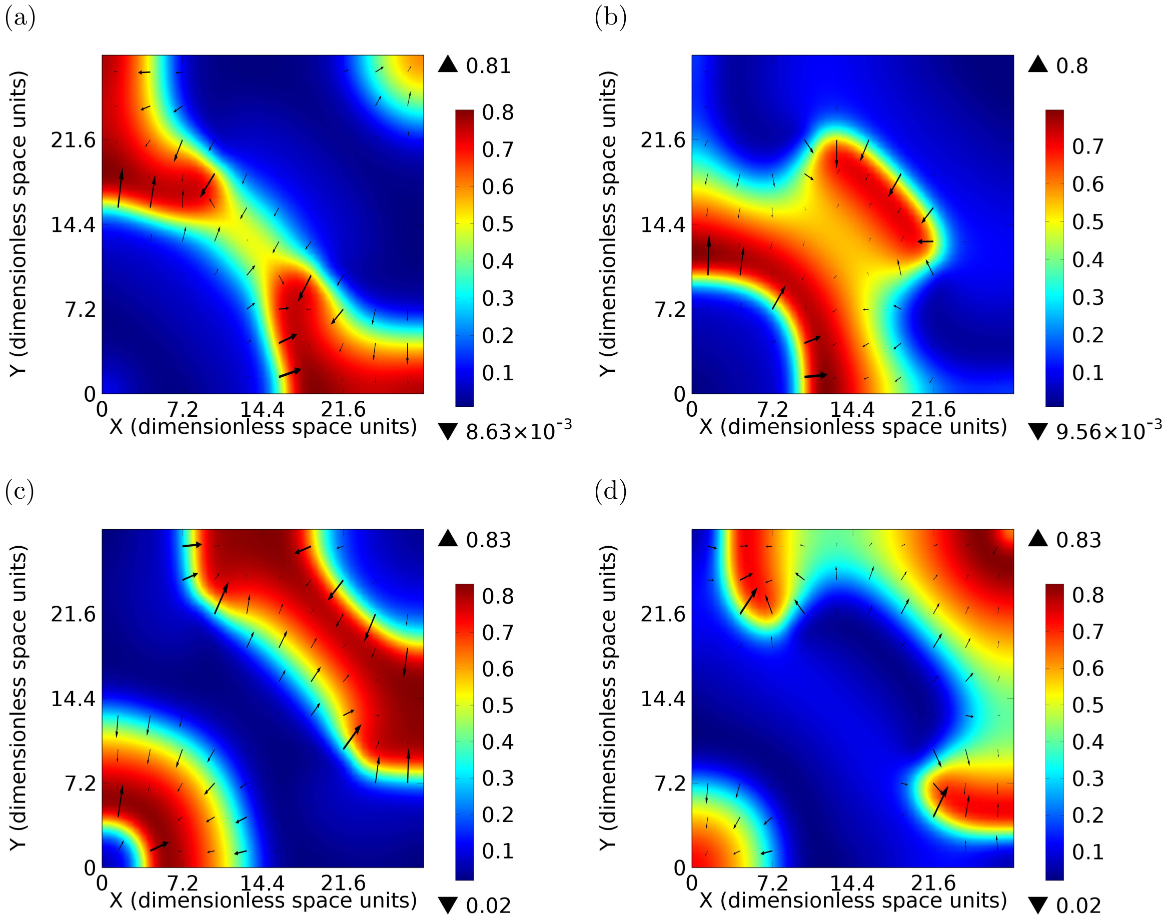

Fig. 5.85 – Snapshots of the spatial distribution of the dimensionless membrane potential, $\bar{V}$, at $\bar{t} = 532.8$ and $\bar{t} = 545.2$ (a), $\bar{t} = 536$ (b), $\bar{t} = 539$ (c), and $\bar{t} = 542.2$ (d). Parameter values: Tab. 5.6 with $\bar{L} = 28.8$, $\bar{g}_{\text{sac}} = 1$, $\bar{\kappa}_{\sigma_{\text{active}}} = 20$, and $T = 37\,°\text{C}$.

Therapeutic hypothermia: $T = 33\,°\text{C}$

Now, the effects of a decrease in the temperature value are examined. The temperature is set to 37 °C from 0 to 90 dimensionless time units. It is then progressively decreased and reaches 33 °C at approximately $\bar{t} = 91$. As shown in Fig. 5.86, the spatio-temporal behavior of the dimensionless membrane potential is characterized by a similar periodic phenomenon as the one observed for 37 °C implying two concomitant spiral waves. However, in this case, the time period is equal to approximately 14.6 dimensionless time units instead of 12.4. As a consequence, it can be stated that a decrease in the temperature value induces a decrease in the time period. Note that the spatial pattern of the dimensionless membrane potential corresponding to $\bar{t} = 568.6$ is exactly the same as the one depicted in Fig. 5.86a.

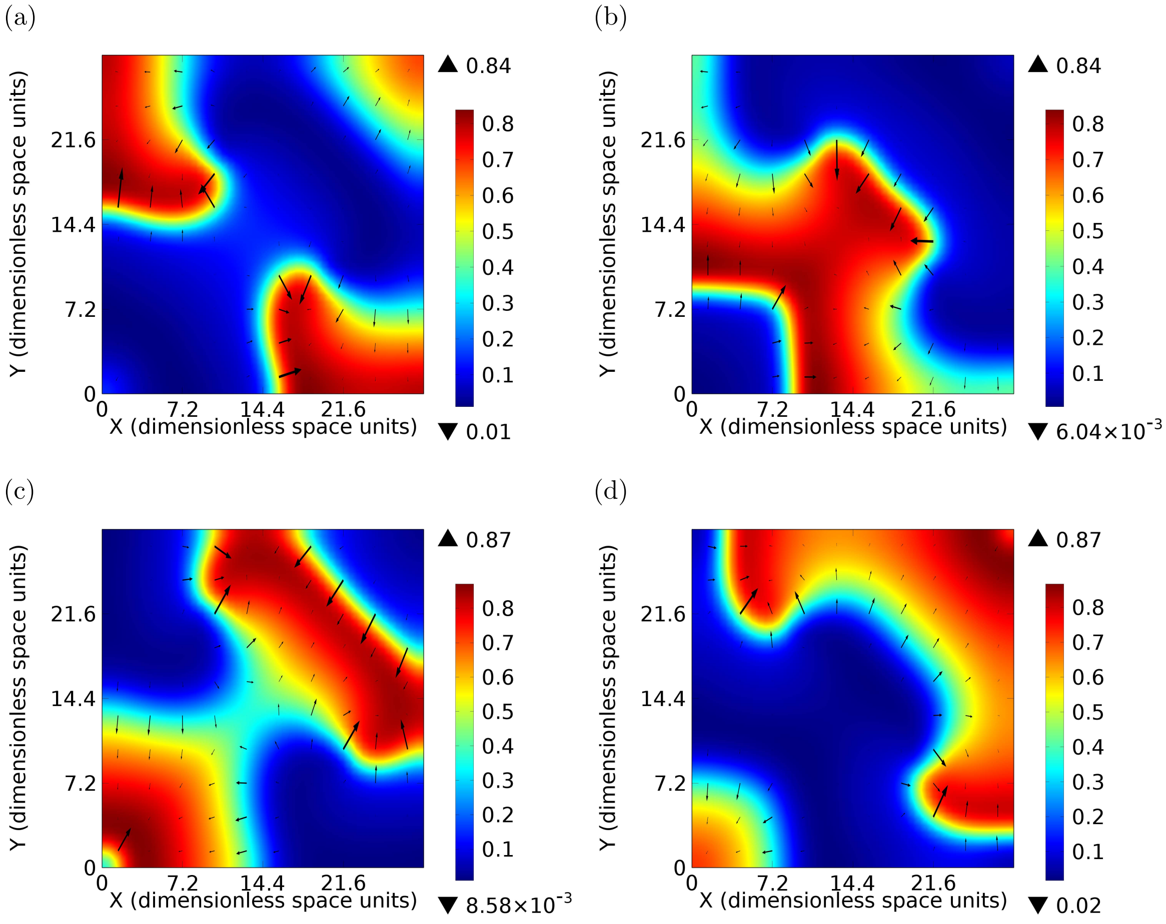

Fig. 5.86 – Snapshots of the spatial distribution of the dimensionless membrane potential, $\bar{V}$, at $\bar{t}$ = 564 and $\bar{t}$ = 578.6 (a), $\bar{t}$ = 567.6 (b), $\bar{t}$ = 571.4 (c), and $\bar{t}$ = 575 (d). Parameter values: Tab. 5.6 with $\bar{L} = 28.8$, $\bar{g}_{\text{sac}} = 1$, $\bar{\kappa}_{\sigma_{\text{active}}} = 20$, and $T = 33\,°\text{C}$.

Hyperthermia: $T = 41\,°\text{C}$

Here, the effects of an increase in the temperature value are examined. The temperature is set to 37 °C from 0 to 90 dimensionless time units. It is then progressively increased and reaches 41 °C at approximately $\bar{t} = 91$. As shown in Fig. 5.87, two concomitant spiral waves are also implied in the AEA but there is an additional excitatory source in comparison with the previous two cases ($T = 37\,°\text{C}$ and $T = 33\,°\text{C}$).

As shown in Figs 5.87a and 5.87d, this additional excitatory source is generated before that the two aforesaid spiral waves collide. These spiral waves and this additional excitatory source coexist in a rather regular way for a while but the phenomenon is not really periodic anymore.

After approximately 340 dimensionless time units, the AEA eventually vanishes due to a change in the spatio-temporal structure of the dimensionless membrane potential as observed by comparing the regular-like spatio-temporal structure depicted in Fig. 5.87 with Fig. 5.88.

Note that another temperature value, 42 °C, slightly larger than 41 °C has also been examined. The behavior is quite different from the one observed for 41 °C after the increase of the temperature value which occurs between 90 and 91 dimensionless time units: there is not an additional excitatory source and the two concomitant spiral waves vanish, at approximately $\bar{t} = 111.4$, just after they collide for the first time after the temperature change as shown in Fig. 5.89.

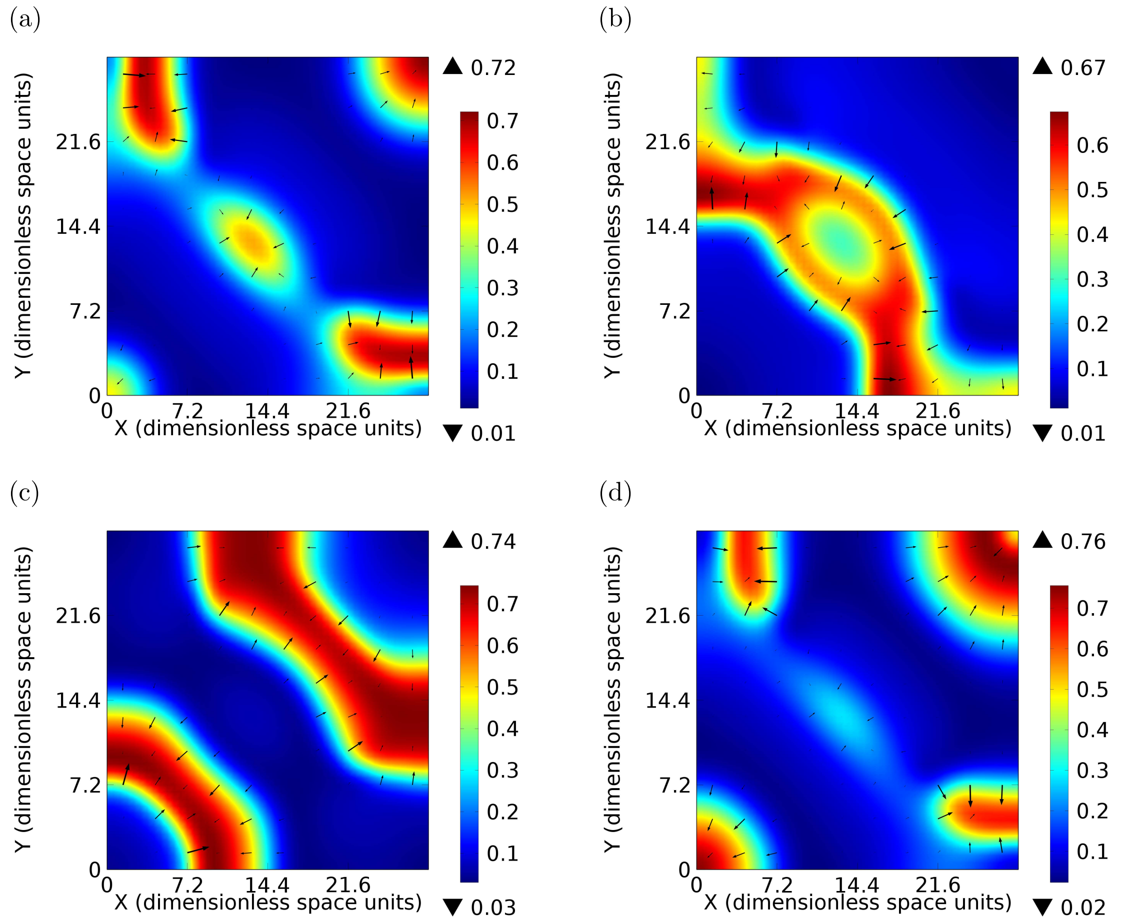

Fig. 5.87 – Snapshots of the spatial distribution of the dimensionless membrane potential, $\bar{V}$, at $\bar{t} = 195.8$ (a), $\bar{t} = 199$ (b), $\bar{t} = 203$ (c), and $\bar{t} = 207$ (d). Parameter values: Tab. 5.6 with $\bar{L} = 28.8$, $\bar{g}_{\text{sac}} = 1$, $\bar{\kappa}_{\sigma_{\text{active}}} = 20$, and $T = 41\,^{\circ}\text{C}$.

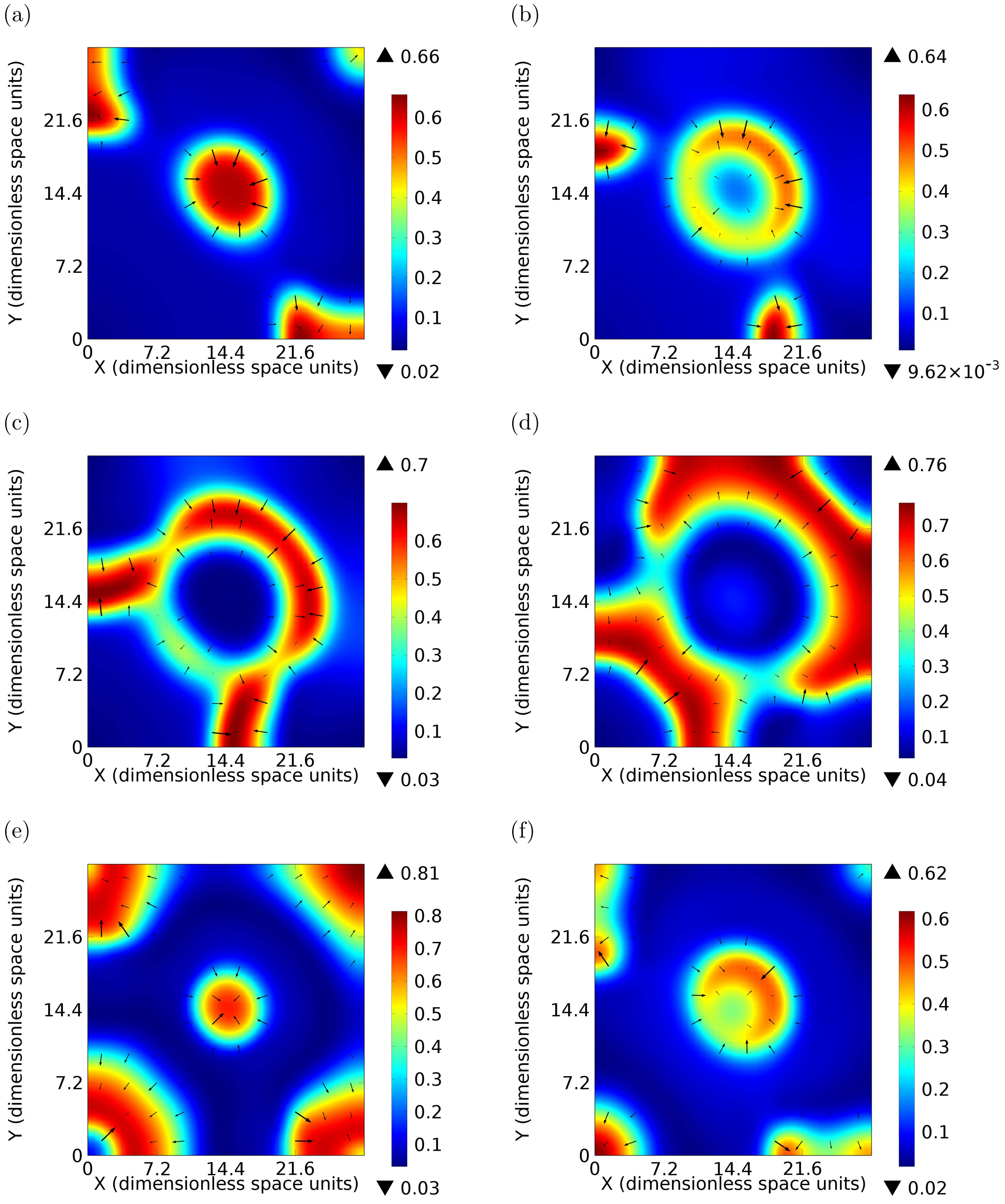

Fig. 5.88 – Snapshots of the spatial distribution of the dimensionless membrane potential, $\bar{V}$, at $\bar{t} = 323.4$ (a), $\bar{t} = 326$ (b), $\bar{t} = 328.4$ (c), $\bar{t} = 331$ (d), 333.6 (e), and 336.2 (f). Parameter values: Tab. 5.6 with $\bar{L} = 28.8$, $\bar{g}_{\text{sac}} = 1$, $\bar{\kappa}_{\sigma_{\text{active}}} = 20$, and $T = 41\,^{\circ}\text{C}$.

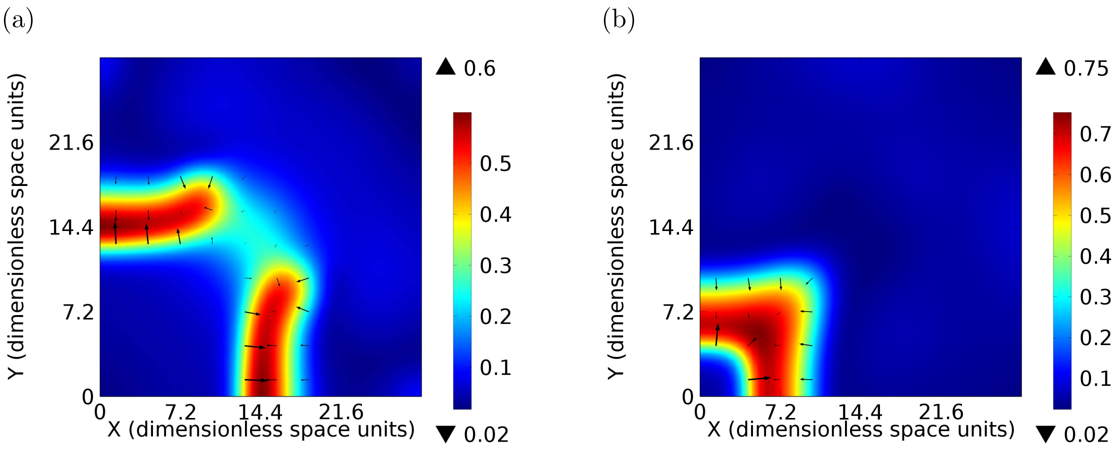

Fig. 5.89 – Spatial distribution in the square-shaped slice of cardiac tissue of the dimensionless membrane potential, $\bar{V}$, with $\bar{L} = 28.8$, $\bar{g}_{\mathrm{sac}} = 1$, $\bar{\kappa}_{\sigma_{\mathrm{active}}} = 20$, and $T = 42\,^{\circ}\mathrm{C}$ at $\bar{t} = 100.4$ (a) and $\bar{t} = 106$ (b).

5.2.4.5 Summary of the two-dimensional time-dependent TEM study

In summary, this two-dimensional time-dependent TEM study has enabled to highlight the arrhythmogenic consequences of the cardiac MEF within a TEM framework. The AEA induced by the MEF has been shown to occur under specific conditions. The existence and the persistence of this AEA has been characterized in terms of the size of the domain and the SAC conductance, which are the key parameters regarding the cardiac MEF. As in the one-dimensional case, this AEA occurs only for specific values of the aforesaid parameters and its persistence also depends heavily on these parameter values.

The location of the initial excitation has been observed to play a central role in the spatio-temporal behavior of the electromechanical phenomena within a TEM framework as in the one-dimensional study. Temperature variations also alter in a significant way the electromechanical behavior of the cardiac muscle tissue. For instance, for a given set of parameter values and a range of temperature values leading to similar periodic AEAs (*e.g.* two concomitant spiral waves such as those shown for $T = 37\,^{\circ}\mathrm{C}$ and $T = 33\,^{\circ}\mathrm{C}$), the APD and the time period of the AEA increase when the temperature value decreases. The same behavior was also observed in the one-dimensional case for periodic AEAs.

It is interesting to underline that the AEA generated by the MEF can be associated with different spatio-temporal patterns depending on the size of the domain, and the physiological and mechanical properties as in the one-dimensional case. Moreover, drift phenomena have been highlighted in certain conditions and depend on the size of the domain.

This time-dependent two-dimensional TEM study, which can be viewed as a first qualitative extension of the quantitative one-dimensional time-dependent TEM study described in the first part of this chapter, has enabled to pave the way for further more extensive and quantitative studies. The numerical simulations performed in this two-dimensional framework have shown that the additional dimension enables the development of complex structures, such as spiral waves and fibrillation-like patterns, under specific conditions. These results corroborate the fact that mechanical changes can lead to arrhythmias due to the MEF as shown in [3, 4].

Conclusion

Cardiac arrhythmias such as *atrial fibrillation* and *ventricular fibrillation* consist in rapid and irregular electrical activity, which lead to either an inefficient or a completely null pumping function of the heart. The underlying mechanisms generating such phenomena are not all thoroughly elucidated and must be better characterized. In that context, this doctoral study has aimed at gaining insight into a particular arrhythmogenic mechanism: the *mechano-electric feedback (MEF)*. This MEF consists in the modulation of electrical activity induced by mechanical deformation of cells and tissues of the heart. In a healthy heart, the MEF acts as a regulatory mechanism able to damp a mechanical perturbation undergone by the heart, at a specific moment, by modulating electrical activity, shortly after this perturbation. In this way, a new healthy electromechanical situation is recovered. However, it has been shown that cardiac arrhythmias can sometimes be caused by abnormal mechanical changes inducing several electrophysiological alterations *via* the MEF [3, 4].

On the other hand, *therapeutic hypothermia (TH)* is known nowadays as the most efficient treatment for reducing post-resuscitation brain damage from a cardiac arrest. In that context, this work has tackled the MEF by taking into account temperature variations as those undergone by the heart during TH, or those corresponding to *hy-*

perthermia. Therefore, this doctoral study comes within a *thermo-electro-mechanical (TEM)* framework.

The arrhythmogenic consequences of the MEF in a TEM framework, have been clearly highlighted by performing a huge amount of numerical simulations and meticulously analyzing results from these simulations. Time-dependent TEM models of cardiac muscle tissue have been especially developed to examine the role played by the MEF in cardiac arrhythmogenesis in a TEM framework.

First, a general time-dependent TEM model has been developed from the model proposed by *Panfilov et al.* [98]. This model takes into account three different couplings:

i. *excitation-contraction coupling (ECC)*
ii. *thermo-electric coupling (TEC)*
iii. MEF

The ECC, which describes the contraction of cardiomyocytes resulting from an electrical excitation, has been modeled by assuming a direct dependence of the active tension development with respect to the membrane potential. A single ordinary differential equation is used to describe the dynamics of the active tension. It enables to mimic the time delay between the beginning of the depolarization of a cell and the final contraction resulting from a complex signaling pathway triggered by the initial depolarization. The electrical excitation process in cardiomyocytes has been described by using a phenomenological model combining the *Rogers–McCulloch model* [18] and the *Aliev–Panfilov model* [19].

The TEC accounts for the modulation of electrical activity due to a temperature variation. In this work, three temperature-dependent properties have been considered. On the one hand, the gating kinetics of ion channels and the active tension development have been assumed to be dependent on temperature in an exponential way. On the other hand, the ionic conductances have been described as linear temperature-dependent functions. This TEC is a one-directional coupling (weak coupling).

The MEF, which provides the modulation of the electrophysiology by mechanical deformation of cells and tissues of the heart, may be split into two components: the physiological MEF and the geometric MEF. *Stretch-activated currents (SACs)*, which are the physiological contribution to the MEF, have been modeled by using the generic description suggested in [98, 100]. Regarding the geometric contribution to the MEF, it is induced by structural deformation of the cardiac tissue, controlled by the mechanical response of this tissue. This response is provided by material constitutive laws which describe intrinsic properties of materials. This geometric contribution is hidden in the diffusive term from the *deformable monodomain equation*, which has been adopted to model propagation of depolarization waves in cardiac muscle tissue.

The passive mechanical behavior of the cardiac muscle tissue has been modeled by assuming a compressible hyperelastic isotropic material. The active mechanical behavior of the cardiac tissue is taken into account by linearly superimposing active stresses to the passive ones. The active stresses depend on the active tension, which is controlled by the ECC model, and the Green-Lagrange strain tensor. It is important to underline that the formulation used in this study for the active part of the second Piola–Kirchhoff stress tensor has been analyzed in detail and contrasted with other previous formulations.

Second, the general time-dependent TEM model has been particularized to cardiac muscle tissue subject to deformation only in one dimension, corresponding to a patch of cardiac muscle tissue subject to a one-dimensional deformation or a one-dimensional cardiac muscle fiber. The patch or the fiber is assumed to be surrounded by an electrical insulator and their boundaries (perpendicular to the direction of the one-dimensional deformation regarding the patch) are held fixed. Assuming small deformations of the cardiac muscle tissue, a simplified model has been derived from the one-dimensional time-dependent TEM model: the *modified global coupling minimal model (modified GC minimal model)*.

A numerical comparison between the one-dimensional TEM model and the modified GC minimal model has been performed. The differences between these two models have been identified and discussed in detail. In addition, for specific parameter values, large deformations, characterized by stretchings and shortenings reaching up to 15 % and 20 %, have been highlighted with the one-dimensional TEM model. Besides, this comparison has shown that, from a pragmatic point of view, the modified GC minimal model is suitable to study TEM cases involving large one-dimensional deformations with an order of magnitude equal to that encountered in the cardiac muscle tissue

(10 %-20 %). Moreover, these first simulations have shown that the MEF can induce an *autonomous electrical activity (AEA)* in the cardiac muscle tissue due to particular mechanisms, which have been extensively discussed.

To understand the role played by each parameter of the model, a parametric study has been performed for a given length of the fiber and a given temperature value. This parametric study has highlighted the main effects of each parameter on the TEM system. Depending on the parameter values, different spatio-temporal behaviors of the AEA, have been shown and described. The AEA has been observed to be characterized by periodic phenomena with period-1 cycles, spatially synchronized or desynchronized alernans phenomena, and periodic phenomena for which several wavefronts are involved in one period for different set of parameter values. For period-1 phenomena, the periods have been shown to be very dependent on the parameter values. Drift phenomena have also been emphasized regarding the excitatory source in the cardiac fiber. Finally, this parametric study has clearly demonstrated that the AEA is only induced by the MEF for specific ranges of parameter values. Further to this parametric study, a more quantitative examination aiming at characterizing the arrhythmogenic effects of the MEF in a TEM framework has been conducted. More precisely, the AEA induced by the MEF has been studied in terms of the two key parameters regarding the MEF: the dimensionless ionic conductance of the SACs, $\tilde{g}_{\mathrm{sac}}$, and the length of the fiber, L. The effects of a temperature change have then been considered before examining the role played by the location and the magnitude of the initial stimulus applied to the cardiac muscle tissue enabling to trigger the first depolarization wave.

A systematic scanning of the $(L, \tilde{g}_{\mathrm{sac}})$ space has proved that the AEA induced by the MEF is heavily dependent on these two parameters. For each value of L, ranging from 2 cm to 13.96 cm, a lower critical value and an upper critical value of $\tilde{g}_{\mathrm{sac}}$ have been identified, under and above which the AEA is not indefinitely sustained by the MEF, respectively. Inversely, a lower critical value and an upper critical value of L have been determined for each value of $\tilde{g}_{\mathrm{sac}}$. In other words, a region, referred to as the *main dark red spot (DRS)* in this work, in which the AEA lasts infinitely has been drawn in the $(L, \tilde{g}_{\mathrm{sac}})$ space.

The analysis of spatio-temporal features of the AEA in different parts of the main DRS has shown that the AEA always behaves in a periodic way with a *period*-1 cycle as long as the AEA is observed not ‘too’ close to the boundary of the main DRS. However, the AEA observed for the points in the $(L, \tilde{g}_{\text{sac}})$ space located on the boundary of this region or close to it behaves in a different way: the AEA is not characterized by a period-1 cycle anymore. Depending on the value of L and whether the value of $\tilde{g}_{\text{sac}}$ is close to its lower critical value or its upper critical value, under and above which the AEA is not perpetual, different spatio-temporal patterns define the AEA.

As indicated by the Floquet stability analysis conducted in this work, these different patterns observed close to the boundaries of the main DRS are induced by specific bifurcations. These bifurcations correspond to the loss of stability of the branch of period-1 solutions. Shortly after these bifurcations, particular phenomena are induced such as *intermittencies* and periodic solutions with *period*-2 or *period*-3 cycles. Slightly further than these bifurcations, these spatio-temporal phenomena eventually lead to the end of the AEA. In addition, some small isolated regions in the $(L, \tilde{g}_{\text{sac}})$ space correspond to an AEA which is indefinitely sustained. The solutions corresponding to these regions are also characterized by particular spatio-temporal patterns as emphasized in this study. However, no clear explanation has been found to understand why perpetual or finite AEAs are observed far from the main DRS.

This study has also shown that a temperature variation, such as that undergone by the heart during TH or hyperthermia, has a significant effect on the AEA induced by the MEF. In particular, this work has highlighted that a decrease of temperature dramatically reduces the area of the main DRS and modulates the shape of this region. These effects have been explained mainly due to the lengthening (shortening) of the *action potential duration* resulting from a decrease (increase) of the temperature value.

Besides, numerical simulations have shown that the AEA depends heavily on the location of the initial excitation. The role played by the location of the initial excitation in the arrhythmogenic effects of the MEF has been underlined for different temperature values. The existence of attractors in the cardiac fiber has also been highlighted. The number of these attractors, their locations, and the sizes of their basins of attraction have been shown to be dependent on the temperature value. The analysis has also underlined that the spatial width of the final excitatory source is heavily dependent on the location of the initial excitation. Finally, the time period which characterizes the AEA was also shown to depend on the location of the initial excitation and the temperature value.

Finally, an extension of the one-dimensional time-dependent TEM study to a two-dimensional framework has been addressed. This extension which was mainly qualitative has been conducted to pave the way for further more quantitative studies. As in the one-dimensional configuration, the existence of an AEA has been highlighted under specific conditions. In particular, a region in the $\left(\bar{L}, \bar{g}_{\text{sac}}\right)$ space in which the AEA is indefinitely sustained can be defined. Inside this region, different spatio-temporal behaviors occur. For an initial depolarization applied to the center of the square-shaped slice of cardiac tissue, circular-like waves, spiral waves, and more complex situations such as fibrillation-like patterns have been observed.

The influence of the location of the initial excitation has clearly been emphasized. In particular, for all the parameter values held fixed, the existence itself of an AEA depends heavily on the location of the initial excitation. In addition, this study has enabled to highlight the presence of attractors located at specific sites in the two-dimensional geometry. The location of these attractors has been shown to depend on the size of the domain. The temperature has also been observed to play a significant role in the electromechanical behavior of the cardiac tissue.

Perspectives

This doctoral study was developed in a multidisciplinary framework and has involved several complex fields: cardiac electrophysiology, mathematics, engineering, and programming. A big challenge has been to deal with the specific skills related to each area and even more the interactions between these fields.

The one-dimensional study has shown that the electromechanical behavior of cardiac tissue in a TEM framework is intrinsically complex, even in a very simple geometry. Many interesting results have been established and analyzed. In further modeling works, it could be interesting to corroborate the conclusions drawn from the Floquet stability analysis by using a Floquet theory specially designed for partial differential equations, namely for spatially extended systems. It could also be interesting to develop a tracking algorithm able to follow the solutions after that Floquet multipliers have crossed the unit circle.

The two-dimensional study has enabled to underline, in a qualitative way, some interesting phenomena occurring due to the cardiac MEF in a TEM framework. To carry on these first investigations, a more systematic quantitative approach should be used such as the one adopted in the one-dimensional study. In addition, more realistic hypotheses with respect to electrical propagation and passive mechanical behavior should be examined (*e.g.* anisotropy properties of the cardiac tissue). In terms of geometries, other two-dimensional configurations and more complex three-dimensional configurations, including specific structural details, should also be tested. Finally, it could be also interesting to examine the possibility to develop some reduce models in two- or three-dimensional configurations as the modified GC minimal model developed in the one-dimensional framework.

This work has clearly highlighted that the MEF can generate fibrillation under specific conditions. In addition, temperature variations have been shown to significantly alter the properties of the AEA induced by the MEF. Therefore, from these results, it could be thought that hypothetical defibrillation techniques based on mechanical shocks, thermal shocks, or thermo-mechanical shocks could be developed and would be much less traumatic for patients than the present defibrillation techniques.

APPENDIX **A**

Mechanics

Contents

A.1 Observer, coordinate system, and Euclidean transformation

To describe a physical process in a three-dimensional Euclidean space, a *frame of reference* or an *observer*, labeled O, which can measure *relative positions* of points in space (with a ruler) and *instants of time* (with a clock) must be introduced. In a general way, it is important to underline that two distinct observers will describe the same physical process in a different way. Moreover, for a given observer, the description of the physical process depends on the choice of a particular *coordinate system*. Actually, there is an infinite number of choices of coordinate systems for a given observer. As a result, a change of observer and a change of coordinate system are two different notions.

An *event* is noticed by an observer in terms of position $\mathbf{x}$ and time t. That being so, assume two arbitrary events observed by two different observers, O and O^+. The two events are characterized by the pairs $(\mathbf{x}_0, t_0)$ and $(\mathbf{x}, t)$ for the first observer and by the pairs $\left(\mathbf{x}_0^+, t_0^+\right)$ and $(\mathbf{x}^+, t^+)$ for the second one. The distance measured by the observers O and O^+ between the two events are $|\mathbf{x} - \mathbf{x}_0|$ and $|\mathbf{x}^+ - \mathbf{x}_0^+|$, respectively. Moreover, the time intervals between the two events recorded by O and O^+ are given by $t - t_0$ and $t^+ - t_0^+$, respectively. Here, the case where the pairs $(\mathbf{x}_0, t_0)$ and $(\mathbf{x}, t)$ map onto $\left(\mathbf{x}_0^+, t_0^+\right)$ and $(\mathbf{x}^+, t^+)$, in such a way that the distance and the time interval are preserved, is considered. Choosing one Cartesian coordinate system rigidly attached to each observer, the mapping between $\mathbf{x} - \mathbf{x}_0$ and $\mathbf{x}^+ - \mathbf{x}_0^+$ can be described by the *time-dependent transformation*

$$\mathbf{x}^+ - \mathbf{x}_0^+ \quad = \quad \mathbf{Q}\left(t\right) \cdot \left(\mathbf{x} - \mathbf{x}_0\right) \,, \tag{A.1}$$

where $\mathbf{Q}\left(t\right)$ is a proper orthogonal tensor: $\mathbf{Q}^{-1} = \mathbf{Q}^{\mathrm{T}}$ and $\det \mathbf{Q} = 1$. Although, in a general way, a change of coordinate systems is not the same thing as a change of observer, the relative motion of the two Cartesian coordinate systems can be identified with the rigid-body relative motion of the two observers [49].

Actually, $\mathbf{x}^+ - \mathbf{x}_0^+$ and $\mathbf{x} - \mathbf{x}_0$ can be viewed as vectors which are related through $\mathbf{Q}\left(t\right)$.

Therefore, taking into account Eq. (A.1), the following relation can be written:

$$\mathbf{x}^+ \;=\; \mathbf{c}\,(t) + \mathbf{Q}\,(t) \cdot \mathbf{x}\,, \tag{A.2}$$

with $t^+ = t + \alpha$ where α is a real number denoting the time-shift and $\mathbf{c}\,(t) = \mathbf{x}_0^+ - \mathbf{Q}\,(t) \cdot \mathbf{x}_0$. In Eq. (A.2), $\mathbf{x}^+$ and $\mathbf{x}$ can be thought as position vectors characterizing two points and the one-to-one mapping described by Eq. (A.2) is often referred to as a *Euclidean transformation*.

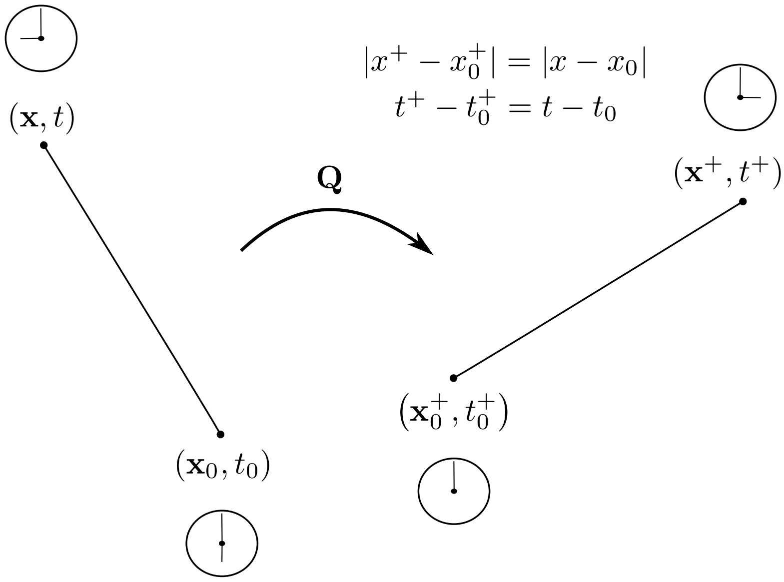

Fig. A.1 – Mapping between two events preserving distance and time interval.

A.2 The principle of virtual work (PVW)

In this section, a fundamental *variational principle*, namely the *principle of virtual work (PVW)* (also called by some authors the *principle of virtual displacements*), is introduced. The Cauchy's first equation of motion [Eq. (3.126)] may also be written, in terms of the displacement field, $\mathbf{u}$, in the following form:

$$\rho\,\ddot{\mathbf{u}} \;=\; \mathrm{div}\boldsymbol{\sigma} + \rho\,\mathbf{b}\,. \tag{A.3}$$

In Eq. (A.3), the body force (measured per unit mass), $\mathbf{b}$, is assumed to be a prescribed force and the term $\rho\,\ddot{\mathbf{u}}$ represents the inertia force (measured per unit current volume). Note that $\dot{(\bullet)}$ denotes the material time derivative operator, previously referred to as

$\mathrm{D}\left(\bullet\right)/\mathrm{D}t$. To find the displacement field, $\mathbf{u}$, induced by the motion, $\mathbf{x} = \boldsymbol{\chi}\left(\mathbf{X}, t\right)$, associated with some boundary conditions (BCs) and initial conditions (ICs), the so-called (nonlinear) *initial boundary-value problem (IBVP)* (formulated in the *strong form*) must be solved:

$$\rho\,\ddot{\mathbf{u}} = \mathrm{div}\boldsymbol{\sigma} + \rho\,\mathbf{b} \quad \text{in} \quad \Omega\,, \tag{A.4}$$

$$\mathbf{u} = \bar{\mathbf{u}} \quad \text{on} \quad \partial\Omega_{\mathbf{u}}\,, \tag{A.5}$$

$$\mathbf{t} = \boldsymbol{\sigma}\cdot\hat{\mathbf{n}} = \bar{\mathbf{t}} \quad \text{on} \quad \partial\Omega_{\boldsymbol{\sigma}}\,, \tag{A.6}$$

$$\mathbf{u}|_{t=0} = \mathbf{u}_0 \quad \text{in} \quad \Omega\,, \tag{A.7}$$

$$\dot{\mathbf{u}}|_{t=0} = \dot{\mathbf{u}}_0 \quad \text{in} \quad \Omega\,. \tag{A.8}$$

As shown in Eqs (A.5) and (A.6), there are two different classes of BCs applied to two disjoint parts of the the boundary surface, $\partial\Omega$, of the considered continuous body, $\mathcal{B}$, occupying the region Ω such that $\partial\Omega = \partial\Omega_{\mathbf{u}} \cup \partial\Omega_{\boldsymbol{\sigma}}$ with $\partial\Omega_{\mathbf{u}} \cap \partial\Omega_{\boldsymbol{\sigma}} = \emptyset$ (Fig. A.2).

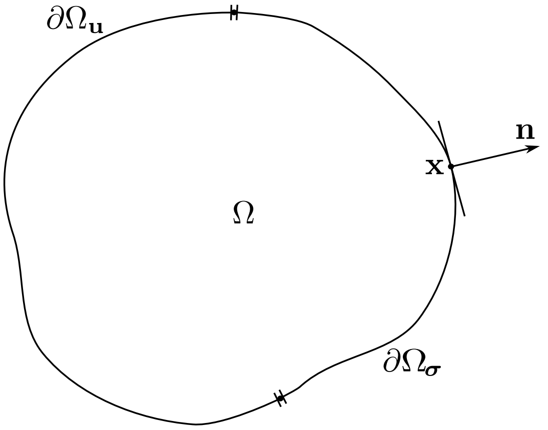

Fig. A.2 – The boundary surface $\partial\Omega$ of a continuous body $\mathcal{B}$ occupying the region Ω is decomposed in two disjoint parts such that $\partial\Omega = \partial\Omega_{\mathbf{u}}\cup\partial\Omega_{\boldsymbol{\sigma}}$ with $\partial\Omega_{\mathbf{u}} \cap \partial\Omega_{\boldsymbol{\sigma}} = \emptyset$.

The BCs applied to $\partial\Omega_{\mathbf{u}}$ are known as the *Dirichlet boundary conditions*, which correspond to the prescription of a displacement field. The BCs applied to $\partial\Omega_{\boldsymbol{\sigma}}$ are known as the *von Neumann boundary conditions*, which are identified physically with the surface traction. Note that quantities written as $(\bar{\bullet})$ denote prescribed functions on the boundaries whereas quantities written as $\left(\bullet\right)_0$ denote prescribed functions in the reference configuration, Ω_0. Eqs (A.7) and (A.8) give the displacement field and the velocity field at initial time $t = 0$, respectively. In addition, the *compatibility* of the BCs and ICs is achieved because the functions $\mathbf{u}_0$ and $\bar{\mathbf{u}}$ are equal on $\partial\Omega_{\mathbf{u}}$.

A.2.1 PVW in spatial description on the current configuration

An analytical solution of the (nonlinear) IBVP is only possible for a few special cases. That is why, a numerical method is very often necessary to achieve an approximate solution such as the *finite element method (FEM)* based on variational principles or weak forms as previously mentioned in section A.2. To establish the PVW in spatial description, we start with the Cauchy's first equation of motion which we multiply by an arbitrary vector-valued function $\boldsymbol{\eta}(\mathbf{x})$, defined on the current configuration, Ω. The result is then integrated over the region Ω occupied by the considered continuous body, $\mathcal{B}$, resulting in the following scalar-valued function:

$$f(\mathbf{u}, \boldsymbol{\eta}) \;=\; \int_{\Omega} (-\mathrm{div}\boldsymbol{\sigma} - \rho\,\mathbf{b} + \rho\,\ddot{\mathbf{u}}) \cdot \boldsymbol{\eta}\,\mathrm{d}\mathcal{V} \;=\; 0\,. \tag{A.9}$$

The vector-valued function $\boldsymbol{\eta}(\mathbf{x})$ is known as a *test function* or *weighting function.* This is a smooth function such that $\boldsymbol{\eta} = \mathbf{0}$ on $\partial\Omega_{\mathbf{u}}$. Eq. (A.9) is known as the *weak form* of the Cauchy's first equation of motion with respect to the current configuration, Ω. Actually, since $\boldsymbol{\eta}$ is an arbitrary function, $(-\mathrm{div}\boldsymbol{\sigma} - \rho\,\mathbf{b} + \rho\,\ddot{\mathbf{u}})$ must vanish to satisfy Eq. (A.9). Therefore, the solution of Eq. (A.3) (strong form) is equivalent to the solution of Eq. (A.9) (weak form). In addition, the term $-\mathrm{div}\boldsymbol{\sigma} \cdot \boldsymbol{\eta}$ can be written as

$$-\mathrm{div}\,\boldsymbol{\sigma} \cdot \boldsymbol{\eta} \;=\; -\mathrm{div}\,(\boldsymbol{\sigma} \cdot \boldsymbol{\eta}) + \boldsymbol{\sigma} : \mathrm{grad}\,\boldsymbol{\eta}\,. \tag{A.10}$$

Substituting Eq. (A.10) into Eq. (A.9), the following relation can be written:

$$f(\mathbf{u}, \boldsymbol{\eta}) \;=\; \int_{\Omega} [\boldsymbol{\sigma} : \mathrm{grad}\,\boldsymbol{\eta} - \mathrm{div}\,(\boldsymbol{\sigma} \cdot \boldsymbol{\eta}) - \rho\,(\mathbf{b} - \ddot{\mathbf{u}}) \cdot \boldsymbol{\eta}]\;\mathrm{d}\mathcal{V} \;=\; 0\,. \tag{A.11}$$

Applying the divergence theorem, Eq. (A.11) is eventually written as

$$f(\mathbf{u}, \boldsymbol{\eta}) \;=\; \int_{\Omega} [\boldsymbol{\sigma} : \mathrm{grad}\,\boldsymbol{\eta} - \rho\,(\mathbf{b} - \ddot{\mathbf{u}}) \cdot \boldsymbol{\eta}]\;\mathrm{d}\mathcal{V} - \int_{\partial\Omega} (\boldsymbol{\sigma} \cdot \boldsymbol{\eta}) \cdot \mathbf{n}\,\mathrm{d}\mathcal{A} \;=\; 0\,. \tag{A.12}$$

The surface integral in Eq. (A.12) only needs to be integrated on $\partial\Omega_{\boldsymbol{\sigma}}$ given that $\boldsymbol{\eta}$ vanishes on $\partial\Omega_{\mathbf{u}}$ where the displacement field is prescribed. Taking into account Eq. (A.6), Eq. (A.12) can be written as

$$f(\mathbf{u}, \boldsymbol{\eta}) \;=\; \int_{\Omega} [\boldsymbol{\sigma} : \mathrm{grad}\,\boldsymbol{\eta} - \rho\,(\mathbf{b} - \ddot{\mathbf{u}}) \cdot \boldsymbol{\eta}]\;\mathrm{d}\mathcal{V} - \int_{\partial\Omega_{\boldsymbol{\sigma}}} \bar{\mathbf{t}} \cdot \boldsymbol{\eta}\,\mathrm{d}\mathcal{A} \;=\; 0\,. \tag{A.13}$$

Moreover, the ICs given by Eqs (A.7) and (A.8) can be formulated in the weak form:

$$\begin{aligned} \int_\Omega \mathbf{u}|_{t=0} \cdot \boldsymbol{\eta} \, \mathrm{d}\mathcal{V} &= \int_\Omega \mathbf{u}_0 \cdot \boldsymbol{\eta} \, \mathrm{d}\mathcal{V} \,, && \text{(A.14)} \\ \int_\Omega \dot{\mathbf{u}}|_{t=0} \cdot \boldsymbol{\eta} \, \mathrm{d}\mathcal{V} &= \int_\Omega \dot{\mathbf{u}}_0 \cdot \boldsymbol{\eta} \, \mathrm{d}\mathcal{V} \,. && \text{(A.15)} \end{aligned}$$

The set constituted by Eqs (A.13)-(A.15) characterizes the weak form of the IBVP. In addition, note that the stress BCs [Eq. (A.6)] applied on $\partial\Omega_{\boldsymbol{\sigma}}$ are part of the weak form and for this reason, they are often referred to as *natural* BCs. In turn, the BCs given by Eq. (A.5) which are prescribed on $\partial\Omega_{\mathbf{u}}$ are referred to as *essential* BCs of the variational problem. Moreover, as previously mentioned, in Eq. (A.13), $\boldsymbol{\eta}$ is an arbitrary function. Therefore, $\boldsymbol{\eta}$ can be considered as the *virtual displacement field* (section A.2.1.1), $\delta\mathbf{u}$, defined on the current configuration, Ω. In this case, Eq. (A.13) leads to the fundamental PVW. As result, the PVW can be thought as a particular weak form of the Cauchy's first equation of motion in which the arbitrary function is a virtual displacement.

A.2.1.1 Notion of virtual displacement field

The virtual displacement field, referred to as $\delta\mathbf{u}$, is assumed to be an *arbitrary*, *infinitesimal*, and *virtual change* such that

$$\delta\mathbf{u} \; = \; \mathbf{u}^\star - \mathbf{u} \; = \; \varepsilon \, \mathbf{w} \,, \tag{A.16}$$

where ε is a scalar value which tends towards 0 ($\varepsilon \rightarrow 0$), $\mathbf{u}^\star$ is the modified displacement vector field which characterizes the virtual configuration, $\Omega^\star$, induced by $\mathbf{w}$ which is an arbitrary vector field (Fig. A.3). In addition, the variation of the time-dependent displacement vector field, $\delta\mathbf{u}$, is performed at a *fixed* instant of time t. Now, substituting $\delta\mathbf{u}$ for $\boldsymbol{\eta}$ into Eq. (A.13) and taking into account the symmetry of the Cauchy stress tensor, the PVW in the spatial description expressed in terms of $\delta\mathbf{u}$ can be written in the following form:

$$\begin{aligned} f\left(\mathbf{u}, \delta\mathbf{u}\right) \; = \; & \int_\Omega \left[\frac{1}{2} \boldsymbol{\sigma} : \left(\mathrm{grad}^{\mathrm{T}} \, \delta\mathbf{u} + \mathrm{grad} \, \delta\mathbf{u} \right) - \rho \left(\mathbf{b} - \ddot{\mathbf{u}} \right) \cdot \delta\mathbf{u} \right] \mathrm{d}\mathcal{V} \\ & - \int_{\partial\Omega_{\boldsymbol{\sigma}}} \bar{\mathbf{t}} \cdot \delta\mathbf{u} \, \mathrm{d}\mathcal{A} \; = \; 0 \,, \end{aligned} \tag{A.17}$$

with the following associated ICs:

$$\int_\Omega \mathbf{u}|_{t=0} \cdot \delta\mathbf{u}\,\mathrm{d}\mathcal{V} = \int_\Omega \mathbf{u}_0 \cdot \delta\mathbf{u}\,\mathrm{d}\mathcal{V}\,, \tag{A.18}$$

$$\int_\Omega \dot{\mathbf{u}}|_{t=0} \cdot \delta\mathbf{u}\,\mathrm{d}\mathcal{V} = \int_\Omega \dot{\mathbf{u}}_0 \cdot \delta\mathbf{u}\,\mathrm{d}\mathcal{V}\,. \tag{A.19}$$

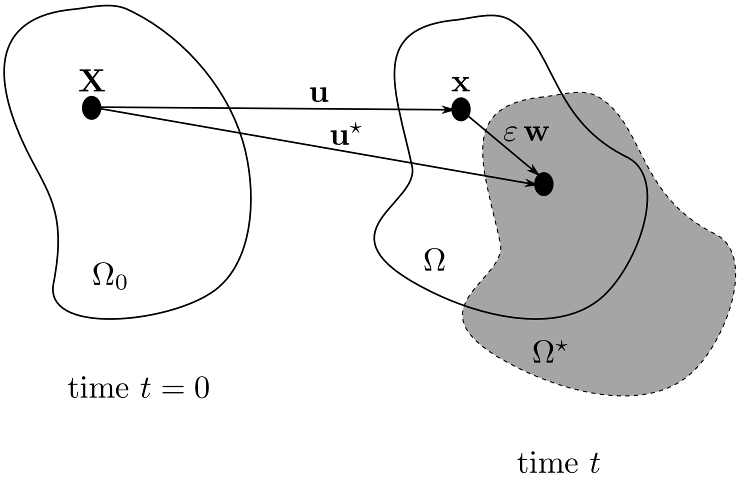

Fig. A.3 – Virtual slightly modified deformed configuration $\Omega^\star$ in the neighborhood of u induced by an arbitrary vector field w.

Note that the virtual displacement field, $\delta\mathbf{u}$, is a *kinematically admissible displacement field*[1]. In addition, Eq. (A.17) can be formulated in terms of the so-called *internal virtual work*, δW_{int}, and *external virtual work*, δW_{ext}:

$$\int_\Omega \rho\,\ddot{\mathbf{u}} \cdot \delta\mathbf{u}\,\mathrm{d}\mathcal{V} + \delta W_{\mathrm{int}} = \delta W_{\mathrm{ext}}\,. \tag{A.20}$$

Using the *Euler–Almansi strain tensor*, $\mathbf{e}$, δW_{int} and δW_{ext} can be written as

$$\begin{aligned} \delta W_{int} &= \int_\Omega \left[\frac{1}{2}\boldsymbol{\sigma} : \left(\mathrm{grad}^{\mathrm{T}}\,\delta\mathbf{u} + \mathrm{grad}\,\delta\mathbf{u}\right)\right]\,\mathrm{d}\mathcal{V} \\ &= \int_\Omega \left[\boldsymbol{\sigma} : \delta\mathbf{e}\right]\,\mathrm{d}\mathcal{V}\,, \end{aligned} \tag{A.21}$$

$$\delta W_{ext} = \int_\Omega \mathbf{b} \cdot \delta\mathbf{u}\,\mathrm{d}\mathcal{V} + \int_{\partial\Omega_{\boldsymbol{\sigma}}} \bar{\mathbf{t}} \cdot \delta\mathbf{u}\,\mathrm{d}\mathcal{A}\,. \tag{A.22}$$

In the case where data depend on time and the acceleration is assumed to vanish, namely $\ddot{\mathbf{u}} = \mathbf{0}$, the considered problem is called *quasi-static* and the PVW states that

---

[1] A kinematically admissible displacement field is one satisfying any prescribed displacement boundary conditions and possessing continuous first partial derivatives in the interior of the body [49].

the internal virtual work equals the external virtual work:

$$\delta W_{\text{int}} \;=\; \delta W_{\text{ext}}\,. \tag{A.23}$$

Note that, in the PVW, stresses and forces are assumed to remain unchanged during the virtual displacement.

A.2.2 PVW in material description on the reference configuration

Taking into account Eqs (3.107) and (3.136), the PVW [Eq. (A.17)] can be written in the material description in terms of the PK1 stress tensor:

$$\begin{aligned} \mathcal{F}\left(\mathbf{U},\delta\mathbf{U}\right) \;=\; & \int_{\Omega_0}\Big[\mathbf{P} : \mathrm{Grad}\,\delta\mathbf{U} - \rho_0\left(\mathbf{B}-\ddot{\mathbf{U}}\right)\cdot\delta\mathbf{U}\Big]\,\mathrm{d}\mathcal{V}_0 \\ & -\int_{\partial\Omega_{0\,\boldsymbol{\sigma}}}\bar{\mathbf{T}}\cdot\delta\mathbf{U}\,\mathrm{d}\mathcal{A}_0 \;=\; 0\,, \end{aligned} \tag{A.24}$$

where $\mathbf{T}$ is the traction vector associated with the PK1 stress tensor, $\mathbf{P}$. Using the relation $\mathbf{F}\cdot\mathbf{S}=\mathbf{P}$ [Eq. (3.141)], where $\mathbf{S}$ is the PK2 stress tensor, Eq. (A.24) can also be written as

$$\begin{aligned} \mathcal{F}\left(\mathbf{U},\delta\mathbf{U}\right) \;=\; & \int_{\Omega_0}\Big[(\mathbf{F}\cdot\mathbf{S}) : \mathrm{Grad}\,\delta\mathbf{U} - \rho_0\left(\mathbf{B}-\ddot{\mathbf{U}}\right)\cdot\delta\mathbf{U}\Big]\,\mathrm{d}\mathcal{V}_0 \\ & -\int_{\partial\Omega_{0\,\boldsymbol{\sigma}}}\bar{\mathbf{T}}^{\star}\cdot\delta\mathbf{U}\,\mathrm{d}\mathcal{A}_0 \;=\; 0\,, \end{aligned} \tag{A.25}$$

where $\mathbf{T}^{\star}$ is the traction vector associated with the PK2 stress tensor, $\mathbf{S}$. Moreover, it is important to note that the three different formulations of the PVW given by Eqs (A.17), (A.24), and (A.25) are completely equivalent.

APPENDIX **B**

Numerical issues

Contents

B.1 Global interpolations

Consider a one-dimensional function of the independent variable x and assume that the value, f, of this function, $f\left(x\right)$, is known at a set of N points, namely x_0, x_1, $\ldots$, x_{N-2}, x_{N-1} with $x_0 < x_1 < \ldots < x_{N-2} < x_{N-1}$. In other words, the N pairs constituted by x_i and $f_i = f\left(x_i\right)$ with $i = 0,\ 1,\ \ldots\ ,\ N-2,\ N-1$ are known. In some cases, it is useful to know the value of the function in an arbitrary point inside the interval bounded by x_0 and x_{N-1}: in any $x \in [x_0, x_{N-1}]$. This problem is called *interpolation*. From a conceptual point of view, the interpolation process can be split into two steps. First, an *interpolating function*, $\hat{f}\left(x\right)$, must be fitted to the N data points provided (x_0, x_1, $\ldots$, x_{N-2}, x_{N-1}) and second, the considered interpolating function at the desired target point must be evaluated.

In a general way, the interpolating function can be written in terms of N unknown coefficients, α_k, and N *basis functions*, $\phi_k\left(x\right)$ ($k = 0,\ 1,\ \ldots\ ,\ N-2,\ N-1$), which are known:

$$f\left(x\right) \approx \hat{f}\left(x\right) = \sum_{k=0}^{N-1} \alpha_k\, \phi_k\left(x\right). \tag{B.1}$$

The N unknown coefficients, α_k, are found by imposing the following N relations:

$$\hat{f}\left(x_i\right) = \sum_{k=0}^{N-1} \alpha_k\, \phi_k\left(x_i\right) = f_i\,. \tag{B.2}$$

B.1.1 Lagrange interpolation

A *Lagrange polynomial* of degree n is defined by the following relation:

$$\mathcal{L}_j^n\left(x\right) = \prod_{i=0,\ i\neq j}^{n} \frac{x - x_i}{x_j - x_i}\,. \tag{B.3}$$

As an example, the three Lagrange polynomials of degree two ($n = 2$) are explicitly written as follows:

$$\mathcal{L}_0^2(x) = \frac{(x - x_1)(x - x_2)}{(x_0 - x_1)(x_0 - x_2)}, \tag{B.4}$$

$$\mathcal{L}_1^2(x) = \frac{(x - x_0)(x - x_2)}{(x_1 - x_0)(x_1 - x_2)}, \tag{B.5}$$

$$\mathcal{L}_2^2(x) = \frac{(x - x_0)(x - x_1)}{(x_2 - x_0)(x_2 - x_1)}. \tag{B.6}$$

Note that the Lagrange polynomials of degree n satisfy the relations

$$\mathcal{L}_j^n(x_k) = \delta_{j\,k}, \tag{B.7}$$

where δ represents the *Kronecker symbol* and $\delta_{j\,k}$ is equal to 1 if $j = k$ else 0 if $j \neq k$. Using the Lagrange polynomials as basis functions, the interpolating function is written as

$$\hat{f}(x) = \sum_{k=0}^{N-1} \alpha_k\, \mathcal{L}_k^{N-1}(x). \tag{B.8}$$

Due to the properties of the Lagrange polynomials, $\alpha_k = f_k = f(x_k)$. Therefore, Eq. (B.8) can be rewritten as

$$\hat{f}(x) = \sum_{k=0}^{N-1} f(x_k)\, \mathcal{L}_k^{N-1}(x). \tag{B.9}$$

B.1.2 Hermite interpolation

In this section, the *Hermite interpolation*, where both function and derivatives are involved in the process, is introduced. As before, assume that the value, f, of the function $f(x)$ is known at a set of N points (x_0, x_1, … , x_{N-2}, x_{N-1}). Moreover, assume also that its first derivative is known at each point. Therefore, a polynomial interpolating function, $\hat{f}(x)$, which satisfy the $2\,N$ constraints

$$\hat{f}(x_k) = f(x_k), \tag{B.10}$$

$$\frac{\mathrm{d}\hat{f}(x_k)}{\mathrm{d}x} = \frac{\mathrm{d}f(x_k)}{\mathrm{d}x}, \tag{B.11}$$

with $k = 0, 1, \ldots, N-2, N-1$ must be constructed. As a result, the unique polynomial interpolating function of least degree agreeing with Eqs (B.10) and (B.11) is the polynomial of degree at most $2\,N-1$ given by

$$\hat{f}(x) = \sum_{k=0}^{N-1} f(x_k)\,\mathcal{H}_k^{N-1}(x) + \sum_{k=0}^{N-1} \frac{\mathrm{d}f(x_k)}{\mathrm{d}x}\,\tilde{\mathcal{H}}_k^{N-1}(x)\,, \tag{B.12}$$

with

$$\mathcal{H}_k^{N-1}(x) = \left[1 - 2\,(x - x_k)\,\frac{\mathrm{d}\mathcal{L}_k^{N-1}(x_k)}{\mathrm{d}x}\right]\left[\mathcal{L}_k^{N-1}(x)\right]^2\,, \tag{B.13}$$

$$\tilde{\mathcal{H}}_k^{N-1}(x) = (x - x_k)\left[\mathcal{L}_k^{N-1}(x)\right]^2\,. \tag{B.14}$$

Note that the Lagrange polynomials used in Eqs (B.13) and (B.14) have been already defined in section B.1.1.

B.2 Local interpolations

B.2.1 Local or natural coordinate system

To introduce the *local coordinate system*, a one-dimensional case is assumed and an element delimited by the nodes x_a and x_b is considered.

From a computational point of view, it is convenient to define a *local* or *natural coordinate system* with respect to each element. For the present element, $x \in [x_a,\, x_b]$ in terms of the global coordinates. The procedure consisting in using one of the following changes of variables

$$x = x_a + \xi\,(x_b - x_a)\,, \tag{B.15}$$

$$x = \frac{1}{2}\,(x_b - x_a)\,\xi^\star + \frac{1}{2}\,(x_a + x_b)\,, \tag{B.16}$$

where $\xi \in [0,\, 1]$ and $\xi^\star \in [-1,\, +1]$, enables to define one kind of shape functions independently of the discretization used and thus to systematize the computations.

B.2.2 Lagrange one-dimensional basis functions in the ξ-coordinate system

Using the local coordinate system defined by Eq. (B.15) in a one-dimensional case and assuming an element involving two data points, an arbitrary field $f\left(\xi\right)$ can be interpolated by an interpolating function in the present element in terms of its two nodal values $f\left(0\right)$ and $f\left(1\right)$ as follows:

$$\hat{f}\left(\xi\right) = f\left(0\right)\ \mathcal{L}_0^1\left(\xi\right) + f\left(1\right)\ \mathcal{L}_1^1\left(\xi\right)\ , \tag{B.17}$$

where the two first-order Lagrange polynomials (Fig. B.1a) are given by

$$\mathcal{L}_0^1\left(\xi\right) = 1-\xi\,, \tag{B.18}$$

$$\mathcal{L}_1^1\left(\xi\right) = \xi\,. \tag{B.19}$$

In a similar way, assuming a three data points element, the interpolating function $\hat{f}\left(\xi\right)$ is written in terms of the three nodal values $f\left(0\right)$, $f\left(1/2\right)$, and $f\left(1\right)$ in the following way:

$$\hat{f}\left(\xi\right) = f\left(0\right)\ \mathcal{L}_0^2\left(\xi\right) + f\left(1/2\right)\ \mathcal{L}_2^2\left(\xi\right) + f\left(1\right)\ \mathcal{L}_1^2\left(\xi\right)\ , \tag{B.20}$$

where the three second-order Lagrange polynomials (Fig. B.1b) with respect to the ξ-coordinate system are written as

$$\mathcal{L}_0^2\left(\xi\right) = \left(\xi-1\right)\left(2\,\xi-1\right), \tag{B.21}$$

$$\mathcal{L}_1^2\left(\xi\right) = \xi\left(2\,\xi-1\right), \tag{B.22}$$

$$\mathcal{L}_2^2\left(\xi\right) = 4\,\xi\left(1-\xi\right). \tag{B.23}$$

B.2.3 Hermite one-dimensional basis functions in the ξ-coordinate system

Assuming a two data points element bounded by x_a and x_b in the global coordinate system ($x \in [x_a, x_b]$ within the element) and using the ξ-coordinate system, the interpolating function $\hat{f}\left(\xi\right)$ is written, in terms of the four cubic Hermite shape functions

(Fig. B.2), as follows:

$$\hat{f}(\xi) = f(0)\,\mathcal{H}_0^1(\xi) + \left.\frac{\mathrm{d}f}{\mathrm{d}\xi}\right|_{\xi=0} \tilde{\mathcal{H}}_0^1(\xi) + f(1)\,\mathcal{H}_1^1(\xi) + \left.\frac{\mathrm{d}f}{\mathrm{d}\xi}\right|_{\xi=1} \tilde{\mathcal{H}}_1^1(\xi)\,, \quad \text{(B.24)}$$

where

$$\begin{aligned} \mathcal{H}_0^1(\xi) &= (1-\xi)^2\,(1+2\,\xi)\,, && \text{(B.25)}\\ \tilde{\mathcal{H}}_0^1(\xi) &= (1-\xi)^2\,\xi\,, && \text{(B.26)}\\ \mathcal{H}_1^1(\xi) &= \xi^2\,(3-2\,\xi)\,, && \text{(B.27)}\\ \tilde{\mathcal{H}}_1^1(\xi) &= \xi^2\,(1-\xi)\,. && \text{(B.28)} \end{aligned}$$

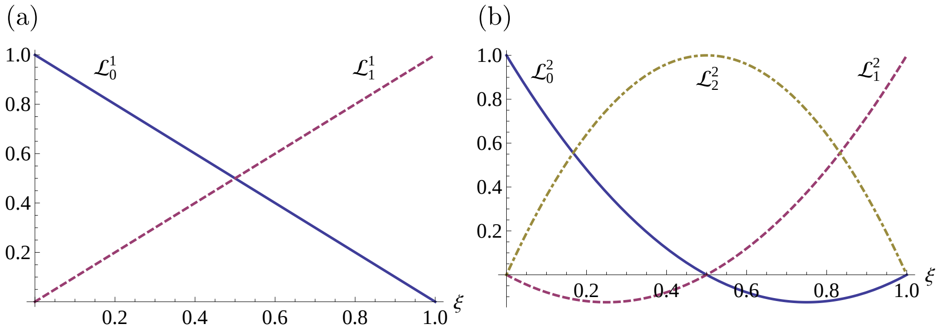

Fig. B.1 – Linear (a) and quadratic (b) Lagrange basis functions in terms of the ξ-coordinate.

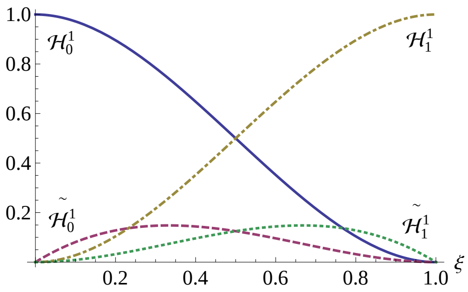

Fig. B.2 – Cubic Hermite basis functions in terms of the ξ-coordinate.

B.2.4 Lagrange basis functions in two dimensions

To generalize in a higher spatial dimension, assume a two-dimensional square element such that $\xi \in [0,1]$ and $\eta \in [0,1]$ and considering a discretization of ξ and η involving $m+1$ equidistant nodes (namely $\xi_i = i/m$ and $\eta_j = j/m$ with $i = 0, 1, \ldots, m-1, m$ and

$j = 0, 1, \dots, m-1, m$). In this context, a two-dimensional field $f(\xi, \eta)$ is interpolated in terms of the $(m+1) \times (m+1)$ nodal values of the present field within the element as follows:

$$\hat{f}(\xi, \eta) = \sum_{j=0}^{m} \sum_{i=0}^{m} f(\xi_i, \eta_j)\, \mathcal{L}_i^m(\xi)\, \mathcal{L}_j^m(\eta)\,. \tag{B.29}$$

In the case where $m = 1$ and $m = 2$, the two-dimensional basis functions are called *bilinear* and *biquadratic*, respectively.

B.2.5 Hermite basis functions in two dimensions

Assuming the same kind of element (square) with $m = 1$, a two-dimensional field $f(\xi, \eta)$ is interpolated with *bicubic Hermite basis functions* as follows:

$$\begin{aligned} \hat{f}(\xi, \eta) = \sum_{j=0}^{1} \sum_{i=0}^{1} & f(\xi_i, \eta_j)\, \mathcal{H}_i^1(\xi)\, \mathcal{H}_j^1(\eta) \\ & + \left.\frac{\partial f}{\partial \xi}\right|_{(\xi_i, \eta_j)} \tilde{\mathcal{H}}_i^1(\xi)\, \mathcal{H}_j^1(\eta) \\ & + \left.\frac{\partial f}{\partial \eta}\right|_{(\xi_i, \eta_j)} \mathcal{H}_i^1(\xi)\, \tilde{\mathcal{H}}_j^1(\eta) \\ & + \left.\frac{\partial^2 f}{\partial \xi\, \partial \eta}\right|_{(\xi_i, \eta_j)} \tilde{\mathcal{H}}_i^1(\xi)\, \tilde{\mathcal{H}}_j^1(\eta)\,. \end{aligned} \tag{B.30}$$

As shown in Eq. (B.30), the bicubic Hermite interpolation requires four parameters per node.

Bibliography

[1] A. Alwan. *Global status report on noncommunicable diseases 2010*. World Health Organization, 2011.

[2] C. Mathers and D. Loncar. Projections of global mortality and burden of disease from 2002 to 2030. *PLoS medicine*, 3(11):e442, 2006.

[3] M. Franz. Mechano-electrical feedback in ventricular myocardium. *Cardiovascular Research*, 32(1):15–24, 1996.

[4] S. Nazir and M. Lab. Mechanoelectric feedback and atrial arrhythmias. *Cardiovascular Research*, 32(1):52–61, 1996.

[5] M. Lab. Contraction-excitation feedback in myocardium. Physiological basis and clinical relevance. *Circulation Research*, 50(6):757–766, 1982.

[6] D. Bers. Cardiac excitation-contraction coupling. *Nature*, 415(6868):198–205, 2002.

[7] F. Sachse, G. Hunter, D. Weiss, and G. Seemann. A framework for modeling of mechano-electrical feedback mechanisms of cardiac myocytes and tissues. In

Engineering in Medicine and Biology Society, 2007. EMBS 2007. 29th Annual International Conference of the IEEE, pages 160–163, 2007.

[8] M. Hägerdal, J. Harp, L. Nilsson, and B. Siesjöu. The effect of induced hypothermia upon oxygen consumption in the rat brain. *Journal of Neurochemistry*, 24(2):311–316, 1975.

[9] C. Palmer, R. Vannucci, M. Christensen, and R. Brucklacher. Regional cerebral blood flow and glucose utilization during hypothermia in newborn dogs. *Anesthesiology*, 71(5):730–737, 1989.

[10] M. Erecinska, M. Thoresen, and I. Silver. Effects of hypothermia on energy metabolism in mammalian central nervous system. *Journal of Cerebral Blood Flow and Metabolism*, 23(5):513–530, 2003.

[11] M. Carrier, A. Tourigny, N. Thoribé, M. Montpetit, A. Khalil, B. Solymoss, and L. Pelletier. Effects of cold and warm blood cardioplegia assessed by myocardial ph and release of metabolic markers. *The Annals of Thoracic Surgery*, 58(3):764–767, 1994.

[12] G. Chien, R. Wolff, R. Davis, and D. Van Winkle. Şnormothermic rangeŤ temperature affects myocardial infarct size. *Cardiovascular Research*, 28(7):1014–1017, 1994.

[13] X.-H. Ning, C.-S. Xu, Y. Song, Y. Xiao, Y.-J. Hu, F. Lupinetti, and M. Portman. Hypothermia preserves function and signaling for mitochondrial biogenesis during subsequent ischemia. *American Journal of Physiology - Heart and Circulatory Physiology*, 274(3):H786–H793, 1998.

[14] X.-H. Ning, C.-S. Xu, and M. Portman. Mitochondrial protein and hsp70 signaling after ischemia in hypothermic-adapted hearts augmented with glucose. *American Journal of Physiology - Regulatory, Integrative and Comparative Physiology*, 277(1):R11–R17, 1999.

[15] X.-H. Ning, S.-H. Chen, C.-S. Xu, L. Li, L. Yao, K. Qian, J. Krueger, O. Hyyti, and M. Portman. Selected contribution: Hypothermic protection of the ischemic heart via alterations in apoptotic pathways as assessed by gene array analysis.

Journal of Applied Physiology, 92(5):2200–2207, 2002.

[16] A. Hodgkin and A. Huxley. A quantitative description of membrane current and its application to conduction and excitation in nerve. *Journal of Physiology*, 117(4):500–544, 1952.

[17] R. FitzHugh. Impulses and physiological states in theoretical models of nerve membrane. *Biophysical Journal*, 1(6):445–466, 1961.

[18] J. Rogers and A. McCulloch. A collocation-Galerkin finite element model of cardiac action potential propagation. *IEEE Transactions on Biomedical Engineering*, 41(8):743–757, 1994.

[19] R. Aliev and A. Panfilov. A simple two-variable model of cardiac excitation. *Chaos, Solitons & Fractals*, 7(3):293–301, 1996.

[20] F. Fenton and A. Karma. Vortex dynamics in three-dimensional continuous myocardium with fiber rotation: Filament instability and fibrillation. *Chaos*, 8(1):20–47, 1998.

[21] P. Hunter, A. McCulloch, and H. ter Keurs. Modelling the mechanical properties of cardiac muscle. *Progress in Biophysics and Molecular Biology*, 69(2-3):289–331, 1998.

[22] A. Guyton and J. Hall. *Medical physiology.* Elsevier Saunders, 2006.

[23] J. Keener and J. Sneyd. *Mathematical physiology.* Springer, 2009.

[24] W. Echevarría and M. Nathanson. Gap junctions in the liver. *Molecular Pathogenesis of Cholestasis*, pages 36–47, 2004.

[25] B. Hille. *Ion channels of excitable membranes.* Sinauer Associates, Inc., 2001.

[26] P. Iaizzo and T. Laske. *Anatomy and Physiology of the Cardiac Conduction System*, pages 73–89. Springer, 2010.

[27] A. Katz. *Physiology of the Heart.* Wolters Kluwer Health, 2011.

[28] F. Sachse. *Computational cardiology: modeling of anatomy, electrophysiology, and mechanics*, volume 2966. Springer, 2004.

[29] A. Pullan, L. Cheng, and M. Buist. *Mathematically modelling the electrical activity of the heart: from cell to body surface and back again.* World Scientific, 2005.

[30] A. Hodgkin, A. Huxley, and B. Katz. Measurement of current-voltage relations in the membrane of the giant axon of Loligo. *Journal of Physiology*, 116(4):424–448, 1952.

[31] A. Hodgkin and A. Huxley. Currents carried by sodium and potassium ions through the membrane of the giant axon of Loligo. *Journal of Physiology*, 116(4):449–472, 1952.

[32] A. Hodgkin and A. Huxley. The components of membrane conductance in the giant axon of Loligo. *Journal of Physiology*, 116(4):473–496, 1952.

[33] A. Hodgkin and A. Huxley. The dual effect of membrane potential on sodium conductance in the giant axon of Loligo. *Journal of Physiology*, 116(4):497–506, 1952.

[34] D. Noble, A. Varghese, P. Kohl, and P. Noble. Improved guinea-pig ventricular cell model incorporating a diadic space, ikr and iks, and length- and tension-dependent processes. *Canadian Journal of Cardiology*, 14(1):123–134, 1998.

[35] N. Lovell, S. Cloherty, B. Celler, and S. Dokos. A gradient model of cardiac pacemaker myocytes. *Progress in Biophysics and Molecular Biology*, 85(2):301–323, 2004.

[36] M. Courtemanche, R. Ramirez, and S. Nattel. Ionic mechanisms underlying human atrial action potential properties: insights from a mathematical model. *American Journal of Physiology*, 275(1):H301–H321, 1998.

[37] D. Noble. A modification of the Hodgkin-Huxley equations applicable to purkinje fibre action and pace-maker potentials. *Journal of Physiology*, 160(2):317–352, 1962.

[38] K. ten Tusscher, D. Noble, P. Noble, and A. Panfilov. A model for human ventricular tissue. *American Journal of Physiology - Heart and Circulatroy Physiology*, 286(4):H1573–H1589, 2004.

[39] S. Strogatz. *Nonlinear dynamics and chaos: with applications to physics, biology, chemistry, and engineering.* Westview Press, 2001.

[40] R. FitzHugh. Thresholds and Plateaus in the Hodgkin-Huxley Nerve Equations. *Journal of General Physiology*, 43(5):867–896, 1960.

[41] J. Sundnes, G. Lines, X. Cai, B. Nielsen, K.-A. Mardal, and A. Tveito. *Computing the Electrical Activity in the Heart.* Springer, 2006.

[42] C. Luo and Y. Rudy. A dynamic model of the cardiac ventricular action potential. I. Simulations of ionic currents and concentration changes. *Circulation Research*, 74(6):1071–1096, 1994.

[43] R. Plonsey and D. Heppner. Considerations of quasi-stationarity in electrophysiological systems. *Bulletin of Mathematical Biology*, 29(4):657–664, 1967.

[44] L. Tung. *A bi-domain model for describing ischemic myocardial d-c potentials.* PhD thesis, Massachusetts Institute of Technology, 1978.

[45] D. Geselowitz and W. Miller. A bidomain model for anisotropic cardiac muscle. *Annals of Biomedical Engineering*, 11(3):191–206, 1983.

[46] C. Henriquez. Simulating the electrical behavior of cardiac tissue using the bidomain model. *Critical Reviews in Biomedical Engineering*, 21(1):1–77, 1993.

[47] E. Remme, M. Nash, and P. Hunter. Distributions of myocyte stretch, stress and work in models of normal and infarcted ventricles. *Cardiac Mechano-Electric Feedback and Arrhythmias: From Pipette to Patient. Saunders-Elsevier*, 2005.

[48] C. Truesdell. *A first course in rational continuum mechanics*, volume 71. Access Online via Elsevier, 1992.

[49] L. Malvern. *Introduction to the mechanics of a continuous medium.* Prentice-Hall International, 1969.

[50] G. Holzapfel and R. Ogden. Constitutive modelling of passive myocardium: a structurally based framework for material characterization. *Philosophical Transactions of the Royal Society. Series A*, 367(1902):3445–3475, 2009.

[51] G. Holzapfel. *Nonlinear Solid Mechanics: A Continuum Approach for Engineering*. John Wiley & Sons Ltd., 2000.

[52] P. Flory. Thermodynamic relations for high elastic materials. *Transactions of the Faraday Society*, 57(0):829–838, 1961.

[53] M. Mooney. A theory of large elastic deformation. *Journal of Applied Physics*, 11(9):582–592, 1940.

[54] R. Rivlin. Large elastic deformations of isotropic materials. IV. further developments of the general theory. *Philosophical Transactions of the Royal Society of London. Series A*, 241(835):379–397, 1948.

[55] P. Ciarlet, editor. *Chapter 4 Hyperelasticity*, volume 20, pages 137–198. Elsevier, 1988.

[56] R. Ogden. Large deformation isotropic elasticity - on the correlation of theory and experiment for incompressible rubberlike solids. *Proceedings of the Royal Society of London. Series A*, 326(1567):565–584, 1972.

[57] I. LeGrice, B. Smaill, L. Chai, S. Edgar, J. Gavin, and P. Hunter. Laminar structure of the heart: ventricular myocyte arrangement and connective tissue architecture in the dog. *American Journal of Physiology - Heart and Circulatory Physiology*, 269(2):H571–H582, 1995.

[58] I. LeGrice, P. Hunter, and B. Smaill. Laminar structure of the heart: a mathematical model. *American Journal of Physiology - Heart and Circulatory Physiology*, 272(5):H2466–H2476, 1997.

[59] A. Young, I. LeGrice, M. Young, and B. Smaill. Extended confocal microscopy of myocardial laminae and collagen network. *Journal of Microscopy*, 192(2):139–150, 1998.

[60] G. Sands, D. Gerneke, D. Hooks, C. Green, B. Smaill, and I. LeGrice. Automated imaging of extended tissue volumes using confocal microscopy. *Microscopy Research and Technique*, 67(5):227–239, 2005.

[61] J. Frank and G. Langer. The myocardial interstitium: its structure and its role

in ionic exchange. *The Journal of cell biology*, 60(3):586–601, 1974.

[62] S. Dokos, B. Smaill, A. Young, and I. LeGrice. Shear properties of passive ventricular myocardium. *American Journal of Physiology - Heart and Circulatory Physiology*, 283(6):H2650–H2659, 2002.

[63] L. Demer and F. Yin. Passive biaxial mechanical properties of isolated canine myocardium. *Journal of Physiology*, 339:615–630, 1983.

[64] F. Yin, R. Strumpf, P. Chew, and S. Zeger. Quantification of the mechanical properties of noncontracting canine myocardium under simultaneous biaxial loading. *Journal of Biomechanics*, 20(6):577–589, 1987.

[65] B. Smaill and P. Hunter. *Structure and function of the diastolic heart: material properties of passive myocardium*, pages 1–29. Springer, 1991.

[66] V. Novak, F. Yin, and J. Humphrey. Regional mechanical properties of passive myocardium. *Journal of Biomechanics*, 27(4):403–412, 1994.

[67] J. Vossoughi, R. Vaishnav, and D. Patel. Compressibility of the myocardial tissue. *Advances in Bioengineering*, pages 45–48, 1980.

[68] M. Nash and P. Hunter. Computational mechanics of the heart. *Journal of Elasticity*, 61(1):113–141, 2000.

[69] M. Nash and A. Panfilov. Electromechanical model of excitable tissue to study reentrant cardiac arrhythmias. *Progress in Biophysics and Molecular Biology*, 85(2-3):501–522, 2004.

[70] D. Nordsletten, S. Niederer, M. Nash, P. Hunter, and N. Smith. Coupling multiphysics models to cardiac mechanics. *Progress in Biophysics and Molecular Biology*, 104(1-3):77–88, 2011.

[71] J. Whiteley, M. Bishop, and D. Gavaghan. Soft tissue modelling of cardiac fibres for use in coupled mechano-electric simulations. *Bulletin of Mathematical Biology*, 69(7):2199–2225, 2007.

[72] N. Trayanova and J. Rice. Cardiac electromechanical models: from cell to organ. *Frontiers in Physiology*, 2(43):1–19, 2011.

[73] S. Campbell, S. Flaim, C. Leem, and A. McCulloch. Mechanisms of transmurally varying myocyte electromechanics in an integrated computational model. *Philosophical Transactions of the Royal Society. Series A*, 366(1879):3361–3380, 2008.

[74] D. Bers. *Excitation-contraction coupling and cardiac contractile force.* Springer, 2001.

[75] P. de Tombe. Cardiac myofilaments: mechanics and regulation. *Journal of Biomechanics*, 36(5):721–730, 2003.

[76] P. Kohl and F. Sachse. Mechanoelectric feedback in cardiac cells. *Philosophical Transactions of the Royal Society of London. Series A*, 359(1783):1173–1185, 2001.

[77] F. Sachse. *Modeling mechanical-electrical transduction in the heart*, pages 308–328. Springer, 1994.

[78] P. Kohl, K. Day, and D. Noble. Cellular mechanisms of cardiac mechano-electric feedback in a mathematical model. *Canadian Journal of Cardiology*, 14(1):111–119, 1998.

[79] F. Guharay and F. Sachse. Stretch-activated single ion channel currents in tissue-cultured embryonic chick skeletal muscle. *Journal of Physiology*, 352(1):685–701, 1984.

[80] A. Fabiato and F. Fabiato. Dependence of the contractile activation of skinned cardiac cells on the sarcomere length. *Nature*, 256:54–56, 1975.

[81] H. Hu and F. Sachse. Stretch-activated ion channels in the heart. *Journal of Molecular and Cellular Cardiology*, 29(6):1511–1523, 1997.

[82] W. Craelius, V. Chen, and N. El-Sherif. Stretch activated ion channels in ventricular myocytes. *Bioscience Reports*, 8(5):407–414, 1988.

[83] D. Kim. A mechanosensitive k+ channel in heart cells. activation by arachidonic acid. *Journal of General Physiology*, 100(6):1021–1040, 1992.

[84] P. Kohl, P. Hunter, and D. Noble. Stretch-induced changes in heart rate and

rhythm: clinical observations, experiments and mathematical models. *Progress in Biophysics and Molecular Biology*, 71(1):91–138, 1999.

[85] A. Nesbitt, P. Cooper, and P. Kohl. Rediscovering commotio cordis. *The Lancet*, 357(9263):1195–1197, 2001.

[86] P. Cooper, M. Lei, L.-X. Cheng, and P. Kohl. Selected contribution: axial stretch increases spontaneous pacemaker activity in rabbit isolated sinoatrial node cells. *Journal of Applied Physiology*, 89(5):2099–2104, 2000.

[87] D. Allen and S. Kurihara. The effects of muscle length on intracellular calcium transients in mammalian cardiac muscle. *Journal of Physiology*, 327(1):79–94, 1982.

[88] D. Allen and J. Kentish. The cellular basis of the length-tension relation in cardiac muscle. *Journal of Molecular and Cellular Cardiology*, 17(9):821–840, 1985.

[89] J. Kentish and A. Wrzosek. Changes in force and cytosolic Ca^{2+} concentration after length changes in isolated rat ventricular trabeculae. *Journal of Physiology*, 506(2):431–444, 1998.

[90] E. White, J. Le Guennec, J. Nigretto, F. Gannier, J. Argibay, and D. Garnier. The effects of increasing cell length on auxotonic contractions; membrane potential and intracellular calcium transients in single guinea-pig ventricular myocytes. *Experimental Physiology*, 78(1):65–78, 1993.

[91] J. Gamble, P. Taylor, and K. Kenno. Myocardial stretch alters twitch characteristics and Ca^{2+} loading of sarcoplasmic reticulum in rat ventricular muscle. *Cardiovascular Research*, 26(9):865–870, 1992.

[92] R. Bremel and A. Weber. Cooperation within actin filament in vertebrate skeletal muscle. *Nature*, 238(82):97–101, 1972.

[93] C. Butters, K. Willadsen, and L. Tobacman. Cooperative interactions between adjacent troponin-tropomyosin complexes may be transmitted through the actin filament. *Journal of Biological Chemistry*, 268(21):15565–15570, 1993.

[94] E. Alvarez-Lacalle and B. Echebarria. Global coupling in excitable media provides a simplified description of mechanoelectrical feedback in cardiac tissue. *Physical Review E*, 79(3):031921, 2009.

[95] S. Göktepe and E. Kuhl. Electromechanics of the heart: a unified approach to the strongly coupled excitation-contraction problem. *Computational Mechanics*, 45(2):227–243, 2010.

[96] R. Clayton, O. Bernus, E. Cherry, H. Dierckx, F. Fenton, L. Mirabella, A. Panfilov, F. Sachse, G. Seemann, and H. Zhang. Models of cardiac tissue electrophysiology: Progress, challenges and open questions. *Progress in Biophysics and Molecular Biology*, 104(1-3):22–48, 2011.

[97] M. Zabel, B. Koller, F. Sachse, and M. Franz. Stretch-induced voltage changes in the isolated beating heart: importance of the timing of stretch and implications for stretch-activated ion channels. *Cardiovascular Research*, 32(1):120–130, 1996.

[98] A. Panfilov, R. Keldermann, and M. Nash. Self-organized pacemakers in a coupled reaction-diffusion-mechanics system. *Physical Review Letters*, 95(25):258104, 2005.

[99] F. Sachse, C. Riedel, G. Seemann, and C. Werner. Stretch activated ion channels in myocytes: parameter estimation, simulations and phenomena. In *Engineering in Medicine and Biology Society, 2001. Proceedings of the 23rd Annual International Conference of the IEEE*, volume 1, pages 52–55, 2001.

[100] A. Panfilov, R. Keldermann, and M. Nash. Drift and breakup of spiral waves in reaction-diffusion-mechanics systems. *Proceedings of the National Academy of Sciences of the United States of America*, 104(19):7922–7926, 2007.

[101] R. FitzHugh. Theoretical effect of temperature on threshold in the Hodgkin-Huxley nerve model. *Journal of General Physiology*, 49(5):989–1005, 1966.

[102] D. Bini, C. Cherubini, and S. Filippi. Heat transfer in Fitzhugh-Nagumo models. *Physical Review E*, 74(4):041905, 2006.

[103] R. Keldermann, M. Nash, and A. Panfilov. Pacemakers in a reaction-diffusion mechanics system. *Journal of Statistical Physics*, 128(1):375–392, 2007.

[104] W. Hundsdorfer and J. Verwer. *Numerical solution of time-dependent advection-diffusion-reaction equations*, volume 33. Springer, 2003.

[105] J. Cash and A. Karp. A variable order Runge-Kutta method for initial value problems with rapidly varying right-hand sides. *ACM Transactions on Mathematical Software*, 16(3):201–222, 1990.

[106] J. Butcher. *The numerical analysis of ordinary differential equations: Runge-Kutta and general linear methods.* Wiley-Interscience, 1987.

[107] N. Trayanova. Whole-heart modeling: applications to cardiac electrophysiology and electromechanics. *Circulation Research*, 108(1):113–128, 2011.

[108] K. Hall, D. Christini, M. Tremblay, J. Collins, L. Glass, and J. Billette. Dynamic control of cardiac alternans. *Physical Review Letters*, 78(23):4518, 1997.

[109] P. Bergé, Y. Pomeau, and C. Vidal. *L'ordre dans le chaos.* Hermann, 1984.

[110] J. Argyris, G. Faust, and M. Haase. *An exploration of chaos: an introduction for natural scientists and engineers.* North-Holland Netherlands, 1994.

[111] W. Arnoldi. The principle of minimized iterations in the solution of the matrix eigenvalue problem. *Quarterly of Applied Mathematics*, 9(1):17–29, 1951.

[112] G. Karniadakis. *Parallel scientific computing in C++ and MPI: a seamless approach to parallel algorithms and their implementation.* Cambridge University Press, 2003.

[113] R. Seydel. *From equilibrium to chaos.* Elsevier, 1988.

[114] P. Kuchment. *Floquet Theory for Partial Differential Equations: Operator Theory*, volume 60. Springer Science & Business Media, 1993.

[115] M. Wellner and O. Berenfeld. Theory of reentry. *Cardiac Electrophysiology from Cell to Bedside*, pages 317–326, 2004.

[116] J. Starobin, Y. Zilberter, E. Rusnak, and C. Starmer. Wavelet formation in excitable cardiac tissue: the role of wavefront-obstacle interactions in initiating high-frequency fibrillatory-like arrhythmias. *Biophysical Journal*, 70(2):581–594,

1996.

[117] R. Gray and J. Jalife. Spiral waves and the heart. *International Journal of Bifurcation and Chaos*, 6(03):415–435, 1996.

[118] M. Allessie, M. Schalij, C. Kirchhof, L. Boersma, M. Huybers, and J. Hollen. Experimental electrophysiology and arrhythmogenicity. Anisotropy and ventricular tachycardia. *European Heart Journal*, 10(suppl E):2–8, 1989.

[119] P. Chen, A. Garfinkel, J. Weiss, and H. Karagueuzian. Computerized mapping of fibrillation in normal ventricular myocardium. *Chaos: An Interdisciplinary Journal of Nonlinear Science*, 8(1):127–136, 1998.

[120] R. Gray, A. Pertsov, and J. Jalife. Spatial and temporal organization during cardiac fibrillation. *Nature*, 392(6671):75–78, 1998.

[121] F. Witkowski, L. Leon, P. Penkoske, R. Clark, M. Spano, W. Ditto, and W. Giles. A method for visualization of ventricular fibrillation: Design of a cooled fiberoptically coupled image intensified ccd data acquisition system incorporating wavelet shrinkage based adaptive filtering. *Chaos: An Interdisciplinary Journal of Nonlinear Science*, 8(1):94–102, 1998.

[122] F. Witkowski, L. Leon, P. Penkoske, W. Giles, M. Spano, W. Ditto, and A. Winfree. Spatiotemporal evolution of ventricular fibrillation. *Nature*, 392(6671):78–82, 1998.

[123] M. Janse, F. Wilms-Schopman, and R. Coronel. Ventricular fibrillation is not always due to multiple wavelet reentry. *Journal of Cardiovascular Electrophysiology*, 6(7):512–521, 1995.

[124] S. Pogwizd, R. Hoyt, J. Saffitz, P. Corr, J. Cox, and M. Cain. Reentrant and focal mechanisms underlying ventricular tachycardia in the human heart. *Circulation*, 86(6):1872–1887, 1992.

[125] M. Courtemanche and A. Winfree. Re-entrant rotating waves in a Beeler-Reuter based model of two-dimensional cardiac electrical activity. *International Journal of Bifurcation and Chaos*, 1(02):431–444, 1991.

[126] A. Karma. Spiral breakup in model equations of action potential propagation in cardiac tissue. *Physical Review Letters*, 71(7):1103–1106, 1993.

[127] C. Bradley, A. Pullan, and P. Hunter. Geometric modeling of the human torso using cubic hermite elements. *Annals of Biomedical Engineering*, 25(1):96–111, 1997.

[128] P. Hunter, A. Pullan, and B. Smaill. Modeling total heart function. *Annual Review of Biomedical Engineering*, 5(1):147–177, 2003.

[129] A. Hindmarsh, P. Brown, K. Grant, S. Lee, R. Serban, D. Shumaker, and C. Woodward. SUNDIALS: Suite of nonlinear and differential/algebraic equation solvers. *ACM Transactions on Mathematical Software (TOMS)*, 31(3):363–396, 2005.

[130] P. Brown, A. Hindmarsh, and L. Petzold. Using krylov methods in the solution of large-scale differential-algebraic systems. *SIAM Journal on Scientific Computing*, 15(6):1467–1488, 1994.

[131] O. Schenk and K. Gärtner. Two-level dynamic scheduling in pardiso: Improved scalability on shared memory multiprocessing systems. *Parallel Computing*, 28(2):187–197, 2002.

[132] O. Schenk and K. Gärtner. Solving unsymmetric sparse systems of linear equations with pardiso. *Future Generation Computer Systems*, 20(3):475–487, 2004.